MODELING, SIMULATION, AND RATIONAL DESIGN OF POROUS SOLID OXIDE FUEL CELL CATHODES

A Thesis
Presented to
The Academic Faculty

by

Matthew E. Lynch

In Partial Fulfillment
of the Requirements for the Degree
Doctor of Philosophy in the
School of Materials Science and Engineering

Georgia Institute of Technology
December 2011

MODELING, SIMULATION, AND RATIONAL DESIGN OF POROUS SOLID OXIDE FUEL CELL CATHODES

Approved by:

Professor Meilin Liu,
Committee Chair
School of Materials Science and Engineering
Georgia Institute of Technology

Professor Yingjie Liu
School of Mathematics
Georgia Institute of Technology

Professor Arun Gokhale
School of Materials Science and Engineering
Georgia Institute of Technology

Professor David McDowell
School of Materials Science and Engineering
Georgia Institute of Technology

Professor Tom Fuller
School of Chemical and Biomolecular Engineering
Georgia Institute of Technology

Professor Hamid Garmestani
School of Materials Science and Engineering
Georgia Institute of Technology

Date Approved: 3 October 2011

To Lisa.

ACKNOWLEDGEMENTS

I would like to thank Prof. Meilin Liu, my advisor, under whose excellent guidance, leadership, and encouragement I have completed this work. I would also like to thank Dr. David Mebane for providing a great foundation and giving me technical insight and guidance throughout the process. My collaborators in experiments have contributed greatly and include Dr. Dong Ding, Dr. Mingfei Liu, Dr. Lei Yang, Dr. Wentao Qin, Kevin Blinn, Xiaxi Li, Dr. Jong-Jin Choi, Dr. Jae-Wung Lee, Dr. Xiaoyuan Lou, Dr. Ze Liu, and Dr. Songho Choi at Georgia Tech and Jeffrey Lombardo, William Harris, Dr. George Nelson, and Prof. Wilson Chiu at the University of Connecticut. I would also like to thank Dr. YongMan Choi, Xiaxi Li, Shi Feng, Parveen Sood, Andre McNeill, Wes Emeneker, and the members of my committee for very helpful discussions and advice.

This work was supported by the U.S. Department of Energy, in particular by the SECA Core Technology Program and by the HeteroFoaM Center (an Energy Frontier Research Center), and by a National Science Foundation Graduate Research Fellowship. I am very grateful for the financial support and the opportunity to work on such great projects.

I would also like to thank my parents, Larry and Sandra Lynch, for always encouraging education and teaching me to pursue it, providing the means to do so, and giving me emotional support over the many years that it has taken to come this far. I would like to thank as well my wife's parents, Mike and Cindy Mandigo. Finally, I thank my wife, Lisa Lynch, for her unfailing and generous support, encouragement, and patience throughout this process.

TABLE OF CONTENTS

LIST OF TABLES

LIST OF FIGURES

SUMMARY

Solid oxide fuel cells (SOFCs) are a promising means of generating electricity in a manner that is more efficient and environmentally friendly than traditional stationary methods. As such, SOFCs are one element of a long-term energy strategy to conserve limited resources and reduce pollution, making optimal SOFC performance good for the economy, energy independence, and the environment.

An SOFC consists of several primary ceramic components including the anode, electrolyte, and cathode. The cathode is critical to the performance of the cell and in need of further development to aid widespread SOFC commercialization. This need for improvement is especially true at intermediate temperatures where cheaper components in other parts of the fuel cell may be used. Among the main challenges facing SOFC cathodes are the activity toward the oxygen reduction reaction and the competition between active surfaces and transport pathways. Heretofore, design of SOFC cathodes has tended to be empirical owing to the lack of mechanistic understanding and multi-scale modeling tools. In order to achieve rational design, though, better fundamental understanding and quantitative engineering tools are required.

The focus of this work is the modeling, simulation, and rational design of porous SOFC cathodes via development, extension, and use of the key tools to aid in the fundamental understanding and engineering design of cathode materials. These tools include those which may first be applied to thin-film or other test cells of well-controlled geometry for fundamental study, such as development of phenomenological reaction rate expressions and models for the design of such test cell electrodes. Such efforts inform models applied onto porous cathodes. Other modeling tools include finite

element routines for transport and reaction rates conformal to the fine microstructure of porous cathodes and use of conservative point defect ensembles so that the phenomenological reaction rates may be applied generally onto a porous structure. Building and using these components is critical in the overall effort to enable rational design.

One area of focus is the triple phase boundary between gas, the solid oxide electrolyte, and an oxide mixed conductor. A phenomenological reaction rate expression was derived to include the triple phase boundaries between the mixed conductor and electrolyte, taking into account transport limitations on local electrical state, concentration fields of point defect and adsorbed oxygen atoms, and material geometry. This treatment was used to examine the possible role of the TPB versus bulk pathway in $La_{1-x}Sr_xMnO_{3\pm\delta}$ (LSM) test cells and is important to the rational design of SOFC cathodes because it provides a detailed description of the physical processes occurring along one of the primary routes of oxygen reduction.

Next, a continuum modeling investigation was performed to aid in the design of thin-film test cells with respect to sheet resistance. The model was applied to generate design charts for the placement of metal current collectors in different configurations as a function of intrinsic film area-specific resistance, thickness, and conductivity. It was found that it is generally possible to design thin-film tests cells to avoid sheet resistance, but some highly-active materials may have difficulties at certain temperatures. This step was important to enabling rational design of SOFC cathodes by providing guidance and insight into how platforms for fundamental study may be designed to avoid troublesome interference from sheet resistance.

A third area of emphasis was on fundamental understanding of the surface modification of a mixed-conducting material. Phenomenological modeling was applied to LSCF thin-film test cells with and without a coating of LSM to explain an experimentally observed increase in electrocatalytic activity and long-term stability of

coated test cells and porous electrodes. This work was informed by transmission electron microscopy (TEM) observations of the near-interface region. Enhanced cathodic activation, superior oxygen adsorption properties, and interdiffusion to create a hybrid LSM-$La_{1-x}Sr_xCo_{1-y}Fe_yO_{3-\delta}$ (LSCF) surface layer were suspected as the causes of the increased performance and stability. Since numerous possibilities for surface modification of porous electrodes exist, some of which may be beneficial and some detrimental, gaining an understanding of how and why LSM coatings cause beneficial effects via phenomenological modeling is very important to further rational enhancement strategies.

A novel application of the principle of conservative point defect ensembles was developed to further enable modeling of disparate types of candidate SOFC materials by simplifying the treatment at heterogeneous solid interfaces and providing a means to access the important chemical and electrical state quantities used in phenomenological rate boundary conditions under large cathodic bias. This approach may be used in conjunction with finite element modeling for a powerful way to simulate electrochemical response for composite cathodes formed with multiple candidate mixed-conducting materials. Coupled with developed phenomenological expressions, it also further expands capability for modeling and simulation of porous cathodes.

Finally, a 3D finite element method modeling approach was developed that allows the constitutive bulk and surface transport equations to be solved conformal to the microstructure of a porous electrode. This technique used commercial and open-source software packages to ensure maximum availability to a wide audience. It is suitable for linking multiple length scales together by the use of rate equations as boundary conditions, which may be informed by patterned electrode experiments, quantum chemical calculations, or other fundamental investigations. The bulk and surface pathways of LSM were examined and the surface pathway determined to be dominant. The modeling approach can be used in the rational design of SOFC

cathodes because it captures the local details of microstructure as well as fundamental material and oxygen-reduction properties.

The work detailed in this thesis provides necessary steps for modeling, simulation, and rational design of SOFC cathodes. It will aid future fundamental investigations of cathode MIEC properties, including thin-film and patterned electrode investigations through the TPB phenomenological model and the sheet resistance-mitigation modeling. It will also be of use to the engineering design of porous cathodes through the use of conformal FEM modeling with or without conservative defect ensembles. The 3D FEM technique accounts for the local fine details of microstructure and can use sophisticated, phenomenological reaction rate kinetics that consider the complexities of point defect chemistry, local electrical state, and adsorbed oxygen concentration. Rational design approaches to SOFC cathode development can use these tools and apply these gains in fundamental knowledge for a more effective and scientific means of improving the prospects of commercial SOFC viability.

CHAPTER I

INTRODUCTION

Solid oxide fuel cells (SOFCs) are a promising means of generating electricity in a manner that is more efficient and environmentally friendly than traditional stationary methods [106]. As such, SOFCs are one component of a long-term energy strategy to conserve limited resources and reduce pollution, making optimal SOFC performance good for the economy, energy independence, and the environment.

Most modern planar SOFCs are anode-supported, with a relatively thin [160] electrolyte and cathode. In a single-cell oxygen-based SOFC, fuel is oxidized on the anode side, oxygen is reduced on the cathode side, and oxygen ions (O^{2-}) are transported from cathode to anode through the electrolyte. Electricity is harvested by forcing electrons generated in the anode through an external circuit before they reach the cathode [106].

The cathode in particular is poorly understood and optimized, leaving much room for improvement to aid widespread SOFC commercialization. This need for improvement is especially true at intermediate temperatures where cheaper components in other parts of the fuel cell may be used. Among the main challenges facing SOFC cathodes are the activity toward the oxygen reduction reaction and the competition between active surfaces and transport pathways. Because the cathode presents separate technical design challenges from the anode, the anode will not be considered explicitly here, being reserved instead for future work.

1.1 SOFC cathodes

SOFC cathode technology has taken three primary directions. The first is the use of porous mixed ionic-electronic conducting (MIEC) cathode materials, which conduct

both electronic species and oxygen ions (O^{2-}) through the bulk. An MIEC material may support the reduction of O_2 to two O^{2-} ions either at the TPB between the MIEC, electrolyte, and air with oxygen supplied through surface transport of adsorbed oxygen species, or on the surface away from the TPB. When O_2 reduction is far from the TPB, O^{2-} is incorporated into the bulk of the mixed conductor and transported. Along either path, O^{2-} is eventually transferred to the electrolyte, either by direct incorporation at the TPB (surface path) or by bulk diffusion through the MIEC and over the two-phase interface between the MIEC and electrolyte (bulk path). Important MIEC materials include $La_{1-x}Sr_xCoO_{3-\delta}$ (LSC) and $La_{1-x}Sr_xCo_{1-y}Fe_yO_{3-\delta}$ (LSCF) [3]. A schematic diagram of the solid-phase and surface transport pathways in a mixed conducting cathode is given in Figure 1a. A vacancy based oxygen-ion conducting mechanism is assumed in the mixed conductor and electrolyte.

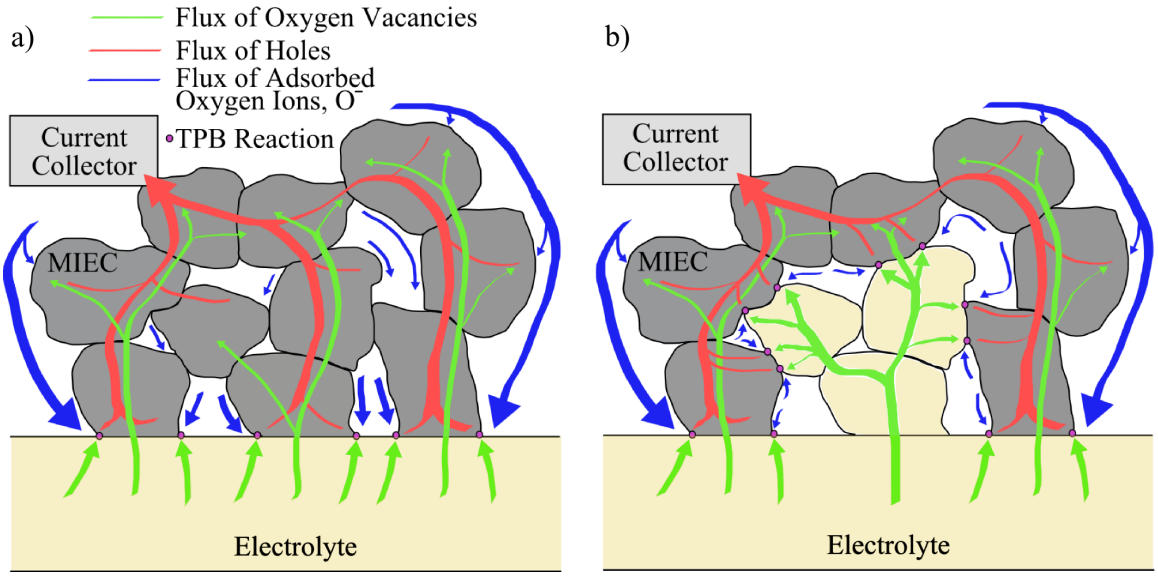

Figure 1: Schematics of a) mixed-conducting cathode and b) composite cathode.

The second major SOFC cathode direction is the use of composite cathodes [75, 76]. These electrodes are porous with two solid phases - one is a primary electronic conductor and the other is a primary ionic conductor. Intimate mixing between the particles of both phases produces an effective mixed-conducting medium which

allows transport of ionic and electronic point defects throughout the electrode. It also serves to provide active TPBs away from the electrode-dense electrolyte interface out into volume of the cathode. Thus, transport limitations are reduced and better performance [75, 129] is achieved. A schematic illustration of a composite cathode is given in Figure 1b. The most common and current state-of-art composite cathode materials are $La_{1-x}Sr_xMnO_{3\pm\delta}$ (LSM, primarily an electronic conductor) and yttria-stabilized zirconia (YSZ, ZrO_2 doped with 8 mol% Y_2O_3, ionic conductor).

The third major approach to cathode formation is infiltration of active cathode material onto a scaffold of porous electrolyte material [166]. This strategy is very similar to the formation of a composite cathode, but is not arrived at via traditional ceramic processing as is the composite cathode. Instead, the electrolyte scaffold is usually pre-sintered and active cathode material is infiltrated through some liquid deposition process to form a layer of particles on the surface of the scaffold. Connectivity of these particles is important for a complete and facile electronic pathway.

In practice, there is often a two-layer cathode [25, 160], where the bottom layer near the electrolyte is a composite or mixed conductor with very fine particle size (functional layer) and the upper layer near the interconnect is single-phase cathode material (current collector layer). The functional layer is where most of the electrochemical reactions take place while the current collector layer provides an easier path for electronic current and gas diffusion [25, 160].

1.2 Challenges associated with fundamental understanding and design of SOFC cathodes

The solid oxide fuel cell is an all solid-state system, with dense oxide electrolyte and porous electrodes composed of solid materials. This solid construction prevents a number of typical electrochemical characterization techniques from being useful, including the rotating disk electrode measurement and cyclic voltammetry. Interaction with the gas phase can also prompt some kinetics not driven strictly by interfacial

electrical polarization and therefore not adequately described by Butler-Volmer type expressions, particularly at the surface of mixed conductors. In addition, the chemical species involved are often point defects - oxygen vacancies, interstitials, electrons, electron holes - inside the solid phases and therefore can be known only indirectly under equilibrium conditions.

As a consequence, it is very difficult to measure the fundamental properties and kinetics of cathode materials pertaining to oxygen reduction. This challenge has led to several approaches to try to access this information as well as possible. One approach is the use of thin-film or patterned electrodes. Another is the use of quantum chemical modeling. A third approach is the development of continuum-type modeling techniques to try to interpret experimental data and aid engineering design.

1.3 Thin-film and patterned electrode measurements

The porous SOFC cathode is a very complicated system due in no small part to the complications arising from the porous geometry. An approach that has been helpful in separating the effect of geometry from the fundamental surface catalytic properties of the material is the use of thin-film or patterned electrodes [9, 17, 50, 81, 114]. Thin films of MIECs are deposited by physical vapor deposition or another process onto a polished or single-crystal electrolyte with a counter electrode opposite and possibly a reference electrode. Electrochemical tests may be performed at high temperature to assess the kinetics of surface processes and to some extent transport processes within the material.

One problem with this approach is the role of sheet resistance in the measurements [82]. This effect arises due to the long distances traveled by electrons from a current collector to the site of the oxygen reduction reaction, distributed uniformly on the air-exposed surface of the MIEC film, and can complicate the global results observable by high-temperature electrochemical experiments. Theoretical modeling work has

demonstrated the role of sheet resistance [103].

1.4 Quantum chemical calculations

Insight into the mechanism of oxygen reduction can be given by quantum chemical simulations. Recent efforts have demonstrated that the transition metal site of mixed-conducting perovskites is possibly the favored site for adsorption and that the presence of any oxygen vacancy in the vicinity of the transition metal can aid adsorption and dissociation of oxygen [23]. Other results have predicted rate coefficients [22] and examined the possible effects of different transition metal ions upon oxygen binding and hence adsorption and oxygen vacancy formation [24]. Such simulations are typically performed with DFT and/or DFT+U [91] calculations.

1.5 Continuum-type cathode models

There are several classical models of porous SOFC electrodes that focus on different aspects of operation. Fleig groups these models into four categories [48], a division that is suitable for this context and includes local current density distribution, discrete particle/resistor network, chemical kinetics/surface, and porous electrode theory (PET, alternatively known as the Adler-Lane-Steele, or ALS, model).

The discrete particle/resistor network model is very useful for composite electrodes [48]. Generally, the focus is on the anode [48], but many formulations are general enough to apply to either electrode [149–151, 171] and cathodes have been given some specific consideration [1, 67, 142]. Microstructure is simulated by a simple method such as randomly placed, interpenetrating spheres. Particles and their interfaces are then assigned some discrete value of resistance and the electrochemical performance is solved for as a circuit based on this network. The model captures some impact of microstructure on the global level, but is not capable of capturing other important phenomena on the local level or examining realistic particle geometries.

Kinetic models predict the general nature of the electrochemical reactions occurring on the cathode while surface models describe surface diffusion and reaction kinetics at the TPB. The first of these models were developed for Pt [109–111,120,121] electrodes. This type of approach was extended to other surface-active materials like LSM [108], though with considerable lingering questions about the role of various processes such as surface transport versus charge-transfer at the TPB and the state of adsorbed species. These models aid understanding of the nature of reactions, but are limited in their geometric flexibility and use in design.

Local current distribution models examine the effect of intra-particle variations in potential. They indicate that substantial gradients can exist within particles and that resistors that lump the entire contribution from a TPB neglect some important features caused by details of local microstructure.

The PET model is so far the most successful overall model for good mixed conductors in porous cathodes. The entire cathode is treated as a 1D homogenized medium with all microstructural features lumped into several all-encompassing parameters like porosity, surface area, and solid-phase/gas-phase tortuosity. This approach was developed for MIEC cathodes in [5] as an adaptation of the porous model made popular in [125]. Experimental impedance results were in qualitative agreement with the calculated results for good mixed conductors; however, for LSM with its relatively limited bulk transport, the theoretical prediction is of very limited use. A similar model was developed that considered either pure surface or pure bulk transport [152–154] and was later extended to consider both mechanisms simultaneously [28]. The PET model has also been extended to composite electrodes [29, 30, 37, 38, 77] with the discrete particle methodology used to determine average parameters such as porosity and effective conductivity for the composite cathode. The 1D porous electrode theory does not adequately describe the results when the Fermi level is nonuniform, when the ionic transference number is not large, or the utilization length is smaller than

the geometric feature size of the material [94].

One recent approach by Mebane [101] and others [4, 49, 53] was to develop a set of phenomenological equations to describe the rate of oxygen reduction on mixed-conductor surfaces. Mebane took another step and set the rates as boundary conditions to a simulation conformal to the geometry of a MIEC [103]. This approach can be flexible with respect to morphology in a porous electrode if electronic and ionic transport equations are cast onto a simulation domain with a grid that is conformal to the material's microstructure.

1.6 Rational design in SOFC cathodes

Despite the available modeling tools, design of SOFC cathodes remains heuristic. Most approaches to electrode materials development tend to be very empirical in nature: a qualitative idea is developed, an electrode is fabricated, and a test is performed. The idea is considered a success if the performance meets or exceeds expectations. Nevertheless, the concept of *rational design* provides important insights into how to achieve higher cathode efficiencies through new architectures and new materials.

There exists a gap in fundamental knowledge pertaining to oxygen reduction in the cathode. It is still not clear exactly which elementary steps are involved or how different components affect them. Better understanding can prompt better-designed materials with respect to the constitutive elements chosen for a mixed-conducting oxide or more creative ways to construct interfaces.

There also exists a gap in the tools to apply fundamental principles onto detailed microstructural representations. There are the modeling tools at different levels and length scales described in the previous sections, but there is a lack of multi-scale techniques to put them together for more effective scientific understanding and design. PET models do not account for fine details of local microstructure, but local

current density distribution models have lacked applicability to large segments of a microstructure. Chemical kinetics models can probe detailed reactions, but lack the large-scale applicability of resistor network models. A tool that synthesizes all of the important features into one approach would be able to capture details of microstructure including particle morphology and triple phase boundaries. It would incorporate these microstructural considerations with transport considerations including those of point defects within the solid mixed-conducting phases. It would rely on phenomenological kinetics to inform local reaction rates, which could in turn be informed by the results and predictions of quantum chemical calculations. Finally, it would be able to sum the local electrochemical responses distributed over the detailed microstructure and determine a global response.

1.7 Contributions of this work

The contents of this thesis describe in detail advancements in modeling, simulation, and rational design of porous SOFC cathodes through focus on fundamental understanding of mechanisms and development of modeling tools. The emphasis is at two levels: first, on studies and techniques applied to thin-film or other test cells of well-controlled geometries and second, on studies/tools for direct simulation using real porous structures. Both levels are critical to rational design of porous SOFC electrodes: the former group informs the latter group, which enriches the latter's capabilities, accuracy, and applicability.

The layout of this thesis is as follows. Chapter 2 details the extension of existing continuum/phenomenological modeling tools to treat the triple phase boundaries (TPBs) of mixed conductors, with specific application to LSM. Chapter 3 provides a set of design tools based upon continuum modeling in thin films to aid the design of test cells for examination of fundamental properties. Chapter 4 describes a collaborative effort with experimentalists to use thin-film test cells with phenomenological

modeling to understand the nature of the oxygen reduction reaction on the surface of LSCF with and without a coating of LSM. Chapter 5 presents a novel use of the concept of conservative point defect ensembles to allow extension of these modeling techniques to cathodes with several disparate types of mixed conductors and under a large cathodic bias. Chapter 6 develops a finite element method for modeling cathode processes that is conformal to porous microstructure, using both steady state and electrochemical impedance formulations. The totality of this work further enables the rational design of SOFC cathodes, as well as other electrochemical systems, by investigating fundamental mechanisms and developing critical and mutually dependent tools for multi-scale modeling and simulation.

CHAPTER II

TRIPLE PHASE BOUNDARY AND SURFACE TRANSPORT IN MIXED CONDUCTING PATTERNED ELECTRODES

2.1 Introduction

Mixed ionic-electronic conducting (MIEC) electrode materials are important in solid oxide fuel cell (SOFC) technology because their bulk transport pathway extends the reaction zone away from the triple phase boundary (TPB) and thus increases performance [92, 148]. Due to competition between pathways, the various transport and reaction kinetics of these materials are often amalgamated and are difficult to examine individually. To facilitate scientific study, thin film and patterned electrode geometries have been developed to simplify electrode complexity by isolating specific mechanisms. Such experiments [9, 16, 17, 41–43, 63–65, 72, 73, 81, 82, 84, 105, 114, 123, 133, 136, 157, 173, 174] have yielded valuable information on several candidate fuel cell materials, including $La_{1-x}Sr_xMnO_{3\pm\delta}$ (LSM) and $La_{1-x}Sr_xCoO_{3-\delta}$ (LSC).

Recently, a two-dimensional (2D) numerical model was introduced to describe charge and mass transport in, as well as chemical kinetics on the surface of, a mixed conducting thin film [101–103]. This model provides insight into thin film electrode response, specifically into the nature of the transport of reactants as well as the effect of sheet resistance. It is potentially useful for making quantitative estimations of

*M.E. Lynch, D. S. Mebane, Y. Liu and M. Liu, "Triple Phase Boundary and Surface Transport in Mixed Conducting Patterned Electrodes," Journal of The Electrochemical Society, 155 (6), B635-B643 (2008).

phenomenological parameters of electrode materials, directly linking first principles-based calculations to higher levels of modeling, and predicting the performance of thin film test cells. When decoupled from its rigid geometric framework, the approach has the possibility to be applied onto an arbitrary MIEC geometry.

The purpose of this chapter is to extend the model to account for the presence of a TPB and the resulting surface transport. This extension allows greater applicability for a number of multi-scale modeling efforts, especially those applied to patterned test cells and to the determination of fundamental materials properties. The specific geometry under consideration for development and qualitative validation is shown in Figure 2 and consists of an array of thin film MIEC electrodes patterned on top of an electrolyte (Figure 2a). The model domain (Figure 2b) is obtained by taking a symmetric 2D cross-section from the center of one patterned electrode to the center of the air-exposed electrolyte separating it from the adjacent electrode. On top of each electrode, a current collector is patterned and covered by an insulator (neither is depicted in Figure 2a for simplicity). The insulator blocks the TPB at the current collector/MIEC contact and can also selectively block active MIEC surface [16, 81].

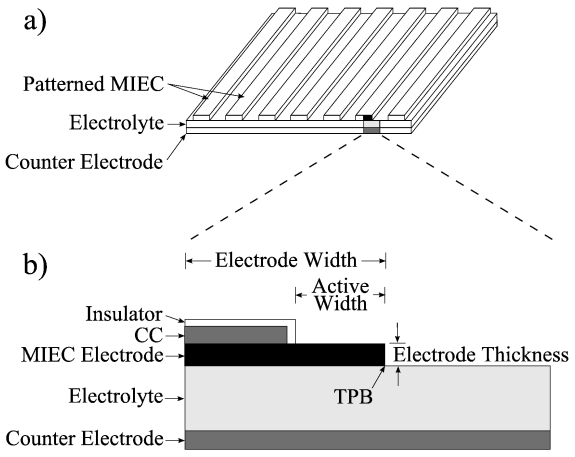

Figure 2: Schematics of a) patterned electrode array and b) symmetric 2D cross-sectional model domain. The components of the 2D model domain are indicated by shading where the MIEC is black, the electrolyte is light gray, the current collector and counter electrode are dark gray, and the insulator is white. The current collector and insulator are not indicated in a) for simplicity.

In the thin film model, interaction of oxygen with the surface of the MIEC is assumed to involve two elementary steps: dissociative adsorption resulting in partial reduction, Equation 1, and direct incorporation, Equation 2

$$\frac{1}{2}O_2 + s \rightarrow O'_{ads} + h^{\cdot} \tag{1}$$

$$O'_{ads} + V_O^{\cdot\cdot} \rightarrow O_O^x + h^{\cdot} + s \tag{2}$$

where $V_O^{\cdot\cdot}$ represents an oxygen vacancy (in Kröger-Vink notation), s is a surface site, and $h^{\cdot}$ is an electron hole. Each step involves one electron transfer. The oxygen ion incorporated into the MIEC by reaction 2 is eventually transferred to the electrolyte by exchange with a vacancy across the interface

$$O_{O,m}^x + V_{O,e}^{\cdot\cdot} \rightarrow O_{O,e}^x + V_{O,m}^{\cdot\cdot} \tag{3}$$

where the subscript m signifies that the species is in the MIEC and the subscript e signifies the electrolyte.

Transport in the bulk MIEC is modeled by explicit consideration of oxygen vacancies and electron holes. The governing equations are the ones regarding the drift-diffusion flux, $\overrightarrow{N}_k$, mass conservation, and bulk charge neutrality:

$$\overrightarrow{N}_k = -u_k c_k \nabla \tilde{\mu}_k \approx -RTu_k \nabla c_k - z_k F u_k c_k \nabla \phi \tag{4}$$

$$\frac{\partial c_k}{\partial t} = -\nabla \cdot \overrightarrow{N}_k + G_k \tag{5}$$

$$F \sum_k z_k c_k + \rho_b = 0. \tag{6}$$

Here, $\tilde{\mu}_k$ is the electrochemical potential of species k (oxygen vacancy or electron hole), c_k is its concentration, z_k is its charge, u_k is its mobility, ϕ is the electrostatic potential, G_k is a homogeneous generation term, ρ_b is the background charge density, R is the universal gas constant, T is the temperature, and F is the Faraday constant.

These equations are discretized according to a conservative finite volume method and solved iteratively to steady-state using a line-by-line solver [103]. Kinetic rate

expressions [101, 102], derived to take into account polarization and other relevant electrochemical factors, serve as the boundary conditions. In this chapter, the above approach is used as a basis and expanded upon to include the reaction at a TPB as well as surface transport necessitated by such a reaction.

2.2 Theory

2.2.1 TPB

The reaction at the TPB assumes full reduction of adsorbed, partially reduced oxygen and subsequent direct incorporation into the electrolyte:

$$O'_{ads} + V^{\cdot\cdot}_{O,e} \rightarrow O^{x}_{O,e} + h^{\cdot}_{m} + s. \tag{7}$$

The kinetic rate model is similar to those already derived for the adsorption, etc., using transition state theory [101, 102]. The electrochemical potential of the initial (I) and final (II) states may be written as the sum of chemical potential (μ) and electrical potential (ϕ) terms

$$\tilde{\mu}^{0}_{I,tpb} = \mu^{0}_{O',s} - F\phi_s + \mu^{0}_{v,e} + 2F\phi_e \tag{8}$$

$$\tilde{\mu}^{0}_{II,tpb} = \mu^{0}_{h,m} + F\phi_m \tag{9}$$

where the subscript s represents the surface. Using the transfer coefficient, α, the electrical component (elect.) of the electrochemical potential at transition state A may be expressed as:

$$\tilde{\mu}^{0}_{A,elect.} - \tilde{\mu}^{0}_{I,elect.} = \alpha(\tilde{\mu}^{0}_{II,elect.} - \tilde{\mu}^{0}_{I,elect.}). \tag{10}$$

Substituting the electrical potential components from Equations 8 and 9 into 10 and adding the chemical potential component at state A,

$$\tilde{\mu}^{0}_{A} = \mu^{0}_{A} + F(2\phi_e - \phi_s) + \alpha F(\phi_m + \phi_s - 2\phi_e). \tag{11}$$

After some algebra, the difference in electrochemical potential between states I and A is

$$\mu_A^0 - \mu_I^0 = \mu_A^0 - \mu_{O',s}^0 - \mu_{v,e}^0 - \alpha F(2\phi_e - \phi_m - \phi_s) = (\mu_A^0 - \mu_{O',s}^0 - \mu_{v,e}^0) - \alpha F(\chi_{em} + \chi_{es}) \quad (12)$$

where $\chi_{em} = \phi_e - \phi_m$ and $\chi_{es} = \phi_e - \phi_s$. Also, between states II and A,

$$\mu_A^0 - \mu_{II}^0 = \mu_A^0 - \mu_{h,m}^0 - F(\alpha - 1)(2\phi_e - \phi_m - \phi_s) = (\mu_A^0 - \mu_{h,m}^0) - F(\alpha - 1)(\chi_{em} + \chi_{es}). \quad (13)$$

The reaction rate constant, k, can now be calculated using

$$k = \kappa \frac{k_B T}{h_P} \exp\left(-\frac{\Delta G_A^0}{RT}\right) \quad (14)$$

where κ is the transmission coefficient, k_B and h_P are the well-known Boltzmann and Planck constants, and ΔG_A^0 is the standard activation energy for state A. The rate constants of the forward and backward reactions are now given:

$$\begin{aligned} \overrightarrow{k} &= \overrightarrow{\kappa} \frac{k_B T}{h_P} \exp\left(-\frac{\mu_A^0 - \mu_I^0}{RT}\right) \\ &= \overrightarrow{\kappa} \frac{k_B T}{h_P} \exp\left(-\frac{\left((\mu_A^0 - \mu_{O',s}^0 - \mu_{v,e}^0) - \alpha F(\chi_{em} + \chi_{es})\right)}{RT}\right) \\ &= \overrightarrow{k'} \exp\left(\frac{\alpha F(\chi_{em} + \chi_{es})}{RT}\right), \end{aligned} \quad (15)$$

$$\begin{aligned} \overleftarrow{k} &= \overleftarrow{\kappa} \frac{k_B T}{h_P} \exp\left(-\frac{\mu_A^0 - \mu_{II}^0}{RT}\right) \\ &= \overleftarrow{\kappa} \frac{k_B T}{h_P} \exp\left(-\frac{\left((\mu_A^0 - \mu_{h,m}^0) - F(\alpha - 1)(\chi_{em} + \chi_{es})\right)}{RT}\right) \\ &= \overleftarrow{k'} \exp\left(-\frac{(1 - \alpha) F(\chi_{em} + \chi_{es})}{RT}\right). \end{aligned} \quad (16)$$

The empirical rate constants $\overrightarrow{k'}$ and $\overleftarrow{k'}$ incorporate constant terms in order to simplify. Under the assumption that the reaction is first order and the activity coefficients are constant, the respective reaction rates can be described as follows:

$$\overrightarrow{r} = \overrightarrow{k} \cdot a_{O',s} \cdot a_{v,e} = \overrightarrow{k''} \exp\left(\frac{\alpha F(\chi_{em} + \chi_{es})}{RT}\right)(\Gamma\theta) c_{v,e} \quad (17)$$

$$\overleftarrow{r} = \overleftarrow{k} \cdot a_s \cdot a_{h,m} = \overleftarrow{k''} \exp\left(-\frac{(1-\alpha)F(\chi_{em}+\chi_{es})}{RT}\right)\Gamma(1-\theta)c_{h,m} \tag{18}$$

where the fraction of available surface sites is θ, the density of available surface sites is Γ, $c_{O',s} = \Gamma\theta$, and the empirical rate constants $\overrightarrow{k''}$ and $\overrightarrow{k''}$ are related to those developed in Equations 15 and 16 but incorporate more constant terms, including activity coefficients and concentration-normalizing constants. Setting the forward rate equal to the backward rate leads to the determination of the equilibrium rate constant, k^0_{tpb},

$$\begin{aligned} k^0_{tpb} = \overrightarrow{k''}\Gamma\theta_0 c^0_{v,e} \exp\left(\frac{\alpha F(\chi^0_{em}+\chi^0_{es})}{RT}\right) \\ = \overleftarrow{k''}\Gamma(1-\theta_0)c^0_{h,m}\exp\left(-\frac{F(1-\alpha)(\chi^0_{em}+\chi^0_{es})}{RT}\right) \end{aligned} \tag{19}$$

where the index 0 signifies the equilibrium value. Now, solving for $\overrightarrow{k''}$ and $\overleftarrow{k''}$ and substituting, the complete rate equation is obtained

$$\begin{aligned} r_{tpb} = k^0_{tpb}\left[\frac{c_{v,e}}{c^0_{v,e}}\frac{\theta}{\theta_0} exp\left(\frac{\alpha F(\Delta\chi_{em}+\Delta\chi_{es})}{RT}\right)\right. \\ \left. - \frac{c_{h,m}}{c^0_{h,m}}\frac{1-\theta}{1-\theta_0}\exp\left(-\frac{F(1-\alpha)(\Delta\chi_{em}+\Delta\chi_{es})}{RT}\right)\right] \end{aligned} \tag{20}$$

where $\Delta\chi_{em} = \chi_{em} - \chi^0_{em}$ and $\Delta\chi_{es} = \chi_{es} - \chi^0_{es}$. The value of χ_{em} is easily determined by $\phi_e - \phi_m$, but determining χ_{es} is more complicated. Fortunately, the change in potential $\chi_{ms} = \phi_m - \phi_s$ is calculated routinely in other parts of the model (adsorption, incorporation) by using a parallel plate capacitor approximation

$$\chi_{ms} = \phi_m - \phi_s \approx \frac{dQ}{A\epsilon_0} = \frac{d(F\Gamma\theta)}{\epsilon_0} \tag{21}$$

where d is the distance of charge separation, Q is the total charge, and A is the area of the plates. Now, χ_{ms} can be used to indirectly calculate χ_{es} with known values:

$$\begin{aligned} \chi_{es} = \phi_e - \phi_s = \phi_e + (-\phi_m + \phi_m) - \phi_s = (\phi_e - \phi_m) + (\phi_m - \phi_s) \\ = \chi_{em} + \chi_{ms} = \chi_{em} + \frac{d_{ms}F\Gamma\theta}{\epsilon_0}. \end{aligned} \tag{22}$$

The equilibrium case follows

$$\chi_{es}^0 = (\phi_e^0 - \phi_m^0) + (\phi_m^0 - \phi_s^0) = \chi_{em}^0 + \frac{d_{ms} F \Gamma \theta_0}{\epsilon_0} \tag{23}$$

and now $\Delta\chi_{es}$ may be obtained:

$$\Delta\chi_{es} = \chi_{es} - \chi_{es}^0 = \left(\chi_{em} + \frac{d_{ms} F \Gamma \theta}{\epsilon_0}\right) - \left(\chi_{em}^0 + \frac{d_{ms} F \Gamma \theta_0}{\epsilon_0}\right) = \Delta\chi_{em} + \frac{d_{ms} F \Gamma (\theta - \theta_0)}{\epsilon_0}. \tag{24}$$

Assuming $\chi_{em}^0 = 0$ between the MIEC and electrolyte bulks at equilibrium, then $\Delta\chi_{em} = \chi_{em}$ and so Equation 24 may be simplified accordingly. Now, $\Delta\chi_{es}^0$ may be obtained:

$$\Delta\chi_{es}^0 = \chi_{es} - \chi_{es}^0 = \chi_{em} + \frac{d_{ms} F \Gamma (\theta - \theta_0)}{\epsilon_0} = (\phi_e - \phi_m) + \frac{d_{ms} F \Gamma (\theta - \theta_0)}{\epsilon_0}. \tag{25}$$

Finally, the TPB reaction rate can be provided with χ_{em} and χ_{es} and taking $\alpha = \frac{1}{2}$,

$$r_{tpb} = k_{tpb}^0 \left[\frac{c_{v,e}}{c_{v,e}^0} \frac{\theta}{\theta_0} \exp\left(\frac{F\left(2(\phi_e - \phi_m) + \frac{d_{ms} F \Gamma (\theta - \theta_0)}{\epsilon_0}\right)}{2RT} \right) - \frac{c_{h,m}}{c_{h,m}^0} \frac{1 - \theta}{1 - \theta_0} \exp\left(-\frac{F\left(2(\phi_e - \phi_m) + \frac{d_{ms} F \Gamma (\theta - \theta_0)}{\epsilon_0}\right)}{2RT} \right) \right]. \tag{26}$$

2.2.2 Surface transport

Surface transport is enabled by the consumption of adsorbed oxygen either at the TPB or by non-uniform incorporation into the MIEC, both of which create an electrochemical potential gradient on the surface. A schematic of the discretized domain is given in Figure 3. The surface cells are indicated just off the surface of the horizontal and vertical faces of the MIEC. The horizontal cells have dimension Δx and the vertical cells have dimension Δy and so the surface cells have dimension either $\Delta g_x = \Delta x$ or $\Delta g_y = \Delta y$, where g simply indicates the surface domain as a way to symbolically set it apart from the bulk.

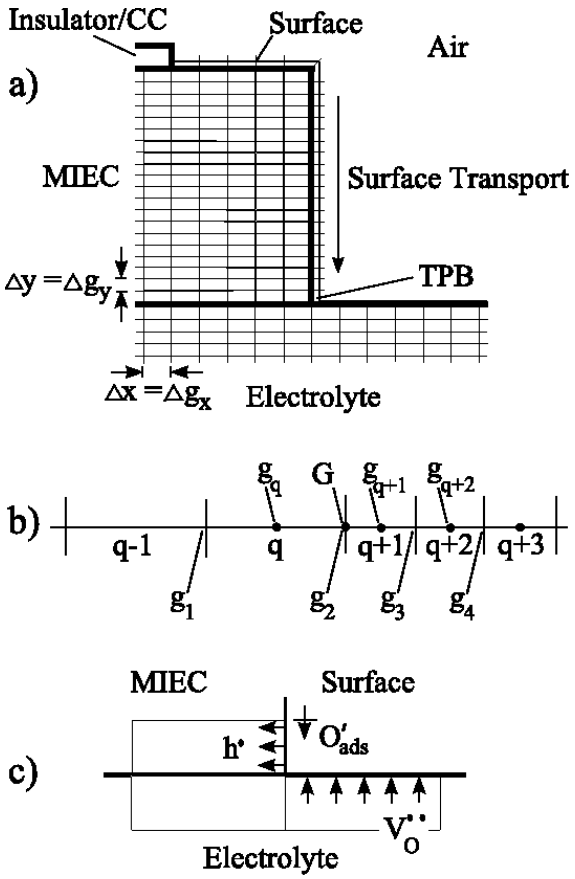

Figure 3: Schematics of a) 2D finite volume discretization of the surface, MIEC, and electrolyte in the region near the TPB, b) 1D discretized surface at the corner (straightened) where cell q is the rightmost horizontal surface cell and cell $q+1$ is the uppermost vertical surface cell, c) cells adjacent to the TPB with flow of reactants. Number of cells in a) and dimension of cells in a) - c) not to scale.

Equations 4 and 5 are applied in one dimension along the surface with the homogeneous generation term, G_k, set equal to the difference between the rate of adsorption and the rate of incorporation of oxygen. Thus,

$$\frac{\partial c_{O',s}}{\partial t} = -\nabla \cdot (-RTu_{O',s}\nabla c_{O',s} - z_{O',s}Fu_{O',s}c_{O',s}\nabla\phi_s) + (r_{ads} - r_{inc}) \tag{27}$$

$$\Rightarrow \frac{\partial \theta}{\partial t} = -\nabla \cdot (-RTu_{O',s}\nabla\theta - z_{O',s}Fu_{O',s}\theta\nabla\phi_s) + \frac{1}{\Gamma}(r_{ads} - r_{inc}). \tag{28}$$

This equation is discretized over the 1D surface and solved iteratively to steady state, analogous to the bulk transport equations [103]. The semi-discrete finite volume

expression is

$$\frac{\partial\hat{\theta}}{\partial t} = -\frac{\left(\hat{M}_{p+1/2} - \hat{M}_{p-1/2}\right)}{\Delta g} + \frac{(\hat{r}_{ads} - \hat{r}_{inc})}{\Gamma} \tag{29}$$

where $\hat{M}$ is the flux normalized by Γ, the carat indicates the average value, p is a cell index distinct from the indices i and j in the bulk, and Δg indicates either Δg_x or Δg_y depending whether the cell is in the horizontal or vertical portion of the surface, respectively. Applying the backward Euler time discretization,

$$\frac{\hat{\theta}^{n+1} - \hat{\theta}^{n}}{\Delta t} = -\frac{\left(\hat{M}^{n+1}_{p+1/2} - \hat{M}^{n+1}_{p-1/2}\right)}{\Delta g} + \frac{\left(\hat{r}^{n+1}_{ads} - \hat{r}^{n+1}_{inc}\right)}{\Gamma}. \tag{30}$$

The flux across the boundary from cell p to cell $p+1$ is

$$\hat{M}^{n+1}_{p+1/2} = -RTu_{O',s}\frac{\left(\hat{\theta}^{n+1}_{p+1} - \hat{\theta}^{n+1}_{p}\right)}{\Delta g} - z_{O',s}Fu_{O',s}\frac{\left(\hat{\theta}^{n+1}_{p+1} + \hat{\theta}^{n+1}_{p}\right)}{2}\frac{\left(\hat{\phi}^{n+1}_{s,p+1} - \hat{\phi}^{n+1}_{s,p}\right)}{\Delta g} \tag{31}$$

with $\mathcal{O}(\Delta g_x^2)$ approximation error at the steady state. An analogous formula is used for $\hat{M}^{n+1}_{p-1/2}$.

It is desirable to solve for the entire 1D surface at once, from the boundary at the insulator on the horizontal portion of the surface to the endpoint of the vertical portion at the TPB, while preserving second-order accuracy in space. As a consequence, the horizontal and vertical subdomains must be linked despite the fact that they have different cell sizes (Δg_x and Δg_y, respectively).

There are several existing numerical methods in the electrochemical literature that treat cells of different sizes [18, 46, 71]. These methods were developed for the case of exponentially expanding cell size and approach the problem from several angles, including transformation into an equal-cell-size space [71] and direct approximation of the flux by computing the finite difference at some average point within each cell [46]. Unfortunately, the latter approach is only first-order accurate in space [18]. Furthermore, the present problem is restricted to two separate subdomains of very regularly-spaced cells (determined by the bulk discretization) and so no elegant transformation into a more uniform space is possible. Therefore, an alternate approach

has been taken for the point where the 1-D domain transitions from horizontal to vertical, specifically an adjustment of the definition of $\hat{M}$ to one using recovered polynomials [60, 164, 165].

Let the cell q be the rightmost horizontal surface cell, cell $q+1$ be the uppermost vertical surface cell, and cells $q-1$, $q+2$, and $q+3$ be those adjacent to q and $q+1$ (see Figure 3b, where the corner is straightened for simplicity). Also, let the positions g_q, g_{q+1}, and g_{q+2} be located at the geometric center of their respective cell and assume that the average concentration of the cell, $\hat{\theta}$, corresponds to its geometric center. Let position g_1 be at the boundary between cells $q-1$ and q, $g_2 = G$ be at the boundary between cells q and $q+1$, g_3 be at the boundary between cells $q+1$ and $q+2$, and g_4 be at the boundary between cells $q+2$ and $q+3$.

Let the function $f(x)$ be defined as the integral of θ from g_1 to some point x along the surface such that

$$f(x) = \int_{g_1}^{x} \theta dg \tag{32}$$

then, because $\hat{\theta}$ represents the average cell value, $f(g_1) = f_1 = 0$, $f(g_2) = f_2 = \hat{\theta}_q \Delta g_x$, $f(g_3) = f_3 = \hat{\theta}_q \Delta g_x + \hat{\theta}_{q+1} \Delta g_y$, and $f(g_4) = f_4 = \hat{\theta}_q \Delta g_x + \hat{\theta}_{q+1} \Delta g_y + \hat{\theta}_{q+2} \Delta g_y$. Now, using Lagrangian basis functions to define a cubic polynomial, $\beta(g)$, the function f can be interpolated to fourth-order accuracy in space (at steady-state) for the region $[g_1, g_4]$:

$$\begin{aligned}\beta(g) = f_1 \frac{(g-g_2)(g-g_3)(g-g_4)}{(g_1-g_2)(g_1-g_3)(g_1-g_4)} + f_2 \frac{(g-g_1)(g-g_3)(g-g_4)}{(g_2-g_1)(g_2-g_3)(g_2-g_4)} \\ + f_3 \frac{(g-g_1)(g-g_2)(g-g_4)}{(g_3-g_1)(g_3-g_2)(g_3-g_4)} + f_4 \frac{(g-g_1)(g-g_2)(g-g_3)}{(g_4-g_1)(g_4-g_2)(g_4-g_3)}.\end{aligned} \tag{33}$$

Due to the definition of f, $\frac{\partial f(g)}{\partial g} = \theta(g)$ and $\frac{\partial^2 f(g)}{\partial g^2} = \frac{\partial \theta(g)}{\partial g}$. Hence, $\frac{\partial^2 \beta(g)}{\partial g^2} = \frac{\partial \theta(g)}{\partial g} + \mathcal{O}(\Delta g_x^2)$ (at steady state). This expression is given by

$$\begin{aligned}\frac{\partial^2 \beta(g)}{\partial g^2} = f_1 \frac{(6g-2g_2-2g_3-2g_4)}{(g_1-g_2)(g_1-g_3)(g_1-g_4)} + f_2 \frac{(6g-2g_1-2g_3-2g_4)}{(g_2-g_1)(g_2-g_3)(g_2-g_4)} \\ + f_3 \frac{(6g-2g_1-2g_2-2g_4)}{(g_3-g_1)(g_3-g_2)(g_3-g_4)} + f_4 \frac{(6g-2g_1-2g_2-2g_3)}{(g_4-g_1)(g_4-g_2)(g_4-g_3)}.\end{aligned} \tag{34}$$

The potential on the surface can treated similarly, say with a function $\gamma(g)$, analogous to $\beta(g)$, such that $\frac{\partial^2\gamma(g)}{\partial g^2} = \frac{\partial\phi_s(g)}{\partial g} + \mathcal{O}(\Delta g_x^2)$. Thus, the spacial derivative of either θ or ϕ_s can be approximated with second-order accuracy.

The value of $\theta(g)$ at $g \in [g_q, g_{q+1}]$ can also be approximated with second-order accuracy in space using a linear interpolation:

$$\theta_{int}(g) = \hat{\theta}_q \frac{(g - g_{q+1})}{(g_q - g_{q+1})} + \hat{\theta}_{q+1} \frac{(g - g_q)}{(g_{q+1} - g_q)}. \tag{35}$$

Now, $\hat{M}_{q+1/2}$ across the boundary from q to $q+1$ is expressed with $\mathcal{O}(\Delta g_x^2)$ approximation error (second-order accuracy) at the steady state by evaluating at the boundary point, G:

$$\hat{M}_{q+1/2} = -RTu_{O',s} \left[\frac{d^2\beta(G)}{dg^2}\right] - z_{O',s}Fu_{O',s} \left[\theta_{int}(G)\right] \left[\frac{d^2\gamma(G)}{dg^2}\right]. \tag{36}$$

Inserting the relevant expressions and letting $\mathcal{C}_a$, $\mathcal{C}_b$, $\mathcal{C}_c$, $\mathcal{C}_d$, $\mathcal{C}_e$, $\mathcal{H}_a$, and $\mathcal{H}_b$ be coefficients determined after substitution of G for g and some algebraic manipulation,

$$\begin{aligned}\hat{M}_{q+1/2}^{n+1} = &-RTu_{O',s} \left[\left(\mathcal{C}_a + \mathcal{C}_b + \mathcal{C}_d\right)\hat{\theta}_q^{n+1} + \left(\mathcal{C}_c + \mathcal{C}_e\right)\hat{\theta}_{q+1}^{n+1} + \mathcal{C}_e\hat{\theta}_{q+2}^{n+1}\right] \\ &-z_{O',s}Fu_{O',s} \left[\mathcal{H}_a\hat{\theta}_q^{n+1} + \mathcal{H}_b\hat{\theta}_{q+1}^{n+1}\right] \left[\left(\mathcal{C}_a + \mathcal{C}_b + \mathcal{C}_d\right)\hat{\phi}_{s,q}^{n+1} + \left(\mathcal{C}_c + \mathcal{C}_e\right)\hat{\phi}_{s,q+1}^{n+1} + \mathcal{C}_e\hat{\phi}_{s,q+2}^{n+1}\right].\end{aligned} \tag{37}$$

This equation is used for the right boundary of cell q and the left boundary of cell $q+1$ in conjunction with the backward Euler time discretization, Equation 30. All fluxes are linked by Equation 30 and solved iteratively using the line-by-line method with a tridiagonal matrix, where θ is computed implicitly. The surface potential, ϕ_s, is updated at every step using Equation 21. The tri-diagonal structure of the matrix can be preserved if the "extra" terms are treated as explicit and their value from the previous iteration is used (e.g., for cell q, the diffusive $\hat{\theta}_{q+2}^{n+1}$ term does not fit in the tri-diagonal band). This treatment of the corner preserves second-order spacial accuracy over the entire surface.

Table 1: Parameter values at T=1023K

Parameter	Value	Units	Reference
k^0_{tpb}	1.0×10^{-11} - 1.0×10^{-12}	$\frac{\text{mol}}{\text{m}\cdot\text{s}}$	-
k^0_{ads}	1.0	$\frac{\text{mol}}{\text{m}^2\cdot\text{s}}$	-
k^0_{inc}	6.5×10^{-7}	$\frac{\text{mol}}{\text{m}^2\cdot\text{s}}$	[35, 103]
k^0_v	9.0×10^{-4}	$\frac{\text{mol}}{\text{m}^2\cdot\text{s}}$	-
$u_{O',s}$	1.0×10^{-12}	$\frac{\text{mol}\cdot\text{m}^2}{\text{J}\cdot\text{s}}$	-
$u_{v,m}$	2.6×10^{-14}	$\frac{\text{mol}\cdot\text{m}^2}{\text{J}\cdot\text{s}}$	[34, 103]
$u_{v,e}$	5.8×10^{-14}	$\frac{\text{mol}\cdot\text{m}^2}{\text{J}\cdot\text{s}}$	[103, 106]
$u_{h,m}$	1.4×10^{-12}	$\frac{\text{mol}\cdot\text{m}^2}{\text{J}\cdot\text{s}}$	[103, 106]
θ_0	2.0×10^{-3}	-	[152]
Γ	1.0×10^{-6}	$\frac{\text{mol}}{\text{m}^2}$	[23, 152]
$c^0_{v,m}$	1.4×10^{-5}	$\frac{\text{mol}}{\text{m}^3}$	[104]
$c^0_{h,m}$	8.2×10^3	$\frac{\text{mol}}{\text{m}^3}$	[104]
$\rho_{b,m}$	-7.9×10^8	$\frac{\text{C}}{\text{m}^3}$	-
$\rho_{b,e}$	-9.7×10^7	$\frac{\text{C}}{\text{m}^3}$	-

A zero-flux boundary condition is imposed at the endpoint adjacent to the insulator. At the TPB endpoint, the boundary condition is governed by the flux due to the TPB reaction, adsorption, and incorporation reactions. Holes created by the summation of these reactions are injected into the MIEC cell adjacent to the TPB while vacancies consumed originate from the adjacent electrolyte cell (Figure 3c).

The time step used was 1×10^{-6} s and the iterations ceased when the change in the local solution was at most 0.00001%.

2.2.3 Parameters

The results reported in this chapter are for the specific composition $La_{0.80}Sr_{0.20}MnO_{3\pm\delta}$ (LSM20), though the model may be applied to other materials with the appropriate choice of parameters. The values chosen for this case are listed in Table 1. Two new parameters, k^0_{tpb} and $u_{O',s}$, are required in addition to those from the thin film model, of which several take on increased importance: k^0_{ads}, θ_0, and Γ. The choice of parameters assumes a temperature of 1023 K.

A recently-developed refined bulk defect model [104] for LSM was used to determine the equilibrium bulk concentration of holes and vacancies, $c^0_{v,m}$ and $c^0_{h,m}$, respectively, in the MIEC. From these values, $\rho_{b,m}$ was calculated using the electroneutrality equation, Equation 6.

A quantum chemical modeling study found that Mn sites on the surface may be preferential locations for oxygen adsorption onto $LaMnO_3$ [23]. Thus, the value chosen for Γ is in rough agreement with the number of Mn sites expected on an exposed $LaMnO_3$-type perovskite. This number is close to a standard assumption in this type of analysis for perovskite surfaces [152], as is the value chosen for θ_0.

Reliable approximations for several of the parameters, specifically k^0_{ads}, k^0_{ktpb} and $u_{O',s}$, were not found after a search of the literature. The parameter k^0_{ads} had been previously set sufficiently high so as to not limit the response of the thin film [103]. This value was used in this chapter because it yielded the expected qualitative response, though k^0_{ads} does affect the TPB reaction and surface transport. For k^0_{tpb}, the value was set sufficiently low to avoid completely dominating the response of the electrode but high enough so that the TPB reaction could be detected under the right circumstances. The value chosen for $u_{O',s}$ was higher than some estimates used in other works [84, 152], but was set so that the qualitative features of thin film and patterned electrode response from the literature were replicated. To the authors' knowledge, no accepted value for oxygen surface mobility on a $LaMnO_3$-type perovskite has been reported in the literature. A seemingly acceptable range of values for each of these parameters was determined and is presented in the next section. Accurate determination of these parameters is beyond the scope of this chapter but will be the subject of future work.

2.3 Results and discussion

2.3.1 Parameters

The reaction rates from the 2D simulation may be summed over the model domain and adjusted by the Faraday constant to obtain current, which can be expressed with the units $\frac{\mathrm{A}}{\mathrm{m}}$, where the m^{-1} refers to the current per unit length of patterned electrode. The current resulting from the TPB and bulk processes as well as the sum of the two is given in Figure 4a-c for varying surface parameters.

The choice of k^0_{tpb} is shown to have a dramatic impact upon the overall electrochemical performance in Figure 4a. If k^0_{tpb} is very low, the TPB current is insignificant and the bulk processes dominate the electrochemical response. If it is very high, the TPB current overshadows the bulk current. For this contribution, k^0_{tpb} values have been chosen in the moderate region of 10^{-11} to 10^{-12} $\frac{\mathrm{mol}}{\mathrm{m{\cdot}s}}$ so that under some conditions, the TPB might determine performance but under others, the bulk might determine performance, as observed in porous [54, 117, 129, 140] versus patterned [16, 64] electrode experiments, respectively.

When $u_{O',s}$ is varied (Figure 4b), low values lead to elimination of surface transport and the TPB reaction is supplied only by adsorption. High values lead to the TPB reaction being supplied by both adsorption and surface transport, eventually causing surface transport to reach a limit. The value of $u_{O',s}$ has been chosen in the middle region for this contribution.

The adsorption reaction is responsible for supplying O'_{ads} to the surface and therefore it supplies both the TPB and the bulk incorporation reactions. At low values (Figure 4c), it limits both. As it increases, there is a region where it limits only the TPB reaction. After increasing further, it is non-limiting to either one. The value assigned to k^0_{ads} in this chapter was on the high end of the TPB-limiting region.

The effect of k^0_{ads} upon the surface concentration is given in Figure 4d. As k^0_{ads} decreases, the TPB reaction is directly supplied with less oxygen and the importance

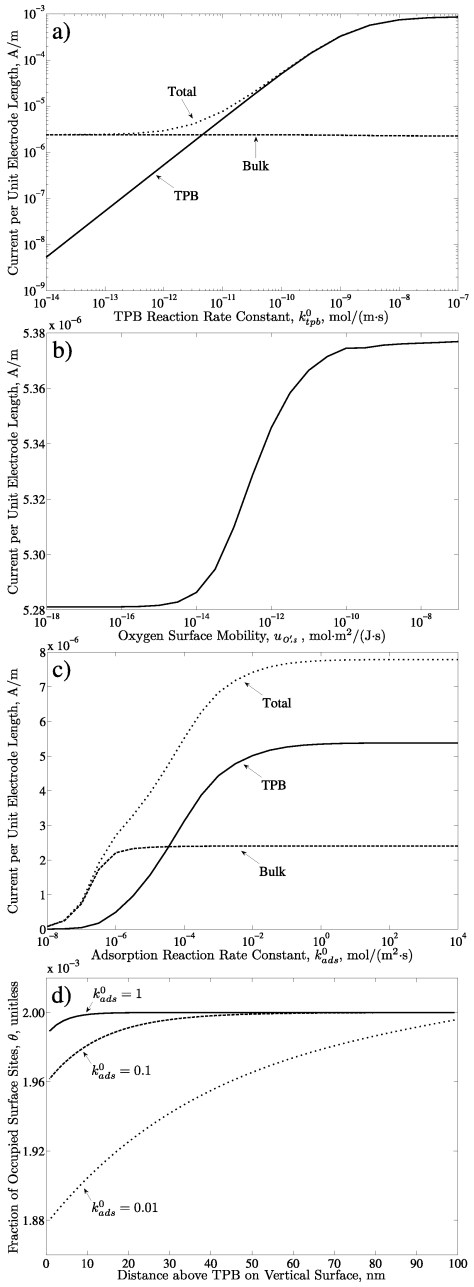

Figure 4: Dependence of electrochemical response upon surface parameters: effect of varying a) k^0_{tpb}, b) $u_{O',s}$, and c) k^0_{ads}. TPB current (solid), bulk current (long dashes), total current (short dashes). d) Dependence of surface concentration (fraction of occupied surface sites, θ) upon value of k^0_{ads}. $k^0_{ads} = 1$ (solid), 0.1 (long dashes), 0.01 $\frac{\text{mol}}{\text{m}^2\cdot\text{s}}$ (short dashes). Extrinsic factors: active width = 48 μm (see Figure 2), thickness = 100 nm, applied voltage = -0.100 V. Except for a), $k^0_{tpb} = 10^{-11}$ $\frac{\text{mol}}{\text{m}\cdot\text{s}}$.

of surface transport is increased. As a result, θ at the TPB endpoint decreases and the depletion distance on the surface increases in length.

It should be noted that changing the parameters causes effects that overlap. For instance, decreasing k^0_{ads} may increase the depletion distance but decreasing $u_{O',s}$ causes the opposite effect. The range selected for the parameters allows qualitative agreement with experimental results, which is discussed in the next sections.

2.3.2 Electrode geometry and applied voltage

The currents resulting from varying electrode width, thickness, and applied potential are given in Figures 5 - 7, respectively. Each plot is shown with two different (moderate) values of k^0_{tpb}.

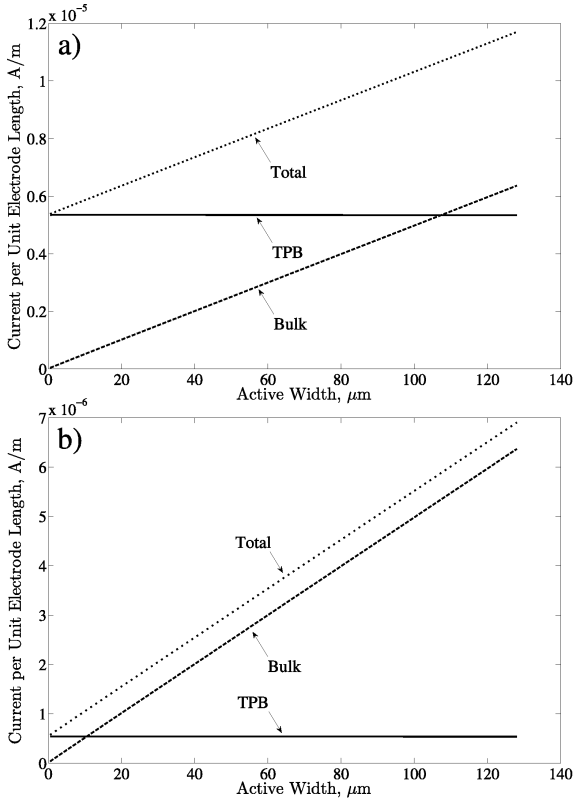

Figure 5: Current per unit electrode length versus active film width for film thickness of 100 nm and applied voltage of -0.100 V: a) $k^0_{tpb} = 10^{-11}$, b) $k^0_{tpb} = 10^{-12}$ $\frac{\text{mol}}{\text{m·s}}$. TPB current (solid), bulk current (long dashes), total current (short dashes).

From Figure 5, the TPB current is relatively constant while the bulk contribution varies almost linearly with active width. A correlation between width and active area may be made due to the specific geometry of the patterned electrode (Figure 2)

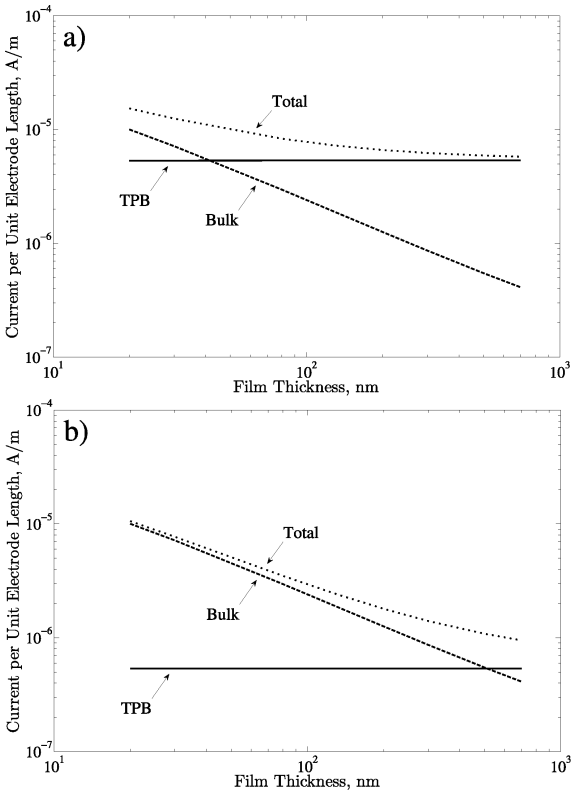

Figure 6: Current per unit electrode length versus film thickness for active width of 48 μm and applied voltage of -0.100 V: a) $k^0_{tpb} = 10^{-11}$, b) $k^0_{tpb} = 10^{-12}$ $\frac{\text{mol}}{\text{m·s}}$. TPB current (solid), bulk current (long dashes), total current (short dashes).

and thus the bulk contribution scales directly with active area while the TPB contribution is relatively constant. The total current approaches the TPB current as width approaches zero. This correlation is in qualitative agreement with Brichzin, *et al.* [16] and Ioroi, *et al.* [64], who determined that electrode resistance (R_{el}) correlated directly with area.

The TPB current can range from a dominant to minuscule portion of the total current based upon the value assigned to k^0_{tpb} as well as the geometry. In Figure 5a, $k^0_{tpb} = 10^{-11}$ $\frac{\text{mol}}{\text{m·s}}$ which makes the TPB current greater than the bulk current for almost all widths shown. However, in Figure 5b, $k^0_{tpb} = 10^{-12}$ $\frac{\text{mol}}{\text{m·s}}$ and so the TPB current is greater only at very small widths. As the electrode width (area) decreases, the TPB contributes a greater fraction of the total current.

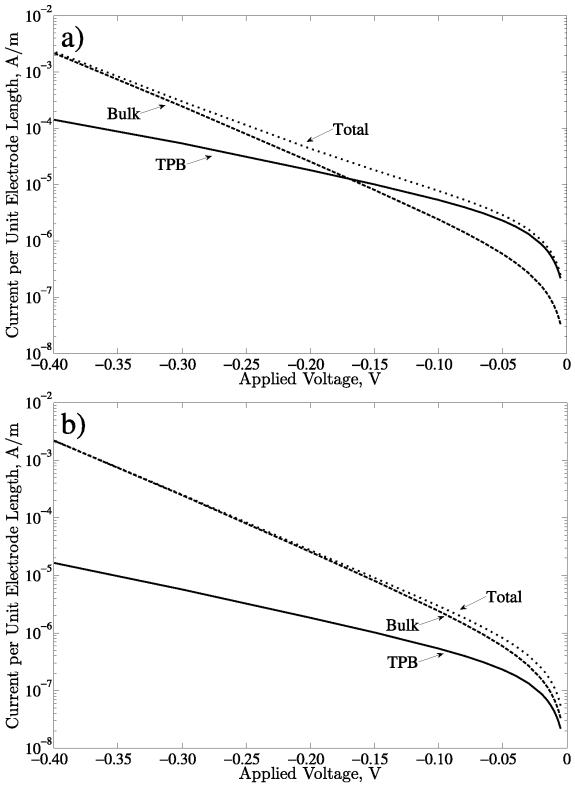

Figure 7: Current per unit electrode length versus applied voltage for active width of 48 μm and film thickness of 100 nm: a) $k^0_{tpb} = 10^{-11}$, b) $k^0_{tpb} = 10^{-12}$ $\frac{\text{mol}}{\text{m}\cdot\text{s}}$. TPB current (solid), bulk current (long dashes), total current (short dashes).

Brichzin, *et al.* [16] and Ioroi, *et al.* [64] both concluded that, for patterned electrodes, the TPB contribution was insignificant compared to the bulk contribution and used the direct correlation of R_{el} versus electrode area as proof. However, Brichzin, *et al.* did not consider the intercept of R_{el} at zero area. If the line is extrapolated to zero area, some measure of TPB resistance may be obtained. Also, Ioroi, *et al.*'s experimental design was heavily weighted towards area-dependent processes (area to TPB length ratio on the order of ~ 1000 $\frac{\mu\text{m}^2}{\mu\text{m}}$ compared to 0.5-128 $\frac{\mu\text{m}^2}{\mu\text{m}}$ in this chapter). Had any defects (such as nanoporosity, cracks, etc.) been present in that film, it is not unreasonable for the TPB contribution from the well-defined line to have been drowned out by the combination of TPB contribution arising from these defects and a large bulk contribution. Others have concluded that the TPB reaction can in fact be detected with carefully controlled experimental geometries [84, 133, 144].

Next, the effect of film thickness is shown in Figure 6. The total contribution of the TPB is again highly dependent upon the magnitude of k^0_{tpb}, but is relatively constant with thickness. In contrast, the bulk current is governed by electrode resistance that is directly proportional to the thickness, leading to the linear trend in the log-log plot. This result is in agreement with experimental results [42, 64]. Given the proper value of k^0_{tpb}, the total current can be dominated by the TPB at high thickness but dominated by the bulk at low thickness.

The dependence of current upon applied voltage is given in Figure 7. At moderate polarizations, the TPB contribution can dominate given a high k^0_{tpb} (Figure 7a) while for smaller k^0_{tpb}, it makes up a large portion of the overall current as well (Figure 7b). As cathodic polarization increases, the bulk current rises at a greater rate than the TPB current. At the most extreme cathodic polarizations, the bulk current is dominant, reflecting the trend toward activation of the bulk due to significant change in stoichiometry of the MIEC [90, 144]. The shape of the curve is a qualitative match to experimental thin film [42, 43, 63, 65, 114, 157] and patterned electrode [64] data.

Based upon these results, it is proposed that the TPB contribution to the overall current can be determined and its kinetics examined by designing patterned electrodes that favor the TPB process. The electrode design may be of the form shown in Figure 2, with essential features that include large thickness, a range of active area, and low polarization. These features are in agreement with predictions made by other authors [16, 84]. The contribution of the TPB may then be isolated by interpolating the zero-area intercept using patterned electrodes of different active area. Such experiments will be the subject of future work.

2.3.3 Sheet resistance

It has been experimentally documented [16, 82] that sheet resistance is noticeable in LSM thin film and patterned electrodes given certain combinations of electrode

geometry and applied voltage. The external factors that produced Figures 5 - 7 were specified in order to show an ideal response under the given set of material parameters, but the model can also predict behavior impacted substantially by sheet resistance (Figures 8 and 9).

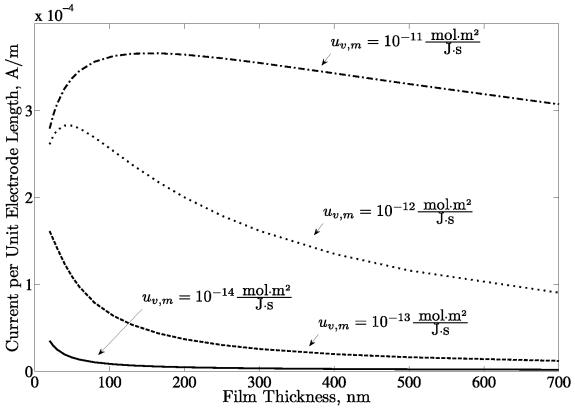

Figure 8: Total current per unit electrode length versus film thickness for different values of $u_{v,m}$. As $u_{v,m}$ increases, the effect of sheet resistance is increased, which is reflected in the decrease in current with decreasing thickness for very low thicknesses. Active width $\sim$400 μm, $k^0_{tpb} = 10^{-12}$, applied voltage = -0.100 V, $u_{v,m} = 10^{-14}$ $\frac{\text{mol·m}^2}{\text{J·s}}$ (solid), 10^{-13} (long dashes), 10^{-12} (short dashes), 10^{-11} (uneven dashes).

In Figure 8, for active width $\sim$400 μm and applied voltage of -0.100 V, the aspect ratio becomes more extreme as thickness decreases. As a consequence, the total current deviates from ideality due to the deactivation of surfaces far away from the current collector. This deviation is very noticeable under the given parameterization when the mobility of vacancies, $u_{v,m}$, is increased: at sufficiently extreme aspect ratios and $u_{v,m}$, the current reaches a maximum and then decreases as film thickness decreases. Therefore, the maximum current does not correspond to the thinnest film. This general type of behavior was observed experimentally by Koep, *et al* [82] Though the patterned electrode geometry, applied voltage, and parameterization used here do not yield an exact match to Koep, *et al.*'s observations, they do yield behavior that is qualitatively similar. It is possible that an exact match might be obtained given the correct parameterization.

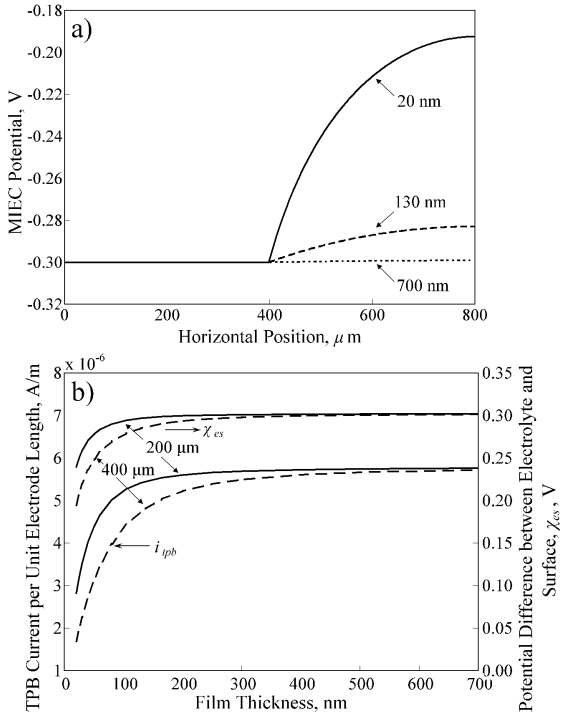

Figure 9: Plots showing the deactivation of the TPB reaction at extreme aspect ratios with $k^0_{tpb} = 10^{-12}$ $\frac{\text{mol}}{\text{m·s}}$ and applied voltage of -0.300 V. a) Potential of the MIEC is shown for films with active width ∼400 μm and different thickness as a function of horizontal distance from left to right across the 2D model domain. Potential is constant in the dead area under the current collector but rises parabolically with distance away from the current collector. The potential of the MIEC at the TPB is located at 800 μm. Film thickness: 20 nm (solid), 130 nm (long dashes), 700 nm (short dashes). b) The TPB current per unit electrode length, i_{tpb}, and the potential difference between the electrolyte and the surface, χ_{es}, are plotted together. The lower set of curves corresponds to i_{tpb} (referred to left axis) while the upper set of curves corresponds to χ_{es} (referred to right axis). Active width ∼200 μm (solid), ∼400 μm (long dashes).

Figure 9 shows how the TPB current is specifically affected by sheet resistance. At moderate aspect ratios, the reaction rate is relatively constant but as the aspect ratio become more distorted by decreasing film thickness, the TPB reaction is deactivated and the current is decreased. This deactivation is the direct result of the potential of the MIEC deviating increasingly from the applied voltage, which decreases the potential difference between the electrolyte and both the MIEC and the surface (χ_{em}

and χ_{es}, respectively), resulting in a decreased reaction rate. In Figure 9a, the potential versus horizontal distance (from left to right across the electrode, where the TPB potential is at 800 μm) is shown for different film thickness. The deviation is approximately parabolic with distance from the current collector and as the aspect ratio becomes more extreme, the deviation increases. The TPB current, i_{tpb}, and χ_{es} are plotted in Figure 9b on separate axes.

It is an important observation that the TPB current trends oppositely with respect to film thickness than the bulk current. As thickness decreases, the bulk current usually increases faster than sheet resistance can limit it, so the net result is that current increases, though not always ideally. However, because the TPB reaction is not limited by bulk transport, the decreasing thickness does not ameliorate transport to or from the reaction site. Thus, the TPB reaction depends only upon the potential difference between the MIEC and the electrolyte at the TPB, which deviates from ideal as film thickness decreases.

2.4 Conclusion

A 2D numerical model of an MIEC thin film electrode has been extended to include a TPB and the accompanying surface transport. This addition enables the modeling of the electrochemical and transport response of a true patterned, multidimensional MIEC electrode. While the exact values for the parameters are yet to be determined, the model replicates qualitatively the results from experimental studies of patterned LSM including the effect of electrode geometry (width, thickness), testing conditions (applied voltage), and sheet resistance. The rate of the TPB reaction was shown to be relatively constant versus film width and thickness when the effect of sheet resistance is insignificant, though it was predicted to decrease with the effect of sheet resistance caused by extreme film aspect ratios. A possible method of experimentally measuring some key kinetic features was proposed, including separating the TPB

and bulk reaction rates. To determine TPB reaction kinetics, for example, a specific patterned electrode geometry is suggested, including large film thickness, small area, and low polarization.

The development of these new model features leads to the potential for quantitative estimates of phenomenological parameters of electrode materials by rigorous comparison to experiment and for prediction of cell performance. Furthermore, this approach can also be used to directly link the predictions from first principles-based calculations with materials performance as measured in test cells of well-controlled geometries, filling a vital role in multi-scale modeling and simulation of SOFC cathodes. If adapted for an unstructured mesh, it has the potential to predict the effect of arbitrary material geometry on chemical, catalytic, and electrochemical properties of SOFC cathodes. Future work will concentrate on these areas.

CHAPTER III

INVESTIGATION OF SHEET RESISTANCE IN THIN-FILM MIXED-CONDUCTING CATHODE TEST CELLS

3.1 Introduction

The oxygen reduction kinetics associated with porous solid oxide fuel cell (SOFC) cathodes are difficult to fully characterize. This difficulty is largely due to the fact that the constituent materials are, to one degree or another, mixed ionic-electronic conductors (MIECs). Simplified thin-film test cell geometries have been used recently to isolate and investigate various kinetic/catalytic properties of the materials [9, 10, 16, 17, 41–43, 47, 63–65, 72, 73, 81, 82, 84, 100, 105, 114, 123, 132, 133, 136, 157, 172–174]. The purpose of this chapter is to provide guidance on the design of such test cells with respect to the phenomenon of sheet resistance and the placement of current collectors (CCs) in the cells.

Test cells consist of thin films of SOFC cathode materials deposited onto single-crystal or finely polished polycrystalline electrolyte substrates via physical vapor deposition into continuous, unbroken layers or into patterns defined by photolithography. Metallic CCs on the surface of the working electrode provide electrical connection for electrochemical impedance spectroscopy (EIS) measurements. A low-impedance porous layer on the opposite side of the electrolyte substrate often serves as a counter electrode.

[†]M.E. Lynch and M. Liu, "Investigation of Sheet Resistance in Thin-Film Mixed-Conducting SOFC Cathodes," Journal of Power Sources, 195, 5155-5166 (2010).

One problem with this setup is sheet resistance in the thin-film working electrode. The local electrical potential within the MIEC can vary from its value at the CC, resulting in nonuniform electrochemical kinetics across the surface of a test cell. Since typical test cells measure macroscopic electrochemical response, the nonuniform response is buried within the cell measurement, convoluting geometric effects with intrinsic material properties and leaving some uncertainty about the true catalytic properties. The effect of sheet resistance is more severe when thinner films and larger CC spacings are used.

The previous chapter illustrated the impact of sheet resistance on patterned thin-film test cells in the context of investigating TPB kinetics. Sheet resistance has been observed in experimental SOFC work [16, 82, 172] and in other models tailored to $La_{1-x}Sr_xMnO_{3\pm\delta}$ (LSM) test cells [103]. The region in a solid electrolyte around an electrode has been investigated numerically [2, 50, 134, 170] and there have been a few studies that address sheet resistance within metallic thin-film working electrodes [40, 74, 162]. However, mixed conduction, a solid electrolyte, and SOFC cell kinetics greatly complicate the issue.

The test cell comprised of a thin-film mixed conductor on a solid electrolyte has a singular set of challenges associated with it that set it apart from related electrochemical systems, such as fuel cell stacks and batteries, and the current collection analysis associated with them. The extreme aspect ratios of the thin film and the low conductivity compared to metals make the working electrode particularly susceptible to deactivation by sheet resistance. Changing the film thickness may alter not only the conductance, but the rate of electrochemical reaction as well, adding another layer of complication. These test cells are also required to function at a variety of temperatures, oxygen partial pressures, and polarizations which may change the governing properties–such as magnitude and type of conductivity–nonlinearly by orders of magnitude without any change to the manner of current collection. Therefore,

some general guidance is still needed to elucidate how potential is distributed within mixed-conducting films of widely varying properties, how it affects cell kinetics, and how test cells may be designed to avoid interference from it. To the knowledge of the authors, these challenges have not been investigated in a systematic and general manner and thus the focus of this chapter is of significant practical importance.

The intention of this chapter is to clarify the key issues and to provide a general and empirical theoretical modeling study of sheet resistance in thin-film test cells for test cell design. The approach is intended to be empirical rather than delving into the specifics of defect chemistry, reaction mechanisms, and other elemental characteristics in order to keep the analysis as generally applicable to a variety of candidate SOFC cathode materials as possible. To accomplish this task, the effect of various CC configurations on performance is elucidated and estimations of the geometry required to avoid a critical amount of sheet resistance under various cell configurations is given by mapping in parameter space.

3.2 Theory

3.2.1 Geometry

There are several ways to provide current collection to a test cell. Among them are removable methods, such as point contact by a microprobe [9, 10, 16, 17, 84] and the application of a platinum or gold mesh [41, 43, 63, 73, 114, 133, 157, 173, 174], which rely upon mechanical force to make a good contact. There are also non-removable methods, such as the deposition of a porous layer by printing, painting, or sputtering [132,136] and also the deposition of patterned CCs via photolithography and physical vapor deposition [81, 82].

Point contact by a microprobe is very useful for conducting local microimpedance measurements, but the sheet resistance may be severe due to the current constriction around the probe [51] and therefore it is best used to investigate small MIEC islands.

Deposition of a porous layer provides good current collection, but can interfere with gas diffusion and the introduction of large MIEC-CC triple phase boundary (TPB) length can add extraneous electrochemical processes to the cell.

Mesh and patterned CCs allow for freer MIEC surface area and fewer MIEC-CC TPBs, but may or may not inhibit sheet resistance depending on their spacing, the film thickness, and the MIEC's intrinsic properties. The free surface area, i.e. that not covered by CC, may be used for other forms of in-situ characterization, such as Raman spectroscopy and x-ray analysis. This chapter addresses mesh and patterned configurations with the goal of maximizing free surface area for in-situ techniques while minimizing the effect of sheet resistance upon global EIS response.

Figure 10 provides top-view optical micrographs of a mesh CC (a) and patterned CC lines (b, with side-view schematic c). Note that due to its woven nature, the mesh is likely to contact an MIEC only at certain, regularly spaced discrete areas where one wire crosses another as opposed to a continuously contacting grid. In contrast, the patterned CC lines in Figure 10b provide intimate contact with the MIEC over their entire length. For the purpose of modeling, the discrete contacts are approximated here as circles. In Figure 10a, the spacing between discrete contacts is approximately 270 μm.

A portion of a representative test cell is shown schematically in Figure 11. The MIEC thin film is deposited with thickness t_m onto a dense electrolyte (with thickness t_e) and the CC is deposited onto the top of the MIEC film. A porous catalyst layer on the bottom of the electrolyte serves as the counter electrode and is exposed to the same gaseous atmosphere as the working electrode. Three distinct CC configurations will be addressed. The "grid" configuration is depicted in Figure 11a. The CCs are arrayed in two sets of mutually perpendicular lines, providing a network of continuous contacts. The distance between parallel lines is given by s, the CC spacing. The second configuration, "parallel," can be depicted if one set of intersecting CCs is

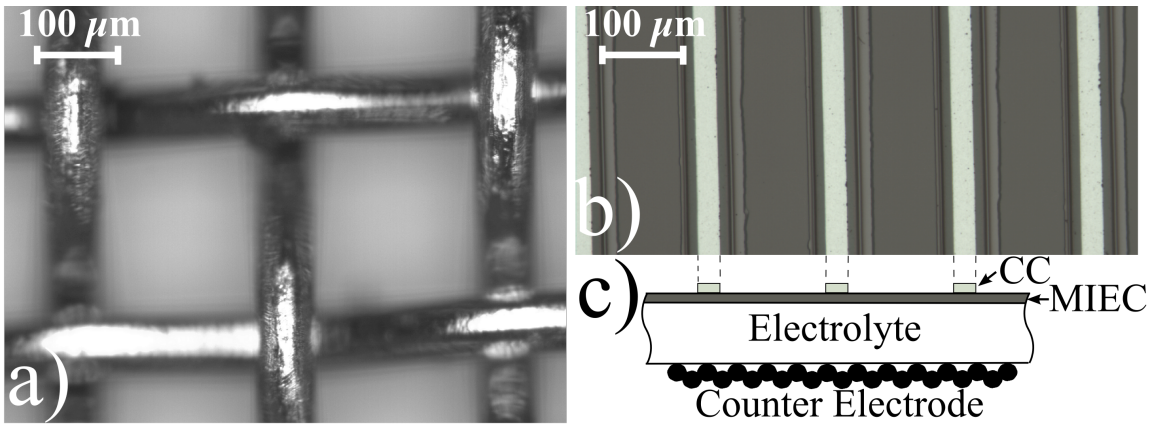

Figure 10: a) Optical micrograph of a typical woven CC mesh. b) Optical micrograph (top view) and c) schematic diagram (cross-sectional view) of a continuous LSM film test cell with patterned, parallel platinum CCs deposited on top. The LSM appears dark while the CCs appear silver. The clear covering on top of the CCs in b) is a thin layer of undoped zirconia intended to block the platinum-LSM TPB and is not considered in the model.

removed from Figure 11a, leaving only CC lines aligned in one direction. These two configurations can be achieved either by deposition via photolithography or from a removable, nonwoven CC mesh appropriately designed for continuous contacts and carefully applied to the surface. The third configuration, "discrete," is achieved if all of the CC lines from Figure 11a are removed and replaced by small, circular contacts where the points of intersection had previously been. This case is an approximation of the contact pattern expected from a woven CC mesh (see Figure 10a), where the mesh only makes contact in certain places. The current collection provided by a mesh, in reality, is probably actually somewhat intermediate between the "discrete" and "grid" configurations depending on the pressure applied, wire diameter, etc.

The actual simulation domain (Figure 11b) is a simplification from the overall geometry and is formed from the symmetry of the CCs, depicted by the dashed outline in Figure 11a. For the grid configuration, the CC contact is along Edges 1 and 2. For the parallel configuration, it is along Edge 1. The discrete configuration's CC contact is within and on the boundary of the quarter-circle region only. The quantities $\Delta\tilde{\mu}_{\mathrm{e}}^{*}(\mathrm{CC})$ and $\Delta\tilde{\mu}_{\mathrm{e}}^{*}(\mathrm{far})$ represent the change to scaled electron electrochemical

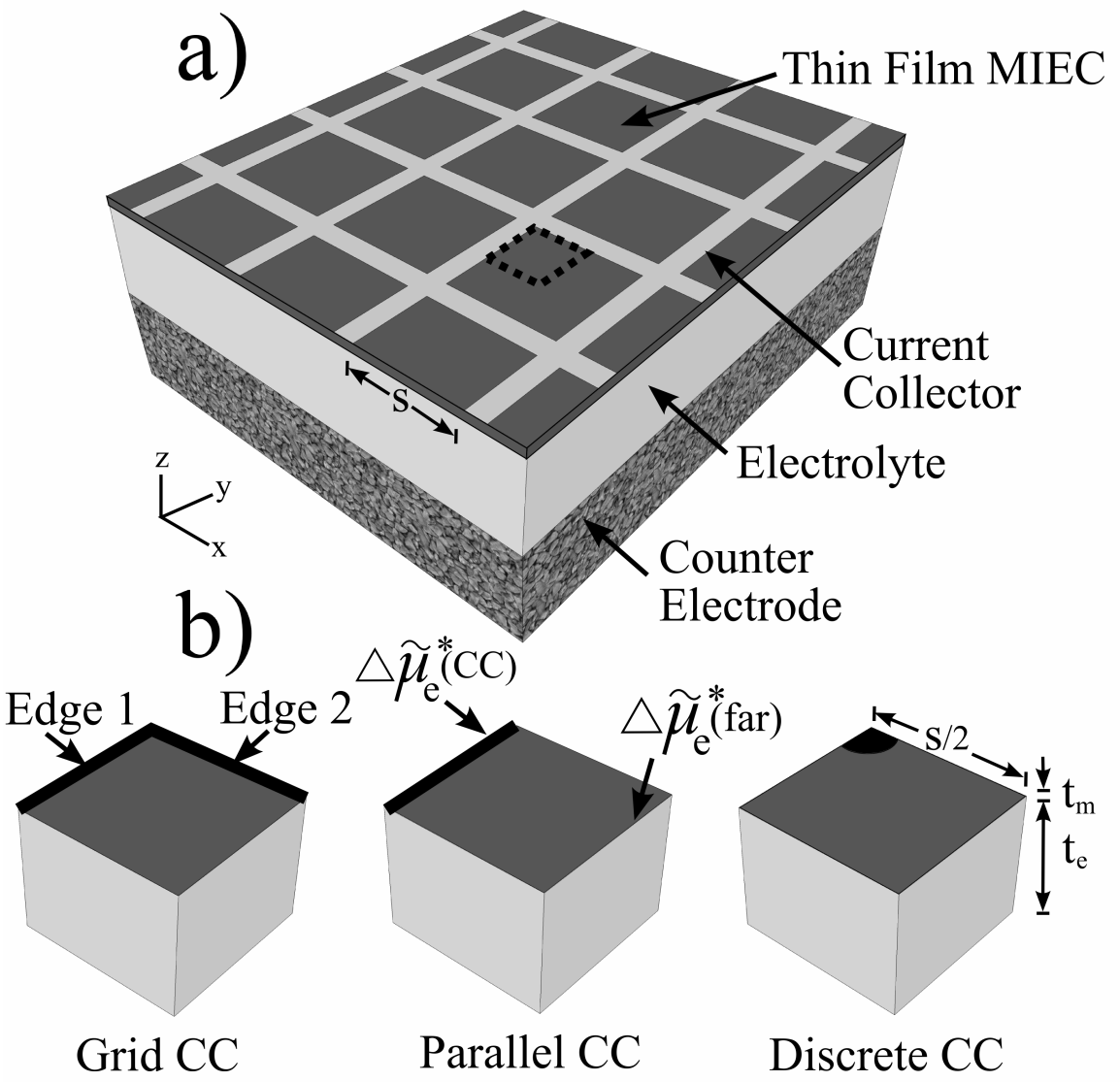

Figure 11: a) Schematic illustration of thin-film test cell geometry, with the thin-film MIEC deposited onto a dense electrolyte and CCs deposited in the "grid" configuration. The "parallel" CC configuration is achieved if one set of intersecting CCs is removed, leaving only parallel CCs. The "discrete" CC configuration is achieved if all of the CC lines are removed and replaced by small, circular contacts where the points of intersection had previously been. The distance between CCs is s. b) Domains for FEM simulation, reduced from a) by symmetry along the dashed line.

potential at the CC and far from the CC, respectively, and will be elaborated upon later.

3.2.2 Nature of MIECs

Candidate mixed-conducting SOFC cathode materials are generally in the perovskite family and show conductivity toward oxygen and electronic species. Oxygen conductivity is common to all of these materials, the transference number being different in each material, and takes the form of oxygen vacancies moving through the oxygen sublattice causing a net flow of O^{2-} in the direction opposite to the net vacancy flux.

Electronic conductivity is generally much larger than the ionic conductivity, but its origin is not the same in all of the materials. The electronic conductivity of $La_{1-x}Sr_xCoO_{3-\delta}$ (LSC), for example, is metallic in behavior and caused by itinerant electrons in a partially filled broad band [87]. Semiconductor-like behavior prevails in some compositions of LSM [118] and $La_{1-x}Sr_xFeO_{3\pm\delta}$ (LSF) [115, 119], caused by the hopping of small polarons on the B-site. They are primarily p-type, with the positively charged defects ($B_B^{\cdot}$ in Kröger-Vink notation) as the majority carrier but with negatively charged defects (B_B') contributing as well.

The different origins of electronic conduction cause small but important differences in the mechanism of the oxygen reduction reaction (ORR). For instance, the overall ORR at the LSC surface may be written as

$$\frac{1}{2}O_2 + V_O^{\cdot\cdot} + 2e^- = O_O^x \tag{38}$$

where $V_O^{\cdot\cdot}$ is an oxygen vacancy and O_O^x is an occupied oxygen site (in Kröger-Vink notation), and e^- is an electron. The overall ORR at the surface of a hopping-type conductor may be written as

$$\frac{1}{2}O_2 + V_O^{\cdot\cdot} + qB_B^x + (2-q)B_B' \;\; = \;\; O_O^x + qB_B^{\cdot} + (2-q)B_B^x \tag{39}$$

where $q = 0, 1,$ or 2 depending on which electronic defects are involved. Generally, each different value of q causes distinct kinetics under a given set of experimental conditions and should be treated independently in an elemental model [125]. However,

a treatment that is sufficiently general to seamlessly model the potential distribution within and the kinetics on the surface of these films, despite their differences in conduction and oxygen reduction, is desired and may be achieved through empirical means.

3.2.3 Potential distribution

In order to avoid specifics of defect chemistry and convolution of chemical and electrical effects (which in general will be different for every composition of MIEC), the change to the electrode potential is best related to the electrochemical potential of electrons in the working electrode, $\tilde{\mu}_{\mathrm{e}}$, without further delineation. The change to $\tilde{\mu}_{\mathrm{e}}$ from its equilibrium value is given by $\Delta\tilde{\mu}_{\mathrm{e}}$. The cell voltage is given by $\mathrm{V_{cell}} = |\Delta\tilde{\mu}_{\mathrm{e}}(\mathrm{CC})/(\mathrm{z_e F})|$, where $\Delta\tilde{\mu}_{\mathrm{e}}(\mathrm{CC})$ is $\Delta\tilde{\mu}_{\mathrm{e}}$ at the CC upon application of the voltage, $\mathrm{z_e} = -1$ is the formal charge of an electron, F is Faraday's constant, and $\Delta\tilde{\mu}_{\mathrm{e}} > 0$ under cathodic polarization. A scaled electrochemical potential of a charged species j is given by $\tilde{\mu}^*_{\mathrm{j}} = \tilde{\mu}_{\mathrm{j}}/(\mathrm{z_j F})$, where $\mathrm{z_j}$ is the formal charge [66]. Then $\mathrm{V_{cell}} = |\Delta\tilde{\mu}^*_{\mathrm{e}}(\mathrm{CC})|$.

3.2.3.1 Metallic conduction in MIEC

In a metallic-conducting MIEC, the mobile charge carriers are electrons and oxygen vacancies. Thus, the total electrical current within the film, $\hat{\mathrm{i}}_{\mathrm{m}}$, is given by

$$\hat{\mathrm{i}}_{\mathrm{m}} = \hat{\mathrm{i}}_{\mathrm{e}} + \hat{\mathrm{i}}_{\mathrm{v}} \tag{40}$$

The currents arising from electrons and vacancies are expressed as $\hat{\mathrm{i}}_{\mathrm{e}} = -\sigma_{\mathrm{e}}\nabla\tilde{\mu}^*_{\mathrm{e}}$ and $\hat{\mathrm{i}}_{\mathrm{v}} = -\sigma_{\mathrm{v}}\nabla\tilde{\mu}^*_{\mathrm{v}}$, respectively, where σ_{e} and σ_{v} are the electron and vacancy conductivities. Since equilibrium electrochemical potentials are spatially uniform, the currents can be expressed in terms of departures from equilibrium values: $\hat{\mathrm{i}}_{\mathrm{e}} = -\sigma_{\mathrm{e}}\nabla(\Delta\tilde{\mu}^*_{\mathrm{e}})$ and $\hat{\mathrm{i}}_{\mathrm{v}} = -\sigma_{\mathrm{v}}\nabla(\Delta\tilde{\mu}^*_{\mathrm{v}})$. Considering that $\sigma_{\mathrm{e}} >> \sigma_{\mathrm{v}}$ [116,146] and that $\|\nabla(\Delta\tilde{\mu}^*_{\mathrm{e}})\| >> \|\nabla(\Delta\tilde{\mu}^*_{\mathrm{v}})\|$ (which can be shown taking the gradient of the electrochemical potentials

of electrons and vacancies when expressed in the appropriate formalism [87]), then $\|\hat{\mathrm{i}}_\mathrm{e}\| >> \|\hat{\mathrm{i}}_\mathrm{v}\|$ and thus

$$\hat{\mathrm{i}}_\mathrm{m} \approx \hat{\mathrm{i}}_\mathrm{e} = -\sigma_\mathrm{m} \nabla \left(\Delta \tilde{\mu}_\mathrm{e}^*\right) \tag{41}$$

where $\sigma_\mathrm{m} \approx \sigma_\mathrm{e}$ is the electrical conductivity of the MIEC material, available from a standard four-probe measurement.

Let $\hat{\mathrm{i}}_\mathrm{plane}$ be given by $\hat{\mathrm{i}}_\mathrm{plane} = \int_0^{\mathrm{t_m}} \hat{\mathrm{i}}_\mathrm{m} \mathrm{dz}$ where z is in the thickness direction of the film. Since the film is thin, $\nabla \tilde{\mu}_\mathrm{e}^*$ can be assumed to be entirely contained in the x-y plane and zero in the z-direction, making $\hat{\mathrm{i}}_\mathrm{m}$ constant in the z-direction as well. Therefore

$$\hat{\mathrm{i}}_\mathrm{plane} = \hat{\mathrm{i}}_\mathrm{m} \mathrm{t_m} = -\sigma_\mathrm{m} \mathrm{t_m} \nabla \left(\Delta \tilde{\mu}_\mathrm{e}^*\right) \tag{42}$$

and the conduction equation is transformed from 3D to 2D (in the x-y plane).

The conservation of charge requires that

$$\frac{\partial \rho_\mathrm{plane}}{\partial \mathrm{t}} = -\nabla \cdot \hat{\mathrm{i}}_\mathrm{plane} + \mathrm{G} \tag{43}$$

where ρ_plane is the 2D free charge density in the MIEC film (C cm^{-2}), t is time (s), $\hat{\mathrm{i}}_\mathrm{plane}$ is the current density in the film (A cm^{-1}), and G is the charge generation rate (C cm^{-2} s^{-1}).

Since the film is thin and vacancy transport in the x-y plane is relatively small, all vacancies entering the MIEC from the electrolyte are approximately transported in the z-direction only and eventually consumed by the ORR at the MIEC-air surface. At steady state, the rate of vacancy injection is equal to the rate of vacancy consumption and thus vacancies contribute nothing to G. In contrast, electrons are constantly consumed at the MIEC-air surface by the ORR and there is a net consumption of negative charge, or effective positive charge generation, that contributes to G on the local level. This contribution to G is effectively a current, proportional to the product of n, the number of electrons in Equation 38 (n = 2) and the rate of the reaction,

r_{ORR}. Denote this quantity i_{ORR} where

$$i_{ORR} = nFr_{ORR} \tag{44}$$

and has units of C cm^{-2} s^{-1} or, equivalently, A cm^{-2}. Finally, at steady state, $\partial\rho_{plane}/\partial t = 0$. This leaves

$$0 = \nabla \cdot (\sigma_m t_m \nabla (\Delta\tilde{\mu}_e^*)) + i_{ORR} \tag{45}$$

as the equation that must be solved in the 2D representation of the MIEC film for the variable $\Delta\tilde{\mu}_e^*(x)$. Figure 12 shows a schematic diagram of the flow of charge, including electrons, e', and oxygen vacancies, $V_O^{\cdot\cdot}$, within the film to an active site on the surface.

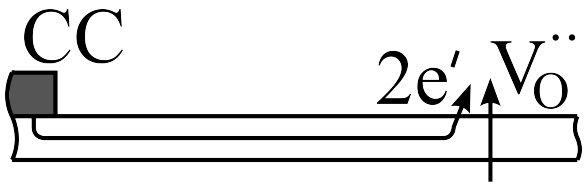

Figure 12: Schematic diagram of the flow of charge in the oxygen reduction reaction. Oxygen vacancies travel in the through-thickness direction, from the electrolyte to the surface. Electrons travel in the in-plane direction from the CC and are consumed at the reaction site.

On the boundary, the potential is fixed at the contact with the CC. In the grid configuration, the potential is fixed along both Edge 1 and 2 (Figure 11b), with $\Delta\tilde{\mu}_e^*(CC) = -V_{cell}$. In the parallel configuration, the potential is fixed only at Edge 1. In the discrete configuration, the potential is fixed within and along the boundary of the quarter-circle region only. The free edges in each configuration are symmetric (Neumann) boundaries. The value of $\Delta\tilde{\mu}_e^*$ at the point in the film farthest from the CC is a dependent variable and is given special notation $\Delta\tilde{\mu}_e^*(far)$.

3.2.3.2 Semiconduction in MIEC

MIEC materials with semiconductor-like behavior present a slightly more complicated situation than those with metallic conduction. In these materials, electrons, electron

holes, and oxygen vacancies comprise the set of mobile charge carriers. Thus, the total current is given by

$$\hat{\mathrm{i}}_{\mathrm{m}} = \hat{\mathrm{i}}_{\mathrm{e}} + \hat{\mathrm{i}}_{\mathrm{h}} + \hat{\mathrm{i}}_{\mathrm{v}} \tag{46}$$

where $\hat{\mathrm{i}}_{\mathrm{e}}$ is the current from electrons (i.e. negatively charged small polarons, B'_{B}), and $\hat{\mathrm{i}}_{\mathrm{h}}$ is the current from electron holes (i.e. positively charged small polarons, $\mathrm{B}^{\cdot}_{\mathrm{B}}$). The following analysis is valid for semiconduction arising via broad bands as well.

Similarly to the case of metallic conduction, $\|\hat{\mathrm{i}}_{\mathrm{v}}\| << \|\hat{\mathrm{i}}_{\mathrm{m}}\|$ (shown by considering the relative magnitude of σ_{v} versus σ_{m} [6] as well as the configurational contribution to diffusion). Thus,

$$\hat{\mathrm{i}}_{\mathrm{m}} \approx \hat{\mathrm{i}}_{\mathrm{e}} + \hat{\mathrm{i}}_{\mathrm{h}} = -\sigma_{\mathrm{e}} \nabla \left(\Delta \tilde{\mu}^*_{\mathrm{e}} \right) - \sigma_{\mathrm{h}} \nabla \left(\Delta \tilde{\mu}^*_{\mathrm{h}} \right) \tag{47}$$

where σ_{h} is the electron hole conductivity. The electron and hole electrochemical potentials are connected to one another through local equilibrium. The reaction can be written as

$$2\mathrm{B}^{\mathrm{x}}_{\mathrm{B}} \rightleftarrows \mathrm{B}^{\cdot}_{\mathrm{B}} + \mathrm{B}'_{\mathrm{B}} \tag{48}$$

Local equilibrium requires

$$\Delta \tilde{\mu}_{\mathrm{h}} \approx -\Delta \tilde{\mu}_{\mathrm{e}} \tag{49}$$

Scaling the electrochemical potentials, $\Delta \tilde{\mu}^*_{\mathrm{h}} \approx \Delta \tilde{\mu}^*_{\mathrm{e}}$. Finally, $\nabla \left(\Delta \tilde{\mu}^*_{\mathrm{h}} \right) \approx \nabla \left(\Delta \tilde{\mu}^*_{\mathrm{e}} \right)$. Thus, the total current may be expressed as

$$\hat{\mathrm{i}}_{\mathrm{m}} \approx -\left(\sigma_{\mathrm{h}} + \sigma_{\mathrm{e}} \right) \nabla \left(\Delta \tilde{\mu}^*_{\mathrm{e}} \right) \approx -\sigma_{\mathrm{m}} \nabla \left(\Delta \tilde{\mu}^*_{\mathrm{e}} \right) \tag{50}$$

with Equation 42 applicable, making $\hat{\mathrm{i}}_{\mathrm{plane}}$ equivalent to the metallic conduction case.

On the surface, assume that both electrons and holes may participate in the ORR to different degrees, with either electrons being consumed or holes being injected. Both processes have the effect of a local increase in positive charge and therefore $\mathrm{i}_{\mathrm{ORR}}$ in this case is given by

$$\mathrm{i}_{\mathrm{ORR}} = \mathrm{i}^{(\mathrm{h})}_{\mathrm{ORR}} + \mathrm{i}^{(\mathrm{e})}_{\mathrm{ORR}} \tag{51}$$

Equation 43 is used again with $G = i_{ORR}$ defined by Equation 51. The final result is exactly equivalent to Equation 45 with $\Delta\tilde{\mu}_e^*(x)$ as the desired quantity.

3.2.3.3 Mixed metallic and semiconducting behavior

Some candidate cathode MIECs, e.g. $La_{1-x}Sr_xCo_{1-y}Fe_yO_{3-\delta}$ (LSCF), show a hybrid conduction mechanism of both metallic and semiconducting character [89]. By following analogous logic to that laid out in the previous two sections and recognizing the minor contribution of oxygen vacancies to total conductivity [6, 167], it can be shown that Equation 45 is the governing equation and that $\Delta\tilde{\mu}_e^*$ specifies the electrical state of the MIEC film.

3.2.3.4 Ionic conduction in electrolyte

In the electrolyte, Equation 52 suffices in the 3D domain assuming no changes in bulk chemical composition

$$0 = \nabla \cdot (\sigma_i \nabla (\Delta\Phi_e)) \tag{52}$$

where σ_i is the electrical conductivity of the electrolyte, in the case of SOFC test cells due primarily to oxygen vacancies, and $\Delta\Phi_e$ is the departure of electrostatic potential from its equilibrium value. The boundary condition along the electrolyte-MIEC interface is given by the current out: $i_{ORR} = z_v Fr_{ORR}$, where z_v is the formal charge of an oxygen vacancy. The bottom electrolyte boundary is Dirichlet, with $\Delta\Phi_e = 0$. The side faces are symmetric boundaries.

3.2.4 Interfacial polarization due to oxygen reduction at open-circuit voltage

The strategy for estimating i_{ORR} at open-circuit voltage (OCV) is linked to the simple, empirical, and linear measurement of the polarization resistance, R_p, obtained by EIS. Figure 13a is a schematic of a complex impedance plot that could belong to a test cell. R_Ω is the Ohmic resistance, generally assumed to result primarily from the resistance

to ionic conduction in the electrolyte. R_p is generally assumed to correspond to the overall chemical/electrochemical process of oxygen reduction. At steady state, these values add to total resistance, R_{tot}.

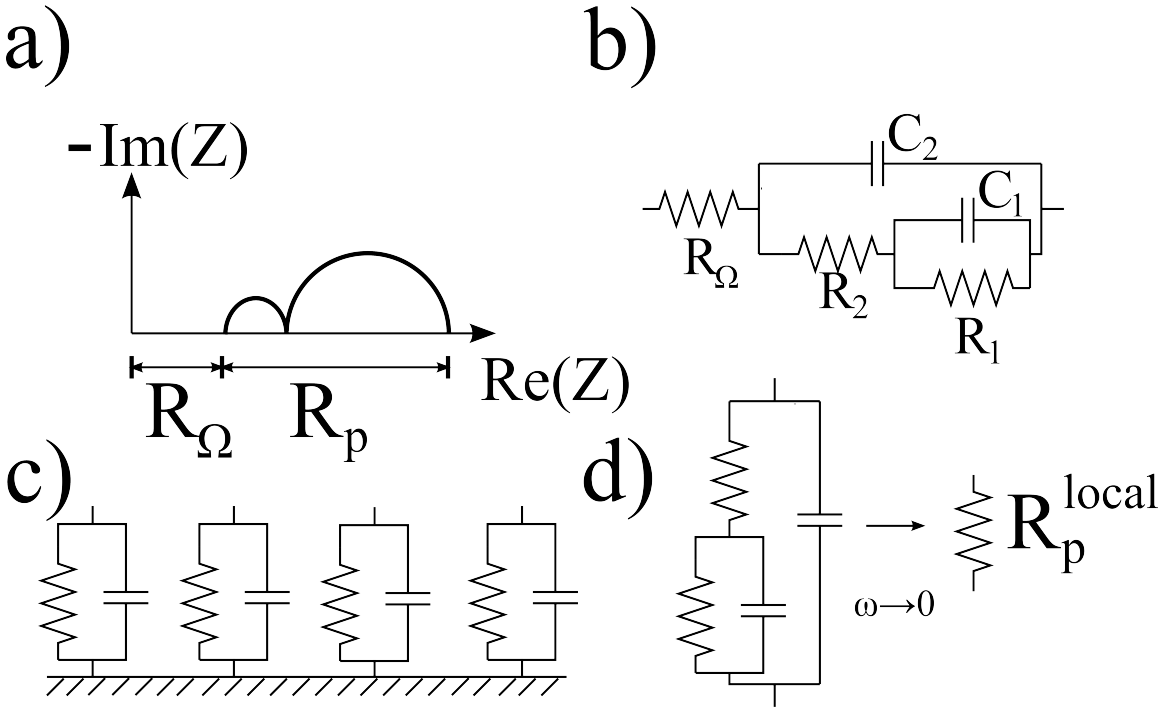

Figure 13: a) Schematic of a possible complex impedance plot of a test cell. b) Typical equivalent circuit assigned to MIEC film reaction kinetics. c) Local RC elements distributed on a surface. d) Reduction of 1D equivalent circuit to a single resistor when $\omega \to 0$.

In general, the complex impedance response of thin films, even on a local level, is not trivial. Some variation of the equivalent circuit shown in Figure 13b has been proposed in a number of studies to account for the kinetics of several different candidate materials, including LSC, LSCF, and LSM [9, 16, 17, 63, 65, 66, 73, 173]. Such an equivalent circuit, distributed over a 2D film, is useful for envisioning the local response of an electrode on an empirical basis [61, 128], as demonstrated in Figure 13c. The local responses may be summed to obtained the global response at various frequencies.

Under steady state conditions (angular frequency $\omega = 0$), even complicated local

equivalent circuits may simplified by a single effective resistor (Figure 13d). As long as a simulation is limited to the steady state condition, this concept can be used to explore sheet resistance without having to speculate too much about the nature of the equivalent circuit. That is, a simple resistor distributed over the 2D film can describe all ORR processes at steady state. The local effective resistance, R_p^{local}, may or may not be close to the global polarization resistance, R_p^{global}, of the cell depending on the impact of the sheet resistance.

At small overpotential (tens of mV), it is assumed that the response is linear and that the macroscopic ORR kinetics of the test cell may be approximated by a linear relationship between the local cathodic overpotential, η_{local}, and current by way of R_p^{local}

$$i_{ORR} = \frac{|\eta_{local}|}{R_p^{local}} \tag{53}$$

The local cathodic overpotential η_{local} is defined as

$$\eta_{local} = \Delta\tilde{\mu}_e^* - \Delta\Phi_e \tag{54}$$

and couples together the electrolyte and MIEC.

With the use of thin films for fundamental SOFC investigations, it is often assumed that the global Ohmic resistance, R_Ω^{global}, is the result of resistance in the electrolyte. The impedance loop is assumed to arise from local electrochemical processes. Unfortunately, sheet resistance can impact both of these quantities, causing R_Ω^{global} to increase and additional features to enter the impedance loop through time constant dispersion. This time constant dispersion has been observed as an effect of potential distribution for the rotating disk electrode in aqueous electrochemistry [61, 128]. Dispersion has also been cited in solid-state systems due to current constriction [51]. In general, additional impedance features tend to increase the global resistance and without proper care they can be interpreted as part of the fundamental kinetics of a candidate material.

For a brief look at the effect of sheet resistance in the thin-film working electrodes at high frequency, a momentarily deviation from the steady state treatment will be taken and for the purpose of example assume a local equivalent circuit with resistor and capacitor in parallel (Figure 13c). A global EIS response over a broad frequency range is simulated for the discrete CC configuration (Figure 14), allowing the local capacitors to contribute to G in Equation 43, enforcing $\partial\rho_{\text{plane}}/\partial t = 0$, and solving for complex variables. Further details of numerical implementation are given in section 3.2.6.

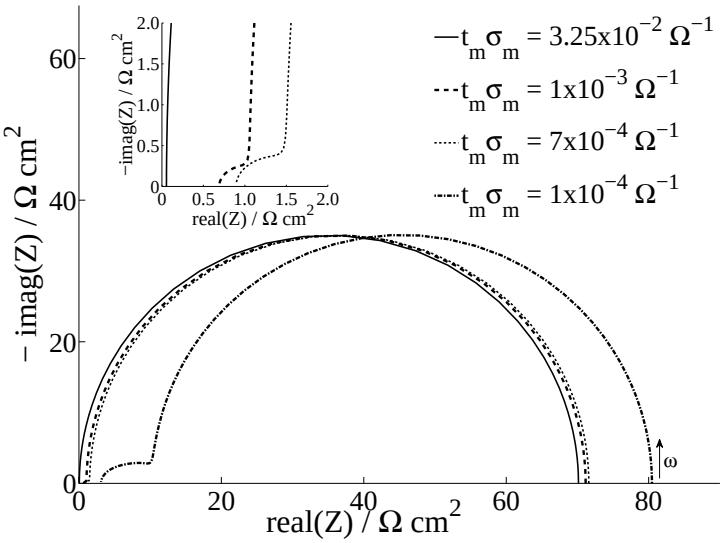

Figure 14: Simulated global EIS spectra at different values of $(t_m\sigma_m)$ for a thin film with discrete current collector configuration. $s = 500\,\mu m$, $t_e = 1\,\mu m$, $R_p^{local} = 70\,\Omega\,cm^2$, distributed local capacitance $= 0.02\,F\,cm^{-2}$, and ω range $10^{-5} - 1.6x10^4$ Hz. The inset plot is a magnification of the high-frequency region.

The quantity $(t_m\sigma_m)$ is used as a figure of merit to assess the conductance of the film and demonstrate the effect of lower conductance on the EIS spectrum. A smaller value indicates more sheet resistance interference. The largest $(t_m\sigma_m)$ in Figure 14 has a global EIS spectrum that is semicircular, nearly perfectly reflecting the ideal local behavior and with a slight Ohmic resistance caused by the thin electrolyte. As $(t_m\sigma_m)$ decreases, sheet resistance causes a time constant dispersion resulting in an

increased Ohmic resistance as well as a second semicircle appearing in the loop at high frequency. The new, extraneous impedance feature can become a large component of the loop, e.g. $(t_m\sigma_m) = 1x10^{-4}\,\Omega^{-1}$, the lowest value of $(t_m\sigma_m)$ shown in the plot. The extraneous loop can dominate the spectrum at even lower film conductance.

The alteration of the EIS spectrum is associated with a simultaneous increase of the total steady state resistance (R_{tot}, the low-frequency real(Z) intercept). There is no second feature discernible for the largest $(t_m\sigma_m)$, and so R_{tot} is shifted merely 0.05% from R_{tot}^{ideal}. Define R_{tot}^{ideal} as

$$R_{tot}^{ideal} = R_p^{local} + R_\Omega^{ideal} \tag{55}$$

where $R_\Omega^{ideal} = t_e/\sigma_i$. The spectra associated with $(t_m\sigma_m) = 1x10^{-3}\,\Omega^{-1}$ and $7x10^{-4}\,\Omega^{-1}$ are shifted from R_{tot}^{ideal} by 1.5 % and 2.1%, respectively. The shift caused by $(t_m\sigma_m) = 1x10^{-4}\,\Omega^{-1}$ is 14.8%. Even lower conductances lead to larger shifts from R_{tot}^{ideal} due to the dominance of the extraneous high-frequency feature.

The additional features contain no intrinsic significance relevant to the ORR, yet they may easily be confused with features arising from adsorption of oxygen at the film surface or with other chemical processes. The goal of this contribution is to guide cell design in such a way that electrochemical uniformity may be maintained in the film without sheet resistance interference under high or low frequency conditions so that the global EIS spectrum may be used to accurately interpret local electrochemical phenomena. The proximity of the actual simulated total resistance, R_{tot}, to R_{tot}^{ideal} will be used as a measure of the impact of sheet resistance. Define R_{tot} as

$$R_{tot} = \frac{V_{cell}}{i_{sim}} \tag{56}$$

where i_{sim} is the calculated total apparent current density of the cell, that is

$$i_{sim} = \frac{\int_{MIEC} (i_{ORR})\, dA}{A_{active}} \tag{57}$$

The numerator is the integral of the local ORR current density taken over the active

MIEC surface (i.e. the total ORR current) and the denominator is the area of the active MIEC surface.

The case generally assumed by experimentalists is sought, i.e. $R_p^{global} \approx R_p^{local}$ and $R_\Omega^{global} \approx R_\Omega^{ideal}$. A deleterious role of sheet resistance would tend to make R_{tot} larger than R_{tot}^{ideal} as a consequence of additional, interfering high-frequency impedance features that force these approximate equalities to be untrue. In the previous example, a specific equivalent circuit was assumed as an example. The exact nature of appropriate circuits will be different from material to material and need not further concern us. Specifics aside, the observation that undesirable high-frequency features can arise and are associated with an increase in R_{tot} can be generalized when limitation of the steady state change to R_{tot} is sought.

Having some estimate of R_p^{local} is important, as its value determines i_{ORR}, which is directly proportional to sheet resistance. Obviously, since the purpose of this contribution is to aid in accurately measuring R_p^{local}, a precise value is not expected. Fortunately, only an estimate from a rough EIS measurement, possibly found in the literature on the specific or a related system, may suffice for general guidance on CC spacing. Getting a good estimate for this value experimentally may or may not be trivial, depending on the material. For instance, R_p of the LSC-LSCF family is relatively insensitive to film thickness at intermediate to high temperatures (provided sheet resistance is mitigated) [43,100,173]. Hence, R_p measured from a relatively thick film can be used as an estimate in Equation 53. On the other hand, R_p of LSM is very sensitive to thickness [16,42,114]. Simply increasing thickness to minimize sheet resistance will also result in an altered R_p and an adjustment, e.g. linear correlation with thickness [42], may be required to estimate R_p. Furthermore, R_p is also well-known as a function of temperature, T, and oxygen partial pressure, P_{O_2}. It is more conservative to underestimate R_p^{local} if the goal is to minimize sheet resistance.

3.2.5 Large-polarization approximation

Any model for large cathodic polarization requires more input than the small polarization case. Unfortunately, behavior under large cathodic polarization is very specific to individual materials. Experimental measurements can provide current-voltage data and a succession of impedance data at intermediate polarizations. These measurements should be conducted in a geometry where sheet resistance is as minimized as possible in order to translate them directly to the local environment. The impedance data can then be used to separate R_Ω from R_p and hence identify the nominal global cathodic overpotential, η, as a component of the cell voltage. A table of cell current density vs. η may then be constructed, from which $i_{ORR} = i(\eta_{local})$ may be interpolated for local use in the model. This approach is very specific to the material under investigation and likely cannot be generalized to others that differ in composition or electrochemical history, but is the best approach when such data is available.

Alternatively, in exchange for more assumptions, a kinetic model may be applied to determine $i_{ORR}(\eta_{local})$. This approach is taken here in order to demonstrate the effect of large polarization. Because test cells often display some exponential character in the current-voltage relationship of dense films [42,65,114], the Butler-Volmer (BV) equation [14]

$$i_{ORR} = \left| i_0 \left(\exp\left(\overleftarrow{\alpha} \frac{F}{RT} \eta_{local} \right) - \exp\left(-\overrightarrow{\alpha} \frac{F}{RT} \eta_{local} \right) \right) \right| \tag{58}$$

will be applied locally here, though it typically is not used in conjunction with thin MIEC films. The variable i_0 is the exchange current density, R is the universal gas constant, T is the temperature, and $\overleftarrow{\alpha}$ and $\overrightarrow{\alpha}$ are the anodic and cathodic transfer coefficients, respectively. The transfer coefficients are related: $\overleftarrow{\alpha} + \overrightarrow{\alpha} = n/\nu$, where n is the number of electrons transferred in the overall reaction and ν is the stoichiometry number, that is the total number of times the rate-limiting step occurs in the overall reaction. Consider the reaction shown in Equation 38. Lacking other information, let

n = 2 and $\nu = 1$. Then, $\overleftarrow{\alpha} + \overrightarrow{\alpha} = 2$. For simplicity, let $\overleftarrow{\alpha} = \overrightarrow{\alpha} = 1$. The exchange current density can be estimated from R_p^{local}

$$i_0 = \frac{1}{R_p^{local}} \frac{\nu RT}{nF}. \tag{59}$$

The BV equation here serves as an empirical estimation of the large polarization case and likely overestimates the local current density of many solid state MIEC electrodes due the fact that specific kinetic limitations, such as mass transport, the intricacies of defect chemistry, and chemical processes at the MIEC surface, are not taken explicitly into consideration. Delving into these issues would require a more sophisticated 3D elemental model [96, 101, 103], which is useful for probing specific materials on a fundamental level and is the subject of continued development but is beyond the simple, empirical, and general scope of this chapter. The purpose of using BV here is simply for some model to link η_{local} to i_{ORR} superlinearly. A more detailed model is recommended for use with a specific material if large cathodic polarization is of interest. However, this approach is certainly accurate in the case where charge-transfer kinetics apply explicitly, especially in other thin-film electrochemical systems.

For the purpose of this model, constant σ_m is assumed. In reality, when the oxygen stoichiometry of a typical MIEC material is altered, say by varying partial pressure of oxygen or temperature, the conductivity is known to change [112]. A similar change in conductivity is expected under cathodic polarization; however, very little is known about how it trends as a function of cathodic overpotential. Constant σ_m is therefore assumed in this model as the best available treatment and for generality.

3.2.6 Numerical implementation

The finite element method (FEM) with adaptive mesh refinement is employed for numerical simulations using the commercial software package COMSOL Multiphysics version 3.5a. The simulations were performed on the domains shown schematically in Figure 11b, which were modeled using the software's computer aided design (CAD)

tools. The MIEC thin film is simplified from a 3D volume with an extreme aspect ratio to a 2D surface, on which Equation 45 is solved using COMSOL's "weak form, boundary" application mode. Equation 52 is solved in 3D in the electrolyte. The weak form boundary mode allows the top surface of the electrolyte block to serve as both the electrolyte boundary as well as the 2D MIEC film domain. The two domains are linked by the local current, a boundary expression. During solution, both the bulk and surface FEM problems are solved simultaneously. In cases with frequency dependence, the parametric solver may be used to simulate over all required frequency. For further details, the software help file contains specifics of rendering model geometry, implementing constitutive equations and boundary conditions, meshing, and solving.

Values of CC spacing, s, or electrolyte thickness, t_e, that are far apart in magnitude cause the simulated geometry to be difficult to draw, mesh, and solve in the FEM software. In order to ease these computational limitations, σ_m and i_{ORR} in Equation 45 and σ_i in Equation 52 are scaled in the x, y, and z directions. The test cell is constructed once in the software's CAD application as a configuration that is convenient to mesh and solve. In order to change the geometry of the simulated physical test cell, the effective conductivity and effective local electrochemical current density is altered rather than the model domain shape to change the geometry of the test cell.

In the specific case of the test cell, let the physical CC separation in the x-direction be given by $s_x^{(physical)}$ and let the illustrated value in the CAD drawing be given by $s_x^{(model)}$. Similarly, the y-direction values are $s_y^{(physical)}$ and $s_y^{(model)}$, respectively. In the electrolyte, let the physical thickness be $t_e^{(physical)}$ while the illustrated thickness is $t_e^{(model)}$. Then, the scaling factors in the x, y, and z-directions are given by

$$f_x = \frac{s_x^{(physical)}}{s_x^{(model)}} \qquad f_y = \frac{s_y^{(physical)}}{s_y^{(model)}} \qquad f_z = \frac{t_e^{(physical)}}{t_e^{(model)}}. \tag{60}$$

The scaled, effective conductivities in the MIEC are

$$\sigma_{m,x}^{(eff)} = \sigma_m \left(\frac{f_y}{f_x}\right) \qquad \sigma_{m,y}^{(eff)} = \sigma_m \left(\frac{f_x}{f_y}\right) \tag{61}$$

and the scaled, effective conductivities in the electrolyte are

$$\sigma_{e,x}^{(eff)} = \sigma_e \left(\frac{f_y f_z}{f_x}\right) \qquad \sigma_{e,y}^{(eff)} = \sigma_e \left(\frac{f_x f_z}{f_y}\right) \qquad \sigma_{e,z}^{(eff)} = \sigma_e \left(\frac{f_x f_y}{f_z}\right). \tag{62}$$

The local effective boundary current is

$$i_{ORR}^{(eff)} = (f_x f_y)\, i_{ORR} \tag{63}$$

due to the compression of the actual surface area in the CAD model by a factor of $f_x f_y$. This adjustment must be made in order to preserve the total current. The effective values are inserted into Equations 45 and 52. The tensor form of the FEM is then used to solve them. This approach makes it relatively easy to change s and t_e and in some cases is the only way to effectively simulate large aspect ratios by FEM. The scaling yields good agreement when tested against the full-scale simulation for different physical geometry test cases.

3.3 Results and discussion

In the following discussion, the model is used to first investigate the effect of various geometric and experimental parameters upon sheet resistance and cell performance and then it is used to provide generalized guidance on cell design.

3.3.1 Parameter investigation

For the parameter investigation, the data from an LSCF film deposited by sputtering onto a gadolinia-doped ceria (GDC) electrolyte substrate and using a mesh CC (Table 2) is used to illustrate specific trends. The value of σ_i was determined from R_Ω using the geometry of the electrolyte. In general, the input parameters vary as a function of the material as well as processing and experimental conditions, but the

qualitative trends will be the same as those illustrated in this section. The reader is referred to the following section for guidance based upon specific configuration.

Table 2: Example film test cell parameters based on LSCF.

Parameter	Value	Units	Description
t_m	1	μm	MIEC film thickness
t_e	$300 - 400$	μm	electrolyte film thickness
R_p	24.8	Ω cm^2	open-circuit polarization resistance
R_Ω	9.3	Ω cm^2	open-circuit Ohmic resistance
σ_m	325	S cm^{-1}	MIEC electrical conductivity[a]

[a]Conductivity value from the literature [155].

Potential distributions at steady state in each of the three CC configurations are given in Figure 15, generated using the t_m = 20 nm and s = 270 μm, and a cell voltage of 10 mV (linear model). Each map was constructed by stitching together sixteen simulation domains along the symmetric boundaries. In each CC configuration, the potential deviates from $\Delta\tilde{\mu}_e^*$(CC), with more deviation as distance from the CC increases, attaining value $\Delta\tilde{\mu}_e^*$(far) at the farthest point from the CC. The decreasing potential deviation in Figure 15 a to c shows that intra-film current collection is superior in the grid CC configuration and inferior in the 20-μm diameter discrete configuration when everything else is equal. The film with the discrete configuration sees a rapid change in potential away from the CC due to the effect of current constriction. The parallel configuration causes less current constriction than the discrete contacts and the average distance between a point on the surface and the CC is smaller. As a consequence, the potential deviates less from $\Delta\tilde{\mu}_e^*$(CC) in the parallel configuration than in the discrete and hence sheet resistance is less severely manifested. The grid configuration experiences less sheet resistance than the previous two configurations for the same reason.

One measure of the degree of sheet resistance is the steady state relative potential

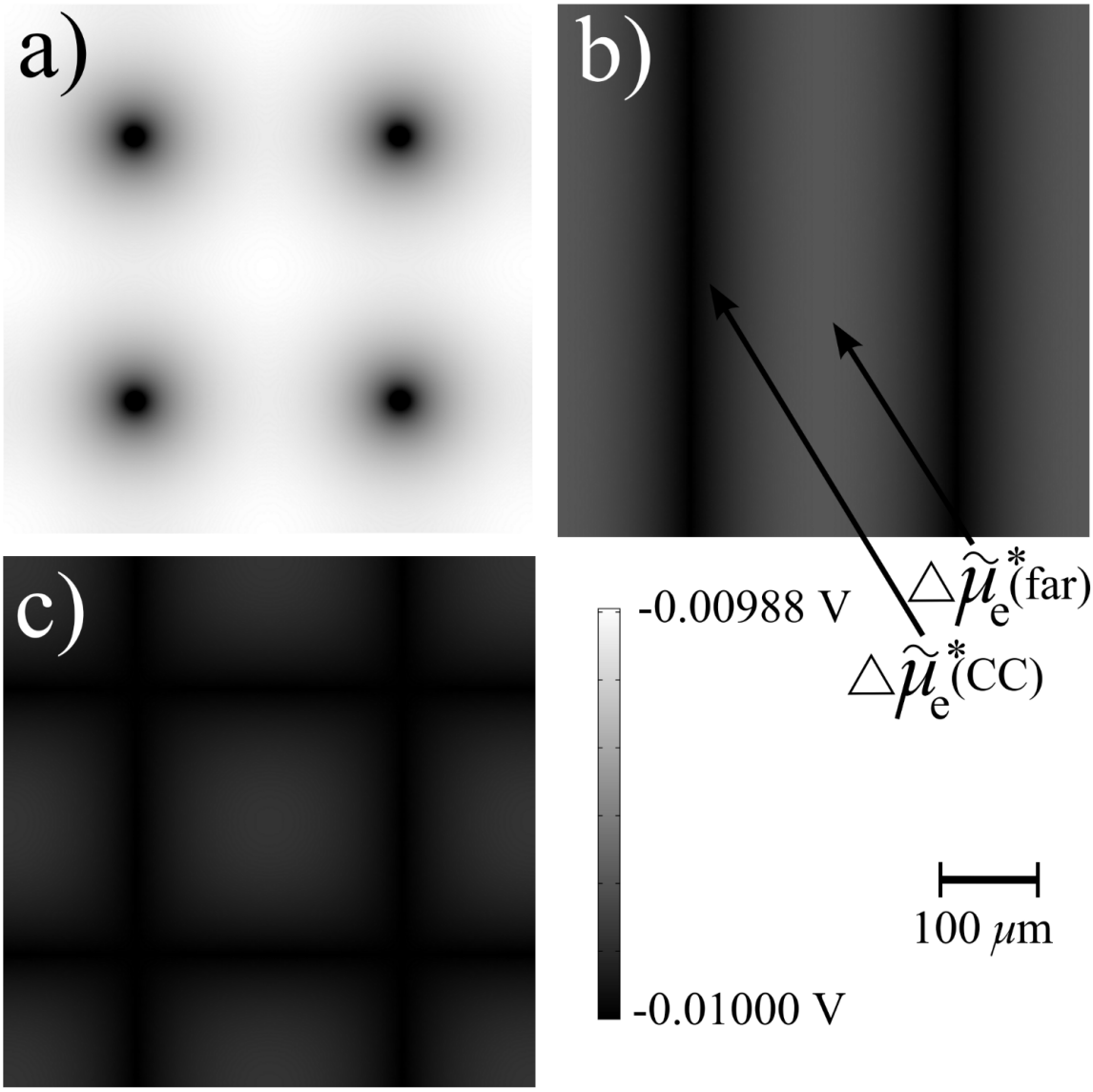

Figure 15: Distribution of $\Delta\tilde{\mu}_e^*$ in the film for three CC configurations: a) 20-μm diameter discrete contacts, b) parallel, and c) grid. R_p and σ_m from Table 2. Electrolyte is assumed very thin. $t_m = 20$ nm, s = 270 μm, $V_{cell} = 10\,mV$.

far from the CC, defined as

$$\text{Relative potential} \equiv \frac{\Delta\tilde{\mu}_e^*(\text{far})}{\Delta\tilde{\mu}_e^*(\text{CC})} \tag{64}$$

The relative potential is essentially the fraction of the applied potential retained by the MIEC far away from the CC. Another measure is the relative cell current

$$\text{Relative current} \equiv \frac{i_{sim}}{i_{hom}} \tag{65}$$

where i_{sim} is the simulated total apparent steady state cell current density from Equation 57 and i_{hom} is the homogeneous cell current density expected in the case of a well current-collected test cell with the potential $\Delta\tilde{\mu}_e^*(CC)$ distributed homogeneously over the film (and hence no sheet resistance). That is, $i_{hom} = V_{cell}/(R_{tot}^{ideal})$. The relative current is the degree to which sheet resistance affects the global current response of the cell.

A similar global measure is the relative resistance

$$\text{Relative resistance} \equiv \frac{R_{tot}}{R_{tot}^{ideal}} \tag{66}$$

where R_{tot} is from Equation 56 and R_{tot}^{ideal} is from Equation 55.

The effect of cell geometry at small cell voltage (10 mV) is illustrated using these measures in Figure 16. When the film is sufficiently thick (hundreds of nanometers to microns), the steady state potential does not deviate substantially from that applied at the CC (Figure 16a). As the film becomes thinner, the potential deviates more severely from the applied value and the relative potential decreases. The consequence of this deviation is that the local overpotential far from the CC is reduced, resulting in a reduction in the local i_{ORR} and impacting the global relative current and relative resistance. The variation of cell current and resistance illustrates that sheet resistance has the capability to significantly alter the global response of a test cell.

Figure 16b shows that both film thickness and CC spacing have a significant impact upon the apparent resistance of the cell. Close CC spacings alleviate the effect of small film thickness. Given CCs sufficiently close to one another, sheet resistance affects the relative resistance very little despite even small thickness and therefore sheet resistance can be neglected in subsequent data interpretation. Likewise, thicker films mitigate sheet resistance. Larger CC spacings and thinner films, though, exaggerate deactivation far from the CC. In general, the effect of sheet resistance becomes worse as the CC-spacing-to-film-thickness ratio increases. If the ratio is large enough, the resistance can be several times its ideal value.

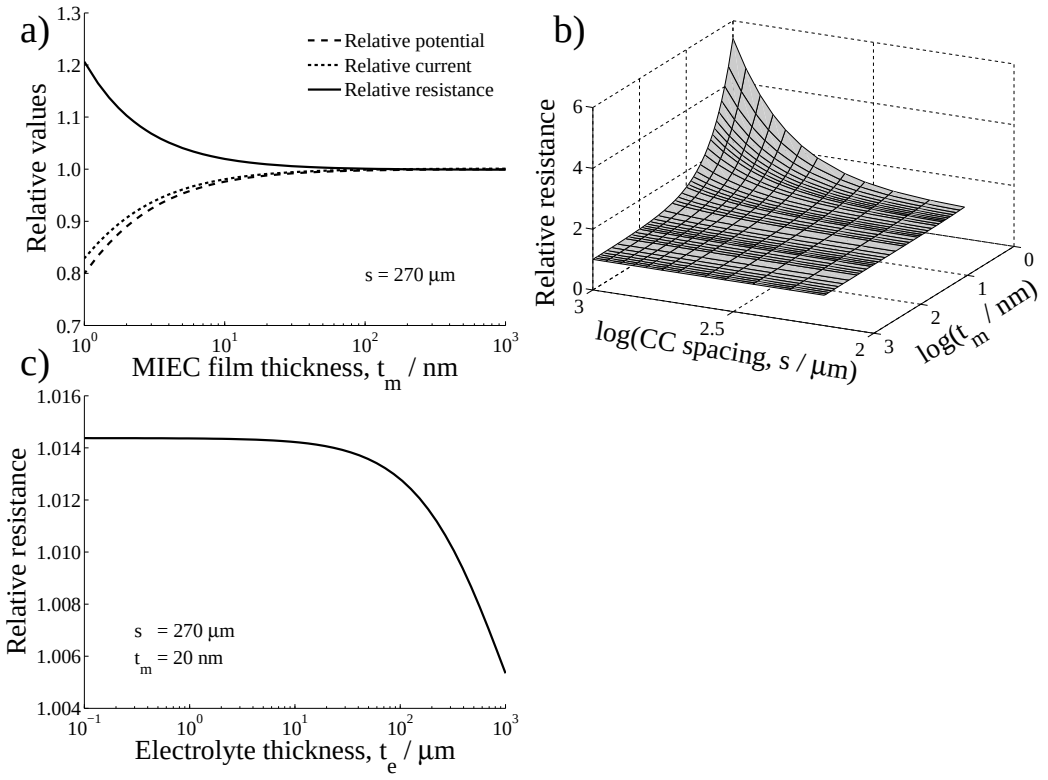

Figure 16: a) Relative values of potential, cell current, and resistance near OCV as a function of t_m for $s = 270\,\mu m$ under small cathodic polarization. b) Relative resistance as a function of s and t_m. For a) and b), R_p^{local}, R_Ω, σ_m, σ_i, and t_e from Table 2. $V_{cell} = 10\,mV$. c) Effect of the electrolyte thickness on the relative resistance in the MIEC thin film for different cell voltages. $t_m = 20\,nm$ and $s = 270\,\mu m$. R_p^{local}, σ_m, and σ_i from Table 2. 20-μm-diameter discrete CC configuration for all.

Electrolyte thickness, t_e, also impacts sheet resistance in the cell (Figure 16c). The small-t_e limit comes about when the electrolyte becomes so thin that its contribution to cell resistance is negligible. Therefore, the cell voltage is converted almost directly into cathodic overpotential, which drives large i_{ORR} across the cell. The large current density causes more severe sheet resistance in the film. Subsequent analysis in this contribution assumes that the electrolyte is vanishingly thin in order to deal with the worst case of sheet resistance.

Under large cathodic bias (Figure 17) the trends in relative potential, current,

and resistance are similar to varying t_m (Figure 16). However, a small change to local overpotential is magnified into a much larger change in the global quantities due to the exponential character of the assumed kinetics. Resistance away from OCV is defined as

$$R_{tot} = \frac{\partial V_{cell}}{\partial i_{sim}} \tag{67}$$

The resistances used in computing the relative resistance in Figure 17 are approximated using discrete data by computing a center difference

$$R_{tot}(V_j) = \frac{V_{cell,\,j+1} - V_{cell,\,j-1}}{i_{sim,\,j+1} - i_{sim,\,j-1}}. \tag{68}$$

around the data pair $(V_{cell,\,j}, i_{sim,\,j})$.

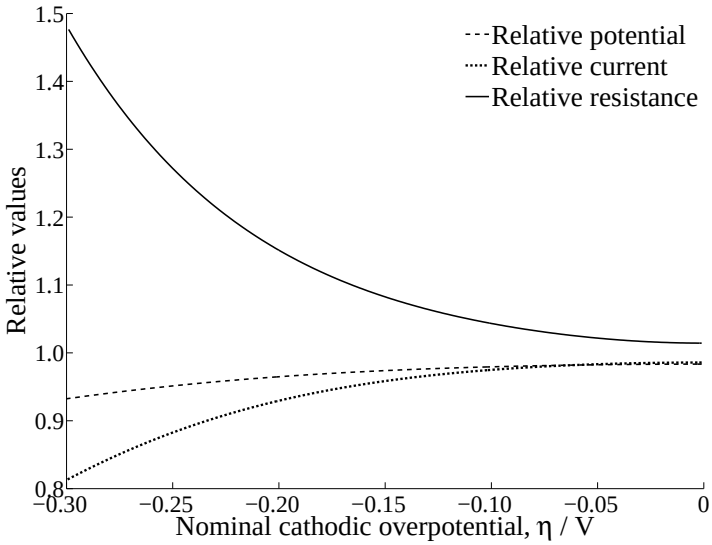

Figure 17: Relative potential, relative cell current, and relative calculated total resistance as a function of nominal global cathodic overpotential (large-polarization kinetics) using the 20-μm diameter discrete CC configuration. The electrolyte is assumed vanishingly thin. t_m = 20 nm, s = 270μm. R_p^{local} and σ_m from Table 2.

3.3.2 General cell design

The principal experimental factors affecting thin-film test cell response are

1. CC configuration (grid, parallel, discrete)

2. CC spacing, s

3. MIEC film thickness, t_m

4. Electric conductivity of the MIEC, σ_m

5. Local polarization resistance, R_p^{local}

6. Electrolyte thickness, t_e, and conductivity, σ_i

7. Cell voltage, V/cathodic overpotential, η

Many of these parameters can be manipulated in such a way that general information on sheet resistance can be extracted. Maps computed from parameter encapsulation are now developed, inspired by those often employed for materials selection in mechanical design [7], that can be applied to arbitrary thin-film SOFC cathode MIEC candidates for the selection of CC spacing.

3.3.2.1 Small cathodic polarization

The following steps may be taken to simplify and generalize the small cathodic polarization case. At small polarization, both R_p^{local} and σ_m are functions of temperature, oxygen partial pressure, and sometimes t_m. Because the structure of the model is such that R_p^{local} and σ_m are input directly from measurement or estimation, the other factors may be used to estimate R_p^{local} and σ_m for the desired experiment. Secondly, from Equation 45, t_m and σ_m appear together. Therefore, they may be lumped into one parameter, $(t_m\sigma_m)$, as discussed previously. Next, as shown in Figure 16c, if $t_e = 0$ and/or σ_i is very large, then sheet resistance in the MIEC film is maximized. Therefore, the electrolyte is assumed vanishingly thin in order to get a conservative estimate of the sheet resistance. Finally, the response is linear with η around OCV, so any choice of small $\Delta\tilde{\mu}_e^*(\mathrm{CC})$ should do; $\Delta\tilde{\mu}_e^*(CC) = -10$ mV is chosen.

Now, assume a specific CC configuration. If a particular relative resistance is desired and the variables R_p^{local} and $(t_m\sigma_m)$ are specified, then s must take on a unique value in order to satisfy the conditions imposed. Let this critical value of s be denoted s_c. Further analysis assumes that s_c is the value of s such that $R_{tot} = 1.005 \cdot R_{tot}^{ideal}$. Choose a 0.5% deviation from the ideal because it allows very few extraneous high-frequency features to be introduced but allows reasonable CC spacings to be retained. Similar plots can be generated with stricter or looser requirements.

Figure 18 shows maps of $\log(s_c)$ given different R_p^{local} and $(t_m\sigma_m)$ for each of the three CC configurations, determined by numerical optimization, using Newton's method to guide the search as needed. Figure 18a is a 3D surface and Figure 18b is the corresponding contour plot for the 20-μm diameter discrete configuration. The black region of the contour plot indicates where the required s_c is less than the diameter of the CC contact. Figure 18c and d are contour plots of $\log(s_c)$ corresponding to the parallel and grid configurations, respectively. Note that s_c has units of μm, so for example the contour labeled 3 corresponds to $s_c = 10^3\,\mu$m. The selection criteria R_p^{local} and $(t_m\sigma_m)$ vary over a range of values including those representative of the families of SOFC cathode candidates. The discrete configuration requires smaller s_c than the parallel configuration, which requires a slightly smaller s_c than the grid configuration. This conclusion is in agreement with the potential distribution in Figure 15.

3.3.2.2 Large cathodic polarization

At large cathodic polarization, the cell response is a direct, nonlinear function of the nominal global cathodic overpotential, η, and temperature. The critical CC spacing, $s_c^{large\,\eta}$, is smaller than the linear case, $s_c^{small\,\eta}$ of the previous section. This deviation may be expressed as an adjustment factor, a.f.:

$$\text{a.f.} = \frac{S_c^{large\,\eta}}{s_c^{small\,\eta}} \tag{69}$$

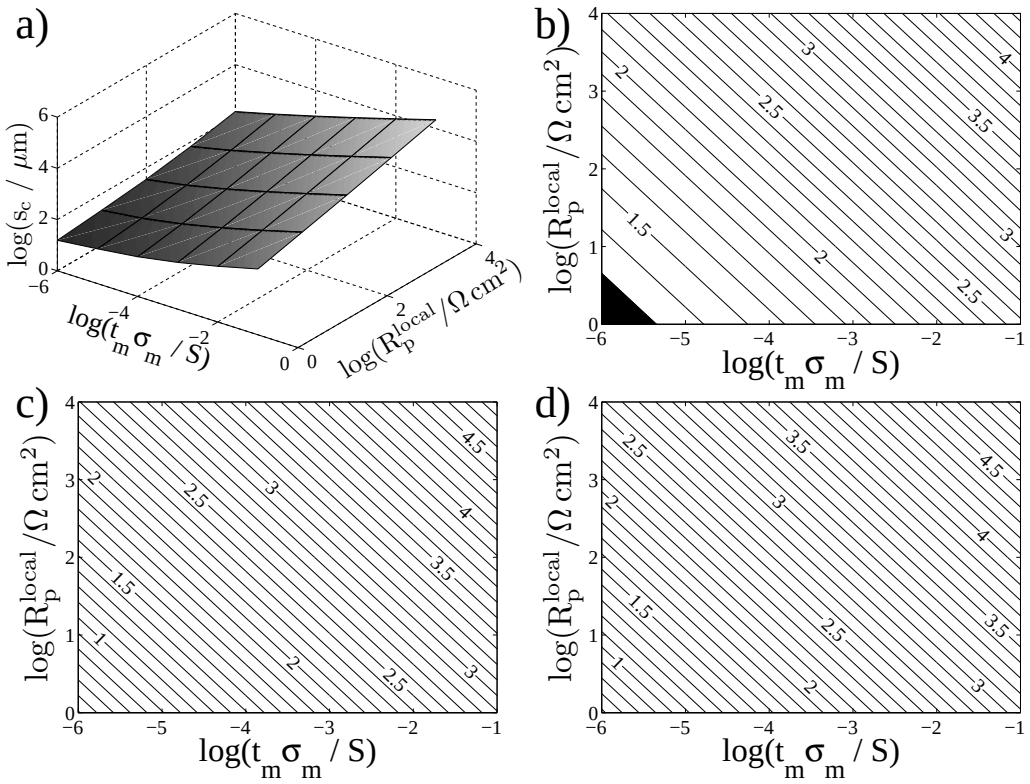

Figure 18: a) 3D surface of $\log(s_c)$ for the 20-μm diameter discrete CC configuration under small cathodic polarization. b)-d): Contour plots of $\log(s_c)$ for the b) 20-μm diameter discrete, c) parallel CC, and d) grid CC configurations. The contours denote the level sets of $\log(s_c)$. The units of s_c are μm.

Figure 19 gives a.f. as a function of η and T for the grid and parallel CC configuration cases. The a.f. is independent of R_p^{local} and $(t_m\sigma_m)$, a result that may be shown analytically and is due primarily to the fact that the potential profiles under any polarization are affected in the same way by varying η and T. Unfortunately, a.f. is not constant in R_p^{local}-$(t_m\sigma_m)$ space when discrete CCs are used because the CC footprint is a different fraction of the active surface area at different values of s_c (see Figure 11b), which is not a concern for the parallel and grid configurations as modeled. Thus, Figure 19 does not apply to the discrete configuration.

To use the adjustment factor, $s_c^{small\,\eta}$ corresponding to a combination of R_p and $(t_m\sigma_m)$ may be selected from Figure 18. Then, to adjust it for larger polarization, a

factor is chosen from Figure 19 based on η and T. Note that if multiple temperatures are to be evaluated, new small-polarization R_p^{local} and $(t_m\sigma_m)$ values should likely be used and a new $s_c^{small\,\eta}$ chosen from Figure 18 for each temperature, since both are typically strong functions of temperature.

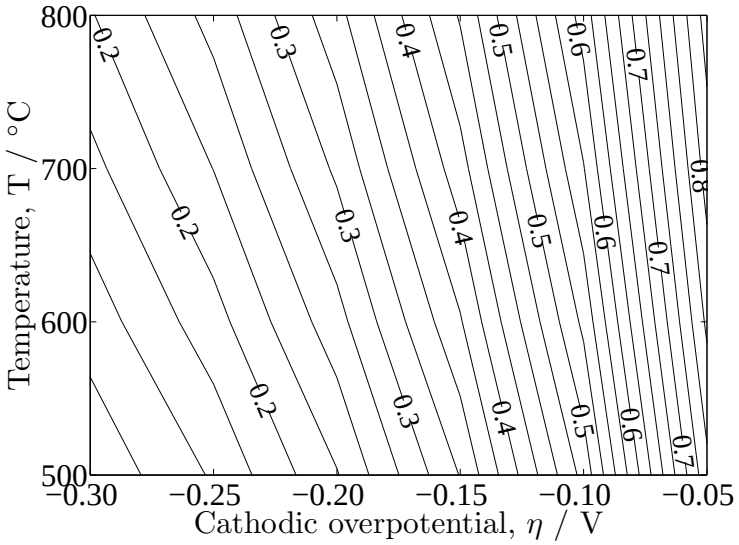

Figure 19: Contour plots of the adjustment factor to small-η s_c at combinations of η and T (large-polarization model) for the grid and parallel CC configurations, but not valid for the discrete CC configuration. Vanishingly thin electrolyte assumed. The a.f. is valid for any R_p^{local}-$(t_m\sigma_m)$ combination.

3.3.2.3 Map discussion

These maps may be used to aid design of thin-film test cell geometries for arbitrary MIEC materials under arbitrary test conditions. At small polarizations, if R_p^{local} and σ_m can be estimated and t_m of the film determined, then the CC spacing required to prevent R_{tot} from exceeding R_{tot}^{ideal} by more than 0.5%, and thus keeping the potential uniform, can be determined from Figure 18. The s_c value can be determined in principle for large polarization with parallel/grid configuration from Figure 19 using the a.f. to adjust the small polarization case. Likewise, if the CC configuration must be fixed, the level sets in the contour plots show which combinations of R_p^{local} and

($t_m\sigma_m$) lead to no more than a 0.5% increase in R_{tot}. Similar maps can be generated for any threshold. If R_p^{local} and σ_m must be estimated and not directly measured, then underestimating both provides a conservative estimate for s_c.

The large polarization calculations assume BV kinetics and constant σ_m. The extrapolation of linear (small cathodic polarization) kinetics to larger polarization is a less severe estimate and is perhaps more appropriate than the large cathodic polarization calculations if the kinetics of the material being studied are not strictly dominated by charge transfer. The BV kinetics in Figure 19 are then in some sense illustrative, they show a trend at large polarization but are not as generally applicable as the small polarization treatment in Figure 18. The reader is recommended to perform similar analysis with material-specific data using the tabular approach described in section 3.2.5 at large polarization to provide more accurate estimations for their particular system.

There is no set CC spacing for any specific MIEC or family of MIECs. Generally, the thinner the film, the smaller CC spacing that is required. Even when the thickness is held constant, though, a change to polarization, temperature, partial pressure of oxygen, or electrochemical history can cause a change to R_p^{local} or σ_m that can significantly alter the required CC spacing. CC spacing should be designed based on the planned experimental conditions or possible worst-case scenario for specific materials.

3.4 Conclusion

In this chapter, an empirical numerical model was presented to simulate potential distribution and current/resistance response under various material and catalytic parameters, CC configurations, cathodic polarizations, and other experimental factors in thin-film, mixed-conducting test cells. Thinner films, larger CC spacings, and thinner electrolytes aggravate sheet resistance, causing the global cell properties such as

cell current and cell resistance to vary, sometimes substantially, from the expected value in the case of a well current-collected film. Mitigating sheet resistance with the proper CC spacing is therefore crucial, lest these variations be incorporated into macroscopic experimental results and convoluted with the material's intrinsic catalytic and transport properties.

The model was used to provide guidance for effective CC placement by mapping in parameter space, using local polarization resistance, R_p^{local}, and the product of electrical conductivity and film thickness, ($\sigma_m t_m$), as selection parameters. In general, continuous crisscrossing metal lines, deposited through e.g. photolithography, provide the best intra-film current collection while small, regularly spaced discrete contacts, provided by e.g. a metal mesh, provide the least efficient intra-film current collection. Most thin-film aspect ratios and CC configurations can be accommodated without severe intra-film sheet resistance provided the CCs are spaced appropriately. With well-designed CCs, a maximum amount of surface area is free to use for other in-situ characterization methods such as Raman spectroscopy while ensuring that EIS measurements reflect the true intrinsic properties of the material being studied.

CHAPTER IV

ENHANCEMENT OF LSCF DURABILITY AND ELECTROCATALYTIC ACTIVITY BY LSM: MODELING INVESTIGATION

4.1 Introduction

As discussed previously in this thesis, the cathode is one of the primary components of the SOFC and in need of improvement to enable widespread commercialization. In particular, the performance must be improved at intermediate temperatures of around 650°C to enable cheaper components to be used in the cell and reduce cost. Recent efforts at developing suitable cathodes for intermediate temperature SOFCs have focused on developing new materials with more favorable intrinsic oxygen reduction properties such as those in the $Ba_{1-x}Sr_xCo_{1-y}Fe_yO_{3-\delta}$ (BSCF) or double perovskite families [177, 178], creating more efficient electrode architectures through infiltration of active material onto an electrolyte scaffold [166], and surface modification through infiltrated catalyst decoration [68, 159, 168]. Improving the cathode through such means is an active area of research because no uniformly acceptable solution has been developed.

Two primary SOFC cathode materials include LSM and LSCF. Cathodes containing LSM are usually combined with an electrolyte material such as YSZ with the primary areas of electrochemical activity being TPBs because the ionic conductivity of LSM is small. Cathodes composed of LSCF typically contain only the one solid

[‡]M. E. Lynch, L. Yang, W. Qin, J.-J. Choi, Mingfei Liu, K. Blinn, and Meilin Liu, "Enhancement of $La_{0.6}Sr_{0.4}Co_{0.2}Fe_{0.8}O_{3-\delta}$ Durability and Surface Electrocatalytic Activity by $La_{0.85}Sr_{0.15}MnO_{3\pm\delta}$ Investigated using a New Test Electrode Platform," Energy & Environmental Science, 4, 2249-2258 (2011).

phase but are very active because their ionic conductivity is very large compared with LSM and therefore the area active to oxygen reduction is extended far from the cathode-electrolyte interface. A few literature reports combine LSM and with other perovskites. LSM/YSZ functional layers have been used in conjunction with LSCF current-collector layers without intermixing of the perovskite phases [80]. Some success was achieved when hybrid phases of LSM and strontium-doped $LaCoO_3$ (LSC) were formed, denoted LSMC, or when the two phases were infiltrated sequentially onto a YSZ scaffold [62].

In this chapter, a novel electrode architecture is detailed wherein a thin film of LSM was deposited onto the surface of LSCF, leading to substantial improvement of the cathode activity and long-term stability. The phenomenon was investigated by several methods including transmission electron microscopy (TEM) of thin LSM layers on LSCF, full-cell electrochemical testing after LSM infiltration into porous LSCF electrodes, and electrochemical testing of sputtered thin-film test cells. Some of the concepts of thin-film test cell investigation developed in previous chapters are used to investigate this novel method of electrode modification. The experimental work was performed by other researchers and therefore the focus of this chapter is upon the theoretical proposed explanations, described by phenomenological modeling starting in section4.3. Nevertheless, a short summary of the experimental results is necessary to provide context for the theoretical work.

4.2 Experimental

The experimental procedure and results are described is this section. For a more detailed discussion, the reader is referred to the publication written in collaboration with the experimentalists who contributed to this work [95].

4.2.1 Model electrode test cells

The purpose of the model electrode test cell platform is to create a well-defined geometry that allows the isolation of surface reactions. The test cell platform used for this study is shown in Figure 20a. The electrolyte was a sintered and polished pellet of polycrystalline gadolinia-doped ceria (GDC). The current collector/backbone layer was LSCF, while the working electrode layer was LSM. Both layers were sputtered, with the LSCF layer having a thickness of 1 μm and the LSM layer having a thickness of 10 nm. The counter electrode opposite was a porous LSCF electrode. Fabrication of the sputtered test cells was performed by Jae-Wung Lee [91] and electrochemical testing was performed by Lei Yang.

The test cell platform design itself was a novel creation. The idea was for the underlying backbone layer to serve as both a facile pathway for oxygen vacancies as well as to alleviate some of the sheet resistance concerns associated with a very thin layer elaborated upon in the previous chapter. LSCF met both of those conditions. The LSM, layer, on the other hand was dense so that the electrochemical measurements of the cell reflected the properties of the LSM surface layer. Such a structure not only replicated the infiltration of LSM onto a LSCF backbone, but allows current collectors to be spaced further apart and therefore allows much of the surface to be exposed for other *in situ* methods such as Raman spectroscopy. Uses for such multifunctional test cells are described in [93].

The electrochemical impedance spectra of the tests cells at 700° under various oxygen partial pressure and as a function of cathodic bias are shown in Figure 20. The trend of the interfacial resistance (low-frequency impedance limit) is shown in Figure 20a while the full spectra at two values of cathodic overpotential are shown in Figure 20b. There are several features of this data. First, the uncoated LSCF (that is, only the thick backbone layer sputtered, but no working electrode layer) has a lower interfacial resistance under no bias (open-circuit voltage, OCV). As the applied

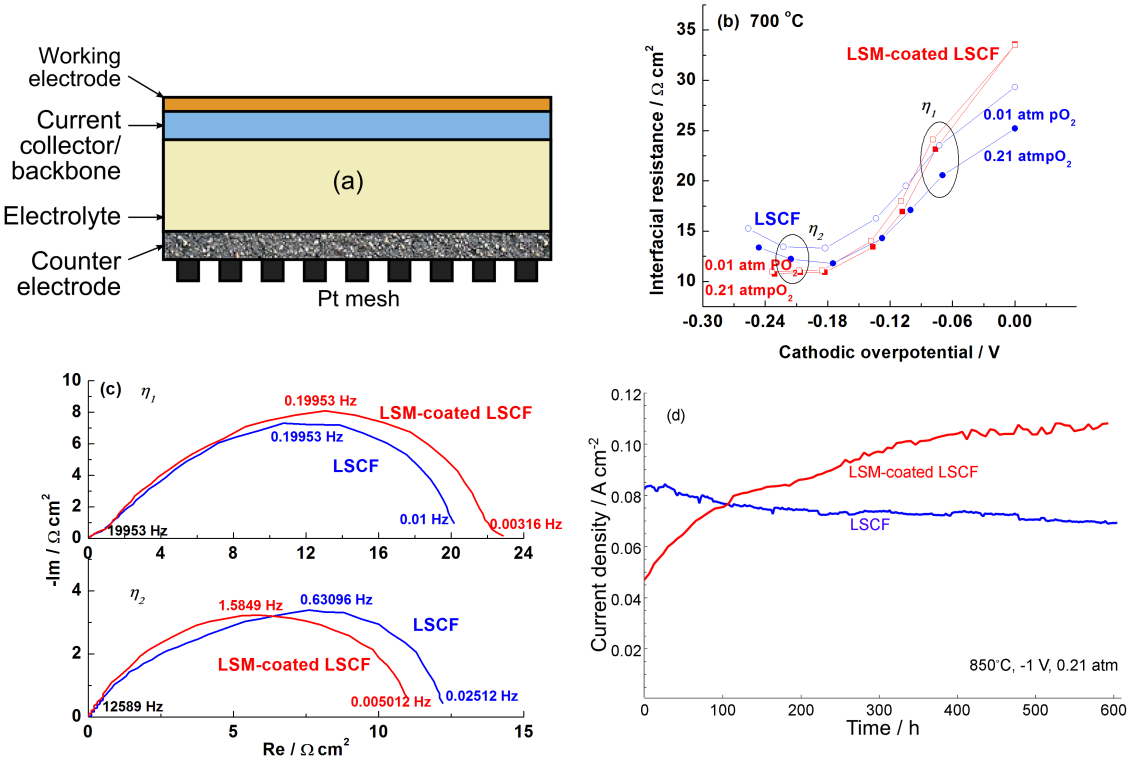

Figure 20: a) Schematic of the thin film test cell architecture used in this study. b) Effect of cathodic overpotential on the interfacial resistances of blank LSCF and LSM-coated LSCF model electrodes under different oxygen pressures. c) Impedance spectra of blank LSCF and LSM coated LSCF cathode without Ohmic portion at 700°C under indicated cathodic overpotential conditions η_1 and η_2. d) Current densities of two model electrode cells with and without LSM coating as a function of time at a constant voltage of -1 V. Plots b-d of experimental results are courtesy of Lei Yang, who performed the measurements.

cathodic bias becomes larger, the resistance of both the coated and uncoated cells decreases. However, the resistance of the LSM-coated LSCF layer decreases more quickly and eventually crosses the resistance of uncoated cell at larger cathodic bias. The performance of the LSM-coated LSCF electrodes is therefore superior under this larger bias.

Another key feature of the data is the relative insensitivity of the LSM-coated LSCF cell's resistance to changing pO_2 contrasted with the sensitivity of the uncoated LSCF cell. When blank and LSM-coated LSCF electrodes were exposed to 1% O_2, the interfacial resistances of the blank LSCF electrode were increased. This behavior

coincides with a result reported elsewhere [41], suggesting that a rate-limiting step is associated with the surface adsorption/dissociation reaction on the LSCF surface. In contrast, LSM-coated LSCF exhibits much less dependence on oxygen pressure, resulting in the crossover point shifting to lower overpotentials compared with that in air.

The tests cells were also tested under potentiostatic test conditions for 600 hours (Figure 20d). The LSCF cell showed a loss of performance with time, while the LSM-coated LSCF cell showed a time-dependent performance activation, resulting in superior current density after approximately 100 hours.

4.2.2 Full cell infiltration and testing

Based on the positive result of the model electrode measurements, a simple aqueous infiltration process using nitrate precursors [21] was employed to deposit a thin layer of LSM onto the surface of a porous LSCF electrode of an anode-supported full cell. A schematic of the desired thin, continuous, conformal, and dense LSM layer on the porous LSCF is shown in Figure 21. Infiltration was performed by Mingfei Liu and Jong-Jin Choi, and electrochemical characterization was performed by Mingfei Liu and Lei Yang.

The electrochemical impedance spectra in Figure 21 show that the interfacial resistance of the LSM-infiltrated cathode-containing cell is larger than the uncoated cathode-containing cell at OCV but smaller under a bias (constant current of 100 mA cm^{-2}), showing superior performance. This bias-dependent activation is analogous to that observed from the thin-film test cells. The long-term performance (Figure 21c) was also similar to the test cells. The performance of the LSM-coated LSCF cathode-containing cell initially had lower performance because the starting cathodic overpotential was approximately -0.1 V, which is closer to OCV than the crossover point leading to superior performance of the infiltrated cell (c.f. model

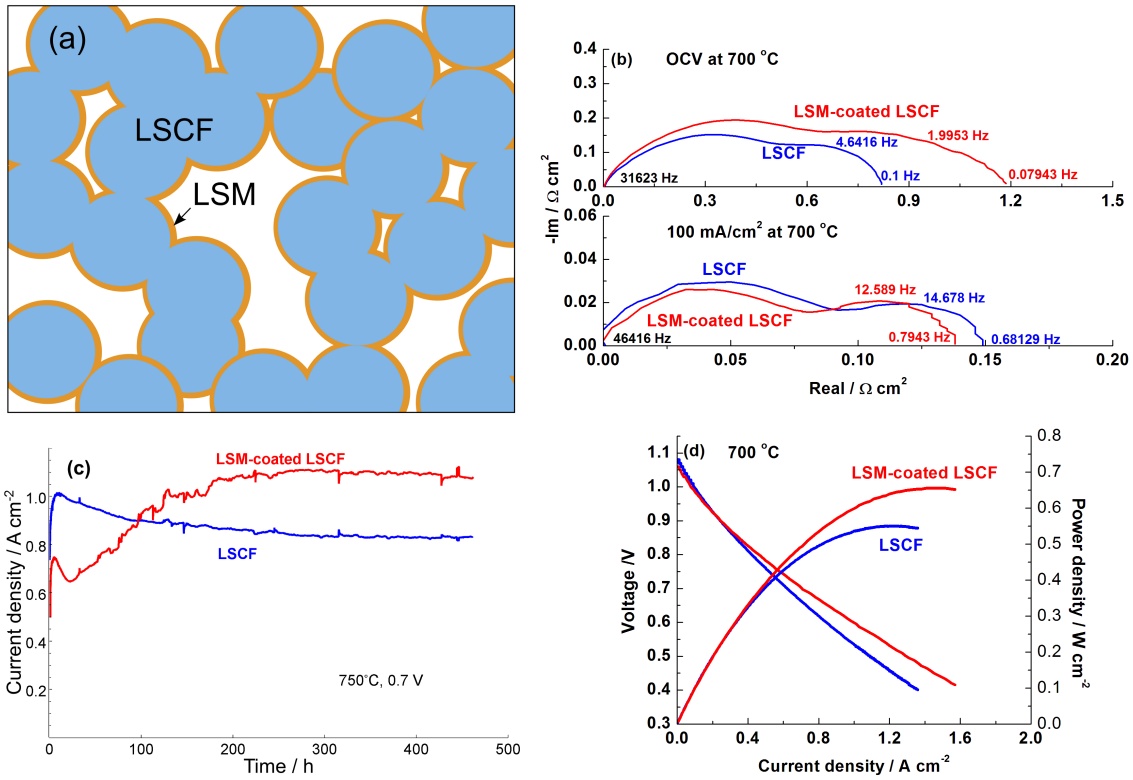

Figure 21: a) Schematic diagram of the LSM-infiltrated LSCF cathode. b) Impedance spectra of fuel cells with and without infiltration of LSM measured at OCV and at 100 mA cm^{-2}, without Ohmic portion. c) Current density of two test cells with and without infiltration as a function of time under a constant voltage at 0.7V and approximate cathodic overpotential of -0.12 V. d) Cell voltages and power densities as a function of current density for full cells with and without infiltration of LSM after long term testing. Plots b-d of experimental results are courtesy of Mingfei Liu and Lei Yang, who performed the measurements.

electrode data, Figure 20b). However, the cell displayed a time-dependent activation that led to a considerable increase in performance in the first 200 hours of operation. This increase contrasts with the rapid decrease in performance of the blank LSCF cell in the same time period. Figure 21d shows the cell voltages and power densities of the two cells, with the bias-dependent activation of the infiltrated cell leading higher cell voltage and power density with large current density.

Transmission electron microscopy was performed by Wentao Qin to examine the near-interface region in the LSM layer and underlying LSCF. Figure 22a shows an

coated LSCF particle from an operated cathode. It can be seen from the view of the particle that it is coated with a uniform, continuous, and dense surface film whose projected thickness varies between 2 and 23 nm, largely validating the schematic design in Figure 21a. The continuity of the coating is attributed to the close structural similarity of LSM and LSCF, which causes a coherent coating to form more easily than in the case of other infiltrated materials that tend to form isolated particles.

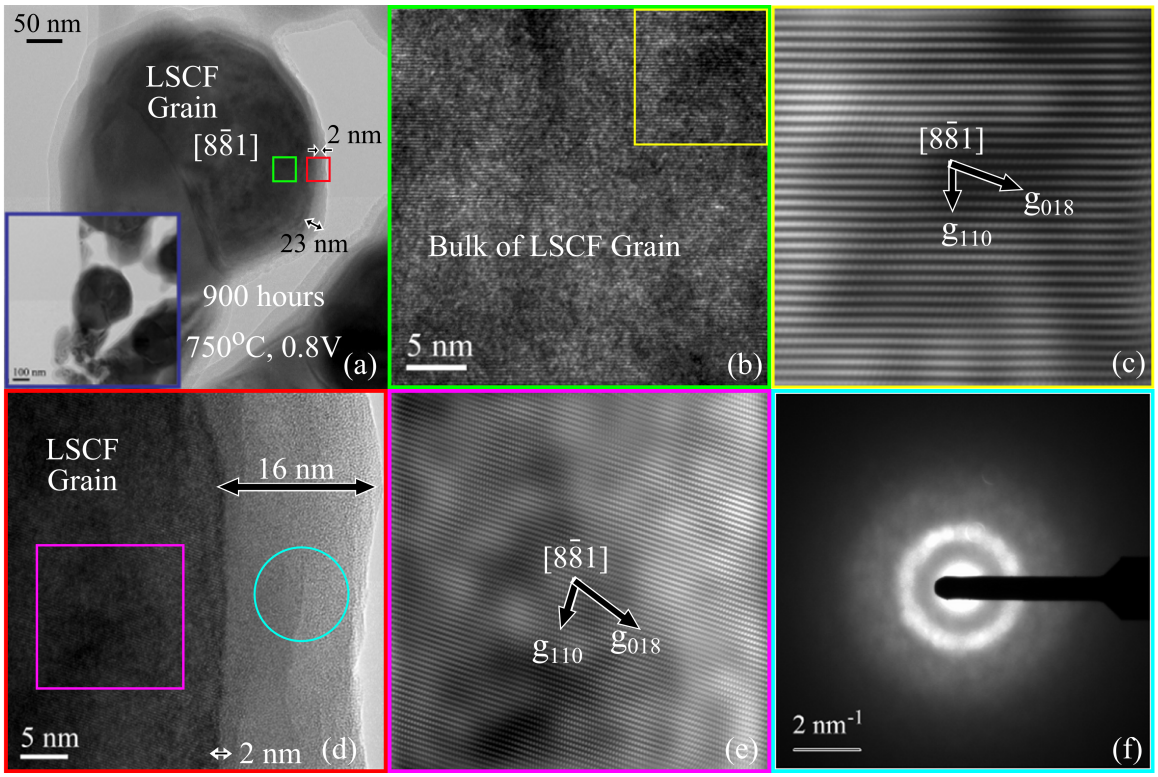

Figure 22: TEM micrographs of an LSCF particle from an infiltrated porous electrode after long-term operation (750°C, 0.8 V, 900 h). a) The whole particle, covered with an amorphous coating. b) zone-axis lattice image of the bulk of the particle in the green rectangle area in (a). c) Fourier-filtered image of the area within the yellow rectangle in (b). d) High-resolution view of the outer portion of LSCF grain and surface layer, highlighted in the red rectangle in (a), and e) Fourier-filtered image of the area within the purple rectangle in (d). Coherent zone-axis images in (c) and (e) indicate the LSCF grain retained perovskite structure after operation. f) CBED of the surface layer, indicating a loss of crystallinity. This figure was created by Wentao Qin, who performed the microscopy.

A close view of the near-surface region in Figure 22d shows the surface in clear

contrast with the LSCF particle. After operation, the LSCF particle retains its perovskite structure, demonstrated by the zone-axis lattice fringes both deep in the bulk and near the surface of the LSCF grain, shown in Figure 22b-e, while the outer portion of the infiltrated layer loses crystallinity, as demonstrated by the convergent beam electron diffraction (CBED) pattern in Figure 22f.

4.3 Proposed electrochemical and structural mechanisms affecting the surface layer

Based upon the model electrode and full-cell data, it appeared that there are two possible means of enhancement active in the LSM-coated LSCF cathode. The first is a purely electrochemical mechanism due to enhanced electrocatalytic activity of the LSM surface under cathodic polarization. The second is a time-dependent activation originating from changes in structure, composition, and morphology of the LSM thin-film coating and the LSM/LSCF interface due to inter-diffusion over a longer period of time (a few hundreds of hours) during operation. The structural evolutions gradually result in superior performance and durability of the LSM-coated LSCF cathodes, even at overpotentials insufficient to cause superior performance through electrochemical activation.

Four possible mechanisms were examined in detail. First, LSM may somehow favorably alter the surface, preventing degradation of performance with time. Second, the bulk pathway of the surface layer may be activated to a larger extent under a given cathodic polarization than is characteristic of bulk LSCF. Third, the presence of the Mn cation on the surface may promote adsorption/dissociation of oxygen relative to LSCF. Finally, structural defects in the film and space-charge effects may provide a fast ionic transport pathway in the surface layer relative to bulk LSM.

4.3.1 Surface stabilization and prevention of LSCF degradation

Advanced electron microscopy and spectroscopy were used to examine the morphology, composition, and structure of the LSM and LSCF surfaces as well as the LSM/LSCF interface before and after long-term annealing. Figure 23a shows the cross-sectional view (TEM image) of a sol-gel deposited surface layer in the as-deposited state on a dense LSCF pellet, while Figure 23b shows the cross-sectional view of a similar surface layer after annealing at 850°C for 900 hours (under zero-current conditions). Figure A-1 gives additional TEM images of the interface prior to annealing. Figure A-2 gives additional TEM images after long-term annealing of a pellet. TEM images of the infiltrated porous cathode after operation have been presented in Figure A-1. These images indicate that the sol-gel deposited layer is crystalline and is epitaxial with the underlying LSCF immediately after deposition and that that the portion of the surface film closest to the LSCF interface remains crystalline and epitaxial while the rest of the film loses long-range order and becomes amorphous after the long-term anneal.

Figure 23c and d show EDS composition profiles of the surface layer and outermost portion of the underlying LSCF in the as-deposited state (c) and in the long-term annealed state (d). The surface layer retains Mn during long-term annealing but also experiences an addition of Co. There were no signs of strontium enrichment or surface phase segregation.

Based upon the composition profiles, it was suspected that during the course of high-temperature annealing and/or operation, Co diffuses from the underlying LSCF into the surface layer while Mn is mostly retained in the surface layer. Concurrently, the outer approximately 80% of the surface layer loses long-range order associated with crystallinity. The surface layer, then, is not truly LSM but rather becomes a hybrid with properties residing between those of LSM and LSCF due to the presence of all three transition metal ions in the surface layer. This hybrid surface layer was

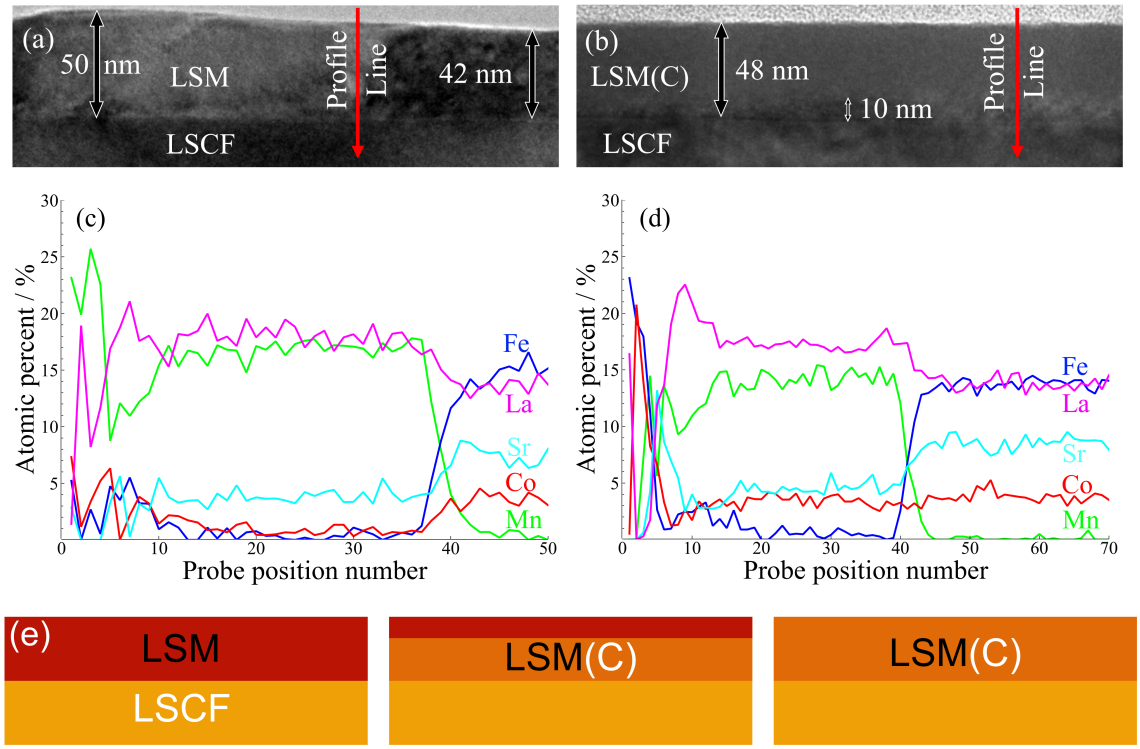

Figure 23: Cross-sectional TEM micrograph of a sol-gel LSM-modified LSCF surface a) in the as-deposited condition and b) after long-term annealing at 850°C for 900 hours. EDS compositional profiles across the sol-gel surface layer and outermost part of LSCF layer c) in the as-deposited condition and d) after long-term annealing. e) Schematic illustration of role of in-diffusion to the LSM surface layer starting from the as-deposited LSM condition (left) and transforming into LSM(C) with high temperature annealing and/or operation. Subfigures a-d were created by Wentao Qin, who performed the microscopy/spectroscopy.

denoted as LSM(C) owing to the majority concentration of Mn, while acknowledging the appreciable concentration of Co. A schematic diagram of the transformation from LSM to LSM(C) is shown in Figure 23e.

4.3.2 Coating cathodic activation

There is evidence in the literature of an appreciable bulk pathway in thin LSM [16,82, 84,144] activated especially under a large cathodic bias [16,144], an effect attributed to a large addition of oxygen vacancies to the LSM under cathodic polarization. With the requirement that the LSM film be thin in order to mitigate bulk oxygen transport

limitations, it is possible for the LSM coating to be strongly activated under cathodic bias due to large relative oxygen vacancy concentration increase.

Very simple surface kinetics were examined to understand the cathodic activation phenomenon. Suppose that the current is proportional to the concentration of oxygen vacancies near the surface

$$\mathrm{i} \propto \left(\frac{\mathrm{c_v}}{\mathrm{c_v^0}} - 1 \right) \tag{70}$$

This expression has a forward and backward term, with only the forward term being significantly affected by a change in the oxygen vacancy concentration. This treatment roughly represents the case where the rate-determining step is oxygen incorporation into the lattice or oxygen adsorption requiring mediation by an oxygen vacancy [124, 158]. Treating the kinetics this way neglects the influence of other important species in the reaction; nevertheless it makes plain the role of oxygen vacancies in bulk activation and is useful for the present discussion. Such dependence allows rough comparison for the case where the limiting step for all overpotentials (not just near OCV) is dependent upon oxygen vacancy concentration.

The surface interfacial resistance, $\mathrm{R_i}$, can be computed from the change of current, i, and overpotential, η, at steady state

$$\mathrm{R_i} = \frac{\partial \eta}{\partial \mathrm{i}} = -\frac{1}{4\mathrm{F}} \frac{\partial \eta}{\partial \mathrm{r}} \tag{71}$$

by calculating the rate of molecular oxygen reduction, r, at given values of η. $\mathrm{R_i}$ does not include the effects of ionic or electronic transport.

Consider the defect chemistry of bulk LSM versus LSCF [13, 104, 131] (see the Brouwer diagrams in Figure A-3). The use of the bulk defect chemistries serves as an instructive guide to the point defect trends that may occur in the surface phase. Oxygen vacancy concentration is quite high in LSCF, whereas it is very low in LSM.

The overpotential was related to the steady state point defect concentrations (e.g.

oxygen vacancy concentration, c_v) via the effective internal oxygen partial pressure, $pO_2^{internal}$, associated with the overpotential. Bulk oxygen vacancy concentrations for a given η were determined by converting η to $pO_2^{internal}$ via Equation A-1 (the Nernst relationship) and then used in the rate equation. A full discussion of this modeling approach is included in appendix A.2. Simulated R_i of LSM and LSCF were computed and are plotted in Figure 24a. Each resistance is normalized to its value at OCV to provide a relative comparison of the trends. R_i of LSCF initially decreases with cathodic polarization but increases again because the rate of vacancy increase slows at more severe cathodic polarizations. R_i of LSM decreases monotonically as the overpotential becomes more negative because the rate of increase of oxygen vacancies does not slow. Therefore, a surface layer that is strongly activated under cathodic polarization has the potential to be very active toward oxygen reduction under cathodic bias and could provide the superior performance observed experimentally in the case of LSM modification. A hybrid LSM(C) film that forms over the long term might be expected to have properties intermediate between LSM and LSCF owing to mixed effects of the transition metal cations. Such a film could be more activated under cathodic bias than pure LSCF. To study cathodic activation as a function of degree of oxygen binding, the defect chemistry for LSCF [13] was computed with different values of the standard free energy of oxygen reduction, ΔG^0_{red}. Changing the energy in this manner has two effects: lowering the equilibrium oxygen vacancy concentration and altering the trend of oxygen vacancies with pO_2, causing the material to display a larger degree of activation with bias and as a consequence become more like LSM. Oxygen vacancy concentrations associated with this changing parameter are plotted in Figure A-5. The interfacial resistances normalized to their OCV values are shown in Figure 24b, again assuming current proportional to oxygen vacancy concentration (Equation 70). As oxygen binding becomes stronger (ΔG^0_{red} multiplied by a factor greater than one), R_i decreases more quickly as bias is applied. At large bias, the

resistance is lower than that of LSCF and does not increase again until much more severe cathodic overpotentials. This trend demonstrates that tighter oxygen binding can result in somewhat superior performance at large cathodic bias. A detailed discussion of this approach is included in appendix A.2.

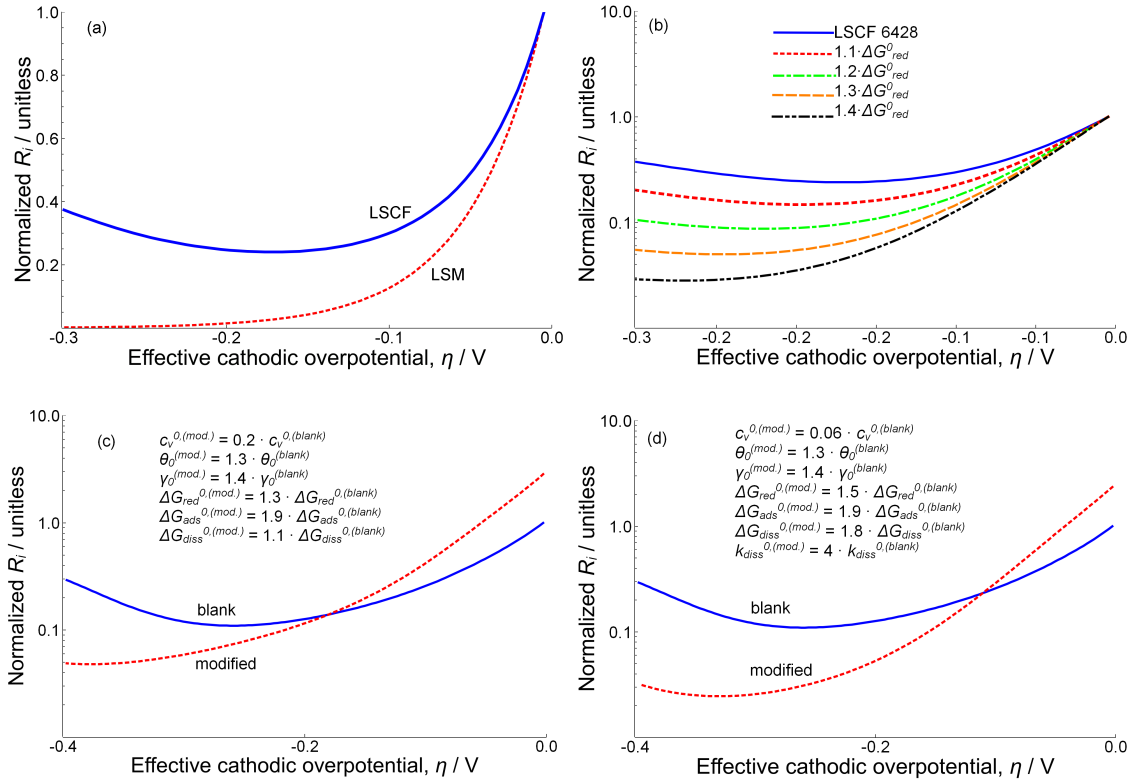

Figure 24: a) Normalized interfacial resistance of LSCF and LSM films assuming that the current at the effective overpotential is described by Equation 70. Normalized to their respective values at OCV. b) Normalized interfacial resistance associated with tighter oxygen binding associated with lower free energy of oxygen reduction assuming current proportional to oxygen vacancy concentration. c) Simulated normalized interfacial resistance versus effective cathodic overpotential for blank LSCF and LSCF with modified surface properties when $\Delta G_{red}^{0(surface)} < \Delta G_{red}^{0(LSCF)}$, $\Delta G_{diss}^{0(surface)} < \Delta G_{diss}^{0(LSCF)}$, and $\Delta G_{ads}^{0(surface)} < \Delta G_{ads}^{0(LSCF)}$. R_i is normalized to the value of the blank LSCF at OCV. d) Simulated normalized interfacial resistance versus effective cathodic overpotential for blank and LSCF with modified surface properties when $\Delta G_{red}^{0(surface)} < \Delta G_{red}^{0(LSCF)}$, $\Delta G_{diss}^{0(surface)} < \Delta G_{diss}^{0(LSCF)}$, and $\Delta G_{ads}^{0(surface)} < \Delta G_{ads}^{0(LSCF)}$, $k_{diss}^{0(surface)} > k_{diss}^{0(LSCF)}$.

4.3.3 Promoted adsorption/dissociation

More favorable adsorption and other surface steps such as oxygen dissociation lead to a large supply of oxygen available for incorporation and also lead to fast replenishment upon incorporation. Recently, DFT calculations [24] showed that adsorption energy is lower (more favorable) on LSM than on LSF and LSC due to the presence of the Mn cation, as opposed to the Co or Fe cations. Despite more strongly adsorbing oxygen, bulk LSM has a much smaller surface oxygen exchange coefficient than LSCF [11, 34, 35] most likely due to incorporation limitation associated with low oxygen vacancy concentration.

To give insight into the promoted adsorption/dissociation hypothesis, the process was modeled by classical, phenomenological chemical kinetics [96, 101] and related the rate to the total interfacial resistance under cathodic steady state operation. Very little is known about the specific mechanisms of oxygen reduction on either LSM or LSCF surfaces. However, vacancy mediated adsorption/dissociation has been suggested for LSF [124, 158] and LSM [23], so a variant was chosen for the present analysis. For the sake of illustration, it was assumed that the oxygen reduction process is characterized by the following reaction set

$$O_2(g) + * \rightleftharpoons O_2^{2-}(s) + 2h^{\cdot} \tag{72}$$

$$O_2^{2-}(s) + V_O^{\cdot\cdot} \rightarrow O_O^x + O^-(s) + h^{\cdot} \tag{73}$$

$$O^-(s) + V_O^{\cdot\cdot} \rightleftharpoons O_O^x + * + h^{\cdot} \tag{74}$$

where $*$ represents a vacant surface site, $h^{\cdot}$ is an electron hole, $V_O^{\cdot\cdot}$ represents an oxygen vacancy and O_O^x represents a filled oxygen lattice site, both in Kröger-Vink notation. The three reactions represent the overall steps of adsorption, dissociation, and incorporation. This scheme [23] is in the general spirit of vacancy-mediated adsorption/dissociation [124, 158]. Moreover, the $O_2^{2-}(s)$ state has been suggested as a stable surface species [23, 91].

The reaction rates of these steps were written as follows:

$$r_{ads} = k_{ads,f} pO_2 (1-\gamma-\theta) \exp\left(-\frac{\alpha_a F}{RT}\chi_{ms}\right) - k_{ads,b}\gamma c_h^2 \exp\left(\frac{(2-\alpha_a)F}{RT}\chi_{ms}\right) \quad (75)$$

$$r_{diss} = k_{diss,f}\gamma c_v \exp\left(\frac{\alpha_d F}{RT}\chi_{ms}\right) - k_{diss,b}\theta c_O c_h \exp\left(-\frac{(1-\alpha_d)F}{RT}\chi_{ms}\right) \quad (76)$$

$$r_{inc} = k_{inc,f}\theta c_v \exp\left(\frac{\alpha_i F}{RT}\chi_{ms}\right) - k_{inc,b}(1-\gamma-\theta) c_O c_h \exp\left(-\frac{(1-\alpha_i)F}{RT}\chi_{ms}\right) \quad (77)$$

where γ is the fractional surface concentration $[O_2^{2-}(s)]$, θ is the counterpart $[O^-(s)]$, c_v is the oxygen vacancy concentration $[V_O^{\cdot\cdot}]$, c_O is the concentration of filled oxygen sites $[O_O^x]$ equal to $c_{Osite} - c_v$, c_h is the concentration of electron holes, and α_a, α_d, and α_i are transfer coefficients. The quantity χ_{ms} is the surface potential difference induced by dipoles associated with the charged adsorbates, equal to $\phi_m - \phi_s$ where ϕ_m is the potential inside the MIEC and ϕ_s is the potential on the surface. Appendix A.3 outlines the derivation of these reaction rates.

The improvement of the LSM coating on blank LSCF was modeled by altering the surface parameters associated with blank LSCF. The overall energetics of the reactions were shifted from the values associated with uncoated LSCF in the direction indicated by theoretical studies for an LSM surface. That is, fewer oxygen vacancies and more favorable adsorption/dissociation compared to the blank LSCF. The point defect chemistry of modified LSCF (LSCF with more negative ΔG_{red}^0) developed in the previous section was used for this purpose. Appendix A.3 provides detail on this approach.

The result is shown in Figure 24c and d. In Figure 24c, R_i is slightly larger for the LSM-coated sample at OCV, but drops faster with increasing negative overpotential eventually decreasing below R_i of the uncoated LSCF 6428. The behavior simulated by the present model is qualitatively similar to that observed experimentally.

If the analysis is taken one step further and an additional catalytic effect is ascribed to the presence of Mn ions, then the barrier to reaction would be expected to shrink as well. The result appears in Figure 24d where k^0_{diss} has been increased (note that dissociation was assumed to be rate limiting on the blank LSCF surface - see appendix A.3). As a result, the oxygen vacancy concentration of the modified layer is nearly ten times smaller than for blank LSCF but the OCV resistance is only slightly larger. R_i drops and soon becomes more favorable as cathodic overpotential becomes more negative in this case due to both *more favorable* and *faster* adsorption/dissociation. Appendix A.3 provides detail on this approach as well.

4.3.4 Mediation by geometry and structural defects

The thickness of the surface layer is likely crucial to its role as a catalyst layer. If too thick, oxygen transport limitations could negate its favorable surface properties. The literature contains evidence for the thickness dependence of the LSM bulk pathway [42, 82, 114]. The surface films formed in this work were dense, and on the order of 2-23 nm (Figure 22).

Dislocations, grain boundaries, and other structural defects in the surface layer may also be important. Oxygen tracer diffusivity along the grain boundary at temperatures near 700°C has been shown to be approximately three orders of magnitude larger than tracer diffusivities in the bulk LSM crystal [36]. This effect arises because the activation energy for diffusion along the grain boundaries is lower than in the bulk, oxygen vacancies segregate to grain boundaries, or both. DFT calculations have shown oxygen vacancies to have lower formation energy on the surface than in bulk [91], with possible applicability to internal boundaries and structural defects.

A space-charge layer in the LSM may also cause the oxygen vacancy concentration to depart substantially from its bulk value. When LSM is deposited onto the LSCF surface, it forms a diffusion couple with vacancies crossing the LSM-LSCF phase

boundary. Since the LSM film is so thin, enrichment of oxygen vacancies may persist to the surface where oxygen reduction is accelerated by the larger-than-bulk oxygen vacancy concentration.

4.4 Conclusion

A thin coating of LSM on LSCF enhances both durability and performance under a bias. In collaboration with experimentalists, the concept of thin-film test cells was used to remove the complicated effects of geometry and focus on the fundamental surface properties of the uncoated and coated cathode material surface. Also in collaboration with experimentalists, TEM was used to investigate the interface structure and local chemical composition. Phenomenological modeling informed by TEM observations and point defect chemistry models was used to explain the observed experimental results in the thin film test cells as well as in porous electrodes.

Possible theoretical explanations developed in this chapter attribute this increase in performance to the formation of a hybrid LSM(C) phase on the surface, superior adsorption of oxygen associated with a Mn cation, large relative increase of oxygen vacancies in the surface phase compared to that of LSCF under cathodic polarization, and structural defects in the surface film with beneficial results on oxygen reduction. A more detailed theoretical explanation, including further micro-kinetic modeling and detailed study of the surface phase defect chemistry, should be developed to fully explain the behavior of blank and LSM-coated LSCF at short times as well as after operation.

CHAPTER V

MODELING OF MIXED-CONDUCTING CATHODES USING CONSERVATIVE POINT DEFECT ENSEMBLES

5.1 Introduction

As emphasized in this thesis, in order to understand the performance of the cathode and optimize its design, modeling techniques have been employed. Many models deal with composite electrodes - mixtures of a cathode material such as LSM and an electrolyte material such as YSZ [19, 37, 38]. These models usually assume that only the TPBs are active, that the cathode material acts as an ideal electronic conductor, and that the electrolyte material acts as an ideal ionic conductor. Cathodic bias is introduced by way of the Butler-Volmer equation.

Many candidate SOFC cathode materials, such as $La_{1-x}Sr_x\ Co_{1-y}Fe_yO_{3-\delta}$ (LSCF), are good mixed ionic-electronic conductors (MIECs), a characteristic that serves to extend the active zone for oxygen reduction from the triple phase boundaries (between the gas phase, cathode material phase, and electrolyte phase), to the two-phase boundaries (the MIEC surface, between the MIEC and air). An operating MIEC cathode therefore involves many different charge and mass transfer processes, including those on the surfaces, across the cathode-electrolyte interfaces, and point defect interactions within the MIEC cathode.

The effect of cathodic bias on such materials adds complexity to the system. It effectively reduces the material, removing O^{2-} ions and decreasing the oxidation state of the constituent transition metal ions. These changes to the point defect chemistry induce the gas-phase oxygen reduction at the MIEC-air interface, therefore providing one of the two fuel cell half-reactions. The trends with cathodic bias are not trivial.

The complications that accompany electrochemical bias in MIECs may be roughly divided into two groups. The first is related to transport considerations. Consider the following example of an MIEC with ionic conductivity arising from oxygen vacancies. As the vacancies are injected at the MIEC-electrolyte interface, they diffuse across the cathode where they are consumed by the oxygen reduction reaction via incorporation of atomic oxygen at the pores. Electrons and electron holes are coupled to the vacancies by the requirement of bulk electroneutrality and internal point defect equilibrium. Therefore, the problem is more complicated than simple diffusion of oxygen vacancies - ambipolar diffusion must be taken into account [20]. A net current adds further complications by creating a gradient in the Fermi level.

One of the principal models of mixed-conducting cathodes is the ALS model [5]. It successfully predicts the impedance of porous MIEC cathodes co-limited by bulk mass transport and surface oxygen exchange. The model handles small perturbations from OCV, assumes a uniform Fermi level, and captures coupling between point defects. Two other models of mixed conducting cathodes which do incorporate bias are those of Svensson [152, 153] and Coffey [28]. These latter models also assume a uniform Fermi level, constant concentration of electronic defects, but do not consider coupling between point defects. All of these models are for single-phase materials.

The second set of complications is associated with oxygen reduction at the air-MIEC surface, where the kinetics of oxygen reduction tend to be nonlinear. Many authors approximate the kinetics with a linear expression around equilibrium, but such models cannot in general be extended far from open-circuit voltage (OCV). Many attempts have been made to understand the nature of oxygen reduction on the surfaces of MIECs involving small perturbations from equilibrium. Such studies include oxygen tracer exchange experiments [79] and electrical conductivity relaxation [158]. Models used to interpret the experimental data generally use equilibrium point defect concentrations in phenomenological models at different temperatures and

oxygen partial pressures.

A model that describes the electrochemical response under large polarization through phenomenological rate expressions must take into account the internal point defect interactions coupled with changes to the electrical state as a function of position and coupled with surface reaction rates. In the past, this problem has been handled by decoupling the concentration of oxygen vacancies from the other point defects by assuming some analytical relationship with cathodic overpotential [49] or by enforcing electroneutrality conditions between only two point defects [103]. Such approaches are accurate if only two point defects are present or if only one species of point defects (e.g. oxygen vacancies) changes by a large relative amount upon a change to oxygen partial pressure or cathodic polarization, as in the case of $La_{1-x}Sr_xMnO_{3\pm\delta}$ (LSM) [104, 131]. Typically the relationship requires that the oxygen vacancy concentration changes as a function of $pO_2^{-1/2}$ and that the concentration be small. The approach needs to be augmented when the concentration of several point defects change under such large perturbations or if the $pO_2^{-1/2}$ trend is not followed over the entire range of interest. For example, the oxygen vacancy concentration and electron/electron hole concentration changes which occur in $La_{1-x}Sr_xFeO_{3-\delta}$ (LSF) [119] and $La_{0.6}Sr_{0.4}Co_{0.2}Fe_{0.8}O_{3-\delta}$ (LSCF 6428) [13].

Other factors also influence the complexity of mixed conductors under a bias. Recent developments in intermediate temperature SOFCs (IT-SOFCs) including infiltration of several mixed-conducting phases [62,95] and the efforts to use doped ceria as a mixed conductor [26,27,176] suggest the need for a method that can handle large bias including point defect coupling and reaction kinetics, phase junctions, and the possibility (but not requirement) for nonuniform Fermi levels.

The purpose of this chapter is to propose a framework for numerical simulation of MIECs with generalized defect chemistry and phenomenological surface rate expressions, under a large electrochemical bias. The goal is to model charge and mass flow

within a general MIEC material under cathodic bias in an operating fuel cell. This requires preserving the thermodynamic link between all point defects, electroneutrality, interfacial reaction rates, and internal electronic/ionic transport. The proposed method should be generally applicable to MIECs of arbitrary geometry of any number of dimensions, unhindered by point defect complexity, and crafted with the case of large biases and with the possibility of nonideal MIEC/electrolyte exchange in mind.

Needed for this framework are 1) a convenient way to couple all ionic and electronic point defects and 2) a method to relate the bulk transport to surface reaction rate laws. The problem is approached by simplifying the number of equations as much as possible using the concept of conservative defect ensembles [98]. The resulting electrochemical ensemble potentials are "unpacked" into explicit point defect concentrations. The point defects are used to determine surface reaction rates, which serve as boundary conditions for the ensembles. The concept is a general one, but the following discussion is limited to the case of an ABO_3 perovskite with point defects consisting of electrons, electron holes, and oxygen vacancies, e.g. LSF or LSCF 6428 [13, 119]. The proposed approach can be generalized, however, to include any number of point defects including those bearing protons or oxygen lattice interstitials with appropriate modification of the ensembles. The approach applies to potentiostatic conditions, a common electrochemical testing requirement.

5.2 Theory

A common assumption is local equilibrium of point defects within a solid, first proposed in the Wagner treatment of mixed conduction [88, 98] . At any location, the point defects fulfill chemical equilibrium provided that that the equilibration is fast compared to transport. A large degree of complexity in the point defect chemistry therefore creates a complicated set of transport equations when several defects are

considered individually. A homogeneous generation/recombination rate must be included when there is the possibility of internal defect reactions. To simplify matters, conservative defect ensembles were introduced [98] to group together like defects. Ensembles enable a single continuity equation to be written for each ensemble without the generation/recombination term. The following discussion uses the theory of conservative point defect ensembles in a novel way to couple with surface reaction rates and represent important cathode transport processes. It simplifies the transport equations, makes it easier to solve them numerically, while enabling rigorous agreement with thermodynamics.

5.2.1 Transport

The reader is referred to the original concept of ensembles [98] and a review of ensembles [88] for a general discussion. Appendix B.1 provides details of the formulation and implications of the ensembles for this particular case. The principal results of the ensemble formulation are summarized in Figure 25 and described as follows.

Within the ensemble framework, oxygen vacancies belong in the oxygen ensemble, O^*, while the electronic defects belong to the electron ensemble, e^*. The electrochemical potential of the O^* ensemble is related to that of oxygen vacancies by

$$\tilde{\mu}_{O^*} = -\tilde{\mu}_{v} \tag{78}$$

The electrochemical potential of the e^* ensemble is related to that of electrons and electron holes by

$$\tilde{\mu}_{e^*} = \tilde{\mu}_{e} = -\tilde{\mu}_{h} \tag{79}$$

Internal equilibrium between electrons and electron holes is enforced everywhere as a result of this definition.

According to irreversible thermodynamics, the fluxes of each ensemble are related to the gradient in electrochemical potential, $\tilde{\mu}$, of each ensemble. For this particular

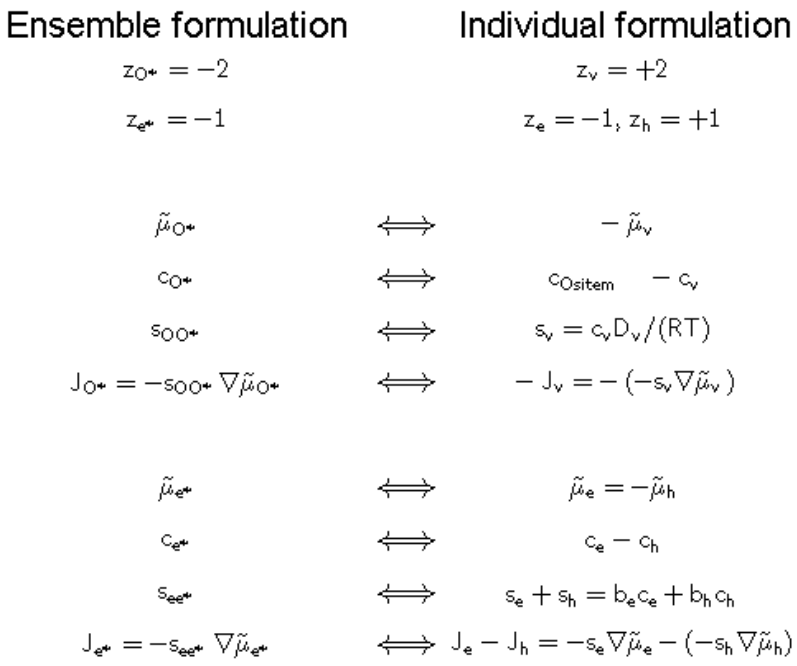

Figure 25: Definitions and connections between conservative defect ensemble quantities and individual point defect quantities used in this contribution.

case and ignoring cross-coefficients,

$$\overrightarrow{J}_{O^*} = -s_{oo^*} \nabla(\Delta(\tilde{\mu}_{O^*})) \tag{80}$$

$$\overrightarrow{J}_{e^*} = -s_{ee^*} \nabla(\Delta(\tilde{\mu}_{e^*})) \tag{81}$$

where Δ represents a change from the equilibrium value. The transport equations are in terms of changes from equilibrium because the equilibrium electrochemical potentials do not lead to any flux. The quantities s_{oo^*} and s_{ee^*} are the Onsager transport coefficients from irreversible thermodynamics, related to electrical conductivity. For the O^* ensemble,

$$s_{oo^*} = s_v = b_v c_v \tag{82}$$

where c_v is the concentration of oxygen vacancies and b_v is mobility of oxygen vacancies. Assuming that electrons and holes have approximately the same mobility, b_{e^*},

for the e^* ensemble

$$s_{ee^*} = s_e + s_h = b_{e^*} c_e + b_{e^*} c_h \tag{83}$$

where concentrations are given by c_e, c_h. In general, s_{oo^*} and s_{ee^*} are non-constant coefficients leading to a nonlinear problem requiring an iterative solution.

Assuming no internal reactions between ensembles, the general continuity equations in the interior of an MIEC would then be

$$\frac{\partial c_{O^*}}{\partial t} = -\nabla \cdot \overrightarrow{J}_{O^*} \tag{84}$$

and

$$\frac{\partial c_{e^*}}{\partial t} = -\nabla \cdot \overrightarrow{J}_{e^*} \tag{85}$$

where c_{O^*} and c_{e^*} are the concentrations of the respective ensembles. At steady state, no change in ensemble concentration occurs and so the continuity equations are

$$0 = -\nabla \cdot \overrightarrow{J}_{O^*} \tag{86}$$

and

$$0 = -\nabla \cdot \overrightarrow{J}_{e^*} \tag{87}$$

Equations 86 and 87 with 80 and 81 must be solved in the bulk of the MIEC for $\Delta\tilde{\mu}_{O^*}$ and $\Delta\tilde{\mu}_{e^*}$ at steady state.

At the current collector, the electrochemical potential of the e^* ensemble should be fixed by equilibrium with the electrons in the current collector

$$\Delta\tilde{\mu}_{e^*} = \Delta\tilde{\mu}_e^{(CC)} = z_e F \Delta E \tag{88}$$

if current collection is ideal, where F is Faraday's constant. ΔE is the change of electrode potential with respect to the counter electrode upon cathodic bias.

At the MIEC-air boundary, the flux of e^* will be set by the rate of electrons consumed and holes injected during the course of the oxygen reduction reactions

(adsorption, dissociation, incorporation)

$$\overrightarrow{J}_{e^*} \cdot \overrightarrow{n} = \sum_{k} r_k \tag{89}$$

where the sum is over all rates of surface reactions r_k that consume an electron or inject a hole into the MIEC. Both rates come from phenomenological rate expressions [101].

Likewise, the flux of O^* is inward

$$\overrightarrow{J}_{O^*} \cdot \overrightarrow{n} = -\sum_{j} r_j \tag{90}$$

where the sum is over all rates of air-MIEC surface reaction r_j that consume an oxygen vacancy, such as incorporation of an adsorbed oxygen into the MIEC lattice.

The MIEC/electrolyte boundary is zero-flux with respect to electronic species and the outward flux of O^* is equal to the inward flux of oxygen vacancies r_v (see section 5.2.2.2)

$$\overrightarrow{J}_{O^*} \cdot \overrightarrow{n} = r_v \tag{91}$$

5.2.2 Local defect concentrations and reaction rates

5.2.2.1 Unpacking the ensembles

The ensemble formulation provides only electrochemical potentials, but there are several reasons why point defect concentrations need to be known as well. One reason is that point defect concentrations are required in order to apply phenomenological rate expressions [101]. Another reason is that the transport coefficients s_{OO^*} and s_{ee^*} are directly proportional to defect concentration in the bulk. The concentrations of the individual point defects therefore need to be "unpacked" from their ensembles. That is, they should be extracted from the electrochemical potentials using a specific point defect model. The point defect model considered here is discussed in detail in appendix B.2, Equations B-43 through B-45 for the case of LSF/LSCF 6428, but the discussion is in general very flexible and adaptable to any point defect model. The following method is proposed to unpack the ensembles into constituent point defect

concentrations. To the author's knowledge, unpacking point defect concentrations in this manner is a novel development.

The quantities $\tilde{\mu}_{\mathrm{O}^*}$ and $\tilde{\mu}_{\mathrm{e}^*}$ should be known from the bulk transport solution. When made into a linear combination with the proper coefficient choice, the sum is the same as that of $\tilde{\mu}_{\mathrm{v}}$ and $\tilde{\mu}_{\mathrm{e}}$ (the change in chemical potential of oxygen vacancies and electrons respectively) with the same coefficients (see appendix B.3 for a proof)

$$2\Delta\tilde{\mu}_{\mathrm{O}^*} - 4\Delta\tilde{\mu}_{\mathrm{e}^*} = -2\Delta\tilde{\mu}_{\mathrm{v}} - 4\Delta\tilde{\mu}_{\mathrm{e}} = -2\Delta\mu_{\mathrm{v}} - 4\Delta\mu_{\mathrm{e}} \tag{92}$$

This quantity corresponds to $\Delta\mu_{\mathrm{O}_2}^{\mathrm{solid}}$

$$\Delta\mu_{\mathrm{O}_2}^{\mathrm{solid}} = -2\Delta\mu_{\mathrm{v}} - 4\Delta\mu_{\mathrm{e}} \tag{93}$$

where $\Delta\mu_{\mathrm{O}_2}^{\mathrm{solid}}$ is the change in virtual oxygen chemical potential in the MIEC. A convenient related quantity is the concept of the local effective, internal partial pressure of oxygen, $\mathrm{pO}_2^{\mathrm{solid}}$.

$$\mu_{\mathrm{O}_2}^{\mathrm{solid},0} = \mu_{\mathrm{O}_2}^{0} + \mathrm{RTln}\left(\mathrm{pO}_2^{\mathrm{solid}}\right) \tag{94}$$

where R is the universal gas constant, T is the temperature and $\mu_{\mathrm{O}_2}^{0}$ is from the gas phase.

Though only a virtual, thermodynamic quantity, $\mathrm{pO}_2^{\mathrm{solid}}$ can be linked to the local point defect equilibrium and is a convenient substitute description for the local chemical state of the MIEC. Appendix B.3 provides a rigorous development and justification for its use. It is expressed

$$\mathrm{pO}_2^{\mathrm{solid}} = \mathrm{pO}_2^{0}\exp\left(\frac{\Delta\mu_{\mathrm{O}_2}^{\mathrm{solid}}}{\mathrm{RT}}\right) \tag{95}$$

where pO_2^{0} is the partial pressure of oxygen in the adjacent gas phase. The MIEC with $\mathrm{pO}_2^{\mathrm{solid}}$ would have the same set of point defects as if it were in an unpolarized state exposed to a gaseous atmosphere with $\mathrm{pO}_2 = \mathrm{pO}_2^{\mathrm{solid}}$. Once computed, $\mathrm{pO}_2^{\mathrm{solid}}$ determines the point defect concentrations and therefore provides a convenient link

between bulk defect ensemble transport and the local defect equilibrium. Fundamentally, this is done through a set of nonlinear defect equations, solved as a function of local pO_2^{solid}.

From a practical standpoint, though, a set of nonlinear equations need not be solved repeatedly at every point. Instead, the equations can be solved over many pO_2 values with the resulting point defect concentrations stored in a list. Local values of concentration can be numerically interpolated with the list using the spatially varying pO_2^{solid} from Equation 95. Numerical interpolation saves substantial time during solution of the problem. More details about the implementation of the interpolation method are given in section 5.2.3.

The value of $\Delta\mu_{e^*}$ should be computed from the specific point defect model. Appendix B.2 details how the quantity is derived for the specific case of localized carriers in LSF/LSCF 6428 considered here. The result is

$$\Delta\mu_e = RTln\left(\frac{c_e}{c_{Bsite} - c_h - c_e}\frac{c_{Bsite} - c_h^0 - c_e^0}{c_e^0}\right) \tag{96}$$

where the 0 superscript indicates the value prior to application of cathodic polarization. The local value of c_e, of course, depends upon $\tilde{\mu}_{O^*}$ and $\tilde{\mu}_{e^*}$ and therefore $\Delta\mu_e$ would change with time as a solution progresses. Overpotential changes from being entirely electrical when $\Delta\mu_e = 0$ at $t = 0$ to partly chemical, partly electrical as the solution progresses toward steady state and $\Delta\mu_e \neq 0$. For other materials, such as those with metallic band structure, the expression for change in electron chemical potential could look very different and would involve primarily band energetics rather than configurational terms [86].

In addition to the local point defect concentrations, the local change in electrostatic potential can also be unbundled when the electrochemical potential of the e^* ensemble is separated into chemical and electrical contributions

$$\Delta\tilde{\mu}_{e^*} = \Delta\tilde{\mu}_e = \Delta\mu_e + z_e F\Delta\Phi^{WE} \tag{97}$$

where $\Delta\mu_e$ is the change in chemical potential and $\Delta\Phi^{WE}$ is the change in internal electrostatic potential. $\Delta\Phi^{WE}$ is available by rearranging

$$\Delta\Phi^{WE} = \frac{\Delta\tilde{\mu}_e - \Delta\mu_e}{z_e F} \tag{98}$$

The computation of sheet or other resistance is built into these simulations because $\Delta\Phi^{WE}$ captures the change of electrostatic potential within the MIEC. No additional consideration such as drift-diffusion is required.

5.2.2.2 Interfacial reaction rates and the electrolyte-MIEC boundary

One reason for unpacking is to use point defect concentrations and electrical potential in phenomenological models [101] at the interfaces.

The electrolyte-MIEC interface is very important in determining the electrochemical response of a cell. It affects the overall kinetics in several ways. First, it directly contributes to series resistance of the cell, a phenomenon identified experimentally by electrochemical impedance spectroscopy [9]. Second, it affects the chemical polarization of the MIEC. The second effect is less obvious and will be examined. To fully describe the response of a cell with resistance at this interface, the kinetics of ion exchange across it should first be considered.

The MIEC is supplied with oxygen vacancies during operation by electrochemical pumping from the electrolyte. The purely electrostatic contribution to the change in electron electrochemical potential in the working electrode, $\Delta\Phi^{WE}$, is the driving force for this oxygen vacancy transfer. The rate has been derived elsewhere [103] for the case of low oxygen vacancy concentration. However, it must be modified to account for large absolute changes in oxygen vacancy concentration, such as those that occur in LSCF. This case is derived rigorously in appendix B.4. The result is:

$$r_v = k_v^0 \left[\frac{c_{O,m}}{c_{O,m}^0} \exp\left(\frac{2\alpha_v F}{RT} \Delta\chi_i \right) - \frac{c_{v,m}}{c_{v,m}^0} \exp\left(\frac{-2(1-\alpha_v) F}{RT} \Delta\chi_i \right) \right] \tag{99}$$

where $c_{v,m}$ is the concentration of oxygen vacancies. The new term $c_{O,m} = c_{Osite,m} -$

$c_{v,m}$ is the concentration of occupied oxygen lattice sites and accounts for a significant change in $[O_O^x]$ upon cathodic bias. The 0 superscript represents equilibrium values. The variable $\Delta\chi_i$ is the change of the electrical potential difference from its equilibrium value: $\Delta\chi_i = \chi_i - \chi_i^0$. The definition of χ_i is

$$\chi_i = \Phi_{elyte} - \Phi_{WE} \tag{100}$$

Thus, $\Delta\chi_i = (\Phi_{elyte} - \Phi_{WE}) - \left(\Phi^0_{elyte} - \Phi^0_{WE}\right)$. Rearranging,

$$\Delta\chi_i = \left(\Phi_{elyte} - \Phi^0_{elyte}\right) - \left(\Phi_{WE} - \Phi^0_{WE}\right) = \Delta\Phi_{elyte} - \Delta\Phi_{WE} \tag{101}$$

The quantity $\Delta\Phi_{elyte}$ is equal to the Ohmic drop in the electrolyte and is available from solving the conduction equations in the electrolyte. This assumes no losses between the counter electrode and electrolyte. The quantity $\Delta\Phi_{WE}$ is taken from Equation 98. It is critical to remove the nonelectrical shift of electron energy from $\tilde{\mu}_e/(z_eF) = \Delta E$ in order to correctly obtain the change electrical driving force when oxygen vacancy concentration is large.

The value of both $\Delta\Phi_{elyte}$ and $\Delta\Phi_{WE}$ must be computed on a local basis. That is, their values are subject to change based on location due to bulk electrical resistance within the MIEC and can alter the global response of a cell. The effect has been investigated in geometrically well-defined cells by modeling [96, 103] and has been observed experimentally [16, 82].

Figure 26 shows how each of these potential drops interact with one another to form an effective local interfacial $\Delta\chi_i(\overrightarrow{x})$. The potentials are with respect to the counter electrode. The total $\Delta\chi_i(\overrightarrow{x})$ is diminished from ΔE by the nonelectrical contribution from electrons, $\Delta\mu_e^{WE}(CC)$, the bulk resistance in the MIEC, and the bulk resistance in the electrolyte. The figure assumes no losses between the counter electrode and electrolyte.

This method of accounting for change in stoichiometry in the electrical driving force is directly analogous to the approach taken in modeling of insertion electrodes

in batteries [39, 125] and electrochromic devices [31, 122]. In those cases, the overpotential for a surface reaction is determined by subtracting the open-circuit potential from the applied interfacial potential where the open-circuit potential is proportional to the chemical potential of the intercalated species.

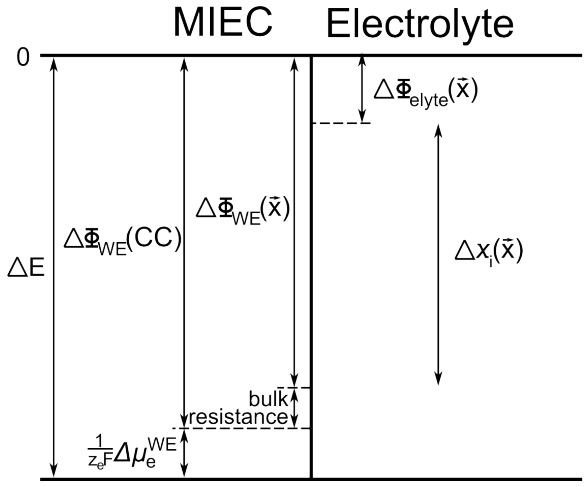

Figure 26: Schematic diagram of the potentials contributing to local $\Delta\chi_{\mathrm{i}}$ on a local basis, assuming no losses between counter electrode and electrolyte. Potential change is with respect to the counter electrode.

5.2.2.3 Relationship to Nernst potential approximation

A common approximation in solid state ionics is that the cathodic polarization can be related to the effective internal oxygen partial pressure of the mixed conductor through the Nernst potential

$$\eta = \frac{\mathrm{RT}}{4\mathrm{F}} \ln \frac{\mathrm{pO}_2^{\mathrm{solid}}}{\mathrm{pO}_2^0} \tag{102}$$

where pO_2^0 is the equilibrium atmospheric partial pressure of oxygen prior to bias. The quantity $\mathrm{pO}_2^{\mathrm{solid}}$ is supposed to be the internal pO_2 corresponding to the change to the defect chemistry caused by the cathodic polarization.

The rate expression in Equation 99 can be shown to agree with it in certain circumstances. Assume first that an MIEC layer has negligible ionic and electronic transport limitations and so the defect chemistry and electrostatic potential at the MIEC-electrolyte interface is the same as that found at the MIEC-CC boundary.

Then, suppose that oxygen exchange over the MIEC-electrolyte interface is facile and fast, i.e. k_v^0 is very large. Therefore, under steady state operation, the quantity inside of the parenthesis in Equation 99 must be close to zero and so

$$\frac{c_{O,m}}{c_{O,m}^0}\exp\left(\frac{2\alpha_v F}{RT}\Delta\chi_i\right) \approx \frac{c_{v,m}}{c_{v,m}^0}\exp\left(\frac{-2\left(1-\alpha_v\right)F}{RT}\Delta\chi_i\right) \tag{103}$$

Rearranging and recognizing Equation B-40,

$$\Delta\chi_i \approx \frac{\Delta\mu_{v,m}}{2F} \tag{104}$$

Now, with a further assumption that the counter electrode is low-impedance, then $\eta = \Delta E - \Delta\Phi_{elyte}$. Recognizing that without transport loss in the MIEC, $\Delta E = \Delta\tilde{\mu}_e/(z_e F)$, separating chemical in electrical terms of $\Delta E = \Delta\tilde{\mu}_e = \Delta\mu_e + z_e F\Delta\Phi$ as in Equation 97, and employing Equation 101 and 104

$$\eta = \Delta E - \Delta\Phi_{elyte} = \frac{\Delta\mu_{e,m}}{z_e F} - \frac{\Delta\mu_{v,m}}{z_v F} \tag{105}$$

Equation B-3 implies that the right hand side of the above equation is equal to

$$\eta = \frac{\Delta\mu_{O_2,m}^{solid}}{4F} \tag{106}$$

Substituting $\Delta\mu_{O_2,m}^{solid} = RTln(pO_2^{solid}/pO_2^0)$ leads to the Nernst formulation of the cathodic overpotential in Equation 102. Therefore, the Nernst potential appears to be a reasonable approximation for the effect of cathodic polarization upon point defects when these certain assumptions are met. The much more general and detailed treatment is required whenever ionic and/or electronic transport limitations exist within the MIEC or when oxygen exchange over the MIEC-electrolyte boundary is not facile.

5.2.3 Implementation

Coupled numerical multiphysics simulations of one-, two-, or three- dimensions enable the simulation of the performance of electrodes of very different geometries.

One-dimensional simulations may be applied to thin films deposited onto electrolytes without the need to consider sheet resistance, as in thin-film test cells [9,16,114]. Two-dimensional simulations may be applied to thin films with sheet resistance [82, 103] or onto a simple representation of a porous microstructure. Three-dimensional simulations may be applied to full porous microstructure reconstructions. In this contribution, one- and two-dimensional simulations are demonstrated. Three dimensional simulations are addressed in the next chapter.

For spatial simulations, the commercial finite element modeling software package COMSOL Multiphysics v. 4.1 was used to solve for $\Delta\tilde{\mu}_{O^*}$ and $\Delta\tilde{\mu}_{e^*}$. This package has an interpolation function feature in the subdomain useful for interpolating defect concentrations from local pO_2^{solid} (Equations 95 and 93). Interpolation functions

$$c_v = cvlookup(pO_2^{solid}) \tag{107}$$

$$c_h = chlookup(pO_2^{solid}) \tag{108}$$

$$c_e = celookup(pO_2^{solid}) \tag{109}$$

were defined, making use of stored defect concentrations at 500 different pO_2 values, distributed uniformly in log-space between 1 and 10^{-11} atm. Piecewise cubic interpolation was used to translate a local value of pO_2^{solid}, obtained via Equation 95 and 93, to local point defect concentrations. The fsolve optimization function and custom code in MATLAB v. R2009b were used to solve the set of nonlinear defect equilibrium equations (appendix B.2) to provide the interpolation table.

5.3 Results

The transport coefficients s_{oo*} and s_{ee^*} were computed (Figure 27) as a function of pO_2^{solid} compared to their values at $pO_2 = 0.21$ atm using Equations 82 and 83. It was assumed that the intrinsic mobility b_{e^*} of electrons and holes were identical and constant. As pO_2 is reduced, the oxygen vacancy concentration increases and so does

s_{oo*}, reflecting the increase in O* conductivity due to a large concentration of oxygen vacancies. A net decrease in $c_h + c_e$ leads to a decrease in s_{ee*} with decreasing pO_2.

The model values of s_{oo*} and s_{ee*} compare favorably with experimental values within the region of interest (that is those pO_2 values that correspond with reasonable cathodic polarizations through the Nernst relationship). The e* ensemble transport coefficient ratios were derived from the ratios of conductivity versus pO_2 for LSCF 6428 reported elsewhere [6, 155]. The O* ensemble transport coefficient ratios were derived from measured oxygen tracer diffusion coefficients, D* [12]. The tracer diffusivity is roughly proportional to s_{OO*} because $D^* = fD_v c_v / c_O$ where the oxygen vacancy diffusion coefficient D_v us equal to $b_v RT$ and f is a structure factor.

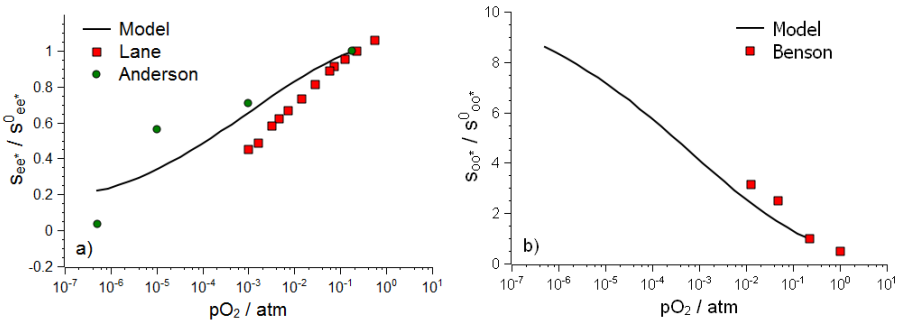

Figure 27: Ratio of transport coefficients a) s_{ee*} and b) s_{oo*} as a function of pO_2 to their values at $pO_2 = 0.21$ atm and 1073K. Experimental e* ratios derived from conductivity measurements performed by Lane [85] and Anderson (for LSCF 8228) [6]. Experimental O* ratios derived from oxygen tracer diffusivity, D*, measurements of Benson [12].

Simulations in 1D representative of a thin-film test electrode were performed on a 1 μm-thick film of LSCF 6428 using various values of interfacial exchange coefficient k^0_v. The rate laws used for the air surface are the same as those used for LSCF in chapter 4. The resulting electrical portion of polarization $\Delta\Phi$, the chemical portion of polarization $\Delta\mu_{e*}/(z_{e*}F)$, effective internal oxygen partial pressure pO_2^{solid}, and oxygen vacancy concentration c_v at the MIEC-electrolyte interface are given in Figure 28 and are compared to the ideal (Nernst) response to the imposed overpotential. At

sufficiently large values of k_v^0, the simulated response is very close to the ideal behavior because oxygen vacancy transfer over the interface occurs almost without resistance. However, for smaller values of k_v^0, a larger electrostatic component is required to drive the interfacial vacancy transfer.

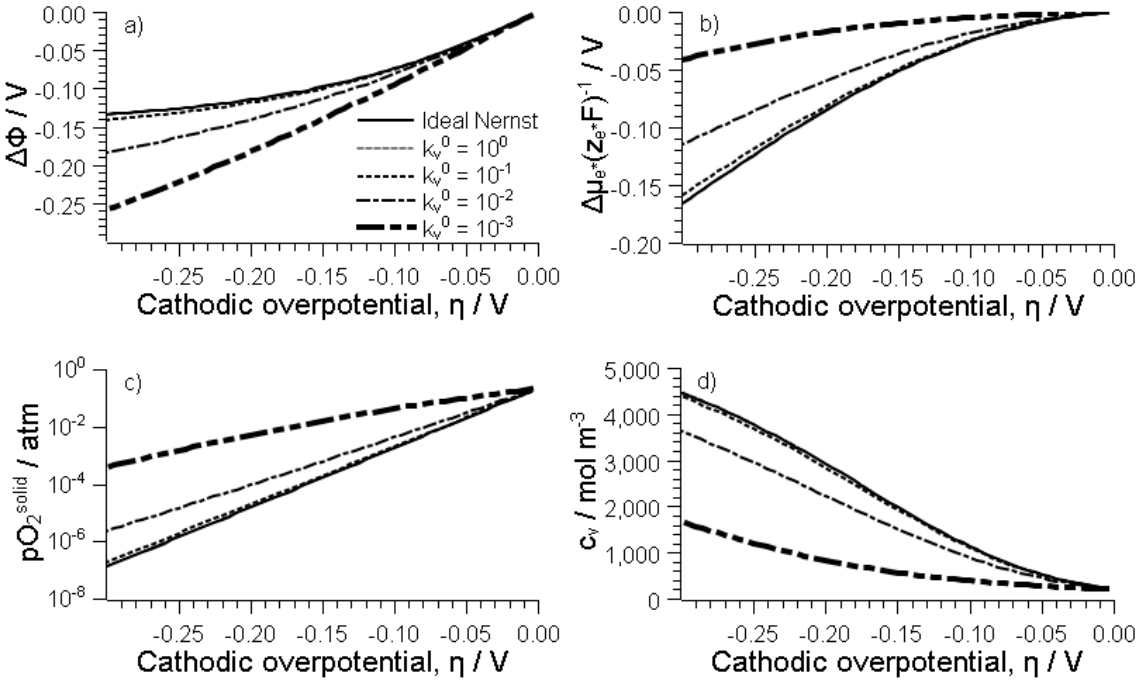

Figure 28: Relevant electrochemical quantities at the buried electrolyte-MIEC interface as a function of cathodic overpotential for different values of rate parameter k_v^0. Units of k_v^0 are $\mathrm{mol\,m^{-2}\,s^{-1}}$.

The results show that fewer oxygen vacancies are available in the MIEC for oxygen reduction if the MIEC-electrolyte interface is nonideal. A nonideal MIEC-electrolyte interface contributes an internal resistance to the overall cathode process and also affects the chemical state of the cathode. The buried interface is therefore very important in determining the oxygen reduction properties of the MIEC.

This effect comes about because the change of the electron electrochemical potential in the MIEC upon application of the cathodic polarization is partitioned according

to Equation 97 differently depending on k_v^0. Figure 28a shows that the purely electrostatic portion of the polarization, $\Delta\Phi$, is more negative for smaller values of k_v^0 and Figure 28b shows that the chemical portion, $\Delta\mu_{e^*}/(z_eF)$, is closer to zero. A smaller amount of the imposed cathodic polarization is devoted to changing the stoichiometry when the interface is nonideal. As a result, pO_2^{solid} is not decreased by as much as in the ideal case (Figure 28c) and the oxygen vacancy concentration is smaller (Figure 28d). This in turn affects the rate of oxygen reduction at the MIEC-air surface, as the concentration of oxygen vacancies is essential for the incorporation of oxygen ions into the MIEC. The Nernst approximation is a good assessment of the effect of a cathodic overpotential on the bulk point defect equilibrium only if the electrolyte-MIEC interface is close to ideal.

Simulated quantities as a function of position in the film are given in Figure 29. There was a large gradient in $\Delta\tilde{\mu}_{O^*}$, driving the flux of O^{2-} from the MIEC-air surface to the electrolyte-MIEC interface. There was no gradient in $\Delta\tilde{\mu}_{e^*}$ because electronic species did not flow in the thickness direction of the film.

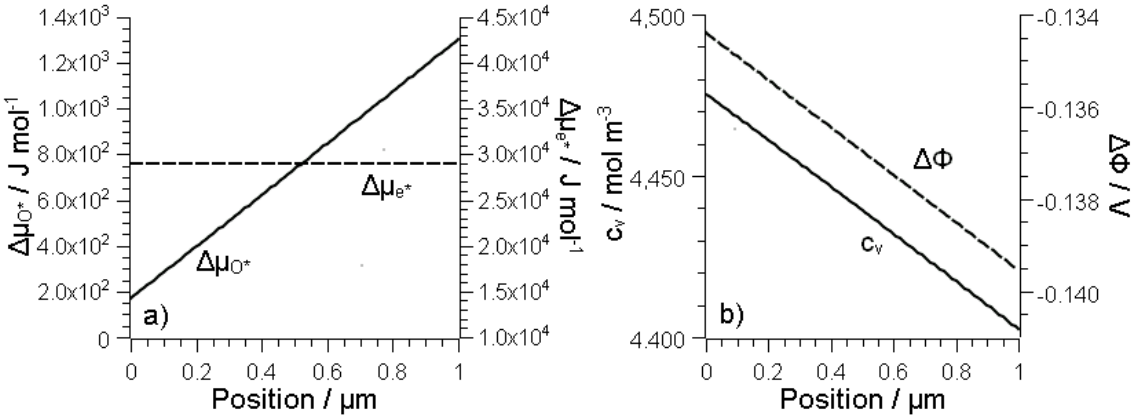

Figure 29: a) Simulated ensemble electrochemical potentials $\Delta\tilde{\mu}_{O^*}$ and $\Delta\tilde{\mu}_{e^*}$ as a function of distance from the electrolyte-MIEC interface in a 1-μm thick LSCF 6428 film. b) Derived oxygen vacancy concentration, c_v, and electrostatic potential, $\Delta\Phi$, as a function of position. T = 973K, $\eta = -0.3$V, $k_v^0 = 10^0\,\mathrm{mol\,m^{-2}\,s^{-1}}$.

Figure 29b shows that the quantities that contribute to $\Delta\tilde{\mu}_{O^*}$ had slight gradients.

The oxygen vacancy concentration, c_v, was maximum at the electrolyte-MIEC interface where vacancies are injected. The electrostatic potential component, $\Delta\Phi$, was more negative near the current collector at the MIEC-air surface of the film where it is applied. The large gradient in $\Delta\tilde{\mu}_{O^*}$ was associated with smaller gradients in c_v and $\Delta\Phi$, which have an opposing effect and tend to cancel one another out: a negative $\Delta\Phi$ produces a positive $\Delta\tilde{\mu}_{O^*}$ while a positive change in c_v results in a negative $\Delta\tilde{\mu}_{O^*}$. Since there was a negative gradient in both c_v and $\Delta\Phi$ with increasing distance from the electrolyte-MIEC interface, the gradient in $\Delta\tilde{\mu}_{O^*}$ was positive.

The transport and rate simulation was also implemented onto a simple two-dimensional representation of a porous electrode microstructure, shown in Figure 30a. The pores between particles are represented by circles and the reaction rate laws described in chapter 4 were applied as boundary conditions. Meshing was performed in COMSOL with free triangular mesh having a maximum element size of $1.3\text{x}10^{-6}$ m and minimum size of $6.0\text{x}10^{-8}$ m on the domain. The set of equations was solved using COMSOL's multifrontal massively parallel sparse direct solver (MUMPS). A bias of $\eta = -0.3$V and temperature of 973 K were also used.

The resulting oxygen vacancy concentration, c_v, electron hole concentration, c_h, electron concentration, c_e, and electric potential, $\Delta\Phi$, distributions are shown in Figure 30b and c. There was large variation of all quantities in the vertical direction of the electrode, indicating the need to account accurately for the variations in complicated point defect chemistry and electrical state as a function of position. The big variations are the result of the large thickness of the porous electrode compared to the film thickness as well as the active electrochemical sites at the pores where vacancies are consumed by oxygen reduction. the resulting large change in oxygen content necessitates similar large changes in the concentrations of electronic species in order to maintain electroneutrality.

As a check on the accuracy, the conservative ensemble method was compared

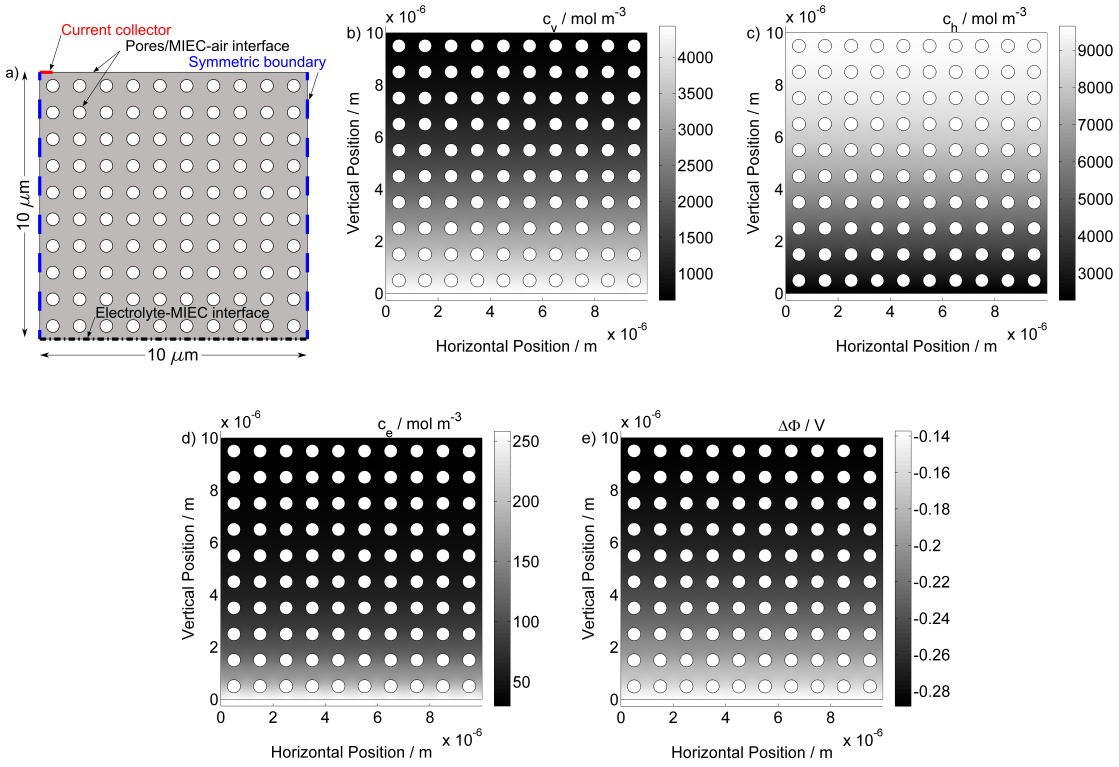

Figure 30: a) Simulation domain: simple 2D representation of a porous electrode microstructure. Computed b) oxygen vacancy concentration, c_v, c) electron hole concentration, c_h, d) electron concentration, c_e, and d) electrostatic potential, $\Delta\Phi$, in a simple 2D representation of a porous electrode microstructure. T = 973 K, $\eta = -0.3$V.

against the conventional three-equation simulation, which uses dilute drift-diffusion equations for transport of oxygen vacancies, electrons, and electron holes

$$\begin{aligned}
\frac{\partial c_v}{\partial t} &= -\nabla \cdot (-D_v \nabla c_v - z_v F c_v b_v \nabla \Phi_m) \\
\frac{\partial c_h}{\partial t} &= -\nabla \cdot (-D_h \nabla c_h - z_h F c_h b_h \nabla \Phi_m) + G \\
\frac{\partial c_e}{\partial t} &= -\nabla \cdot (-D_e \nabla c_e - z_e F c_e b_e \nabla \Phi_m) + G
\end{aligned} \tag{110}$$

where D_k is a diffusion coefficient, z_k is the formal charge, and b_k is a mobility

of species k. The latter two equations include a common homogeneous generation-recombination term [8], G, to account for local disproportionation equilibrium. An expression for G may resemble other phenomenological rate expressions: $G = k_G^0[(c_{Bx}/c_{Bx}^{ss,eq})^2 - c_h c_e/(c_h^{ss,eq} c_e^{ss,eq})]$, where c_{Bx} represents the concentration of neutral B-sites and the superscript "ss,eq" indicates the concentration of electrons or electron holes which satisfies disproportionation equilibrium and electroneutrality with the local concentration of oxygen vacancies.

The results are shown in Figure 31a and b, computed with the same mesh and solver as the conservative ensemble formulation. The constant $k_G^0 = 10^{11}\,\mathrm{mol\,m^{-3}\,s^{-1}}$ was used, which was sufficient to ensure that electrons and electron holes were forced close to local equilibrium with one another as well as fulfilling electroneutrality. The simulated c_v and $\Delta\Phi$ are close to those simulated by the conservative ensemble method. Small differences were present, likely associated with the use of the dilute approximation in the electronic species. The conservative defect ensemble method therefore appeared to be an accurate and viable alternative to the standard explicit-defect method.

A benchmark study was also performed to compare the two methods (Figure 31c) by solving the 2D problem using several mesh element sizes and the MUMPS solver. The system used for the calculations was a desktop computer with an Intel Core 2 Duo E6600 processor and 2 GB of memory. The conservative ensemble solved for fewer degrees of freedom and was therefore faster in all cases. Its time advantage grew as mesh size decreased and degrees of freedom increased. This result suggests that it would be the preferred method for large-scale simulations such as those on realistic microstructure where processing speed and memory limit the problem.

Analogous calculations were carried out for LSM 8020, using the same mesh and solver with the addition of a maximum element size of $2\text{x}10^{-8}$ m on the MIEC electrolyte boundary. Defect chemistry calculations were taken from [104] and the surface

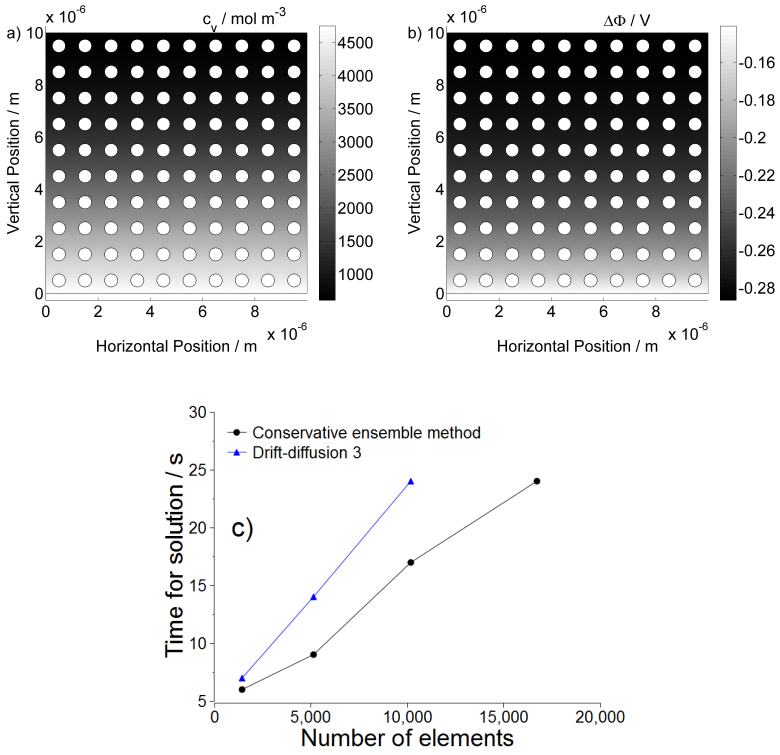

Figure 31: Simulated a) oxygen vacancy concentration, c_v, and b) electrostatic potential, $\Delta\Phi$, using a conventional three-equation approach. c) Benchmark time required for solution as a function of maximum mesh element size for the conservative ensemble and three-equation methods. T = 973 K, $\eta = -0.3$V.

parameters used are from chapter 4. Figure 32a gives c_v from the conservative ensemble simulation. There was enrichment of oxygen vacancies along the electrolyte-MIEC interface and close to the first set of pores. Little change to the defect chemistry occurred away from this region. Since c_v is very small in LSM, c_h, c_e, and $\Delta\Phi$ did not change substantially across the microstructure. The conservative ensemble and three-defect methods agreed very closely. This agreement is due to the applicability of the dilute solution approximation in LSM and the relatively small gradient in c_h and c_e.

Figure 32b gives the benchmark comparison. Again, the conservative ensemble method was faster and required less memory, though it was not as fast relative to the three-defect method as it was for LSCF. This effect is probably because the

solution for LSM involved such small gradients in c_h, c_e, and $\Delta\Phi$. It appears that the conservative ensemble model makes the solution time no worse in this case, but that its main advantage is in highly coupled problems with large changes to several defects or electric potential across a microstructure.

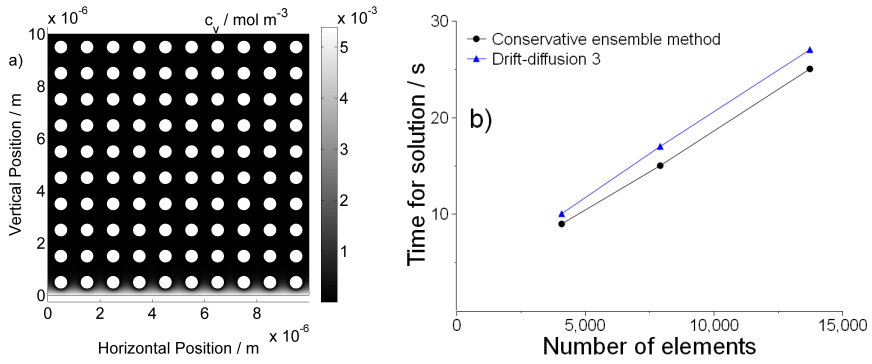

Figure 32: a) Simulated oxygen vacancy concentration, c_v, in LSM 8020 using conservative defect ensemble approach. b) Benchmark time required for solution as a function of maximum MIEC-electrolyte interface mesh element size for the two methods. T = 973 K, $\eta = -0.3$V.

5.4 Discussion

The strengths of the conservative ensemble method make it a good choice for many situations, particularly those relevant to the necessities of intermediate temperature solid oxide fuel cells. This push to reduce cathode operating losses and enable operation at lower and lower temperatures has led researchers to fabricate novel cathodes including heterogeneous MIEC interfaces, new materials, and small features sizes with tenuous particle connections.

5.4.1 Buried interfaces between mixed conductors

The preparation of composite cathodes of such materials as LSM and YSZ, an MIEC and an ionic conductor respectively, is carried out routinely. Recently, there have been efforts to combine two different mixed conductors in an effort to improve performance, in particular using infiltration to achieve multi-phase mixed-conducting composites.

Examples include composites of LSC and LSM formed by sequential infiltration [62] and a strategy that for forming a thin, continuous film of LSM on an LSCF backbone described earlier in this thesis and in [95].

The presence of two mixed conductors presents a modeling challenge especially if the two materials vary significantly in their point defect chemistries. At the buried interfaces between the two phases, there is space-charge region where the point defect distributions must adjust. Strictly speaking, the interface can be modeled using the Poisson equation and explicit consideration of the point defect concentrations and electric potential. If the Debye length is very small, which is usually the case for SOFC MIECs, then the profile can be viewed as a step-change between the two phases. Such a change is depicted in Figure 33, where interfaces between two oxygen-vacancy conductors (left) and an oxygen vacancy and oxygen interstitial conductor (right) are depicted.

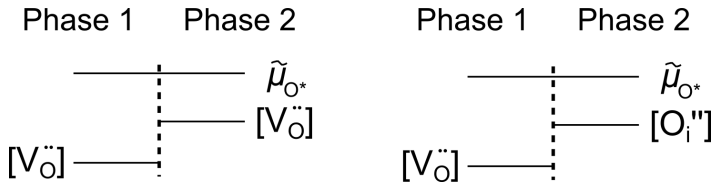

Figure 33: Schematic of a buried interface between two MIECs. The transition between phases is approximated by a step change in point defect concentration, but the ensemble electrochemical potential is continuous.

Examples of this type of situation include an interface between LSM and LSCF, where the oxygen vacancy concentration of LSM is far below that of LSCF and would have to be adjusted accordingly, or an interface between LSCF and $NdBaCo_2O_{5+\delta}$, where oxygen vacancies predominate in the LSCF but oxygen interstitials (O_i'') predominate in the $NdBaCo_2O_{5+\delta}$ [175]. An example for electronic defects could be an interface between LSC with itinerant electrons, and LSCF, with small polarons.

Simulations explicit in point defect concentration and electric potential will have difficultly dealing with this problem. Either Poisson's equation should be solved or

some relationship would need to be established to relate the concentrations and fluxes under a steady state - a relationship that would likely reference the equilibrium states and the continuity of point defect electrochemical potentials across the interface.

The method of conservative ensembles deals directly with an ensemble's electrochemical potential and therefore, if quasi-equilibrium between mixed conductors is assumed, the interface does not require any complicated procedure. Whereas a large step change in point defect concentration can exist across the interface, the electrochemical potential of an ensemble is continuous. The continuity of the O^* is depicted in Figure 33. The conservative ensemble method is therefore easy to use at buried interfaces. Different methods of unpacking would be used on either side in correspondence to the requirements of each material's point defect chemistry. Transport coefficients likewise would be computed differently. The interface merely serves as a dividing line between unpacking and transport properties/procedures but poses no additional difficulty associated with correlating a change of state in one phase with a change in the other. Therefore, the conservative ensemble method is particularly useful when heterojunctions between different MIECs with different point defects are present.

5.4.2 New MIEC materials with different point defects

Developing new materials with superior oxygen reduction properties is another way to increase the performance of the SOFC cathode and anode. Some of these novel materials derive ionic conductivity via the somewhat conventional oxygen vacancy conduction mechanism [178]. Others derive ionic conductivity from interstitial oxygen, O_i'' [175]. The conservative ensemble method itself does not need to be altered based upon the type of oxygen or electron defects present. Only the unpacking procedure should be tailored to the individual material. As depicted in Figure 33, heterojunctions between phases do no present a problem even different types of point

defects exist on either side of the interface.

5.4.3 Electronic losses

A common assumption in the simulation of MIEC electrodes is a uniform Fermi level [5]. This approximation may be appropriate for single-phase mixed-conducting cathodes composed of materials such as LSC with relatively large particle size, but may be inappropriate in some cases, such as where the MIEC configuration promotes Ohmic losses or in cases where electronic conductivity is low. Recently, the case of mixed conductors infiltrated as a thin coating on a YSZ electrolyte backbone was simulated [126]. In general, the drop of potential in the mixed conductor was low, but in some situations there was significant deviation of potential due to the aspect ratio of the coating. From an experimental study, Smith [147] reported that LSM cathodes sintered at low temperatures had not only larger triple phase boundary density and superior electrochemical performance compared to cathodes sintered at higher temperatures, but also contained particles that were not very well connected to one another. Such a case–high TPB length, large current densities, and poor particle connections–increase the likelihood of electronic deactivation due to current constriction [52]. The case will be even more severe when the nonlinear electrochemical activation effects of a cathodic bias are taken into account.

Doped ceria is a mixed conductor with a large ionic transference number and small ionic transference number. Its mixed conductivity has prompted it to receive attention as a candidate to extend the reaction zone away from the triple phase boundaries, especially in composite anodes [26, 27, 176]. Nonuniform electron electrochemical potential is by necessity a much more important consideration in this system than in most perovskite cathode MIECs. The conservative ensemble method is easily extended to ceria and interfaces between ceria and ionic conductors or other mixed conductors.

The conservative ensemble method allows for the solution of nonuniform electron electrochemical potential, but does not require it. In situations where a uniform Fermi level is a good approximation, the constitutive equations for $\Delta\tilde{\mu}_{e^*}$ need not be solved; rather $\Delta\tilde{\mu}_{e^*} = \Delta\tilde{\mu}_{e^*}^{CC}$ can be assumed everywhere and all unpacking done referencing the constant quantity. Further gains in computational efficiency over drift-diffusion would be expected without solving for it. If electronic losses are high, however, the constitutive equations may be solved in addition to those for $\Delta\tilde{\mu}_{O^*}$. No changes to the structure of the model are required in either case.

5.4.4 Unpacking procedures

In this chapter, unpacking is used in the bulk of the mixed conductor and on the surface identically, assuming that the bulk defect chemistry prevails everywhere. This assumption might not always be adequate, particularly at gas-exposed interfaces. Space charge seems to play a role in the electronic and ionic concentration distributions in doped ceria [176]. Oxygen vacancy formation energy in some materials could be more favorable at surfaces [91]. These factors could cause the point defect chemistry that prevails at the surface to differ from that of the bulk.

Fortunately, *electrochemical potential* is constant from the bulk to the surface, which is another advantage of the conservative ensemble method. Different unpacking procedures may be employed on the surfaces, reflecting changed point defect equilibrium constants or distributions due to space charge. For the former, slightly different defect equilibrium equations should be solved. For the latter, the bulk defect concentrations may be altered by an analytical expression relating Poisson's equation to defect distributions in the space-charge region.

Transport coefficients of each ensemble in the bulk were also related to changes in point defect concentration. The prediction appears to agree acceptably with the data, but there is no absolute requirement for an analytical expression. It is possible

to interpolate effective conductivities of each ensemble instead of concentrations used to analytically calculate transport coefficients. This would allow the use of empirical conductivities based on pO_2, which could more accurately fit data if a specific point defect model is in question.

5.5 Conclusion

A comprehensive approach was proposed to handle mixed ionic-electronic conducting cathode materials with complex defect chemistries under large cathodic polarizations and arbitrary geometries. Conservative defect ensembles were used to treat transport in the bulk of the MIEC. Local equilibrium was assumed in order to extract local point defect concentrations from the resulting transport calculations. The point defect concentrations were used to determine transport coefficients for the nonlinear transport problems as well as inform phenomenological rate expressions at the boundaries. The particular case of a nonideal electrolyte-MIEC interfaces was examined. In certain simple situations such as thin film and ideal electrolyte-MIEC interface, this approach reduces to that predicted by the Nernst potential approximation. This approach is particularly useful when the MIEC-electrolyte interface is nonideal, when the electrode faces bulk transport limitations, or when the point defect chemistry of the cathode material is very complicated. It shows good agreement with the conventional three-equation simulation and is a faster and less memory intensive alternative.

CHAPTER VI

FINITE ELEMENT SIMULATIONS CONFORMAL TO REALISTIC MICROSTRUCTURE

6.1 Introduction

The performance of an operational electrode is determined critically by the porous 3D microstructure. Important factors include exposed catalyst surface area, facility of gas-phase transport, connectivity of particles, and length of TPB lines. The complexity of mass and charge transport inside and on the surface of the solid phase is illustrated in Figure 1. Many strategies have been employed to optimize the microstructure including formation of composite electrodes, functionally graded microstructures, and infiltration of active electrode phases on electrolyte scaffold. Optimization of the electrodes is a very difficult task because many of the important features compete with one another; for example, surface area may increase at the expense of gas-phase diffusion.

Modeling on an electrode level [48, 145] is useful for understanding performance. In particular, equivalent circuit models [92,151] describe the performance based upon linearized parameters. Another model type for MIEC electrodes is based upon porous electrode theory (the ALS model) [5] and uses homogenized microstructural parameters and linear irreversible thermodynamics in reaction rates. This is particularly true when the electronic conductivity is very large and a uniform Fermi level is assumed, when the ionic transference number of the mixed conductor is very high, and when the geometric feature size is much smaller than the characteristic length of ambipolar diffusion. The 1D porous electrode theory does not adequately describe the results when these conditions are not met [94]. Local variations of important electrochemical

quantities on the length scale of particle features can be large [58], with important implications upon the global electrochemical response. Homogenized models neglect the fine details of the microstructure and can lack detailed predictive capability.

For this reason, simulations which use the digital representation of microstructure are becoming relevant and important. 3D reconstruction by focused ion beam/scanning electron microscope (FIB/SEM) [57,169] and x-ray computed tomography (XCT) [58] is a recent and promising development to generate accurate digital microstructural images.

Recently, researchers began to use the 3D reconstructions as the domain for electrochemical simulations using the Lattice-Boltzmann method [58, 70, 143] or the finite element method [69, 139]. The former has been applied primarily in the anode using models developed for nickel patterned electrodes, gas diffusion, and ionic transport. The latter has been applied to an LSCF cathode using effective linear irreversible thermodynamic parameters (not detailed reaction rates) based on surface exchange and tracer diffusion coefficients. There is not yet agreement on the best way to carry out these simulations, or on which quantities to simulate. The objective of this chapter is to provide some analysis and develop an efficient, accurate, and tractable approach.

Such simulations can corroborate the accuracy of homogenized models and, when homogenized models break down, provide the most accurate and detailed means of simulation. The detailed microstructure may also be able to act as a sort of well-defined electrode in and of itself: the a priori digital representation of explicit microstructural geometry might allow fundamental study. The ultimate goal is to use the 3D geometry for numerical simulation of electrode performance in engineering design, in conjunction with detailed, mechanistic, nonlinear phenomenological rate expressions serving as boundary conditions and informed by parameters derived from patterned or porous electrodes.

In this chapter, options for a multi-scale modeling approach which enable the transport equations to be solved conformally on a porous structure informed by electrochemical boundary conditions are developed. The focus is on flexibility and the ability to include both a surface and a bulk pathway. The use of commercial and/or open-source software packages is considered to be preferable to custom code where it is possible to use them. Packages are easier to use, lead to faster development times, and allow easy duplication, verification, and use of the simulation once it is publicized. One principal goal of this work is to develop a methodology that is as easy to use a possible.

COMSOL Multiphysics is a commercial software package that provides flexibility to couple volumes, surfaces, edges, and points with a variety of physics. It is also compatible with MATLAB and therefore scriptable. The electrochemistry problem of interest here is very multiphysics in nature: bulk transport equations must be coupled with species existing on the surfaces, both of which must be coupled with surface and boundary reaction rates, all subject to nonlinear constraints. COMSOL's unique capabilities provide an excellent and commonly accessible platform for the necessary model considerations and will be used in the subsequent analysis.

Three methods are considered. The first is "voxel-by-voxel," which is popular for interpreting magnetic resonance imaging (MRI) and computed tomography (CT) scans of biological tissue. The second is extrusion of slices. The third is direct meshing of the structure. Of the three, direct meshing is the most promising. Analysis is performed to establish how meshing is best performed on 3D reconstructions of porous electrodes with important heterogeneous interfaces.

6.2 Experimental

Porous electrodes were fabricated to provide realistic geometry for simulations. The electrodes were composed of single-phase commercial $La_{0.85}Sr_{0.15}MnO_{3\pm\delta}$ powders

spray coated upon a dense YSZ (Daiichi) electrolyte mechanically polished to a 0.05 μm finish. The slurry was composed of 1 g LSM powder, 30 g ethanol, and 0.5 g of 10% polyethylene glycol and was sprayed onto masked samples using an airbrush and nitrogen gas with pressure 10 psi. The samples were sintered at 1150°C for 2 hours and had thickness of approximately 7-10 μm after heat treatment.

Some samples were characterized by scanning electron microscopy (SEM) in 2D. The pores of the electrodes were impregnated by Allied Technologies EpoxySet resin/hardener and allowed to cure overnight. EpoxySet was chosen because the dimensional change upon curing is very small and appropriate for preventing damage to a finely porous microstructure. The samples were then mechanically polished normal to the plane of the dense electrolyte with an Allied Technologies MetPrep 3 down to a 0.05 μm alumina final polish. The surface of the sample was then cleaned with Allied MicroOrganic Soap and wiped with a clean, gloved finger in order to remove residual polishing media. Silver paint was applied to the epoxy plug around the area of interest to reduce charging. A Leo 1530 scanning electron microscope was used to examine the polished cross section of the electrode. A representative image is shown in Figure 34.

Some samples were sent to Professor Wilson Chiu at the University of Connecticut for 3D x-ray microtomography as part of the US Department of Energy Heterogeneous Functional Material (HeteroFoaM) Center, an Energy Frontier Research Center (EFRC). Details of the procedure have been reported elsewhere [58]. Two views of a portion of the reconstructed representative volume element (RVE) is shown in Figure 35. The 3D reconstructions form the domain for coupled electrochemical simulations conformal to the microstructure.

Electrochemical impedance spectroscopy was performed at high temperature by Dr. Dong Ding in ambient air using pressure-contacted platinum mesh current collectors. Impedance spectra normalized to area per electrode and without the Ohmic

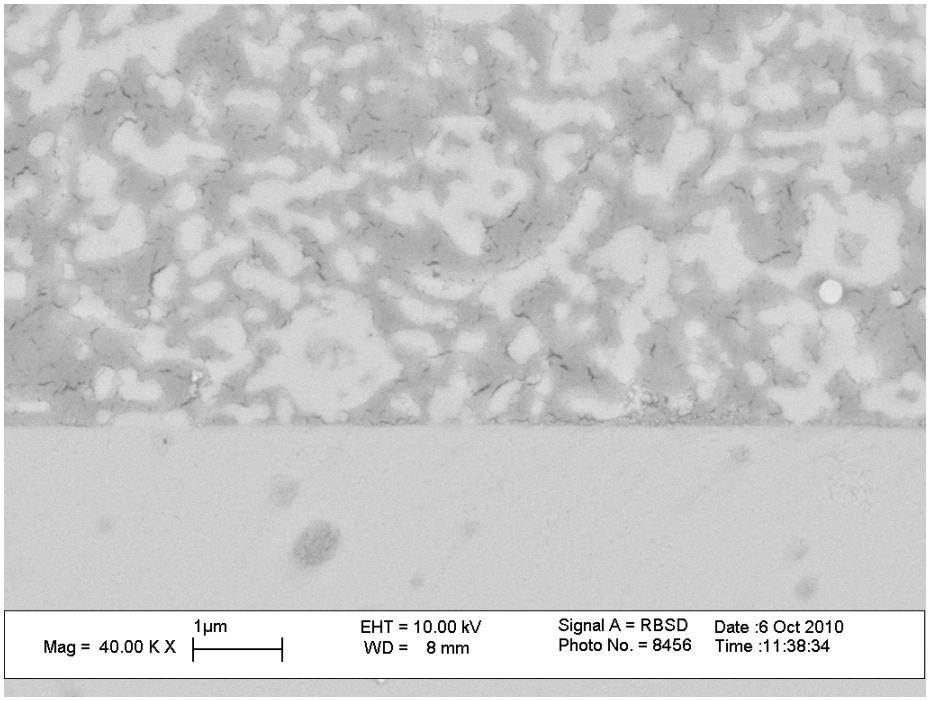

Figure 34: Polished, epoxy-impregnated porous LSM electrode on YSZ electrolyte.

portion at 600, 700, and 800°C are shown in Figure 36a-c. The plot of the polarization resistance versus inverse temperature is given in Figure 36d. The shapes of the impedance loops changed somewhat with temperature, but the polarization resistance was Arrhenius.

6.3 Pseudo voxel-by-voxel approach

The voxel-by-voxel approach was examined in conjunction with the microstructural data. The method involves an area (2D) or volume (3D) partitioned into pixels/voxels which contain phase information. Individual voxels are used as hexahedral mesh elements for a 3D FEM simulation. This method is particularly common in mechanical simulations [55, 78, 107], especially of medical images [32, 59, 78, 127]. No surface smoothing is used because the mechanical properties of interest tend to not be very sensitive to surface roughness.

The voxel-by-voxel method has several disadvantages. The first is that the mesh

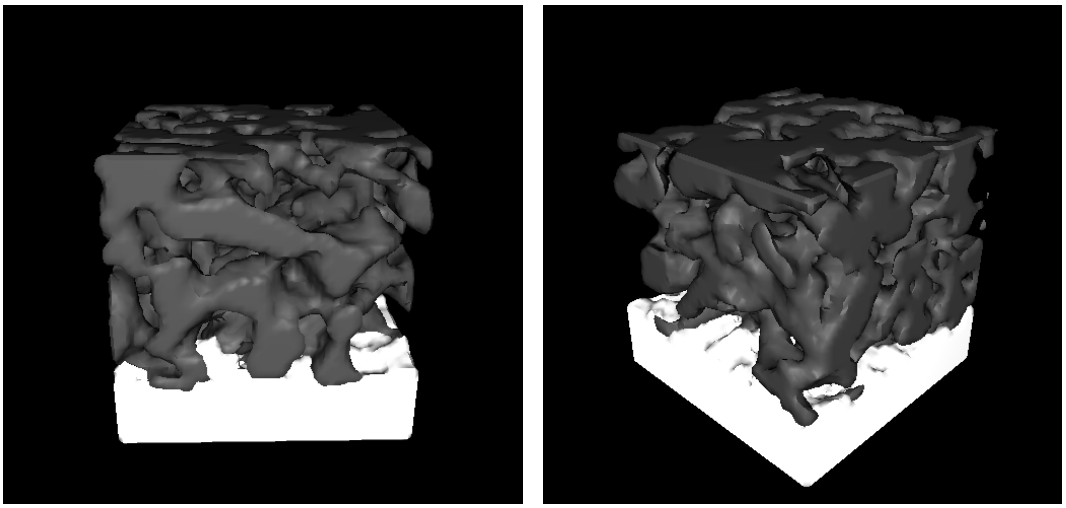

(a) (b)

Figure 35: Two views of a portion of the representative volume element. The porous LSM electrode is shaded gray and the dense YSZ electrolyte is white. Side length is 1.9 μm.

size is fixed and cannot be easily expanded or refined. As an example, the reconstruction in Figure 35 is 101 voxels to a side, leading to solid-phase voxels numbering on the order of 10^6. A voxel-by-voxel mesh derived from this data is extremely fine, which leads to inefficiencies in the FEM solution and limitation to smaller problems than necessary in 3D. Another disadvantage is that the voxel-by-voxel method is inherently volume-based. In systems where surface phenomena are important, this method may introduce artificial roughness or other artificial features.

6.3.1 Consolidation

To avoid the burdensome number of elements associated with true voxel-by-voxel meshing, a variant of the voxel-by-voxel method was implemented. Instead of constructing the mesh directly from pixels/voxels, a COMSOL drawing geometry was instead constructed from geometric primitives. For every pixel/voxel, one primitive was placed with coordinates matching those of the voxel to build the entire structure. An algorithm was developed to consolidate neighboring pixels/voxels into larger rectangles/prisms where possible.

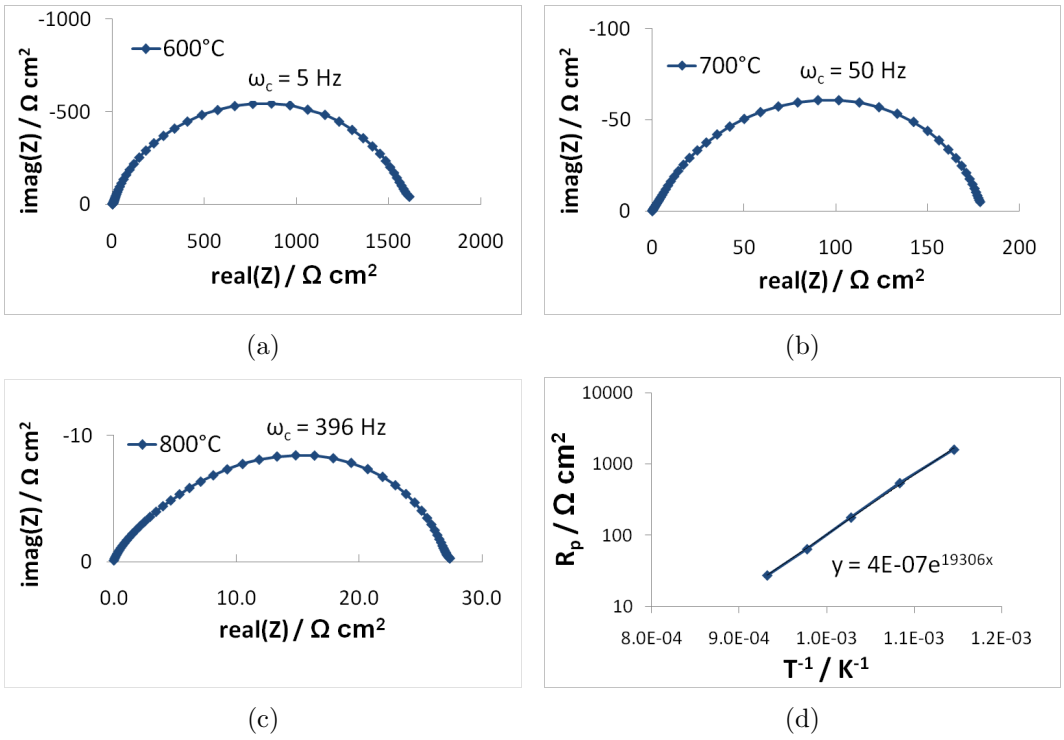

Figure 36: Area-normalized polarization resistance per porous LSM electrode: a) 600°, b) 700°, c) 800°, d) as a function of inverse temperature.

The process of consolidation is illustrated schematically in Figure 37a. The algorithm for this process searches the geometry by individual pixels/voxels and at each pixel/voxel the algorithm checks to see if other pixels/voxels of the same type are adjacent to it and available for expansion. A pixel in 2D with same type neighbors in the north, northeast, and east positions can expand north and east doubling its side length and eliminating the three other voxels (step 1a). The expanded primitive is then evaluated for subsequent expansion from side length two to three and the process is continued until expansion is no longer possible. If expansion in both directions is not possible, expansion in one direction only is evaluated (step 1b). When the primitive can no longer be expanded in any direction the algorithm moves to the next voxel (step 2). Consolidating features in this way led to primitives with side length much longer than one voxel length and therefore the elimination of a great number of individual voxel-sized primitives. This sped up the execution of geometry creation

significantly.

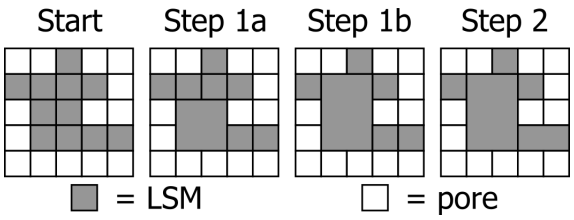

(a)

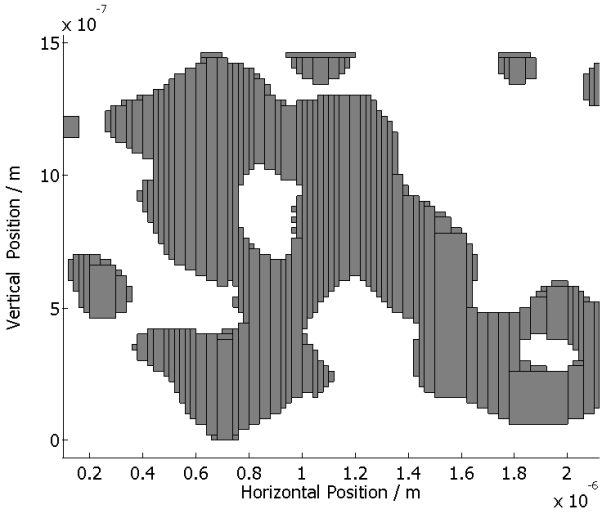

(b)

Figure 37: Consolidation in the pseudo voxel-by-voxel method. a) Schematic diagram illustrating the steps required to consolidate the LSM phase into larger primitives. b) Consolidated 2D microstructural cross-section (c.f. Figure 34 and 39) with internal boundaries enabled for illustration purposes.

After consolidating the primitives, they are joined together with the *union* command to make one large drawing geometry object with boundaries equivalent to that of the actual microstructural image. Internal boundaries are deleted to conserve memory and facilitate the application of physics. Figure 37b shows a created geometry without the internal boundaries deleted for the purpose of illustration. There are far fewer consolidated primitives comprising this structure than the number of starting pixels. The resulting compiled drawing object has many vertices, faces, and boundaries due to the underlying roughness at the pixel level.

6.3.2 Automated feature identification

The problem of interest here is inherently heterogeneous. Reactions at the TPBs take place along edges of the mesh but are coupled to surface diffusion occurring along faces and to bulk transport of point defects occurring in volumetric subdomains. The simulation absolutely requires some way to automatically detect geometric feature types, count and organize them, and apply the appropriate physics in an automated manner.

Many geometric features are generated by the creation of a mesh or COMSOL geometry by any means. These features include faces, edges, and vertices. Due to the number of different types and the inherent stochastic nature of their locations, MATLAB code was written to interpret the geometry object and apply physics, mesh the structure, and solve the problem. Automation with a script ensures rapid execution of the simulation and inclusion of all important features, as opposed to manual assignment which is slow and prone to errors.

The first part of the script consisted of identification of the various geometric subfeatures. The *adjacency matrix* of the object was used to determine adjacency of vertices to one another, edges, and boundaries, adjacency of edges to boundaries, etc. Determination of a feature's type was based primarily on adjacency. For instance, a face shared between the LSM and YSZ subdomain is automatically recognized as an LSM-YSZ interface. The appropriate boundary conditions, rate equations, and other physics are assigned to it. A TPB edge is recognized because it is shared between an LSM-YSZ interface boundary, an air-exposed LSM boundary, and an air-exposed YSZ boundary.

The order of assignment was as follows: subdomains, vertices, boundaries, edges. Vertex assignment generally required knowledge of adjacent subdomain types. Likewise, boundary assignment required knowledge of adjacent subdomain and vertex types. Edge assignment required knowledge of adjacent subdomain, vertex, and

boundary types.

In some cases the coordinates of the vertices were used to determine type instead of adjacency. For instance, some vertices reside on symmetrical boundaries where the position is fixed at a certain x-, y- or z- value. The fixed value identified the vertex as being located on the side.

The process of feature assignment is illustrated schematically in Figure 38. Subdomains are recognized by the original volumetric voxel-based data. Vertices are recognized (left) based on subdomain adjacency (e.g. TPB, LSM-air, YSZ-air), location (e.g. LSM-side), or a combination of both (e.g. LSM-YSZ interface side). Boundaries are then recognized (right) based upon adjacent subdomain and vertex types.

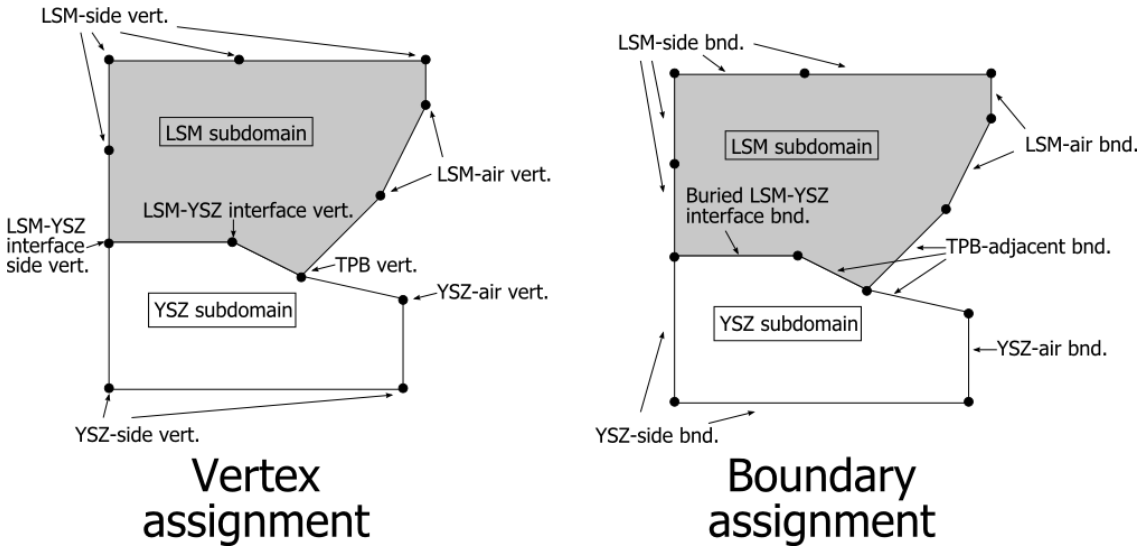

Figure 38: Schematic illustration of automated feature assignment. Vertices are assigned (left) based upon adjacently with subdomains and/or coordinates. Boundaries are then assigned (right) based upon adjacency with those vertices and the subdomains.

Once the geometric features were identified the next step in the scripting is to apply physics to them based upon their identities. A representative example is that of TPB edges. The set of all TPB edges was established in the previous identification step. The TPB rate expression was assigned to the set. Various model couplings that

depend on the TPB rate were associated with these subfeatures so that the coupled surface transport etc. were linked in an automated fashion.

6.3.3 Meshing and solution in 2D

The geometry was then meshed using the built-in COMSOL meshing functions with a free triangular mesh. The mesh elements could be on the order of voxel size or smaller near critical heterogeneous features such as TPBs and be much larger than the voxel size in the bulk away from interfaces. Rectangular mesh elements derived from the true voxel-by-voxel approach would by definition be very small even away from interfaces. After meshing, the problem was solved using one of the built-in nonlinear solvers. Solving and postprocessing were also automated using MATLAB script.

This method of solving the problem worked effectively in 2D cross sections. The microstructure was represented adequately and the solution converged. Figure 39 shows an example applied to a polished cross section from an SEM micrograph (see Figure 34). ImageJ software (developed by the National Institutes of Health) was used to threshold the micrograph into a binary image shown in Figure 39a. A portion of the binary image was converted using the custom script and the described procedure into the conformal COMSOL model with the geometry shown in Figure 39b, which demonstrates that the geometry was adequately represented. Figure 39c shows the mesh applied to the structure. Figure 39d shows the solution of a surface transport problem along the air-exposed boundary of the MIEC. The shaded line represents fractional absorbed surface oxygen concentration. The concentration is at its equilibrium value (red) on the surface far from the TPBs. It is depleted (blue) close to the TPBs reaching a minimum at the heterogeneous interface where the adsorbed oxygen is reduced.

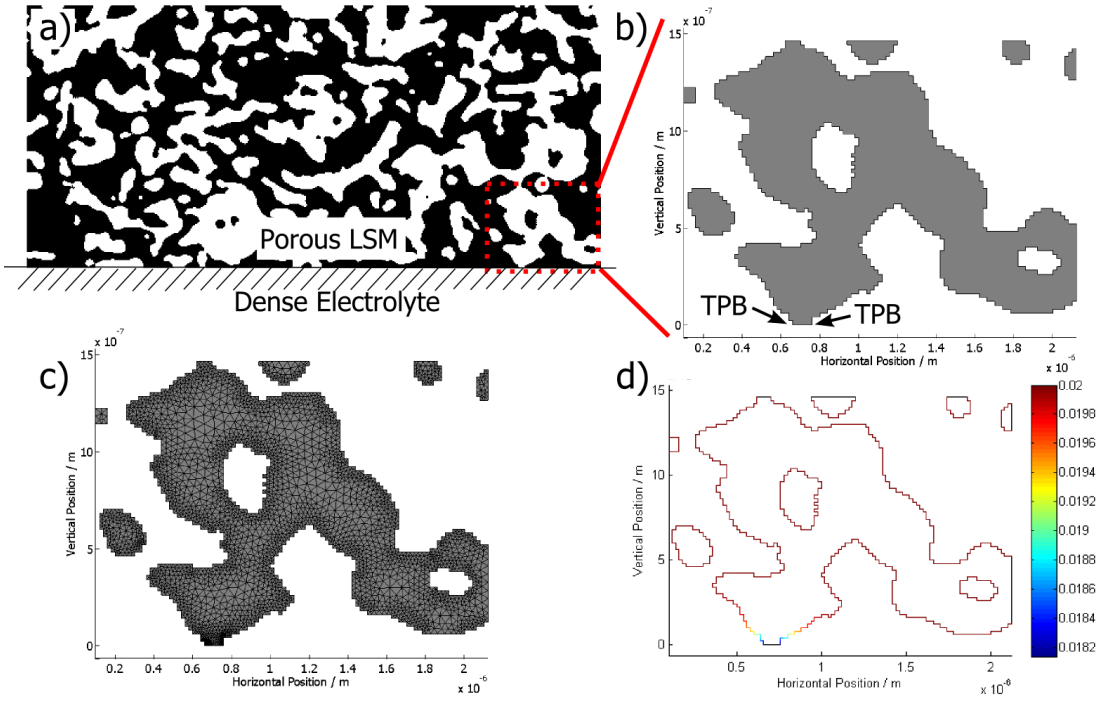

Figure 39: Implementation of the pseudo voxel-by-voxel method. a) Binary, thresholded polished SEM cross section (using original image in Figure 34) with LSM shaded white and pores shaded black. b) COMSOL model geometry of a portion of the binary image built from constituent binary pixels. c) Meshed microstructure. d) Simulated fraction adsorbed oxygen concentration on the surface of the porous LSM representation.

6.3.4 Extension to 3D

The pseudo voxel-by-voxel algorithm with consolidation was implemented in 3D. An example of a structure built using this consolidation is shown in Figure 40. Consolidation most often led to the formation of columns one or two voxels wide due to the irregularity of 3D particle shape.

Though successful in 2D the time required for compilation of the geometry was large in 3D. Most of that time was required for the creation and union of geometric primitives representing voxels and construction of the mesh. Unfortunately, the time requirement was prohibitive. This necessitated the use of a different approach that could run faster with less severe memory requirements.

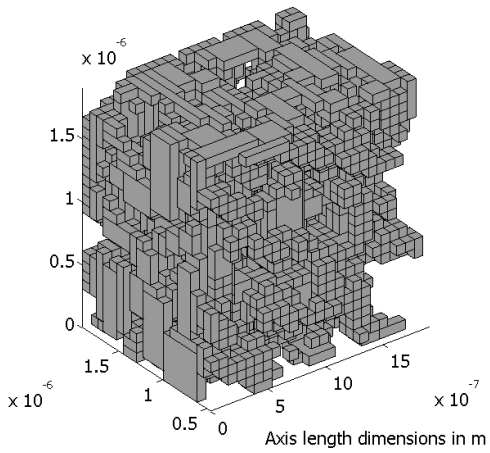

Figure 40: 3D microstructural reconstruction built using pseudo voxel-by-voxel method with consolidation.

6.4 Slice extrusion

As an alternative to constructing a 3D solid from component volume primitives, a method using the *Bezier polygon* feature in COMSOL was developed. A Bezier polygon is constructed from individual line segments defined by vertices forming a closed loop. The Bezier polygon can have convex or concave shape and can be quite complex depending on the number of constituent line segments that form its boundary. The Bezier polygons may then be extruded, providing an approximate representation of the 3D microstructure.

MATLAB script was written to trace particle boundaries from a 2D cross section image. An original image is shown in Figure 41a. The algorithm for the tracing chose one particle at a time and selected one starting point on the particle boundary. It proceeded around the boundary in a clockwise direction from boundary point to boundary point. Once a predetermined x- and y-distance from the starting vertex was reached, that vertex was made the end vertex of the first line segment. The next line segment started at the point and queried subsequent boundary vertices in the clockwise direction until the x- and y-conditions were reached for the ending vertex.

This process was repeated around the entire boundary of a particle until arriving again at the original starting vertex. The result was a Bezier polygon approximating the particle. This tracing process is demonstrated in Figure 41b. The constructed model geometry formed from Bezier polygons for the whole cross section is shown in Figure 41c.

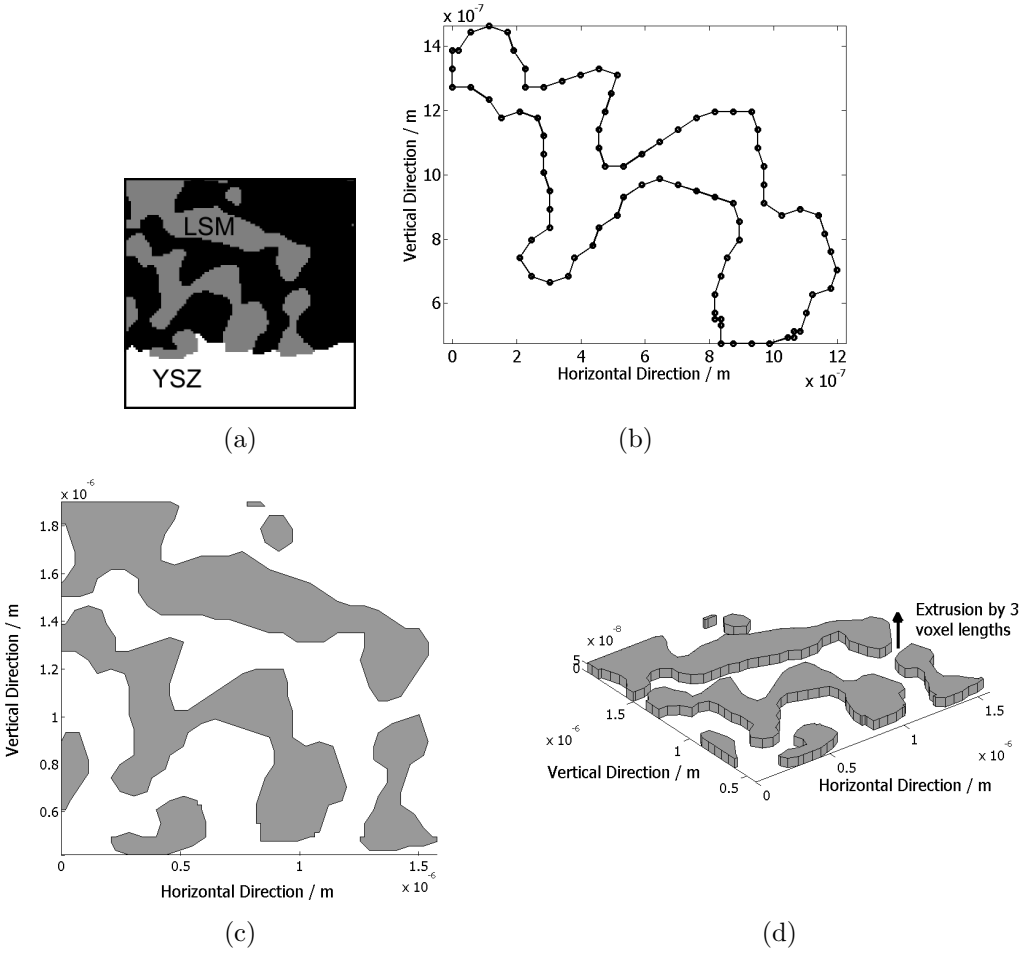

Figure 41: a) Original 2D x-ray microtomography slice from the near-interface region of the porous LSM-YSZ cathode. b) Bezier polygon tracing of a single 2D particle. c) Model geometry constructed from LSM particles approximated in 2D with Bezier polygons. d) Bezier polygons extruded by three voxel lengths.

After tracing the particles, the polygons were extruded in the z-direction using the built-in COMSOL work plane and extrusion features called by MATLAB script. The extrusion distance depended upon the accuracy desired for the 3D approximation. For

maximum accuracy the extrusion distance would be one voxel side length. Sacrificing accuracy for the ability to include a larger portion of the microstructure, the extrusion distance could be several multiples of the voxel length. Figure 41d shows an extrusion consisting of three voxel lengths. Another extrusion would then be stacked on the first extrusion and more extrusions subsequently stacked in order to reconstruct a fully 3D geometry. If the extrusion length is greater than one voxel length, information from intermediate slices is necessarily discarded.

Figure 42a shows the 3D geometry reconstructed by extruding slices. An artifact of the procedure was that the junction of the slice extrusions was sharp. The sudden changes force the surface mesh (Figure 42b and c) to be very fine in the regions close to the unions. Figure 42d shows the solution of a surface transport problem, which was successfully compiled and solved.

The method of slice extrusion was much faster in 3D than the pseudo voxel-by-voxel method. However, where the extrusions meet is often a sharp interface and creates unnecessary and inaccurate geometry complications, forcing the mesh to be much finer in these regions thus restricting the capability of this method. Since tracing the surface and approximating its features was successful in 2D, a method of analogously approximating the surface in 3D was desired. Using such an approach would eliminate the complications arising from sharp transitions between slices.

6.5 Direct reconstructive meshing

The standard process flow in COMSOL is to construct a geometry using built-in CAD tools or by importing a geometry from a CAD program, input physics and establish the domain of application, mesh, solve, and postprocess. The geometry step requires the user to draw a geometry with geometric primitives such as rectangles, circles, and prisms and/or with somewhat more sophisticated tools such as Bezier curves. This process flow is different from the flow of other FEM packages such as Abaqus or

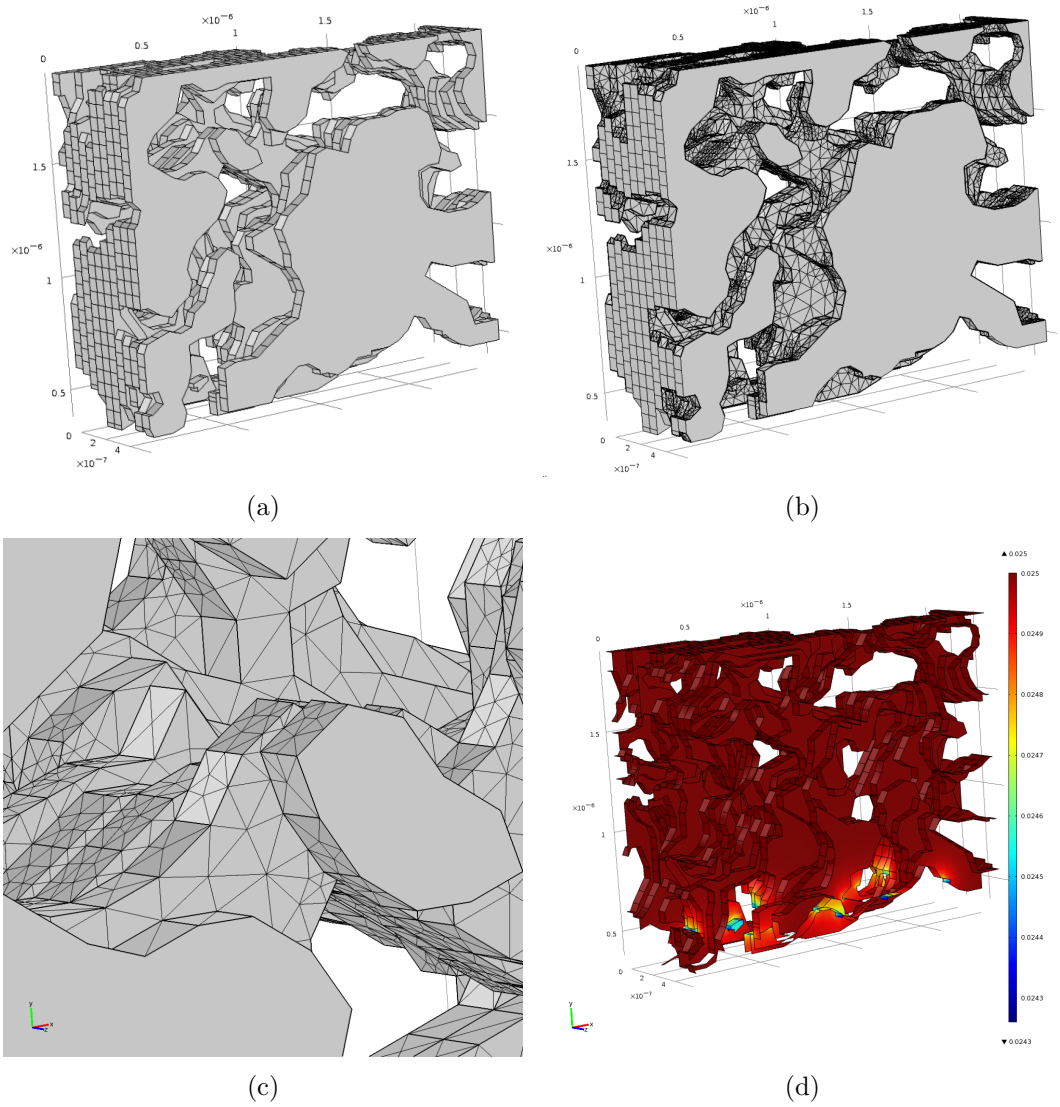

Figure 42: a) 3D reconstructed geometry built by extruding Bezier polygons on 2D cross sections. b) Surface mesh applied to the 3D reconstruction with a close view of a portion of it in c). d) Surface simulation result on the reconstructed microstructure. Axis length dimensions in m.

Nastran where the starting point is a mesh. The mesh used with those packages can can be generated by an external application such as Patran.

There are MATLAB commands available, however, to establish a mesh in COMSOL without the initial geometry step. Physics may be applied directly to a mesh built with these commands. The four key relevant commands are listed in Table 3.

The 'tet' argument creates a 3D tetrahedral mesh in the container *mesh*. The mesh

Table 3: COMSOL version 4.1 MATLAB interface commands for direct tetrahedral meshing.

Command	Role
mesh.data.setVertex(*vertex array*)	Create node array with coordinates in *vertex array*
mesh.data.setElem('tet', *elem. array*)	Create elements with nodes indexed to vertex coordinate array
mesh.data.ElemEntity('tet', *phase array*)	Assign subdomain number to elements
mesh.data.createMesh	Create mesh with the specified structure

can be made 3D hexahedral using 'hex', 2D triangular using 'tri', etc., with appropriate modification of the vertex coordinate dimension in *vertex array* and number and coordination of mesh nodes in *elem. array*. Once a mesh is constructed with these commands, physics may be applied to the subvolumes, boundaries, edges, and vertices as usual but without referring to a drawing object. The FEM problem may be solved without any additional meshing.

Direct meshing can be performed analogously to the voxel-by-voxel method using hexahedral elements derived directly from 3D volume microtomography data. This, however, leads to a very large number of elements. The reconstruction in Figure 35 is 101 voxels to a side, leading to solid-phase voxels numbering on the order of 10^6.

An alternative to direct voxel-to-hexahedron meshing is reconstructive tetrahedral meshing. The microstructure is approximated by the mesh rather than preserving all of the original data. This process can result in fewer mesh elements but preserve a satisfactory rendering of a particle volume and its surface.

Such a procedure is a challenging one, however. It requires first the meshing of a surface with triangular face elements. Then, a volume mesh is created for the interior using the surface triangular mesh as a base for tetrahedral volume elements adjacent to the surface, then meshing the rest of the volume with tessellating tetrahedra. The

algorithm for such a process is difficult and time-consuming to develop.

Fortunately, the open-source package *iso2mesh* was developed elsewhere for creating such volume meshes from MRI and CT data and provides the necessary functionality [44, 45]. This package is a toolbox assembled for MATLAB or Octave. Its core feature operates on a 3D data array of binary or grayscale voxels by reconstructing the surface as a triangular mesh and then forming a tetrahedral volume mesh from it. Though not developed for use with COMSOL, iso2mesh is directly compatible with it: it returns an array of node coordinates and list of element nodes and COMSOL's direct meshing feature requires the very same information.

COMSOL with iso2mesh is a combination of commonly available software packages that performs the difficult task of meshing and solving a microstructure-conformal FEM problem. The possibility of error is minimized due to the rigor involved in developing wide-release packages. Furthermore, any procedures developed for dealing with porous electrodes are portable and widely usable. In order to apply the physics specific to this problem, though, there is custom coding that must be performed but it is minimized by these packages.

6.5.1 Mesh parameters, quality, and modification: test geometries

Prior to applying the packages onto microstructure, some assessment of the mesh quality is important. The mesh should be sufficiently fine to capture the important details but coarse enough to minimize processing time and memory usage. Section 6.5.1.1 describes the effort to understand the meshing parameters leading to the best description of single-phase microstructure. Section 6.5.1.2 describes the assessment of heterogeneous interfaces between the active phase and electrolyte. Some modification of the mesh was necessary in order to provide a physically accurate representation of the interface and several methods for locally modifying the mesh are detailed.

6.5.1.1 Single-phase meshing

The test geometry should provide easy calculation of ideal surface area and volume to which the surface area and volume of the generated mesh can be compared. Simple 3D geometric shapes divided up into voxels are useful for this task.

Particles are usually thought of as spheres and porous electrodes are often approximated by packing spheres together. Spheres are therefore the first and most obvious choice for test shapes. The division of spheres into voxels presents a challenge, though, because the size of the voxels determines the agreement of volume and surface area with the ideal shape. As the voxel size gets smaller, the volume and surface area of the voxelated object approaches that of an ideal surface but never quite equals it as long as the voxel length is nonzero and the surface is curved.

The microtomography data provided for the porous LSM electrode is restricted to a certain voxel size (19 nm) and is therefore not subject to optimization. Only this voxel size is of interest. It would be difficult to compare a mesh generated from a 19-nm voxelation of a sphere to the ideal sphere values because the voxelation step introduces some error.

Rectangular prisms of integer voxel side length were chosen for this task because the voxelated structure is identical to the ideal structure. Volume data was generated and passed to the *vol2mesh* function, part of the iso2mesh package. The volume and surface area of the generated mesh were then computed and compared with the ideal prism values.

The meshing parameters passed as arguments to the vol2mesh function determine the characteristics of the produced mesh. The *threshold* determines how the boundary between different phases is placed. When using binary data where 1 represents a solid voxel and 0 represents a pore voxel, the threshold should be a fractional value in the interval [0,1]. Closer to 1 moves the interface nearer to the solid phase, closer to 0 moves it nearer to the pore. A value of 0.5 places the interface evenly between the

two phases when the surface is flat but can lead to corners and edges being cut off. A threshold slightly lower than 0.5 compensates for lost corners and edges. A second parameter is *maximum triangle size*, which determines how large the triangles in the surface mesh may be. The third parameter is *maximum tetrahedron volume* which determines how large the tetrahedral elements inside the volume may be.

Several test prisms were used to evaluate the meshing. The first was a prism comprised of 10 x 10 x 10 voxels, which represents a particle with small aspect ratio having a feature size of approximately 190 nm. A second prism was comprised of 5 x 5 x 50 voxels, representing a particle with large aspect ratio 95 nm wide and 950 nm tall. These prisms are meshed with varying degrees of fineness in Figures 43 and 44, respectively. The fidelity of the reconstruction is very good with a maximum triangle size of 1 and degrades as the triangle size increases. More elements and node points, or course, are required with the finer meshes leading to higher quality. A desirable set of mesh parameters is one that uses the minimum number of elements required to provide sufficient fidelity. An initial qualitative inspection suggests that a maximum triangle size of 1.5 or 2 with threshold of 0.3 may meet this requirement. Larger prisms were also examined: 20 x 20 x 20 (380 nm to a side) and 50 x 50 x 50 (950 nm to a side). Allowable surface element size was larger than 1.5 or 2 in these cases: 3 or 4 is suitable.

The test prisms were meshed with various parameters using vol2mesh a "dummy" COMSOL model was established in the meshed geometry using simple physics and integration coupling variables. The integration coupling variables accurately determined surface area and volume of the meshed object by integrating a scalar value of one over the subdomain or all surfaces, respectively. The results of the dummy simulation were discarded, except for the volume and area data.

Figure 45 shows these computed quantities as a function of surface element size. Several binary thresholds were examined. The solid horizontal line indicates the

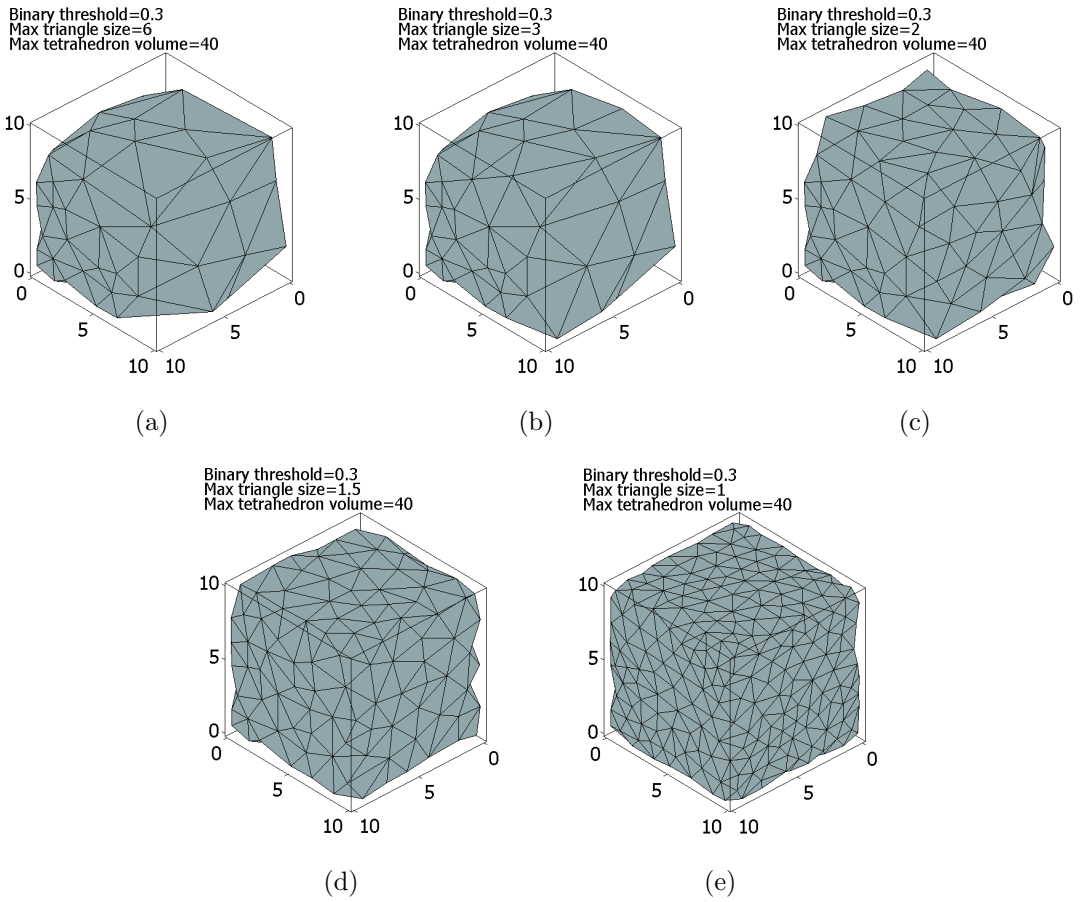

Figure 43: Single-phase 10 x 10 x 10 prism meshed with progressively finer meshing parameters.

volume or surface area of the ideal prism, while the dashed lines represent 10% above or below ideal. Each binary threshold value has a range of maximum face triangle sizes which cause the volume and surface area of the meshed structure to be within 10% of ideal. The vol2mesh function is therefore capable of producing an acceptable representation the test structures.

Generally a lower threshold allows a coarser mesh to be used and still have an adequate surface area and volume. Low-aspect-ratio structures are less sensitive to the meshing parameters. The 5 x 5 x 50 prism (Figure 45c and d) meshing failed to render part of the structure using triangle size between 4 and 6 depending on the threshold whereas the meshing of the 10 x 10 x 10 prism (Figure 45a and b) did not

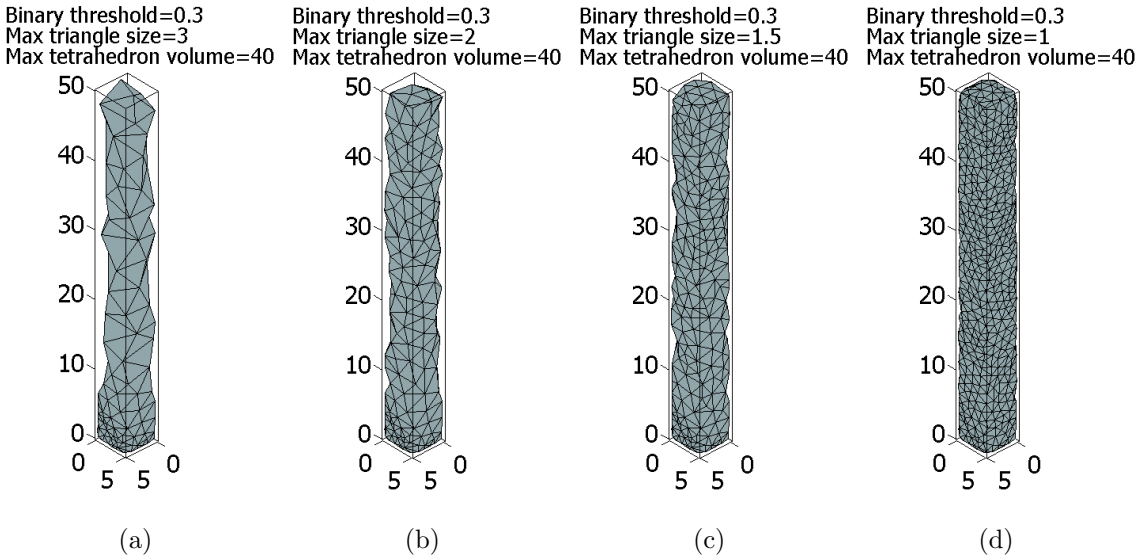

Figure 44: Single-phase 5 x 5 x 50 prism meshed with progressively finer meshing parameters.

fail. Larger structures are less sensitive to mesh parameters than smaller structures - a 50 x 50 x 50 prism (Figure 45g and h) does not have as much variance as a 10 x 10 x 10 prism. In fact, surface triangle size up through 6 produces adequate results for the 50 x 50 x 50 prism. The same is true to a lesser extent for the 20 x 20 x 20 prism (Figure 45e and f), which gets reasonable results with a triangle size of 3 or 3.5. Thresholds of 0.3 and 0.4 with triangle sizes of 1.5 or 2 produced adequate results for all of the structures, demonstrating a compromise between fidelity and element size. Larger triangle sizes may be used for geometric features above approximately 10 voxels to a side.

6.5.1.2 Heterogeneous interface meshing

After establishing satisfactory parameters for the meshing of a test particle consisting of one phase, the meshing of two-phase structures was examined. The same test prisms were used but were divided into two subdomains based upon the y-coordinate of element centroids. If the centroid was below a certain y-value it was assigned to "phase 1", which represented YSZ. Those elements with centroids above the y-value

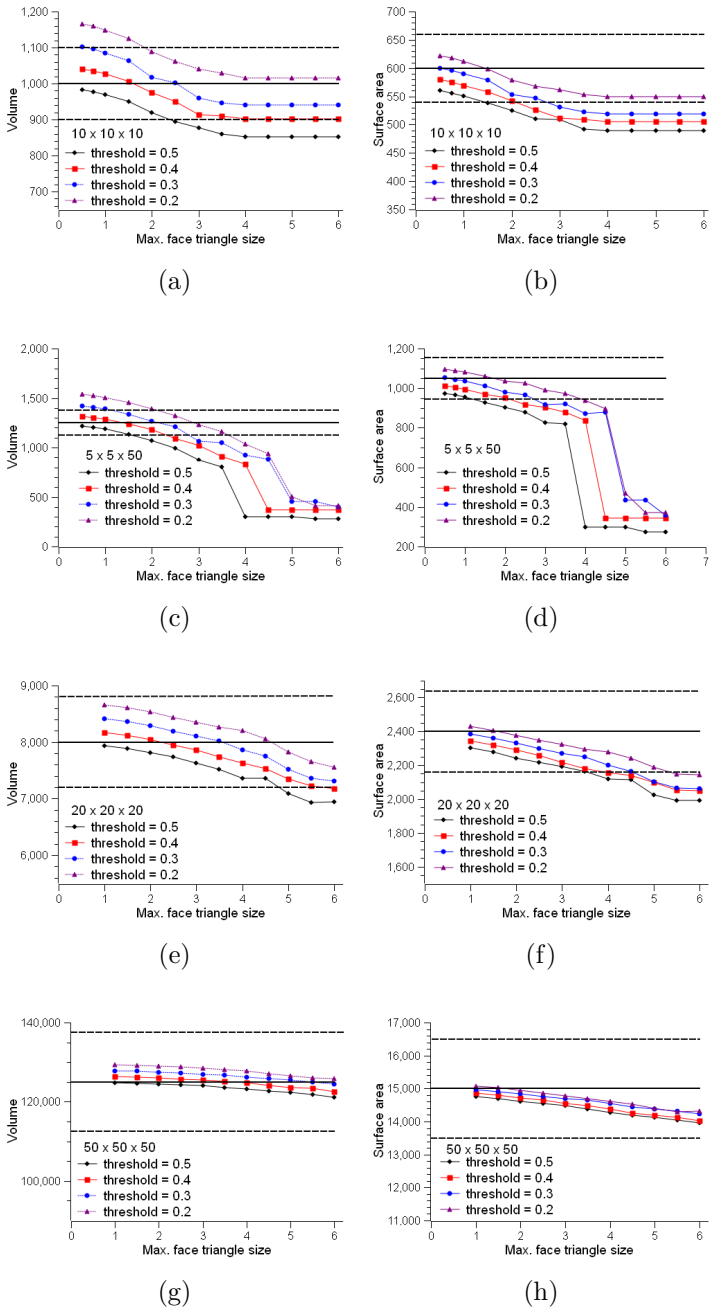

Figure 45: Single-phase mesh characteristics a) 10 x 10 x 10 voxel prism volume, b) 10 x 10 x 10 voxel prism surface area, c) 5 x 5 x 50 voxel prism volume, d) 5 x 5 x 50 voxel prism surface area, e) 20 x 20 x 20 voxel prism volume, f) 20 x 20 x 20 voxel prism surface area, g) 50 x 50 x 50 voxel prism volume, h) 50 x 50 x 50 voxel prism surface area.

were assigned to "phase 2" representing LSM.

This method of assigning elements produced acceptable partitioning of the volume and surface area between the phases. Despite the good agreement between volume and surface area, however, the phase 1-phase 2 interfacial area was larger than expected. The error was caused by the method of assigning the elements to their respective subdomains. The use of element centroids leads to a jagged interface where elements with centroids just above or just below the ideal interface line were assigned to different phases and the faces they shared in common became the phase interface.

Parts a and b of Figure 46 show the roughness of the interface after meshing. Part a demonstrates the jaggedness of the TPB line on the sides of the prisms. Part b gives a side view of the prisms using transparent mesh faces so that the interface between the two phases is seen by "looking through" the structure. In both sets of images phase 2 is highlighted in red while phase 1 is white. The interface is where they meet.

For an electrochemical system where the surface pathway is important, accurately representing the TPB is important. Furthermore, the capacitive response in AC impedance spectroscopy is in large part determined by the interfacial area and accurately representing it is important as well. A method of correcting the interface representation was developed to try to optimize the interface representation.

Meshing both phases at once and then assigning elements to either phase was the only practical method of handling the heterogeneous interface. Meshing either phase separately leads to nodes with disparate coordinates and elements that do not share the same nodes. There is no registry between the two separate meshes, which means there can be no coupling of the physics. Custom code could be written to force registration, but would be very complicated and defeat the purpose of using commonly available commercial and/or open-source software tools.

Instead of writing a complicated custom script, a simpler script was written to

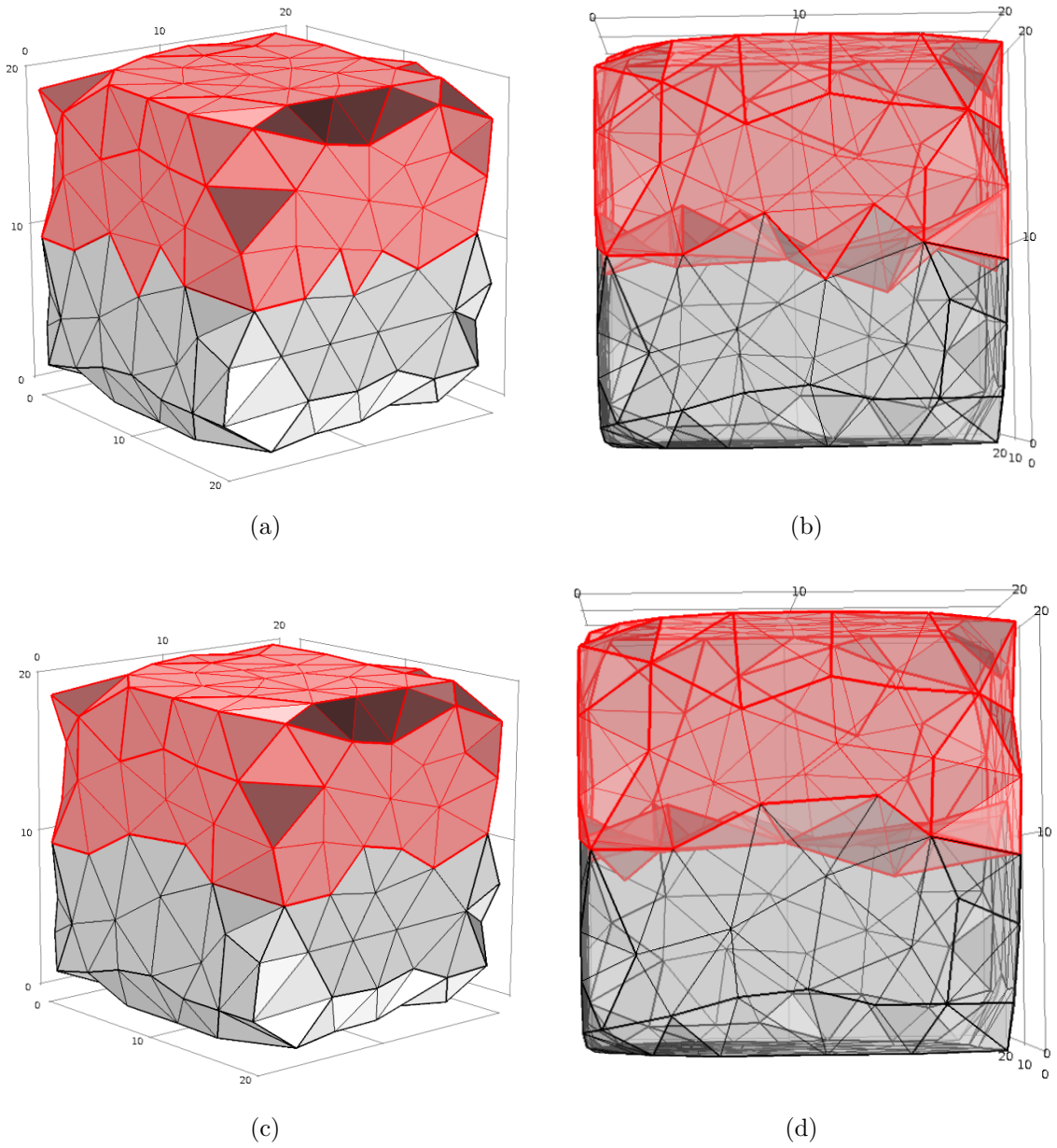

Figure 46: Two-phase meshed 20 x 20 x 20 prism with one of the two phases highlighted. Prism with no additional interfacial processing: a) surface mesh view, b) side transparent view showing interfacial roughness. Prism with all interfacial operations applied: c) surface mesh view showing smoother TPB line, d) side transparent view showing reduced interfacial roughness. Threshold = 0.4, max. triangle size = 3.

take the one mesh, divide it into two phases, and correct the interface. In this way the advantage of using the software package was preserved with only minimal modification made by custom code. The ultimate outcome of this effort produced a

smoother interface, depicted in parts c and d of Figure 46.

Several methods were developed in order to achieve these results. The first method involved interface smoothing. Nodes belonging to projections of one phase into the other were moved towards the ideal interface line to reduce roughness. A 2D schematic illustration consisting of two triangles of the electrode (gray) phase is depicted in Figure 47a. The dark circle labeled A represents the node they share with the adjacent electrolyte elements. The star represents the average of the centroids of the two triangles that comprise the projection. The nodes labeled B are adjacent non-interface nodes. The smoothing method consisted of moving the shared node A toward the average of the element centroids by some fraction ("smoothing fraction') of the line connecting them, depicted in Figure 47b, where node A is moved from its previous location (dashed circle) to a new one. Performing this operation smooths a jagged interface but does not change the phase affiliation of adjacent elements.

Care was required in order to avoid degrading the mesh element quality by creating self-intersections or increasing element aspect ratios to unacceptable levels. A large smoothing fraction tended to move nodes in such a way that element quality was reduced. If large enough, nodes could be moved so far that adjacent elements became inverted, causing mesh self-intersections. A smoothing factor of up to 0.2 (meaning that a projection node was moved 20% of the distance between its original position and the average of the element's centroids) produced significant effects on the interfacial roughness without harming element quality. A factor of 0.3 or above tended to degrade quality.

In addition to moving only the node at the tip of the projection of buried interfaces (node A in Figure 47), two other strategies were attempted. Adjacent non-interface nodes, labeled B in Figure 47, were moved at the same time as node A. These nodes were shifted along the same vector as node A, although only a portion of the distance. The goal was to preserve element aspect ratio. Unfortunately, moving the adjacent

nodes had the effect of tending to cause mesh self-intersections.

Smoothing of the TPB lines along the surface (as opposed to the interior two-phase interface) was also attempted. The surface nodes were moved in a direction in the plane of the surface in order to avoid creating or destroying volume and distorting the shape of the meshed solid. Despite being effective at creating a smoother TPB line, when employed in conjunction with smoothing of the buried interface this method also tended to cause mesh self-intersections.

The smoothing method was restricted to a factor of 0.2 and applied only to the tips of projections along the buried electrolyte-MIEC interface. This method was effective at reducing interfacial roughness and was reliable at preserving mesh quality as well.

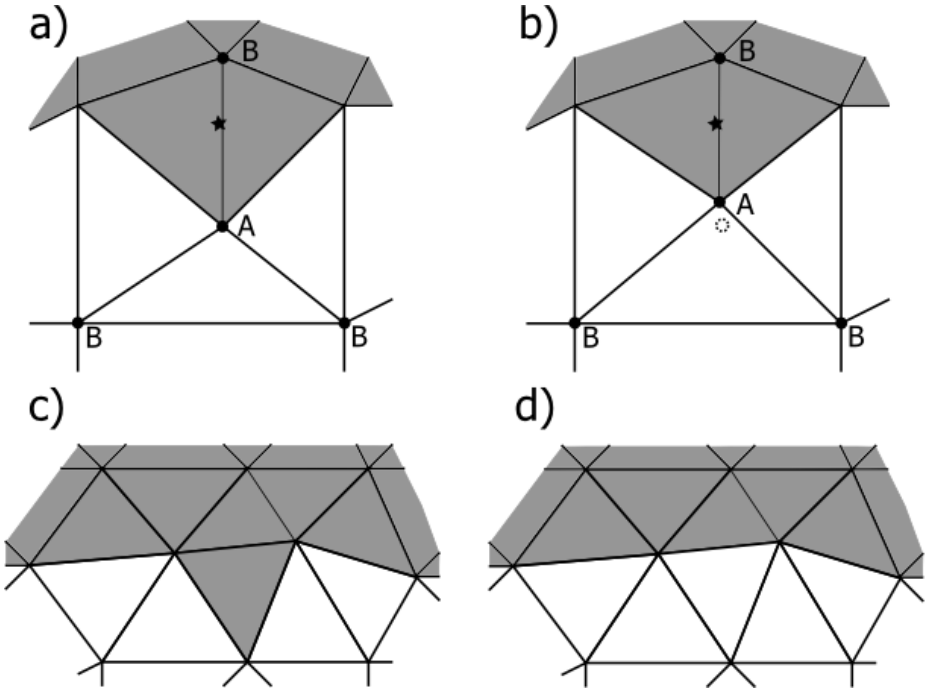

Figure 47: Methods of correcting a meshed heterogeneous interface. Schematic drawing of smoothing: a) interface prior to smoothing, b) interface after smoothing. Schematic drawing of ceding: c) interface prior to ceding, d) interface after ceding.

Another group of methods to correct the interface was called projection ceding wherein obvious convex projections of one phase into the other were reassigned in

order to reduce interfacial area. A schematic illustration of this procedure is given in Figure 47c and d, depicted in 2D. A projection of the electrode phase (gray) that creates an unnecessarily jagged TPB line is identified in part c and ceded to the electrolyte phase (white) in part d. The effect of ceding either was to reduce the roughness of a jagged interfacial plane/line or produce a more realistic and accurate buried electrolyte/electrode phase boundary. Some change in the relative volume of either phase did result because element phase affiliation is altered, but was minor compared with the impact on the fidelity of the interface/TPB representation.

Several types of interfacial ceding were attempted. A major source of interfacial roughness was single tetrahedral elements of one phase sharing three faces with the other phase along the buried interface. These elements are referred to as single-element protrusions. To fix them, single protrusions were simply reassigned ("ceded") to the phase with which they share three faces. Similarly, groups of two elements protruding into the other phase (double-element protrusions) were also an important source of excess roughness. These elements were ceded to the other phase as well. Projections consisting of more than two elements (multi-element protrusions) did not always increase interfacial roughness. Multi-element protrusions were ceded only when doing so would reduce the interfacial area.

Similar logic was applied on the surface as along the buried interface. The underlying tetrahedral element of surface triangles sharing two edges with the other phase were ceded. Due to the prevalence of these surface protrusions, ceding had to be undertaken one phase at a time: first phase 2 protrusions, then phase 1. Occasionally, extra surface interface lines ("orphan TPBs") were produced by this procedure and the underlying elements causing them were ceded to the other phase as well.

Unique operations were also implemented on the surface. If there were isolated phase 2 tetrahedra on the surface (elements assigned to phase 2, but sharing no faces with other phase 2 elements), they were ceded to phase 1. Also, phase 2 elements

along the surface interface with two air-exposed faces, and zero or one surface edges adjacent to phase 2 were ceded to phase 1. These elements were termed "ramps".

In addition to simply dividing the test prisms into two phases, a more realistic test structure was also employed, depicted in Figure 48. A 20 x 20 x 20 voxel prism was placed on a much wider prism. The 20 x 20 x 20 voxel prism was assigned to phase 2, while the wider prism was assigned to phase 1. This was meant to approximate an LSM particle sintered to the surface of the YSZ electrolyte. The ramp elements described in the previous paragraph are visible in Figure 48a. They contribute extra roughness to the TPB line as part of phase 2 and therefore can be reassigned as shown in Figure 48c, thus reducing excess TPB line length and more accurately representing it.

For best effect, these two types of operations were combined in various ways. Table 4 contains a list of the operation combinations, identified by an operation number. The effect of the various procedures is shown by the line charts in Figure 49 for the different simple test prisms divided into two phases. The x-axis displays the operation number and the y-axis displays either TPB length or interfacial area. The horizontal solid line again indicates the TPB length or interfacial area of the ideal prism. Both interfacial and TPB ceding are generally effective at reducing interfacial area and TPB length, respectively. Likewise, interfacial smoothing is also effective. Combining both methods together (operations 6 and 7) are the most effective at producing an accurate interface. The ceding of multi-element protrusions has a tendency to reduce interfacial roughness, but can increase the TPB length. This effect may be seen in comparing operation 5 to operation 4 operation 7 to 6.

The same trends were apparent when the various operations were applied to the test prism on the wider electrolyte. Figure 50 shows the trend of TPB length and interfacial area for the 20 x 20 x 20 prism placed on the wider electrolyte. In general, the interfacial correction operations were effective for reducing TPB length and

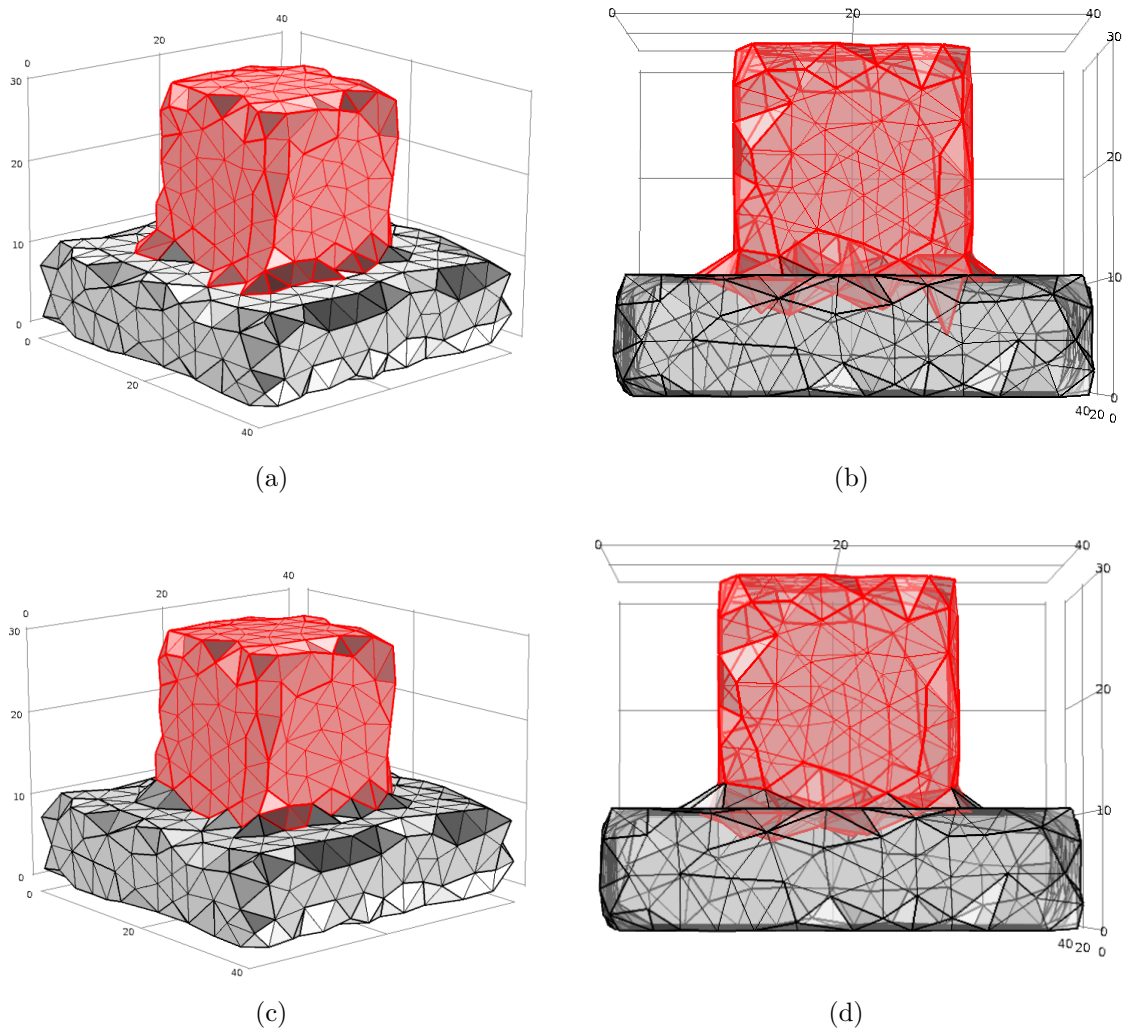

Figure 48: Two-phase meshed 20 x 20 x 20 prism on a wider electrolyte with one of the two phases highlighted. Prism with no additional interfacial processing: a) surface mesh view, b) side transparent view showing interfacial roughness. Prism with operation 6 interfacial corrections applied: c) surface mesh view showing smoother TPB line, d) side transparent view showing reduced interfacial roughness. Threshold = 0.4, max. triangle size = 3.

interfacial area toward their ideal values.

Figure 46 and 48 parts c and d show the interface corrected with operation number 6. The procedure involves first ceding the single- and double-element protrusions on the buried interface, then ceding surface protrusions (phase 2 then phase 1), ceding protrusions along the buried interface again, and then ceding orphan TPBs created by the process. The resulting buried interface is finally smoothed using the smoothing

Table 4: Electrolyte-MIEC heterophase interface smoothing operations.

Operation number	Operation action
0.	no processing
1.	smooth interface (factor = 0.2)
2.	cede isolated phase 2 elements, process ramps
3.	2 then cede (interface: single- and double-element protrusions)
4.	2 then cede (surface: ph. 2 then ph. 1), cede (interface), cede orphan TPBs
5.	4, then cede (interface: multi-element protrusion if favorable)
6.	2, cede (interface: single, double), cede (surface: ph. 2 then ph. 1), cede (interface), cede orphan TPBs, then 1
7.	2, cede (interface: single, double), cede (surface: ph. 2 then ph. 1), cede (interface), cede orphan TPBs, cede (interface: multi), then 1

procedure.

The interface correction was effective for small and large objects. Figure 49e and f show that adequate smoothing was achieved even for a surface triangle size of 3 and 3.5 in the 20 x 20 x 20 prism. Figure 49g and h show that adequate smoothing was achieved over a wide range of surface mesh element sizes for the largest object: triangle size of 1.5, 2, and 6 in the 50 x 50 x 50 prism.

6.5.1.3 Test geometry summary

Using the iso2mesh functions, it is possible to reconstructively mesh structures approximating those that might be found in a microstructure. Several test structures with different aspect ratios and sizes were used. The structures had side length of a number of voxels that might be expected in a microstructure. Good agreement between expected volume and surface area can be achieved using meshing parameters consisting of threshold = 0.3 or 0.4 and maximum surface triangle size depending on the characteristic object feature size. A surface triangle setting of 1.5 or 2 is required

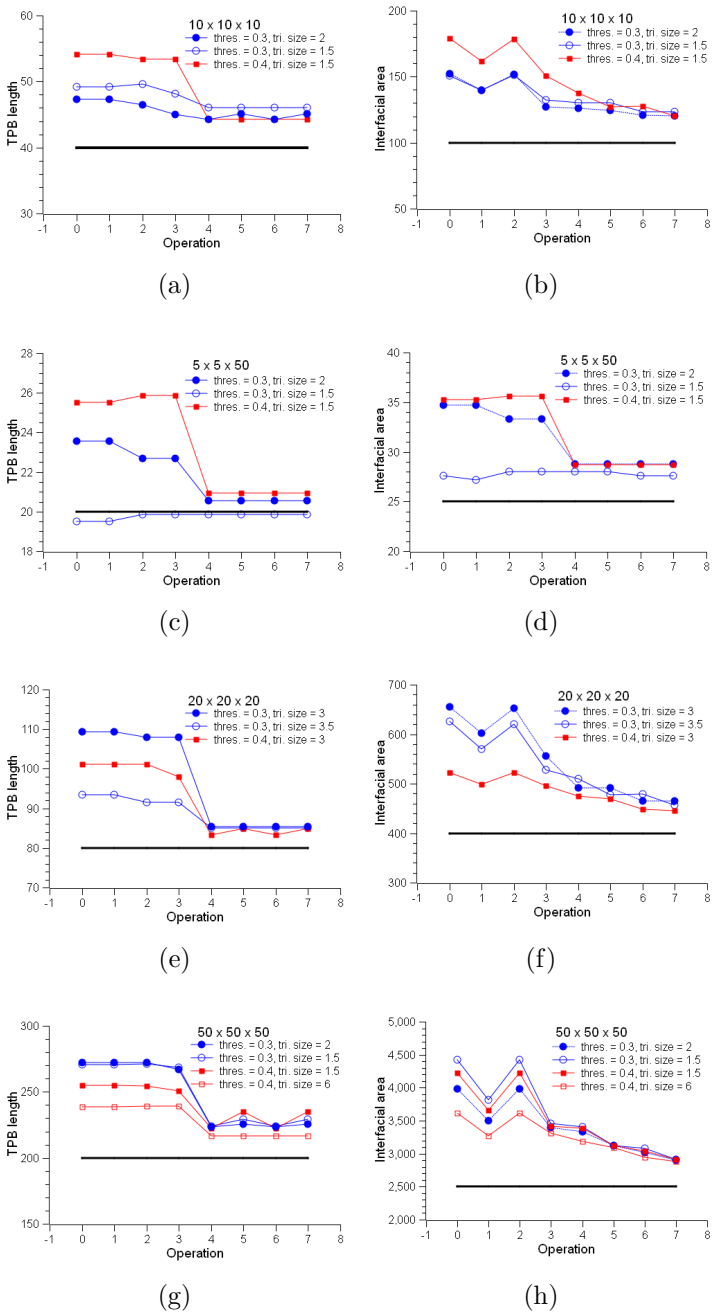

Figure 49: Two-phase mesh characteristics for simple test prisms divided into two phases a) 10 x 10 x 10 voxel prism TPB length, b) 10 x 10 x 10 voxel prism electrolyte-MIEC interface area, c) 5 x 5 x 50 voxel prism TPB length, d) 5 x 5 x 50 voxel prism electrolyte-MIEC interface area, e) 20 x 20 x 20 voxel prism TPB length, f) 20 x 20 x 20 voxel prism electrolyte-MIEC interface area, g) 50 x 50 x 50 voxel prism TPB length, h) 50 x 50 x 50 voxel prism electrolyte-MIEC interface area.

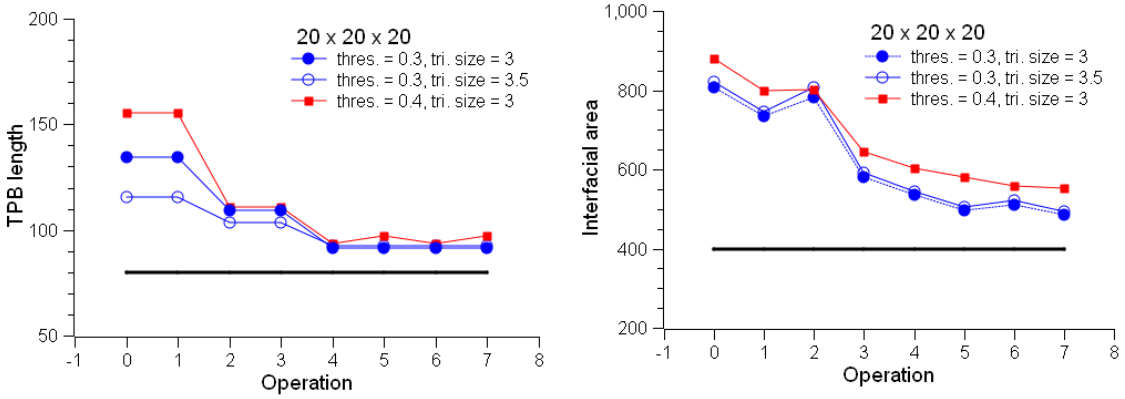

(a) (b)

Figure 50: Two-phase mesh characteristics for a 20 x 20 x 20 prism on a wider electrolyte: a) TPB length, b) electrolyte-MIEC interface area. Threshold = 0.4, max. triangle size = 3.

when the features are 5 -10 voxels to a side. A value of 3 or 3.5 may be used if the features are 20 voxels to a side. A value of 6 or greater may be used for features 50 to a side. When dividing the structure into distinct phases, interfacial correction is required. A combination of projection ceding and node smoothing is capable of reducing superfluous interfacial roughness and producing a physically reasonable interfacial reconstruction suitable for simulations involving heterogeneous interfacial electrochemical reactions.

6.5.2 Mesh parameters, quality, and modification: microstructural representation

A 30 x 34 x 30 voxel (570 nm x 665 nm 570 nm) section of the 3D reconstructed microstructure was used to examine the effect of mesh parameters on the accuracy and fidelity of the mesh when applied to actual morphologies. Two views of the microstructure are shown in Figure 51a and b. The two views of the microstructure are shown meshed without any additional interfacial correction in Figure 51c and d. Figure 51e and f shows the mesh after interfacial correction.

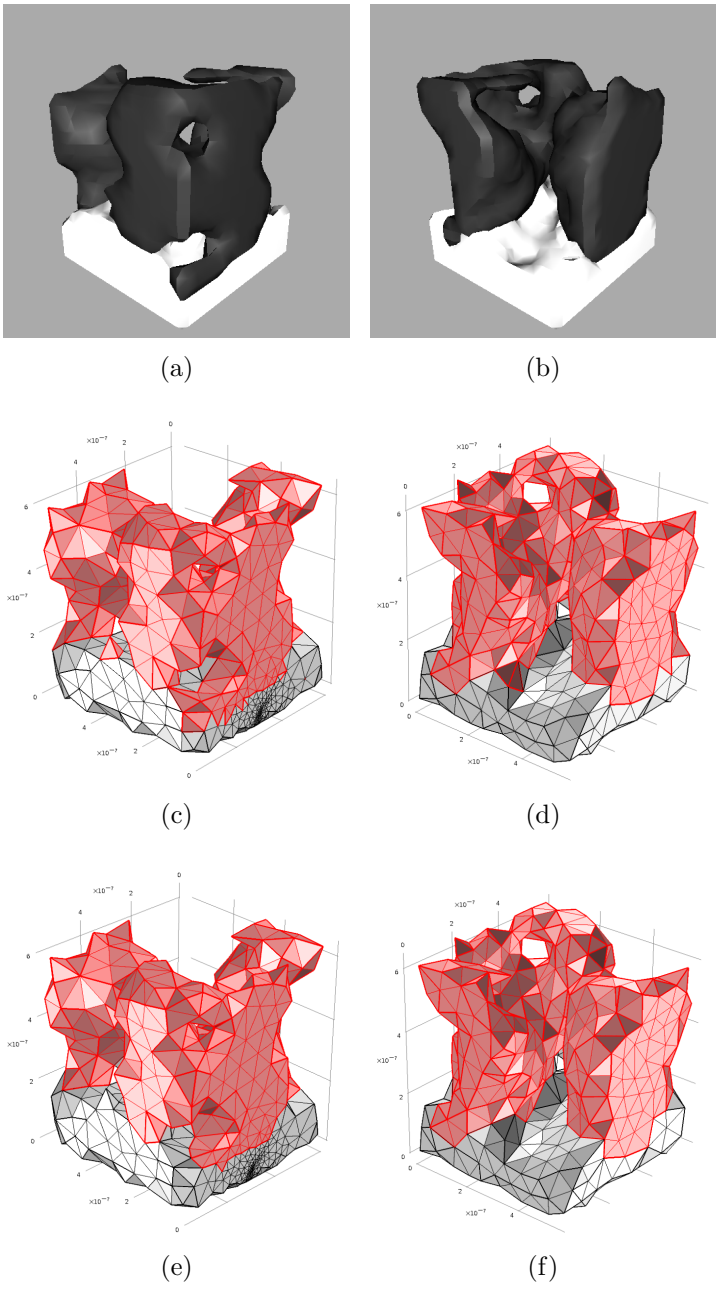

Figure 51: a) and b) Two views of the microstructural segment used for evaluation of the mesh. c) and d) The same structures, meshed with threshold = 0.4, maximum surface triangle size = 3, maximum element size = 40. e) and f) Meshed microstructure with operation 6 interfacial correction applied.

A script was written to calculate the volume, air-exposed LSM surface area, LSM-YSZ interfacial area, and the TPB length from the original voxel data from the mesh imported to COMSOL. Plots of LSM volume, air-exposed LSM surface area, TPB

length, and LSM-YSZ interfacial area are given in Figure 52 (without interfacial correction). The solid horizontal lines indicated the voxel-derived values and the dashed lines represent 10%. There was very good agreement between voxel-derived and mesh volumes in Figure 52a, following a trend very similar to that of Figure 45. Thresholds of 0.3 and 0.4 provided very reasonable volumes at surface element sizes of 3 to 4. This result is in agreement with the 20 x 20 x 20 voxel test prism. The air-exposed surface area was less than the voxel-derived value. This discrepancy was expected because the voxels are an approximation of curved surfaces and introduce artificial roughness which increases the boundary area. Computing voxel phase is an inherently volume-based process, so no similar discrepancy appears in the volume data.

Without interfacial correction, the TPB length and LSM-YSZ interfacial areas were high compared to the voxel-derived values (Figure 52c and d). The voxel-derived values suffered from inflation caused by voxel roughness. Therefore, the TPB length and interfacial areas produced by the mesh were even higher compared to ideal than the comparison with the voxel-derived values would suggest (c.f. air-exposed surface area in Figure 52b).

The role of maximum tetrahedral element size is shown in Figure 53 where the total LSM volume is plotted as a function of triangular face element sizes for different values of binary threshold. The differences in the total volume of the meshed structure when different maximum tetrahedron sizes were used were very small for each of the threshold examined. Small differences were present for the other metrics such as air-exposed surface area. These results suggest that the quality of the mesh is not substantially influenced by the maximum tetrahedron size.

Good agreement of mesh volume with the voxel-derived volume and the adherence to the expected discrepancy in air-exposed surface area suggested that the fidelity of the mesh far from the heterogeneous interface was good. That is, single-phase

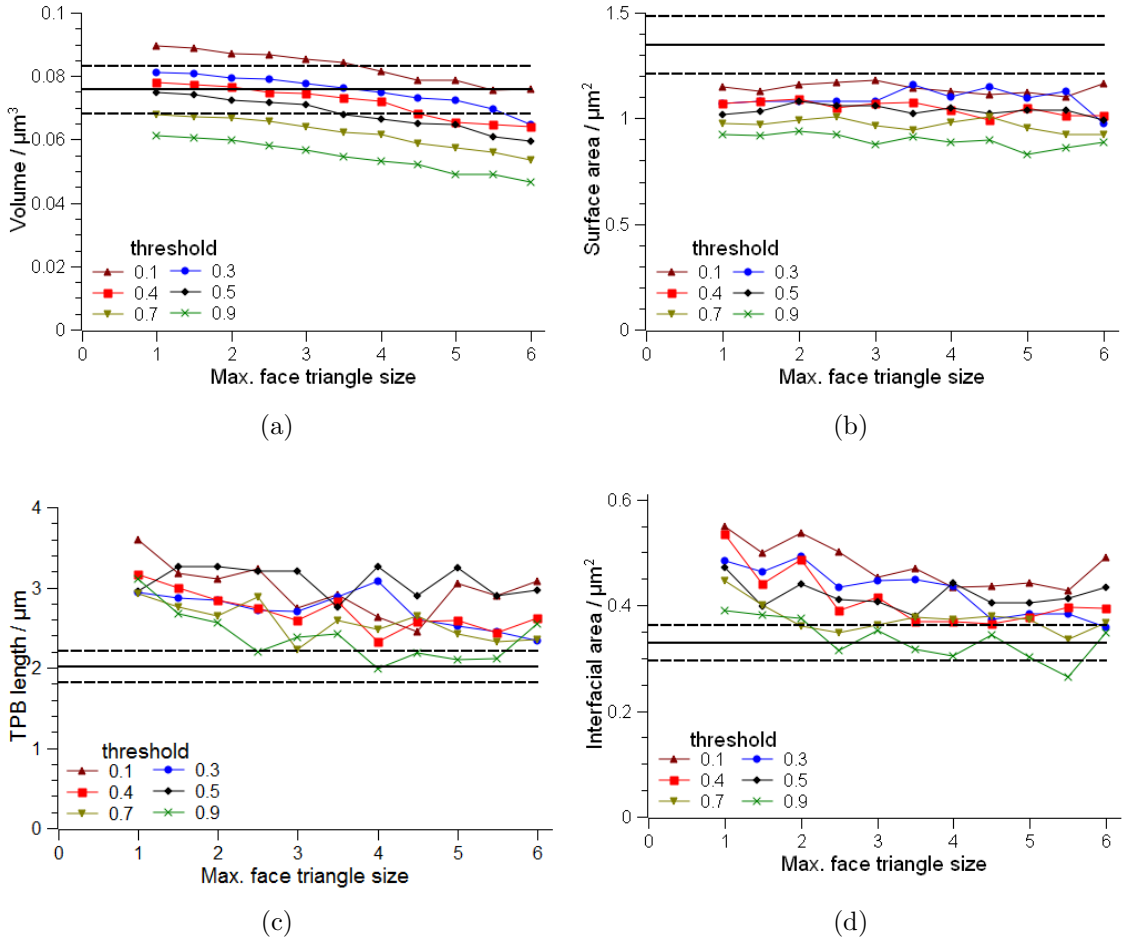

Figure 52: Mesh quality assessment applied onto actual microstructure reconstruction without interfacial correction as a function of surface element size using various binary thresholds: a) LSM volume, b) air-exposed LSM surface area, c) TPB length, d) LSM-YSZ interfacial area. Solid horizontal line represents voxel-derived value and dashed lines indicate ±10%. Maximum tetrahedral element volume = 40.

meshing was accurate and could be implemented with a threshold of 0.3 or 0.4 and a mesh size of 3 to 4. The large values of TPB length and interfacial area, however, indicated the need to deploy the mesh correction algorithm developed for the test geometries in Section 6.5.1.2. The interfacial correction operations enumerated in Table 4 were applied to the microstructure meshed under various parameters. The results are shown in Figure 54e and f. The interfacial correction operations removed superfluous surface elements and caused the mesh to be more representative of the actual microstructure depicted in parts a and b, both qualitatively and quantitatively.

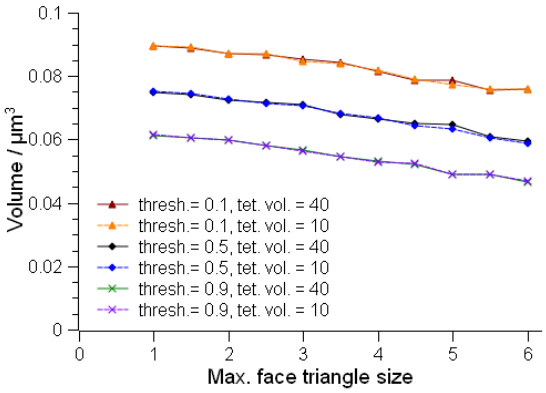

Figure 53: Effect of maximum tetrahedron element volume upon the total LSM volume of the meshed microstructure.

The interface correction schemes were generally effective for removing excess roughness from the TPBs and buried interface. The smoothing (operation 1) did reduce interfacial area. The different element ceding schemes were effective for reducing both quantities. The multi-element ceding operation had mixed effects, reducing interfacial area, but increasing TPB length. The most effective all-around operation appears to be operation 6, which while allowing slightly higher interfacial area than operations 5 and 6 produces TPB length much closer to the voxel-derived value. Images of the microstructure smoothed with operation 6 are given in Figure 51.

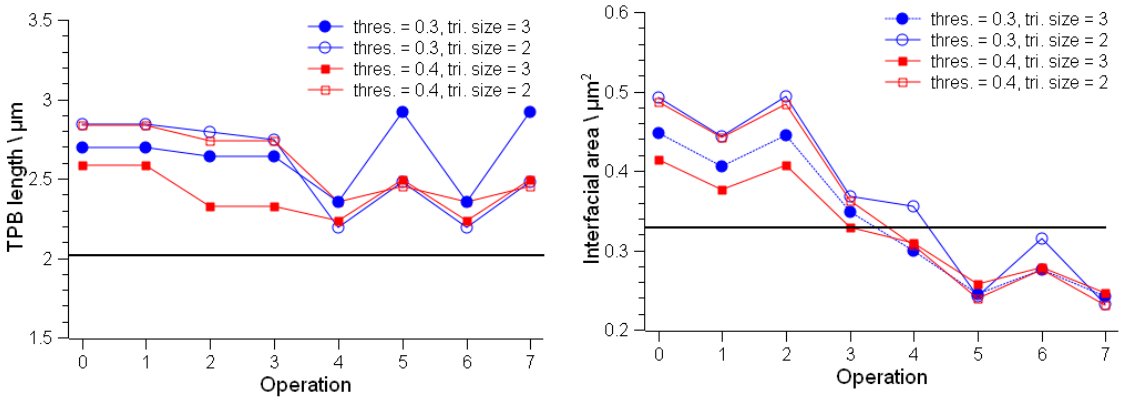

(a) (b)

Figure 54: Effect of smoothing operations applied to the meshed microstructure: a) TPB length, b) electrolyte-MIEC interfacial area.

6.6 Simulations in the bulk

The mesh allows for both finite element simulations on the surface of the mixed conductor involving adsorbed gas as well as finite elements simulations within the mixed conductor involving the transport of point defects. The necessary considerations for bulk simulations are derived in this section. Simple kinetics for the overall oxygen reduction reaction based on linear irreversible thermodynamics are used to eliminate some of the complexity and uncertainty arising from phenomenological reaction rates.

6.6.1 Transport

For LSM, there are several principal point defects including electron holes, electrons, oxygen vacancies, and vacancies on both the La- and Mn- sites. For the sake of tractability, the cation vacancies are assumed here to be immobile. For the sake of simplicity, electronic transport is assumed to be facile. Therefore, a uniform Fermi level will be enforced everywhere, in the form of constant electron electrochemical potential within the microstructure. The electrochemical potential of electrons is related to that of electron holes by

$$\tilde{\mu}_{\mathrm{e}} = -\tilde{\mu}_{\mathrm{h}} \tag{111}$$

Internal equilibrium between electrons and electron holes is enforced everywhere as a result of this definition.

The assumption of constant $\tilde{\mu}_{\mathrm{e}}$ and exclusion of cation vacancies in transport leaves one degree of freedom within the bulk: oxygen vacancies. According to irreversible thermodynamics, the flux is related to the gradient in electrochemical potential, $\tilde{\mu}$, of the species [88, 99, 141]. For this particular case and ignoring cross-coefficients,

$$\overrightarrow{J}_{\mathrm{v}} = -\mathrm{s}_{\mathrm{v}} \nabla \tilde{\mu}_{\mathrm{v}} \tag{112}$$

or, because $\tilde{\mu}_{\mathrm{v}} = \tilde{\mu}_{\mathrm{v}}^{\mathrm{eq}} + \Delta\tilde{\mu}_{\mathrm{v}}$ and $\nabla\tilde{\mu}_{\mathrm{v}}^{\mathrm{eq}} = 0$, then the flux equation restated is

$$\overrightarrow{J}_{\mathrm{v}} = -\mathrm{s}_{\mathrm{v}} \nabla (\Delta\tilde{\mu}_{\mathrm{v}}) \tag{113}$$

where Δ represents a change from the equilibrium value and the v subscript indicates an oxygen vacancy in the MIEC. The transport equations are in terms of changes from equilibrium because the equilibrium electrochemical potentials do not lead to any flux. The quantity s_v is the Onsager transport coefficient from irreversible thermodynamics, related to electrical conductivity. For the vacancies,

$$s_v = b_v c_v \tag{114}$$

where c_v is the concentration of oxygen vacancies and b_v is mobility of oxygen vacancies [88, 99, 141].

The general continuity equation in the interior of such an MIEC would then be

$$\frac{\partial c_v}{\partial t} = -\nabla \cdot \overrightarrow{J}_v \tag{115}$$

without a homogeneous generation term. At steady state, no change in vacancy concentration occurs and so the continuity equation is

$$0 = -\nabla \cdot \overrightarrow{J}_v \tag{116}$$

Equation 116 with 113 must be solved in the bulk of the MIEC for $\Delta\tilde{\mu}_v$ for steady state.

At the current collector, the electrochemical potential of electrons will be fixed by equilibrium with the electrons in the current collector if an ideal interface is assumed

$$\Delta\tilde{\mu}_e = \Delta\tilde{\mu}_e^{(CC)} = z_e F \Delta E \tag{117}$$

where F is Faraday's constant. ΔE is the change of electrode potential with respect to the counter electrode or reference electrode upon cathodic bias [125].

At the MIEC-air boundary, the flux of vacancies is outward as they are healed by reduced, monatomic oxygen

$$\overrightarrow{J}_v \cdot \overrightarrow{n} = r_{rdn} \tag{118}$$

where r_{surf} is the rate of oxygen reduction corresponding to the bulk pathway and $\overrightarrow{n}$ is the outward-pointing normal vector.

At the electrolyte-MIEC boundary, one of two boundary conditions may be imposed. First, if the interface is somewhat resistive to O^{2-} transfer, a property that is suggested sometimes in patterned electrode experiments, the boundary condition may be specified as Neumann

$$\overrightarrow{J}_{v} \cdot \overrightarrow{n} = -r_{em} \tag{119}$$

where r_{em} is the rate of vacancy injection (alternatively, O^{2-} withdrawal across the interface. If the transfer of O^{2-} is very facile, then the boundary condition can be specified as Dirichlet by equality of the electrochemical potential of oxygen vacancies across the interface

$$\Delta\tilde{\mu}_{v} = \Delta\tilde{\mu}_{v,e} \tag{120}$$

where $\Delta\tilde{\mu}_{v,e}$ is the change in electrochemical potential of oxygen vacancies in the electrolyte. If ΔE is defined relative to a reference electrode on the electrolyte then $\Delta\tilde{\mu}_{v,e}$ can be taken to be zero.

6.6.2 Interfacial reaction rates

Reaction rates at the interfaces may be described in several ways. If the system is perturbed far from equilibrium, detailed phenomenological rate expressions provide good insight into the process but introduce considerable complexity and complication. If the system is not perturbed far from equilibrium but is instead perturbed only slightly, then linear approximations may be made. In particular, the use of a direct relationship between the rate of the overall reaction and the reaction affinity can be employed. Such an approach neglects the detailed mechanisms of the reaction in favor of a simplified description of the rate. It will be used here in order to focus on the development of microstructure-conformal methods. In terms of justification, note the simplification to linear kinetics dependent upon chemical affinity have been

successfully used in the ALS model [5].

The reaction of interest is

$$\frac{1}{2}\mathrm{O_2} + \mathrm{V_O^{\cdot\cdot}} + 2\mathrm{e'} = \mathrm{O_O^x} \tag{121}$$

where $\mathrm{e'}$ refers to an itinerant electron or, alternatively, for polarons

$$\frac{1}{2}\mathrm{O_2} + \mathrm{V_O^{\cdot\cdot}} + 2\mathrm{B'_B} = \mathrm{O_O^x} + 2\mathrm{B_B^x} \tag{122}$$

where $\mathrm{B'_B}$ symbolizes an electron localized on the B-site of the perovskite and $\mathrm{B_B^x}$ is a neutral B-site. Expressed in terms of building units, then

$$\frac{1}{2}\mathrm{O_2} + \{\mathrm{V_O^{\cdot\cdot}}\} + 2\{\mathrm{e'}\} = \mathrm{nil} \tag{123}$$

where the vacancy building unit $\{\mathrm{V_O^{\cdot\cdot}}\} = \mathrm{V_O^{\cdot\cdot}} - \mathrm{O_O^x}$ and the electron building unit is either $\{\mathrm{e'}\} = \mathrm{e'}$ for itinerant electrons or $\{\mathrm{e'}\} = \mathrm{B'_B} - \mathrm{B_B^x}$.

Let a small perturbation be assumed. If the rate of reaction, $\mathrm{r_{rdn}}$, is proportional to the affinity of reaction, then

$$\mathrm{r_{rdn}} = \mathrm{k^0_{rdn}}\mathcal{A}_{\mathrm{rdn}} \tag{124}$$

where $\mathrm{k^0_{rdn}}$ is a rate parameter and $\mathcal{A}_{\mathrm{rdn}}$ is the affinity.

The affinity of reaction is equal to

$$\mathcal{A}_{\mathrm{rdn}} = -\Delta_{\mathrm{r}}\mathrm{G} = \sum_{\text{reactants}} \nu_{\mathrm{i}}\mu_{\mathrm{i}} - \sum_{\text{products}} \nu_{\mathrm{j}}\mu_{\mathrm{j}} \tag{125}$$

where ν_{i}, ν_{j} are (positively valued) stoichiometric coefficients. For this particular reaction,

$$\mathcal{A}_{\mathrm{rdn}} = \frac{1}{2}\mu_{\mathrm{O_2}}(\mathrm{g}) + \mu_{\mathrm{v}} + 2\mu_{\mathrm{e}} \tag{126}$$

where the chemical potentials refer to the vacancy and electron building units. Recognizing that all of the chemical potentials can be separated into their equilibrium values and a change from the equilibrium value by $\mu_{\mathrm{k}} = \mu_{\mathrm{k}}^{\mathrm{eq}} + \Delta\mu_{\mathrm{k}}$, then

$$\begin{aligned}\mathcal{A}_{\mathrm{rdn}} =& \left[\frac{1}{2}\mu^{\mathrm{eq}}_{\mathrm{O_2}}(\mathrm{g}) + \mu^{\mathrm{eq}}_{\mathrm{v}} + 2\mu^{\mathrm{eq}}_{\mathrm{e}}\right] + \left[\frac{1}{2}\Delta\mu_{\mathrm{O_2}}(\mathrm{g}) + \Delta\mu_{\mathrm{v}} + 2\Delta\mu_{\mathrm{e}}\right] \\ =& \frac{1}{2}\Delta\mu_{\mathrm{O_2}}(\mathrm{g}) + \Delta\mu_{\mathrm{v}} + 2\Delta\mu_{\mathrm{e}}\end{aligned} \tag{127}$$

because the equilibrium terms must sum to zero.

Making the assumption that the electrochemical potential of a species may be expressed as

$$\tilde{\mu}_{\mathrm{i}} = \mu_{\mathrm{i}} + \mathrm{z_i F}\Phi \tag{128}$$

then it becomes apparent that the electrical components of the sum of $\tilde{\mu}_{\mathrm{v}}$ and $2\tilde{\mu}_{\mathrm{e}}$ cancel out (c.f. discussion of unpacking) so that

$$\Delta\tilde{\mu}_{\mathrm{v}} + 2\Delta\tilde{\mu}_{\mathrm{e}} = \Delta\mu_{\mathrm{v}} + 2\Delta\mu_{\mathrm{e}} \tag{129}$$

therefore the affinity can be expressed as

$$\mathcal{A}_{\mathrm{rdn}} = \frac{1}{2}\Delta\mu_{\mathrm{O_2}}(\mathrm{g}) + \Delta\tilde{\mu}_{\mathrm{v}} + 2\Delta\tilde{\mu}_{\mathrm{e}} \tag{130}$$

since the electrochemical potential are of interest to the FEM simulation.

The rate of oxygen reduction on the surface of a mixed conductor with small deviation from equilibrium is

$$\mathrm{r_{rdn}} = \mathrm{k^0_{rdn}}\left[\frac{1}{2}\Delta\mu_{\mathrm{O_2}}(\mathrm{g}) + \Delta\tilde{\mu}_{\mathrm{v}} + 2\Delta\tilde{\mu}_{\mathrm{e}}\right] \tag{131}$$

The next question is how to identify a value for $\mathrm{k^0_{rdn}}$. Oxygen isotope exchange measurements have been used in the past to probe this reaction [34]. Those experiments yield a surface exchange coefficient, $\mathrm{k^*}$, useful to the present model.

The value of $\mathrm{k^*}$ is determined from the reaction using the isotope $^{18}\mathrm{O}$ (denoted as $\mathrm{O^*}$)

$$\frac{1}{2}\mathrm{O_2^*} + \mathrm{V_O^{\cdot\cdot}} + 2\mathrm{e'} \rightarrow \mathrm{O_O^{*x}} \tag{132}$$

Writing in terms of building units,

$$\frac{1}{2}\mathrm{O_2^*} + \{\mathrm{V_O^{\cdot\cdot}}\} + 2\{\mathrm{e'}\} = \{\mathrm{O_O^{*x}}\} \tag{133}$$

where $\{\mathrm{V_O^{\cdot\cdot}}\} = \mathrm{V_O^{\cdot\cdot}} - \mathrm{O_O^x}$ and $\{\mathrm{O_O^{*x}}\} = \mathrm{O_O^{*x}} - \mathrm{O_O^x}$. Using the same logic as before, the affinity for this reaction is closely related to the previous value

$$\mathcal{A}_{\mathrm{rdn}} = \frac{1}{2}\Delta\mu_{\mathrm{O_2^*}}(\mathrm{g}) + \Delta\mu_{\mathrm{v}} + 2\Delta\mu_{\mathrm{e}} - \Delta\mu_{\mathrm{O_O^*}} \tag{134}$$

The isotope exchange experiment involves exposure of a mixed conductor to a gas with ^{18}O concentration of approximately 97% [34]. The exposure proceeds, allowing ^{16}O inside the mixed conductor to exchange with the isotope in the gas. The exposure is at some point terminated and secondary ion mass spectroscopy (SIMS) performed to determine the profile. During the exposure, the isotope concentration in the gas is assumed to remain constant, and therefore $\Delta\mu_{O_{2*}}(g) = 0$. Another critical assumption is that the presence of oxygen isotopes does not alter the defect chemistry of the mixed conductor [97]. Thus, the chemical potential of oxygen vacancies and electrons are not altered leading to $\Delta\mu_v = \Delta\mu_e = 0$. The affinity of the tracer exchange is therefore simplified to

$$\mathcal{A}_{rdn} = -\Delta\mu_{O^*_O} \tag{135}$$

Substituting in the definition of chemical potential for the tracers assuming primarily configurational contributions and canceling out the standard chemical potential terms, then

$$\Delta\mu_{O^*_O} = \mu_{O^*_O} - \mu^{eq}_{O^*_O} = RTln\left(x_{O^*_O}\right) - RTln\left(x^{eq}_{O^*_O}\right) \tag{136}$$

where x indicates a fractional concentration. The actual concentration of oxygen tracers approaches the "equilibrium" concentration as the experiment proceeds. The equilibrium concentration of oxygen tracers in the mixed conductor is equal to the isotope fraction in the gas [34], which is close to 1: $x^{eq}_{O^*_O} = x_{O^*}(g)$. From measurements, the fractional isotope concentration at the surface is close to 0.95 for LSMC and, as already mentioned, it is 0.97 for the gas phase [34]. Therefore, a linear approximation for the Taylor series expansion of the natural logarithm is justified: $\ln(z) \approx z - 1$ for z close to 1. The change in chemical potential can be approximated as

$$\Delta\mu_{O^*_O} = RT\left[x_{O^*_O} - x_{O^*}(g)\right] \tag{137}$$

and the rate of the reaction is

$$r_{rdn} = k^0_{rdn}\left[-\Delta\mu_{O^*_O}\right] \approx RTk^0_{rdn}\left[x_{O^*}(g) - x_{O^*_O}\right] \tag{138}$$

The equation used to interpret the tracer exchange experiment and identify a rate constant is

$$r_{rdn} = k^* c_{Ositem} \left[x_{O^*}(g) - x_{O^*_O} \right] \tag{139}$$

where c_{Ositem} is the concentration of oxygen lattice sites in $\mathrm{mol\,m^{-3}}$ and the surface exchange coefficient has units $\mathrm{m\,s^{-1}}$. The site density adjusts the flux from fractional to $\mathrm{mol\,m^{-2}\,s^{-1}}$. Setting the two fluxes equal, then

$$k^0_{rdn} = \frac{k^* c_{Ositem}}{RT} \tag{140}$$

which provides the rate constant for use in the bulk simulation. The rate of oxygen reduction via the bulk pathway for use in the simulation is therefore

$$r_{rdn} = \frac{k^* c_{Ositem}}{RT} \left[\frac{1}{2} \Delta\mu_{O2}(g) + \Delta\tilde{\mu}_v + 2\Delta\tilde{\mu}_e \right] \tag{141}$$

At the electrolyte-MIEC interface, a similar reaction rate can be expressed for the Neumann boundary condition

$$r_{em} = k^0_{em} \Delta\tilde{\mu}_{em} \tag{142}$$

where $\Delta\tilde{\mu}_{em} = \Delta\tilde{\mu}_{v,e} - \Delta\tilde{\mu}_v$ if the boundary condition is not Dirichlet.

6.6.3 Parameters

The transport coefficient s_v may be evaluated from the tracer diffusivity. From Einstein's relation, the oxygen vacancy mobility is related to the diffusivity by

$$b_v = \frac{D_v}{RT} \tag{143}$$

The vacancy diffusivity is related to the tracer diffusivity by

$$D^* = f \frac{c^0_v}{c_{Ositem}} D_v \tag{144}$$

where f is the tracer correlation factor, given the value of 0.69 for perovskites, c^0_v is the equilibrium concentration of oxygen vacancies, and c_{Ositem} is again the concentration of oxygen lattice sites. Combining Equations 143 and 144 with the definition of the

transport coefficient s_v in Equation 114 and making the assumption that $c_v \approx c_v^0$ due to the small perturbation, then

$$s_v = \left(\frac{c_{Ositem}}{fRT}\right) D^* \tag{145}$$

Simulations in the bulk involving small perturbations and uniform Fermi level are therefore cast in terms of dependence upon the tracer surface exchange coefficient k^* and tracer diffusivity D^*. These data are available from published studies. The relationship with temperature is assumed to be Arrhenius

$$k^* = k_0^* exp\left(-\frac{\Delta H_k}{RT}\right) \qquad D^* = D_0^* exp\left(-\frac{\Delta H_D}{RT}\right) \tag{146}$$

Table 5 gives the values of the parameters for LSM82.

Table 5: Linearized parameters for LSM82.

Parameter	Value	Units	Reference
k_0^*	$7.9x10^{-5}$	m s^{-1}	[35]
ΔH_k	$1.3x10^5$	J mol^{-1}	[35]
D_0^*	$4.6x10^{-6}$	m^2 s^{-1}	[34]
ΔH_D	$2.6x10^5$	J mol^{-1}	[34]
c_{Ositem}	$8.5x10^4$	mol m^{-3}	[106]

6.6.4 Results

A portion of the microstructure was meshed and used to solve the bulk pathway problem. Figure 55a shows the value of $\Delta\tilde{\mu}_v$ associated with the LSM82 parameters at 700°C. A Dirichlet boundary condition was used at the interface with the electrolyte (shaded red). Blue shading corresponds with a purely electrical change - that is, beyond the utilization length with effectively no change to the point defect composition upon the electrical bias. Clearly, the utilization length is very small, only tens of nanometers. The bulk pathway, therefore, contributes very little because the reaction zone is extended only a very short distance from the TPB lines.

To investigate the effect of superior mixed conductivity, the parameters k^* and D^* were varied. They were not varied randomly, but rather in accordance with a

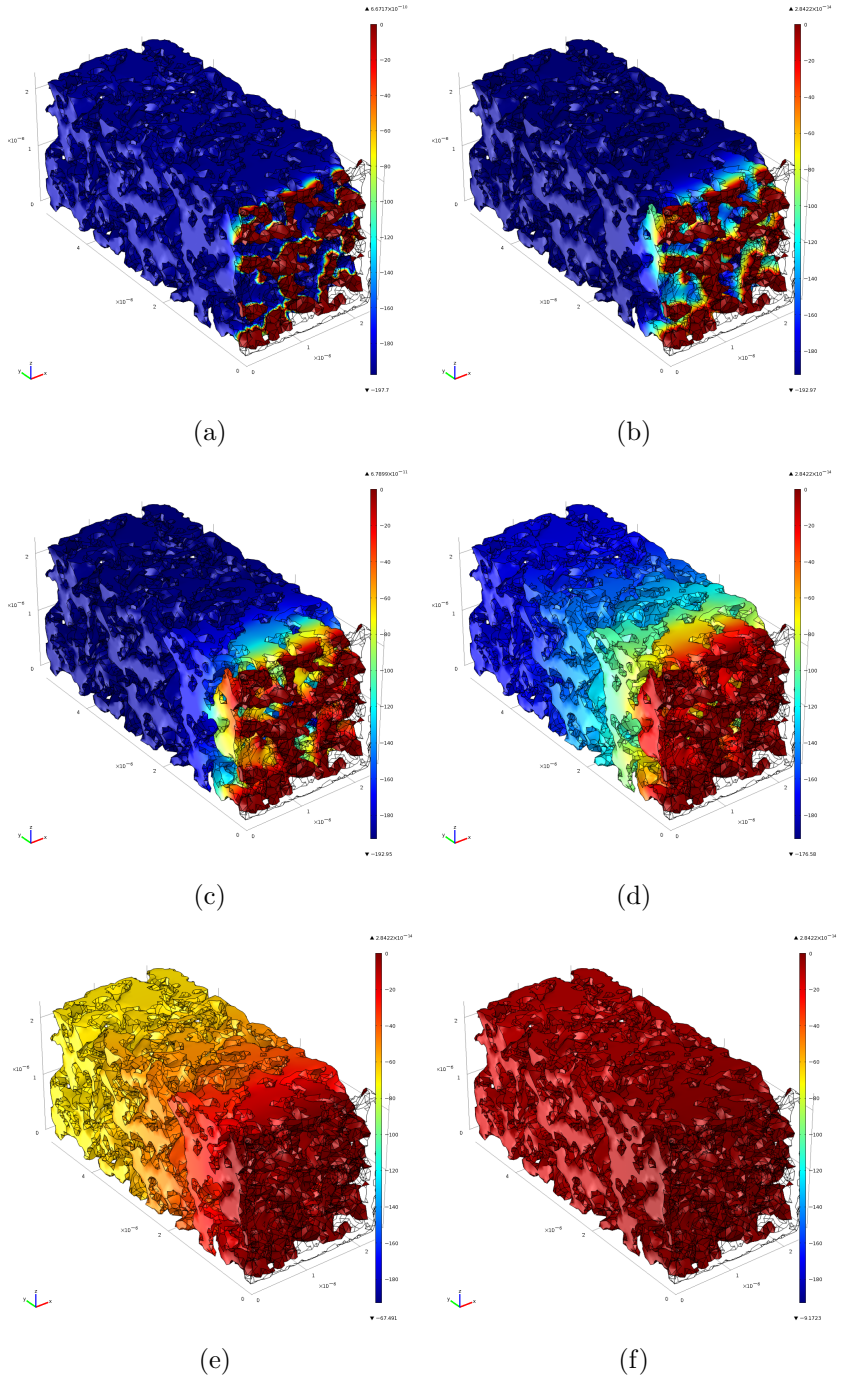

Figure 55: Surface plot of $\Delta\tilde{\mu}_{\mathrm{v}}$ (J/mol) in the bulk pathway simulation using a) k* and D* of LSM82 at 700°C and enhanced by a factor multiplying k* of b) 10^2, c) 10^3, d) 10^4, e) 10^5, b) 10^6 with corresponding quadratic enhancement of D*. Cathodic bias of $-0.001\,V$.

well-established empirical trend [33, 79]. To wit, when a meta-analysis is performed and the values of $\log_{10}(\mathrm{k}^*)$ versus $\log_{10}(\mathrm{D}^*)$ for many different mixed conductors at

many different temperatures and pO_2's, all the values generally form a line with approximate slope of 1/2. The empirical trend is illustrated in Figure 56 with the general location of families of mixed conductors identified. The slope of 1/2 does not hold for each individual family, rather the best fit line applied to all families has this slope.

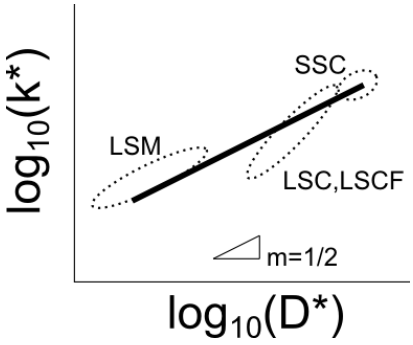

Figure 56: Empirical relationship of k^* and D^* to one another with various families of perovskite mixed conductors indicated.

The conclusion from this trend is that materials with superior mixed conduction properties usually have not only a higher value of D^*, but also a higher value of k^*. Moreover, these parameters do not change in direct proportion to one another. Rather, D^* changes as the *square* of k^*. Suppose some set of parameters is given, say k_1^* and D_1^*. A mixed conductor at a different temperature, pO_2, or with different composition could be approximately described with parameters k_2^* and D_2^*:

$$D_2^* \approx D_1^* \left(\frac{k_2^*}{k_1^*} \right)^2 \tag{147}$$

Of course this is not an exact relationship, but the trend does describe "ballpark" relationships of the linearized parameters.

Starting with the LSM82 parameters in Table 5, the value of k^* was systematically varied. D^* was changed as the square of k^*. This had the effect of making the bulk problem correspond to increasingly superior mixed conductors (as opposed to blindly changing k^* and D^* without relationship to one another - a nonphysical quixotism).

The results of the bulk simulations in terms of $\Delta\tilde{\mu}_{\mathrm{v}}$ profile are shown in Figure 55b-f. Since D^* increases faster, the reaction zone is extended away from the electrolyte-MIEC interface as evidenced by the increasing utilization length indicated by the larger spatial extent of intermediate $\Delta\tilde{\mu}_{\mathrm{v}}$ values.

Enhanced k^* of the order 10^0 to 10^3 shows a great deal of dependence upon particle size and morphology (intra-particle variation), whereas better mixed conductors (10^5 to 10^6) appear to be well-characterized by 1D model assumptions because the $\Delta\tilde{\mu}_{\mathrm{v}}$ profile loses significant side-to-side variation.

LSCF 6428 is well-characterized by the 1D ALS model [5]. At 700°C, k^*_{LSCF} is approximately 800 to 900 times larger than that of LSM 82 [12,34,35] and therefore the 10^3 k^* is most relevant to it. However, the actual value of D^* is approximately 15 times larger than what the simple empirical quadratic law suggests. Therefore, the actual utilization length of LSCF 6428 is larger than that shown in Figure 55c. Nevertheless, Figure 55c is in the approximate ballpark because it describes a hypothetical mixed conductor with similar though not exactly matching properties to LSCF 6428.

The area-specific resistance associated with the bulk pathway only is given in Figure 57. The ASR is very large for $k^*_{\mathrm{hypothetical}}/k^*_{\mathrm{LSM82}} = 1$, meaning that the bulk pathway has very little activity. In fact, the TPB pathway in LSM is likely far more active. For $k^*_{\mathrm{hypothetical}}/k^*_{\mathrm{LSM82}} = 10^3$, near to LSCF 6428's properties, the ASR is approximately 1 $\Omega\,\mathrm{cm}^2$, which is not unreasonable for a porous LSCF 6428 electrode operating at T = 700°C but does likely overestimate the ASR due to the underestimated utilization length.

The power law indicated by the best fit line equation gives an exponent of approximately -1.5. There is deviation from the trend at large $k^*_{\mathrm{hypothetical}}/k^*_{\mathrm{LSM82}}$ because the utilization distance far exceeds the amount of microstructure simulated normal to the electrolyte interface. The trend is caused by the inverse dependence of the ASR upon both the utilization length and how active the surface is. This proportionality

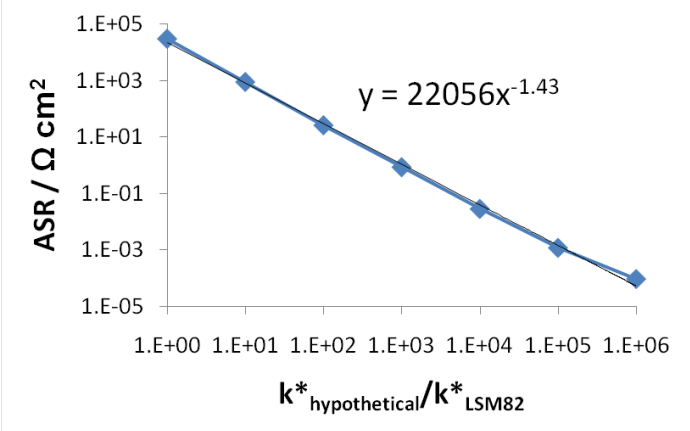

Figure 57: Simulated area-specific resistance as a function of k^* (and required D^*) enhancement corresponding to Figure 55. T = 700°C.

is expressed as

$$\text{ASR} \propto (k^*)^{-1}(\mathcal{L}_\delta)^{-1} \tag{148}$$

where $\mathcal{L}_\delta$ is the utilization length and k^* serves as a proxy to quantify the activity of the surface. The utilization length depends on k^* and D^* as [5]

$$\mathcal{L}_\delta \propto \sqrt{\frac{D^*}{k^*}} \tag{149}$$

Recalling that $D^* \propto (k^*)^2$ according to Equation 147 and substituting, then

$$\text{ASR} \propto (k^*)^{-1}(k^*)^{-1/2} = (k^*)^{-3/2} \tag{150}$$

which recovers the trend of the ASR in Figure 57.

6.7 Meshing and interfacial refinement

The bulk diffusion length in LSM is very small compared to other mixed conductors such as LSCF. The perturbation of oxygen vacancy concentration does not extend far from the interface, only on the order of tens to hundreds of nanometers. For this reason, the mesh size must be small near the interface to accommodate the rapid change of $\Delta\tilde{\mu}_v$ in the vicinity of the interface. The iso2mesh v.1.0 package, the

version available at the time this work was performed, meshes bulk domains with only one mesh size and does not have the capability for mesh refinement. This restricts the mesh of all solid phases, including both LSM and YSZ, to be the same size as that of the interface. Therefore, a very small mesh must be enforced over the entire solid-phase domain, typically smaller than what is required to adequately represent the geometry. The uniformly small mesh has the effect of restricting simulation size by adding superfluous degrees of freedom and therefore restricts the amount of microstructure that may be included in the simulation.

Local mesh refinement allows a coarse mesh to be used far from the interface but for that mesh to be refined to the appropriate size near the interface. It provides a mesh that restricts error in the solution at the interface where $\Delta\tilde{\mu}_{\mathrm{v}}$ changes rapidly but does not give a burdensome number of degrees of freedom away from the interface. This compromise allows more microstructure to be included in the simulation. Any refinement, however, would have to be performed separate from iso2mesh v.1.0.

6.7.1 Electrolyte-MIEC interface refinement

A custom function was written to refine the mesh locally at the interface. The refinement operated on a relatively coarse mesh capable of adequately reproducing the microstructure geometry. It was applied after interfacial correction (ceding, smoothing, etc.) of the coarse mesh so that the interface already had unnecessary roughness removed. A variant of the *longest edge* method of refinement [56, 137, 138] on the tetrahedral mesh supplied by iso2mesh was used.

A schematic of the refinement method is shown in Figure 58 on a portion of the MIEC mesh located along the electrolyte-MIEC interface, which is indicated by the heavy black line. The left column outlines the process of a "Level 0" refinement in which only those elements sharing a face with the interface are to be refined. These elements are highlighted in gray in the first image. The bisection of each of these

elements' longest edge is performed in the second image. The third image highlights any elements with nonconforming nodes caused by the bisection, which are then resolved by bisection of those elements in the fourth image. This proceeds until all nonconforming nodes are eliminated. The process is considered one full refinement. A second full refinement is indicated by the arrow leading to the fifth image. The right column shows the same process applied to a "Level 1" refinement in which all elements sharing a face with the electrolyte-MIEC interface as well as any elements sharing a face with them are targeted for refinement. Any level (2, 3, etc.) may be chosen, wherein the elements targeted for refinement extend increasingly far from the interface.

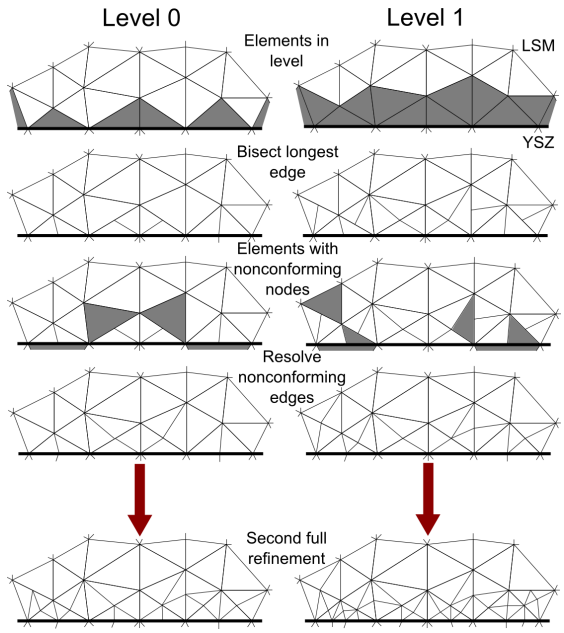

Figure 58: Schematic diagram of the longest edge mesh refinement applied to interfacial LSM elements. Left: Only elements sharing a face with the interface are refined. Right: elements sharing a face with the interface and those that they share a face with are refined.

The figure shows the process schematically for 2D triangular elements, but it is analogously applied to the iso2mesh 3D tetrahedral mesh [138]. Instead of a line drawn between the bisecting node of the longest edge and the opposite vertex which divides the element, a plane between the bisecting node on the longest edge and

the two opposite tetrahedral vertices divides the element. Nonconforming nodes are accommodated by further refinement until they are eliminated.

The interfacial mesh refinement was applied to test prisms meshed with maximum triangle size of three, divided between two phases, and the interfacial correction applied. The meshed 20 x 20 x 20 voxel prism is shown in Figure 59a. Level 0 refinement was applied and is shown in Figure 59b and d. The refinement was applied two times in part b and three times in part d. Level 1 refinement was applied in Figure 59c and e, twice in part c and three times in part e. There is visible refinement of the LSM mesh near the interface in all cases. In general, the mesh is finer when the refinement is applied more times and the refinement extends further from the interface when level 1 refinement is used and when the refinement is applied three times rather than two. Consequently, more total elements are present with the more inclusive refinement. The original mesh size is preserved far from the interface.

After success using the test geometry, the refinement method was then applied to the real, porous microstructure. This microstructure was meshed using a maximum triangle size of three shown in Figure 60a with a close view in part b. Level 0, 1, and 2 meshes were applied two or three times and are plotted as indicated in the Figure 60 caption. The refinement reduced the relatively coarse mesh in part b into much finer divisions in all cases near the electrolyte-MIEC interface and the TPB line. Higher level refinement with more applications generally created a finer mesh with a greater number of elements. The size of the original mesh was preserved away from the interface, as is shown at the top of each of the subfigures.

6.7.2 TPB-line refinement

An alternative to refinement along the entire electrolyte-MIEC interface is to refine the mesh along the TPB. Doing so requires fewer mesh elements but does refine the mesh where the solution changes the fastest. An algorithm for refining the iso2mesh

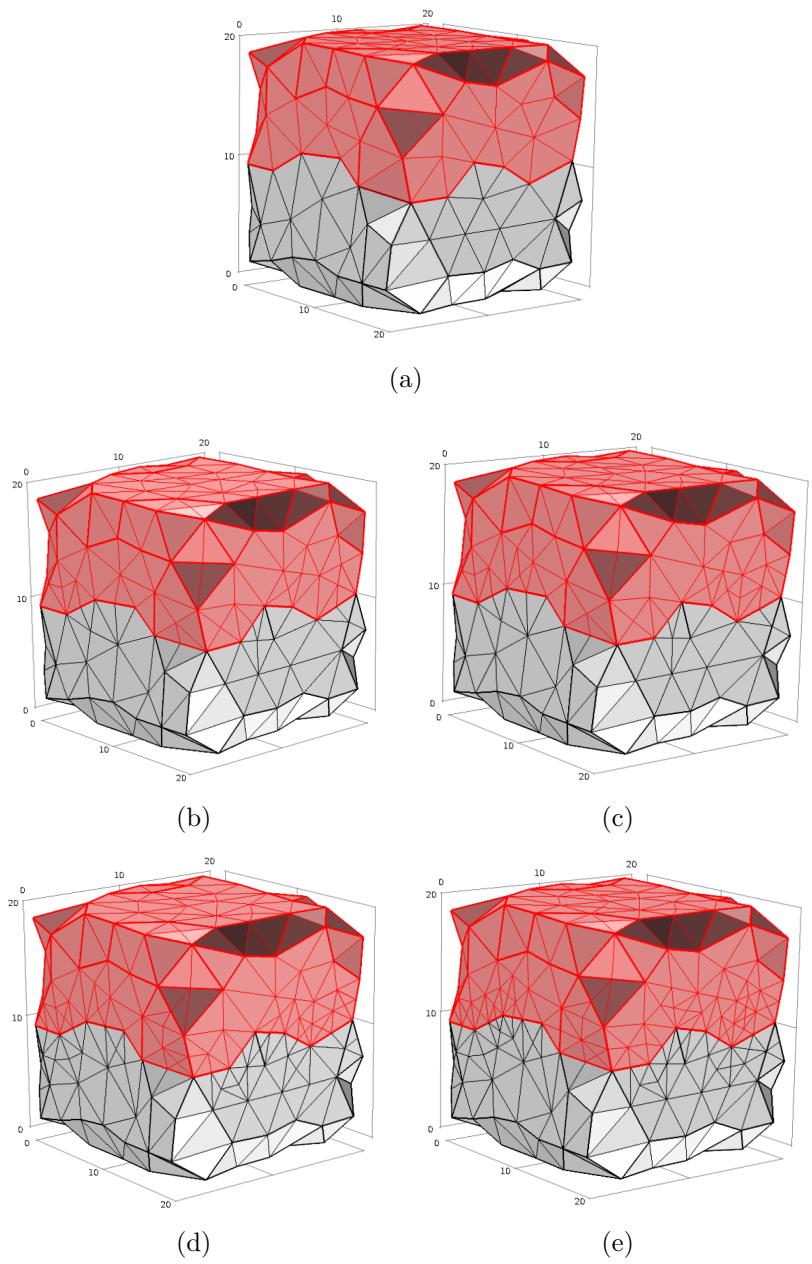

Figure 59: a) 20 x 20 x 20 voxel test prism meshed with maximum triangle size of 3, divided into two phases (LSM in red YSZ in white), corrected at interface. Refined mesh as viewed on the exterior surface: b) Two level 0 refinements, c) two level 1 refinements, d) three level 0 refinements, e) three level 1 refinements.

along the TPB edge only using longest edge refinement was also developed and employed. In this case, the meshing was entirely level 0 in order to reduce the total

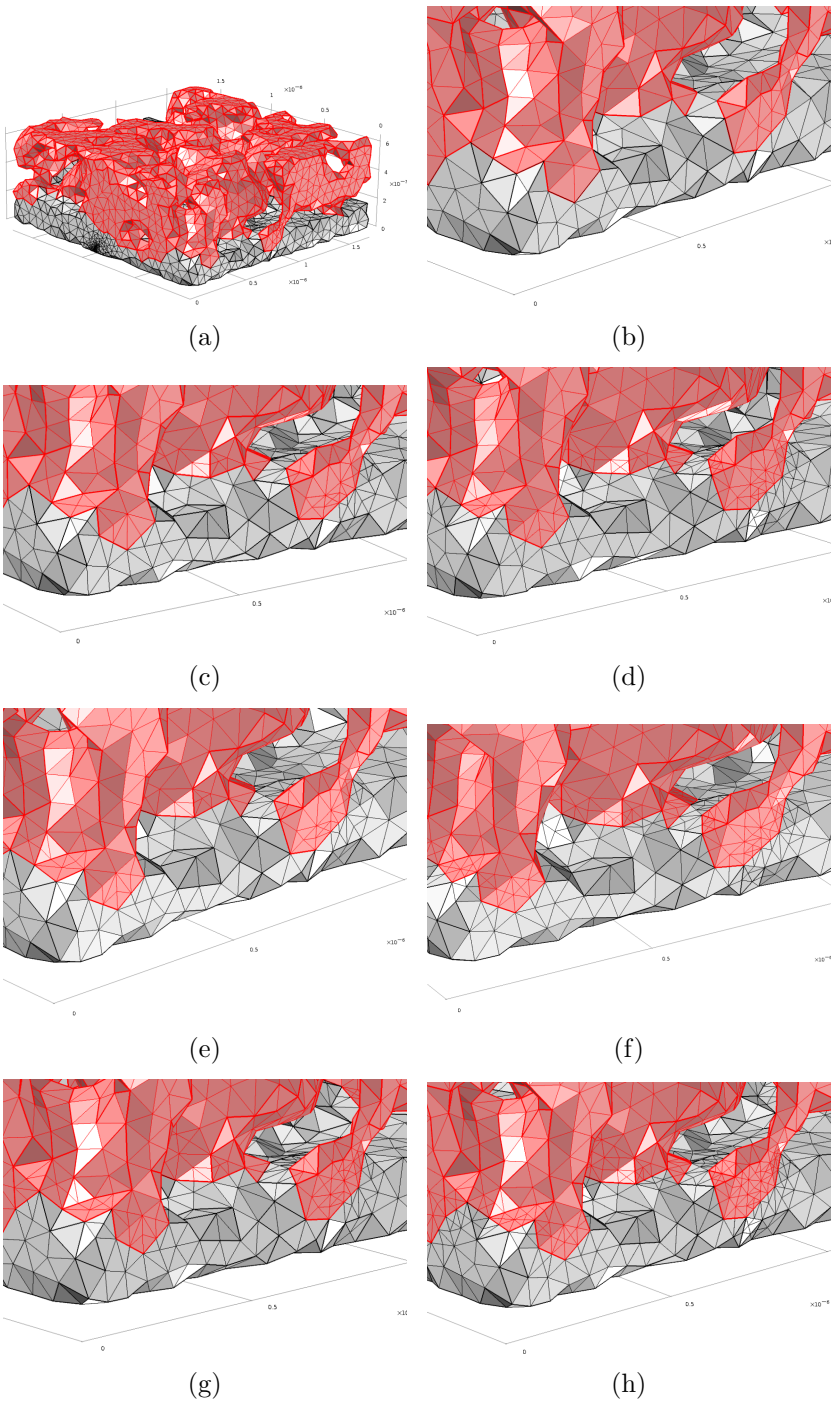

Figure 60: a) Portion of the porous microstructure meshed with a maximum triangle size of three. LSM is red, YSZ is white. b) Close view of the meshed microstructure. Refined microstructures: c) level 0, 2x; d) level 0, 3x; e) level 1, 2x; f) level 1, 3x; g) level 2, 2x; h) level 2, 3x.

number of mesh elements. Images of the meshed microstructure with different number of refinements are shown in Figure 61.

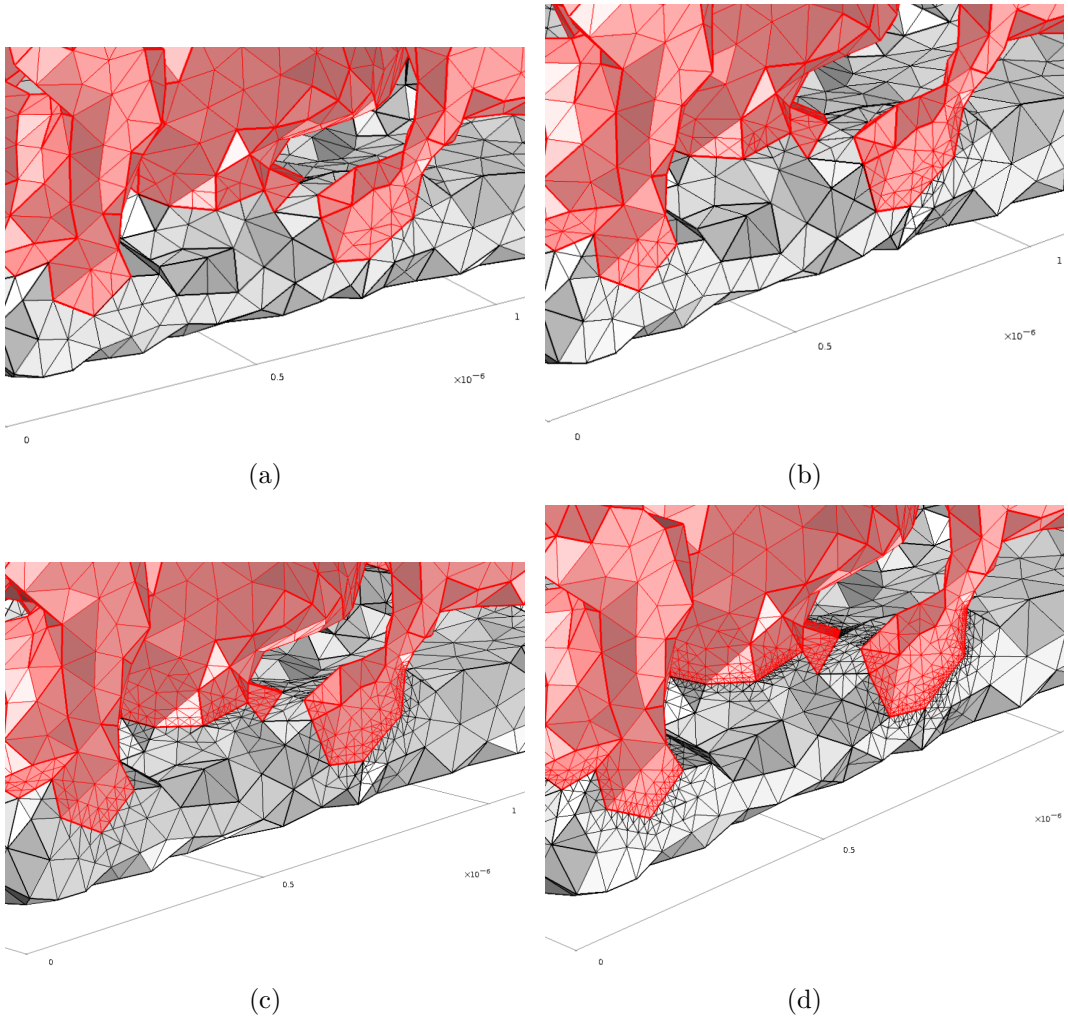

Figure 61: Level 0 refinement of the TPB edge applied a) two, b) four, c) six, and d) eight times. Mesh before refinement: max triangle size = 3, interfacial correction applied (see Figure 60b).

The stability of the global solution was examined as a function of mesh refinement (Figure 62a). Each successive TPB-only mesh refinement led to smaller mesh size along the TPB as well as in the TPB vicinity in order to resolve nonconforming nodes. As the number of mesh refinements increased, the global steady state area-specific resistance increased as well, eventually leveling out at seven or eight refinements. This trend indicates that a very small mesh size along the TPB is required for local

solution accuracy in bulk-only LSM simulations.

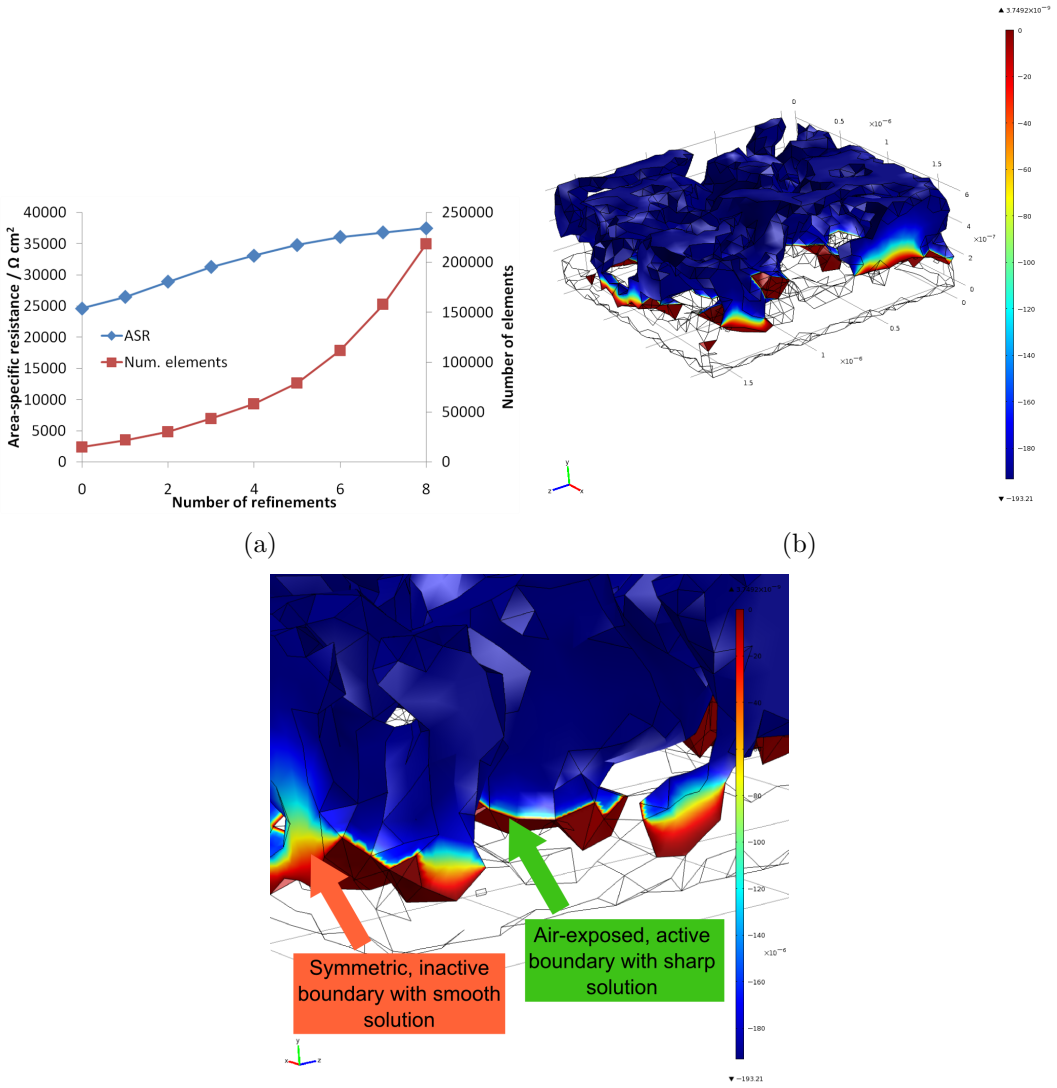

Figure 62: a) Global simulated area-specific resistance (including the bulk pathway only) and number of mesh elements as a function of the number of times the level 0 TPB-only refinement is executed on segment of reconstructed microstructure. b) Bulk pathway solution for $\Delta\tilde{\mu}_v$ in LSM in the region near the interface with the bulk electrolyte. Simulation region is approximately 1.5 μm x 1.5 μm. c) Close view of simulated value of $\Delta\tilde{\mu}_v$ on the surface of a small portion of LSM microstructure annotated to indicate sharply changing, bulk-path active interfaces and symmetric, inactive interfaces with a smoother solution.

The simulated value of $\Delta\tilde{\mu}_v$ resulting from eight TPB refinements is shown in

Figure 62b. The bulk pathway for LSM is characterized by a very short active diffusion length, which is evident along the air-exposed boundaries that are active toward oxygen reduction. The diffusion length along these boundaries is of the order of 20 nm and is the primary reason behind the need to implement so many TPB refinements. The diffusion length is much larger along the symmetric (inactive) boundaries that border the simulation domain. Along these boundaries, the oxygen vacancy electrochemical potential does not change rapidly and therefore a much coarser mesh is allowed.

Following the bulk pathway, oxygen vacancies are injected along the electrolyte-MIEC interface and are consumed along the MIEC-air interface. The shortest distance between these two interfaces occurs in the region of the TPB boundary. The value of $\Delta\tilde{\mu}_{\mathrm{v}}$, therefore, changes very rapidly in this region because the concentration of oxygen vacancies changes rapidly. In contrast, the longest distance between the electrolyte-MIEC interface and MIEC-air interface occurs in the middle of a particle sintered to the bulk electrolyte. Vacancies are injected but must diffuse a long distance, through half the thickness of the particle, to reach the active interface. Therefore, the solution changes rather slowly and may be viewed directly along the inactive symmetric boundaries.

There is a computational penalty associated with the large number TPB refinements required to accurately simulate the bulk solution near the TPB interface. The number of elements increases from an initial value of around 2500 to over 200,000 after eight refinements (Figure 62a). The increase is largely a necessary response to nonconforming nodes generated by the bisection of elements directly along the interface. The process of resolving the nonconforming nodes introduces a great many more new elements to the mesh than are initially targeted for bisection.

Mixed conductors with superior surface exchange and tracer diffusion properties such as LSCF have a much larger diffusion length. Consequently, the mesh need not

be refined to such an extent near the TPB. Some mixed conductors have such a large diffusion length that the intra-particle deviations in point defect chemical potentials are insignificant and allow the 1D porous homogeneous porous electrode assumptions to be valid [5]. A large part of the value of microstructure-conformal FEM simulations such as the ones developed here is that they allow a detailed examination of intra-particle deviations when they are present. LSM is likely to be the worst-case for bulk element refinement because it is widely regarded to be the worst mixed conductor in service as an SOFC cathode material.

The area-specific resistance simulated in Figure 62a is very large, much larger than expected for porous LSM electrode on a YSZ electrode. This result is caused by ignoring the TPB-surface pathway completely in favor of the bulk pathway. The process of oxygen reduction at the TPB is very important in LSM and will be considered later for a fully accurate electrochemical prediction. The role of surface diffusion of adsorbed species along the surface pathway is likely to also create intra-particle deviations and therefore necessitate these types of conformal FEM simulations and therefore benefits from near-TPB refinement.

Both the bulk and surface pathways are worth considering in general. Mixed conductors with superior ionic transference numbers compared to LSM will derive an increasing portion of their electrochemical activity from the bulk pathway. A model that aspires to treat a variety of mixed conductors needs to consider both pathways. Doing so will enable the model to be portable to all SOFC cathode candidate materials.

6.8 LSM bulk pathway under large bias

6.8.1 Modification of linear bulk model

The bulk pathway of LSM is activated under a large bias and makes LSM a better mixed conductor [144]. The reason for this activation is the large influx of oxygen

vacancies caused by the cathodic bias. The linear framework developed for simulation of the bulk pathway under small perturbation in section 6.6 was adapted for a very simplistic model of LSM under a large bias. The problem was made nonlinear in oxygen vacancy transport and in surface reaction rate.

The bulk transport of oxygen vacancies is described by Equations 113-116. The transport parameter s_v is equal to the product of the mobility and the oxygen vacancy concentration (Equation 114). It is assumed to be constant in the case of small perturbation because $\Delta c_v << c_v^0$, where the 0 superscript indicates the equilibrium value. The transport parameter cannot, however, be assumed constant in the case of large perturbation because the change to the vacancy concentration is large and varies a great deal across the microstructure. Therefore, let s_v^0 be the transport parameter determined from Equation 114 using $c_v = c_v^0$. The locally varying transport parameter s_v is defined as

$$s_v = b_v c_v = (b_v c_v^0)\frac{c_v}{c_v^0} = s_v^0 \frac{c_v}{c_v^0} \tag{151}$$

where the factor c_v/c_v^0 is the ratio of the oxygen vacancy concentration under the steady state perturbed condition to the equilibrium value. This factor, obviously, involves concentrations of point defects whereas the linear method avoided any specific statements of point defect chemistry or concentrations altogether and instead dealt entirely with (electro)chemical potentials and empirical measurements. Generally, it is impossible to solve a large-bias mixed conductor problem without knowledge of and explicit inclusion of point defect chemistry in the constitutive equations due to the complex couplings between them. However, because LSM has such low oxygen vacancy concentration and generally has poor relative mixed-conduction properties, several assumptions may be made which reduce the complexity and eliminate the need to deal in specific point defect concentrations in the model. These assumptions are:

1. Oxygen vacancy concentration is very low

2. Electron and electron hole concentrations are relatively constant over moderate values of pO_2 associated with cathodic bias and therefore experience little change in chemical potential upon a moderate change in pO_2

3. Incorporation of an adsorbed oxygen atom into LSM is the rate-determining step in the bulk pathway

The first assumption is widely accepted: LSM's oxygen vacancy concentration is far below that of LSCF or LSC [104, 131, 163]. The second assumption is based upon the Brouwer diagram corresponding to the specific defect models. A change in pO_2 generally prompts large changes in oxygen vacancy as well as A- and B-site vacancy concentrations relative to their equilibrium concentrations, but does not change the concentration of electrons and holes by nearly as much relative to their equilibrium values [104, 131, 163]. Another feature of the lack of change in concentration of electrons and holes is that, approximately, $\log_{10}(c_v) \propto pO_2^{-1/2}$. The third assumption is the consequence of the low vacancy concentration compared with other mixed conductors.

These assumptions can be used to approximate the c_v/c_v^0 factor without delving into solutions of specific defect chemistry equations. From Equation 129, $\Delta\tilde{\mu}_v + 2\Delta\tilde{\mu}_e = \Delta\mu_v + 2\Delta\mu_e$. But since the electron/electron hole concentrations do not change substantially in LSM at moderate pO_2, then $\Delta\mu_e \approx 0$. Therefore,

$$\Delta\mu_v + 2\Delta\mu_e \approx \Delta\mu_v \tag{152}$$

Since the oxygen vacancy concentration is very low in LSM, then $\Delta\mu_v = RTln(x_v) - RTln(x_v^0)$ where x_v is a site fraction, related to c_v by the constant density of oxygen lattice sites in the LSM crystal. Rearranging and putting together with Equation 152,

$$\frac{c_v}{c_v^0} = \exp\left(\frac{\Delta\mu_v}{RT}\right) \approx \exp\left(\frac{\Delta\tilde{\mu}_v + 2\Delta\tilde{\mu}_e}{RT}\right) \tag{153}$$

The change in electron electrochemical potential is fixed at the current collector (Equation 117) and assumed constant in bulk of the mixed conductor. The change

in oxygen vacancy electrochemical potential is the dependent variable of the bulk simulation. The transport parameter s_v therefore becomes

$$s_v \approx s_v^0 \exp\left(\frac{\Delta\tilde{\mu}_v + 2\Delta\tilde{\mu}_e}{RT}\right) \tag{154}$$

and forms the basis of a nonlinear flux (Equation 113) for use in the conservation equation (Equation 116).

The nonlinearity of the surface reaction rate law may also be handled similarly. Assumption 3 requires that the incorporation reaction be rate limiting. An example incorporation reaction is:

$$O(s) + V_O^{\cdot\cdot} + 2e' \rightarrow O_O^x + s \tag{155}$$

where O(s) is an adsorbed, dissociated oxygen atom occupying a surface site and s indicates the liberated surface site. The rate law could be [101]

$$r_{inc} = k_{inc}^0 \left(\frac{\theta}{\theta_0}\frac{c_v}{c_v^0}\frac{c_e^2}{c_e^{0^2}} - \frac{c_O}{c_O^0}\frac{1-\theta}{1-\theta_0}\right) \tag{156}$$

From assumption 1, $c_O \approx c_O^0 \approx c_{Ositem}$. From assumption 2, $c_e \approx c_e^0$. Finally, from the assumption that adsorption is fast compared to incorporation (assumption 3), then $\theta \approx \theta_0$. Simplifying,

$$r_{inc} = k_{inc}^0 \left(\frac{c_v}{c_v^0} - 1\right) \tag{157}$$

This simplification is further justified because it worked well to describe the behavior of LSM-coated LSCF (chapter 4).

The factor k_{inc}^0 corresponds to an exchange current density and is equal to $k^* \cdot c_{Ositem}$ when incorporation is rate-limiting [101, 103], the same factor used in Equation 141. Furthermore, note that when gas diffusion is not important ($\Delta\mu_{O_2}(g) = 0$) and when assumption 2 holds ($\Delta\mu_e \approx 0$), then $\mathcal{A}_{rdn}$ simplifies to $\Delta\mu_v$. Substituting $\Delta\mu_v = RT\ln(c_v/c_v^0) \approx RT(c_v/c_v^0 - 1)$ in the case of small perturbation (the natural log can be simplified because c_v/c_v^0 is close to one) into Equation 141, then Equation 157 is

recovered and so the nonlinear rate law reduces to exactly the linearized rate law under small perturbation. Finally, substituting for the c_v/c_v^0 factor and rate parameter

$$r_{inc} = k^* c_{Ositem} \left(\exp\left(\frac{\Delta\tilde{\mu}_v + 2\Delta\tilde{\mu}_e}{RT} \right) - 1 \right) \tag{158}$$

which is the nonlinear Neumann boundary condition applied on the air-exposed surface of the LSM microstructure.

6.8.2 Results

A section of LSM microstructure was meshed with eight refinements along the TPB line, as described in Section 6.7. The model was solved using a nonlinear iterative solver in COMSOL (GMRES with incomplete LU factorization) at various values of cathodic overpotential, $\eta = \Delta E$.

The resulting simulated current-voltage diagram is given in Figure 63. The behavior is clearly Tafel-like and indicates a dramatic activation of the bulk pathway with increasingly large driving force.

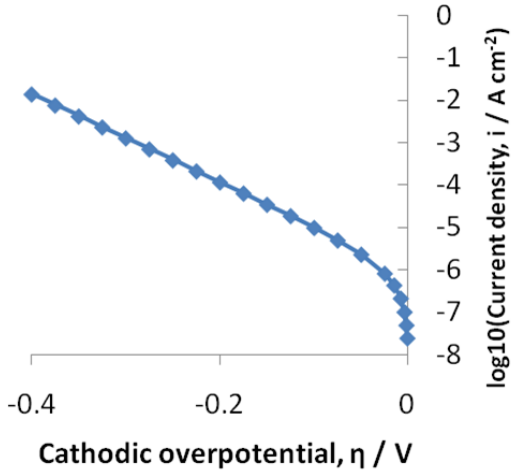

Figure 63: Current-voltage plot simulated using simple large-bias LSM bulk pathway model. T=973K.

The activation of the bulk pathway is visualized in Figure 64 where $\log_{10}(c_v/c_v^0)$ is plotted conformal to the microstructure. At low bias of -1 mV, there is only small deviation from the equilibrium vacancy concentration. The oxygen vacancy

concentration rises dramatically as the bias becomes more severe. Biases of -75 mV and -150 mV produce a local enrichment in the immediate vicinity of the interface. Large bias of -300 and -400 mV produce an extreme enrichment of oxygen vacancies at the interface: more than 10,000 times the equilibrium vacancy concentration. As the concentration increases, the transport parameter s_v increases concomitantly and therefore the region of oxygen vacancy enhancement extends further and further from the interface. An extended region of oxygen vacancy enhancement means that the surface becomes active to oxygen reduction further from the interface and therefore the utilization length is longer. The sequence of images clearly demonstrates LSM becoming a better mixed conductor in response to cathodic bias. The Tafel-like behavior in Figure 63 indicates that this opening of the bulk pathway results in huge increases in current compared to OCV.

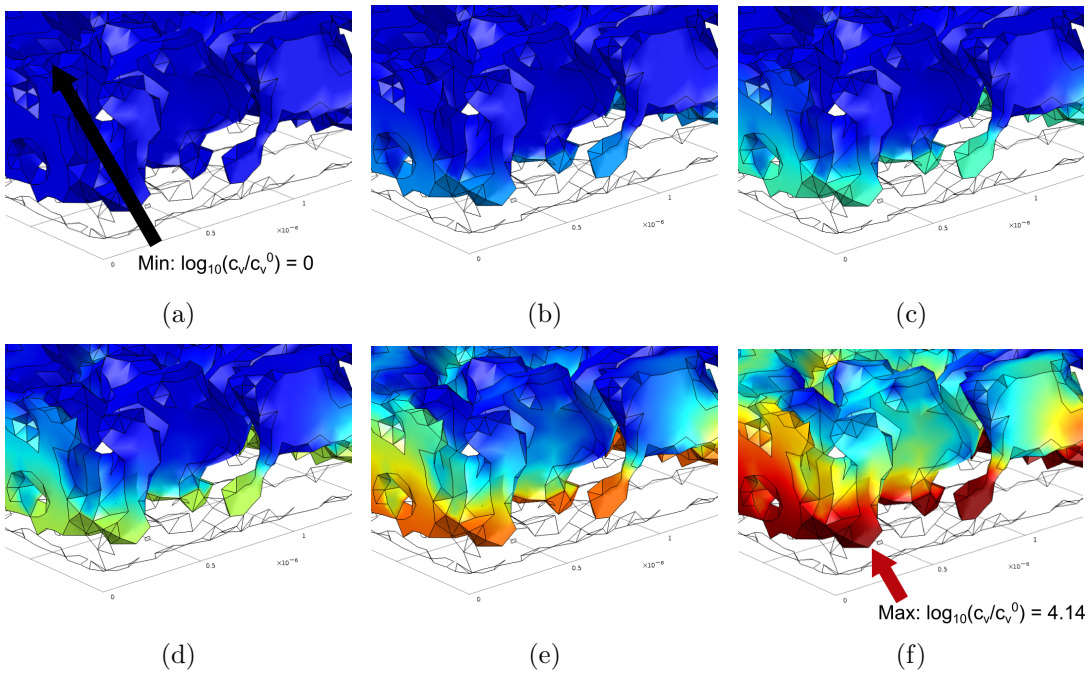

Figure 64: Value of $\log_{10}(c_v/c_v^0)$ at various cathodic bias: a) -1 mV, b) -75 mV, c) -150 mV, d) -200 mV, e) -300 mV, f) -400 mV. T=973 K.

A wide view of the mesh used on the large microstructure section and also the solution of $\log_{10}(c_v/c_v^0)$ at -1 mV and -400 mV is shown in Figure 65. This is believed

to be the first time LSM activation has been visualized in a porous structure.

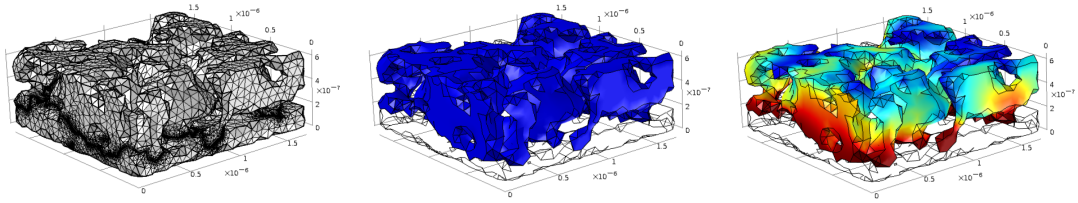

(a) (b) (c)

Figure 65: Wide view of large microstructure section: a) mesh and $\log_{10}(c_v/c_v^0)$ at b) -1 mV and c) -400 mV. T=973 K.

6.9 Simulations on the surface

The necessary considerations for simulation of the surface pathway are outlined in this section. The surface model is very simple, involving dissociative physisorption without partial charge transfer and linear irreversible thermodynamic treatment of the reaction rate for a small perturbation. In order to use COMSOL Multiphysics for surface simulations, the "weak form, boundary" method of adding physics to the simulation should be used, as opposed to the coefficient form which may be used for the bulk simulations. This requirements necessitates the full derivation of the weak form of the surface problem, which will be derived in the following section.

6.9.1 Transport

Suppose that there is an air-exposed surface of a mixed conductor onto which a gas species may adsorb. The adsorbed species is consumed during the course of an electrochemical reaction and replenished by additional adsorption. Consumption may occur heterogeneously at the TPB between the mixed conductor, gas phase, and electrolyte or by incorporation of the gas into the bulk of the mixed conductor (oxygen incorporated into an oxide by filling a vacancy, for example). Adsorbates are transported by diffusion to the TPB.

The following assumptions are employed in this section:

1. Only the surface pathway is considered

2. Surface adsorbate concentration, c_θ, has units $\mathrm{mol\,m^{-2}}$

3. Surface concentration may be expressed in terms of the product of the density of adsorption sites, Γ, and the fractional site occupancy, θ: $c_\theta = \Gamma\theta$

Consider the conservation of surface concentration with a homogeneous generation/consumption term

$$\frac{\partial c_\theta}{\partial t} = -\nabla \cdot \left(\overrightarrow{J}_\theta\right) + G \quad \text{in}\,\Omega \tag{159}$$

where $\overrightarrow{J}_\theta$ is the flux of the adsorbate (units: $\mathrm{mol\,m^{-1}\,s^{-1}}$) and G is the homogeneous generation/consumption term (units: $\mathrm{mol\,m^{-2}\,s^{-1}}$). Ω is the domain of the surface of the mixed conductor. At steady state (chemical/electrochemical reaction balanced by transport and adsorption), the time derivative is zero

$$0 = -\nabla \cdot \left(\overrightarrow{J}_\theta\right) + G \quad \text{in}\,\Omega \tag{160}$$

According to irreversible thermodynamics, the flux is related to the gradient in electrochemical potential, $\tilde{\mu}$, of the species. For this particular case and ignoring cross-coefficients,

$$\overrightarrow{J}_\theta = -s_\theta \nabla \tilde{\mu}_\theta = -s_\theta \nabla(\Delta\tilde{\mu}_\theta) \tag{161}$$

where s_θ is the transport coefficient of the surface species and the equilibrium electrochemical contribution to the flux cancels out. If it is expressed similarly to the bulk vacancy transport coefficient, then the following definition is used for the surface transport coefficient

$$s_\theta = b_\theta c_\theta \tag{162}$$

with units of $\mathrm{mol^2\,J^{-1}\,s^{-1}}$, where b_θ is the mobility of the surface species, with units $\mathrm{mol\,m^2\,J^{-1}\,s^{-1}}$.

Furthermore, set G as the difference between the rate of adsorption, r_1, and the rate of incorporation of the surface species into the oxide by vacancy healing, r_2, on the surface. In the case of a neglected bulk pathway, $r_2 = 0$. The value of r_2 would increase as the ionic transference of a mixed conductor increases.

Substituting, then the conservation equation is

$$0 = -\nabla \cdot \left(-s_\theta \nabla \left(\Delta \tilde{\mu}_\theta\right)\right) + \left(r_1 - r_2\right) \quad \text{in}\, \Omega \tag{163}$$

Introduce a test function $v \in H^1(\Omega)$ where the Sobolev space $H^1(\Omega)$ is defined as

$$H^1(\Omega) = \left\{ v \in L^2(\Omega) : \frac{\partial v}{\partial x_i} \in L^2(\Omega) \,\text{for}\, i = 1, ..., d \right\} \tag{164}$$

where d is the number of dimensions of Ω and the space $L^2(\Omega)$ is

$$L^2(\Omega) = \left\{ v : v \,\text{is defined in}\, \Omega \,\text{and} \int_\Omega |v|^2 d\overrightarrow{x} < \infty \right\} \tag{165}$$

The equation then becomes

$$0 = -v\nabla \cdot \left(\overrightarrow{J}_\theta\right) + vG \quad \text{in}\, \Omega \tag{166}$$

when v is multiplied to both sides.

Integrating over Ω,

$$0 = -\int_\Omega \left[v\nabla \cdot \overrightarrow{J}_\theta\right] d\overrightarrow{x} + \int_\Omega vG d\overrightarrow{x} \tag{167}$$

and applying the product rule

$$\nabla \cdot \left(v\overrightarrow{J}_\theta\right) = v\nabla \cdot \overrightarrow{J}_\theta + \nabla v \cdot \overrightarrow{J}_\theta \tag{168}$$

and substituting,

$$0 = -\int_\Omega \left[\nabla \cdot \left(v\overrightarrow{J}_\theta\right)\right] d\overrightarrow{x} + \int_\Omega \left[\nabla v \cdot \overrightarrow{J}_\theta\right] d\overrightarrow{x} + \int_\Omega vG d\overrightarrow{x} \tag{169}$$

According to the divergence theorem,

$$\int_\Omega \nabla \cdot \left(v\overrightarrow{J}_\theta\right) d\overrightarrow{x} = \int_{\partial\Omega} v\overrightarrow{J}_\theta \cdot \overrightarrow{n}\, ds \tag{170}$$

where $\partial\Omega$ denotes the boundary of Ω and $\overrightarrow{n}$ is the outward-pointing normal vector. Substituting again,

$$0 = -\int_{\partial\Omega} \mathrm{v}\,\overrightarrow{J}_\theta \cdot \overrightarrow{n}\,\mathrm{d}s + \int_\Omega \left[\nabla \mathrm{v} \cdot \overrightarrow{J}_\theta\right] \mathrm{d}\overrightarrow{x} + \int_\Omega \mathrm{vG}\,\mathrm{d}\overrightarrow{x} \tag{171}$$

Rearranging,

$$\int_{\partial\Omega} \mathrm{v}\,\overrightarrow{J}_\theta \cdot \overrightarrow{n}\,\mathrm{d}s = \int_\Omega \left[\nabla \mathrm{v} \cdot \overrightarrow{J}_\theta + \mathrm{vG}\right] \mathrm{d}\overrightarrow{x} \tag{172}$$

Replacing with the definition of flux from Equation 161 and substituting $\mathrm{r}_1 - \mathrm{r}_2$ for G,

$$\int_{\partial\Omega} \mathrm{v}\,\overrightarrow{J}_\theta \cdot \overrightarrow{n}\,\mathrm{d}s = \int_\Omega \left[-\mathrm{s}_\theta \nabla \mathrm{v} \cdot \nabla(\Delta\tilde{\mu}_\theta) + \mathrm{v}(\mathrm{r}_1 - \mathrm{r}_2)\right] \mathrm{d}\overrightarrow{x} \tag{173}$$

This leads to the final statement of the weak form for steady state surface transport and mass balance:

$$\begin{aligned} &\text{Find } \Delta\tilde{\mu}_\theta \in \mathrm{H}^1(\Omega) \text{ such that} \\ &\int_{\partial\Omega} \mathrm{v}\,\overrightarrow{J}_\theta \cdot \overrightarrow{n}\,\mathrm{d}s = \int_\Omega \left[-\mathrm{s}_\theta \nabla \mathrm{v} \cdot \nabla(\Delta\tilde{\mu}_\theta) + \mathrm{v}(\mathrm{r}_1 - \mathrm{r}_2)\right] \mathrm{d}\overrightarrow{x} \\ &\qquad\qquad \text{for all } \mathrm{v} \in \mathrm{H}^1(\Omega) \end{aligned} \tag{174}$$

The boundary flux term $\overrightarrow{J}_\theta \cdot \overrightarrow{n}$ may be both zero and nonzero. The flux is zero at boundaries where there is no TPB reaction. The flux is nonzero where there is a TPB, in which case $\overrightarrow{J}_\theta \cdot \overrightarrow{n} = \mathrm{r}_{\mathrm{tpb}}$ where $\mathrm{r}_{\mathrm{tpb}}$ is the rate of reaction. This rate is in general a complicated function of $\Delta\tilde{\mu}_\theta$, or alternatively θ, point defect concentrations within the mixed conductor, and potential difference between the mixed conductor and electrolyte [96]. In the case of small perturbation, however, it may be dramatically simplified by expressions arising from linear irreversible thermodynamics.

6.9.2 Interfacial reaction rates

Similarly to the treatment of the bulk pathway, reaction rates at the interfaces may be described in several ways. If the system is perturbed far from equilibrium, detailed phenomenological rate expressions provide good insight into the process but introduce

considerable complexity and complication. If the system is not perturbed far from equilibrium but is instead perturbed only slightly, then linear approximations may be made. In particular, the use of a direct relationship between the rate of the overall reaction and the reaction affinity can be employed. Such an approach neglects the detailed mechanisms of the reaction in favor of a simplified description of the rate.

6.9.2.1 Adsorption/dissociation rate

First, some postulation of the adsorption reaction and accompanying rate must be made. Assume the following simple dissociative adsorption

$$\frac{1}{2}\mathrm{O_2(g)} + \mathrm{s} = \mathrm{O(s)} \tag{175}$$

Expressed in terms of building units, then

$$\frac{1}{2}\mathrm{O_2(g)} = \{\mathrm{O(s)}\} \tag{176}$$

where $\{\mathrm{O(s)}\} = \mathrm{O(s)} - \mathrm{s}$. Following a similar definition as full bulk-pathway reduction of oxygen and elimination of the equilibrium terms, the affinity of the reaction is

$$\mathcal{A}_1 = \frac{1}{2}\Delta\mu_{\mathrm{O_2}}(\mathrm{g}) - \Delta\mu_\theta \tag{177}$$

where $\Delta\mu_\theta$ is the change in chemical potential of the building unit $\{\mathrm{O(s)}\}$. Because the adsorbed oxygen here is uncharged, $\Delta\mu_\theta = \Delta\tilde{\mu}_\theta$ and therefore can be used directly with the dependent variable of the surface transport simulation.

Expressing the reaction rate for tracer incorporation in terms of equilibrium thermodynamics,

$$\mathrm{r_1} = \mathrm{k_1^0}\left(\frac{1}{2}\Delta\mu_{\mathrm{O_2}}(\mathrm{g}) - \Delta\mu_\theta\right) \tag{178}$$

for a sufficiently small perturbation, where $\mathrm{k_1^0}$ is a rate parameter with units $\mathrm{mol^2\ J^{-1}\ m^{-2}\ s^{-1}}$ giving $\mathrm{r_1}$ units of $\mathrm{mol\,m^{-2}\,s^{-1}}$.

6.9.2.2 TPB rate

The reaction at the TPB is postulated as

$$\mathrm{O(s)} + \mathrm{V}^{\cdot\cdot}_{\mathrm{O,elyte}} + 2\mathrm{e}' = \mathrm{O}^{\mathrm{x}}_{\mathrm{O,elyte}} + \mathrm{s} \tag{179}$$

or, in terms of building units,

$$\{\mathrm{O(s)}\} + \{\mathrm{V}^{\cdot\cdot}_{\mathrm{O,elyte}}\} + 2\{\mathrm{e}'\} = \mathrm{nil} \tag{180}$$

where $\{\mathrm{O(s)}\} = \mathrm{O(s)} - \mathrm{s}$ is the adsorbed oxygen building unit, $\{\mathrm{V}^{\cdot\cdot}_{\mathrm{O,elyte}}\} = \mathrm{V}^{\cdot\cdot}_{\mathrm{O,elyte}} - \mathrm{O}^{\mathrm{x}}_{\mathrm{O,elyte}}$ is an electrolyte vacancy building unit, and $\{\mathrm{e}'\}$ refers to an itinerant or localized electron building unit. The reaction affinity can be expressed analogously to previous arguments using electrochemial potentials rather than chemical potentials as

$$\mathcal{A}_{\mathrm{tpb}} = \Delta\tilde{\mu}_\theta + \Delta\tilde{\mu}_{\mathrm{v,elyte}} + 2\Delta\tilde{\mu}_{\mathrm{e}} \tag{181}$$

The reaction rate is

$$\mathrm{r_{tpb}} = \mathrm{k^0_{tpb}}\left(\Delta\tilde{\mu}_\theta + \Delta\tilde{\mu}_{\mathrm{v,elyte}} + 2\Delta\tilde{\mu}_{\mathrm{e}}\right) \tag{182}$$

for a sufficiently small perturbation, where $\mathrm{k^0_{tpb}}$ is a rate parameter with units $\mathrm{mol^2\ J^{-1}\ m^{-1}\ s^{-1}}$ giving $\mathrm{r_{tpb}}$ units of $\mathrm{mol\,m^{-1}\,s^{-1}}$. If a uniform Fermi level is assumed, then $\Delta\tilde{\mu}_{\mathrm{e}}$ is fixed. Finally, if a reference electrode is place on the solid electrolyte next to the cathode, then $\Delta\tilde{\mu}_{\mathrm{v,elyte}} = 0$.

6.9.3 Impedance via surface pathway

6.9.3.1 Weak form for surface transport and mass balance in the case of alternating current perturbation

Suppose now that there is some small, alternating current perturbation applied on top of a steady state signal. The surface concentration c_θ then becomes a complex quantity with nonzero time derivative. Express the surface concentration as

$$\mathrm{c}_\theta = \overline{\mathrm{c}_\theta} + |\widehat{\mathrm{c}_\theta}|\mathrm{e}^{\mathrm{j}(\omega \mathrm{t} + \delta)} \tag{183}$$

where $\overline{c_\theta}$ is the steady state concentration, $|\widehat{c_\theta}|$ is the magnitude of the alternating perturbation, $j = \sqrt{-1}$, ω is the frequency of the applied signal, and δ is the phase shift of the concentration from the applied signal. Denote

$$\widehat{c}_\theta = |\widehat{c_\theta}|e^{j\delta} \tag{184}$$

and therefore

$$c_\theta = \overline{c_\theta} + \widehat{c}_\theta e^{j\omega t} \tag{185}$$

The other quantities can be written similarly.

Now, let the electrochemical potential of the adsorbed oxygen be expressed as

$$\tilde{\mu}_\theta = \tilde{\mu}_\theta^{eq} + \Delta\tilde{\mu}_\theta \tag{186}$$

where the change from equilibrium is

$$\Delta\tilde{\mu}_\theta = \overline{\Delta\tilde{\mu}_\theta} + \widehat{\Delta\tilde{\mu}_\theta}e^{j\omega t} \tag{187}$$

where $\overline{\Delta\tilde{\mu}_\theta}$ is the steady state portion and $\widehat{\Delta\tilde{\mu}_\theta}$ is the complex perturbation.

Since the electrochemical potential must be uniform at equilibrium, then

$$\nabla(\tilde{\mu}_\theta) = \nabla(\Delta\tilde{\mu}_\theta) = \nabla\left(\overline{\Delta\tilde{\mu}_\theta} + \widehat{\Delta\tilde{\mu}_\theta}e^{j\omega t}\right) \tag{188}$$

which lets the flux be expressed as

$$\overrightarrow{J}_\theta = -s_\theta\nabla\tilde{\mu}_\theta \tag{189}$$

$$= -\left(\overline{s_\theta} + \widehat{s}_\theta e^{j\omega t}\right)\nabla\left(\overline{\Delta\tilde{\mu}_\theta} + \widehat{\Delta\tilde{\mu}_\theta}e^{j\omega t}\right) \tag{190}$$

where $\overline{s_\theta}$ indicates steady state transport parameter and $\widehat{s}_\theta$ indicates the complex perturbation of the transport parameter.

Distributing and ignoring the second-order perturbed term,

$$\overrightarrow{J}_\theta \approx -\overline{s_\theta}\nabla\left(\overline{\Delta\tilde{\mu}_\theta}\right) - \left(\overline{s_\theta}\nabla\left(\widehat{\Delta\tilde{\mu}_\theta}\right) + \widehat{s}_\theta\nabla\left(\overline{\Delta\tilde{\mu}_\theta}\right)\right)e^{j\omega t} \tag{191}$$

Setting the steady state flux as

$$\overline{\overrightarrow{J}}_{\theta} = -\overline{s_{\theta}}\nabla\left(\overline{\Delta\tilde{\mu}_{\theta}}\right) \tag{192}$$

and the AC flux as

$$\widehat{\overrightarrow{J}}_{\theta} = -\left(\overline{s_{\theta}}\nabla\left(\widehat{\Delta\tilde{\mu}_{\theta}}\right) + \widehat{s}_{\theta}\nabla\left(\overline{\Delta\tilde{\mu}_{\theta}}\right)\right) \tag{193}$$

then

$$\overrightarrow{J}_{\theta} \approx \overline{\overrightarrow{J}}_{\theta} + \widehat{\overrightarrow{J}}_{\theta}\, e^{j\omega t} \tag{194}$$

The homogeneous generation term may similarly be expressed as

$$G = \overline{G} + \widehat{G}e^{j\omega t} \tag{195}$$

where $\widehat{G} = \widehat{r_1} - \widehat{r_2}$. Substituting these definitions into the original continuity equation (Equation 159), recognizing that the steady state terms sum to zero, executing the time derivative $\partial(\widehat{c_{\theta}}e^{j\omega t})/\partial t = j\omega\widehat{c_{\theta}}e^{j\omega t}$, and canceling out the $e^{j\omega t}$ factor,

$$j\omega\widehat{c_{\theta}} = -\nabla\cdot\widehat{\overrightarrow{J}}_{\theta} + \widehat{G} \quad \text{in}\,\Omega \tag{196}$$

Introducing the test function $v \in H^1(\Omega)$ and following analogous steps to the steady state case including integration over Ω and application of the product rule and divergence theorem, the following equation results:

$$\int_{\partial\Omega} v\,\widehat{\overrightarrow{J}}_{\theta}\cdot\overrightarrow{n}\,ds = \int_{\Omega}\left[\nabla v\cdot\widehat{\overrightarrow{J}}_{\theta} + v(\widehat{G} - j\omega\widehat{c_{\theta}})\right]d\overrightarrow{x} \tag{197}$$

Critical assumptions about the nature of the surface species and simulation must now be employed. Since the adsorbed oxygen is assumed to be fully dissociated and uncharged, then the electrochemical potential of the adsorbed oxygen is equivalent to the chemical potential

$$\mu_{\theta} = \mu_{\theta}^{0} + RT\ln\left(\frac{\theta}{1-\theta}\right) \tag{198}$$

where the site-limitation term is included because the chemical potential refers to the adsorbed oxygen building unit [88].

Taking the derivative of the chemical potential with respect to the surface coverage,

$$\frac{\partial \mu_\theta}{\partial \theta} = \frac{\mathrm{RT}}{\theta\,(1-\theta)} \tag{199}$$

Making a further approximation and assuming a linear, small perturbation then

$$\widehat{\theta} = \frac{\partial \theta}{\partial \mu_\theta}(\mathrm{ss}) \cdot \widehat{\mu_\theta} \tag{200}$$

where $\widehat{\mu_\theta}$ is the AC perturbation to the steady-state chemical potential $\overline{\mu_\theta} = \mu_\theta^{\mathrm{eq}} + \overline{\Delta\mu_\theta}$ and the derivative is evaluated using the steady state value of θ. The overall chemical potential is $\mu_\theta = \mu_\theta^{\mathrm{eq}} + \overline{\Delta\mu_\theta} + \widehat{\mu_\theta}\mathrm{e}^{\mathrm{j}\omega\mathrm{t}}$. Since the steady state change to the chemical potential is summed with the equilibrium chemical potential, the AC perturbation may be viewed as a change to the change of the chemical potential, similarly to Equation 187. That is, $\mu_\theta = \mu_\theta^{\mathrm{eq}} + \Delta\mu_\theta$ where $\Delta\mu_\theta = \overline{\Delta\mu_\theta} + \widehat{\Delta\mu_\theta}\mathrm{e}^{\mathrm{j}\omega\mathrm{t}}$. By this logic, $\widehat{\Delta\mu_\theta} = \widehat{\mu_\theta}$ and

$$\widehat{\theta} = \frac{\partial \theta}{\partial \mu_\theta}(\mathrm{ss}) \cdot \widehat{\Delta\mu_\theta} \tag{201}$$

If the perturbation is around OCV (equilibrium), then θ_0 can be used to evaluate the derivative. Recognizing that for this particular case $\Delta\widehat{\mu_\theta} = \Delta\widehat{\tilde{\mu}_\theta}$ because the adsorbed oxygen is not charged and in general that $\mathrm{c}_\theta = \Gamma\theta$, then

$$\widehat{\mathrm{c}_\theta} = \Gamma \frac{\theta_0\,(1-\theta_0)}{\mathrm{RT}} \cdot \widehat{\Delta\tilde{\mu}_\theta} \tag{202}$$

One final problem-specific adaptation is now performed to simplify further. If the AC problem is solved around OCV, then $\overline{\Delta\tilde{\mu}_\theta} = 0$ and $\nabla\left(\overline{\Delta\tilde{\mu}_\theta}\right) = 0$. Thus, the AC flux term (Equation 193) simplifies to

$$\widehat{\vec{J}}_\theta = -\overline{\mathrm{s}_\theta}\nabla\left(\widehat{\Delta\tilde{\mu}_\theta}\right) \tag{203}$$

where $\overline{\mathrm{s}_\theta}$ is simply the equilibrium s_θ parameter.

After substituting definitions for flux (Equation 203), homogeneous generation (Equation 195), and concentration (Equation 202) into the integral equation 197,

this leads to the final expression of the weak form for the perturbed case:

$$\begin{gathered}\text{Find } \widehat{\Delta\tilde{\mu}_\theta} \in \mathrm{H}^1(\Omega) \text{ such that} \\ \int_{\partial\Omega} \mathrm{v}\, \widehat{\overrightarrow{J}}_\theta \cdot \overrightarrow{n}\, \mathrm{ds} = \int_\Omega \left[\nabla \mathrm{v} \cdot \left(-\overline{\mathrm{s}_\theta} \nabla \left(\widehat{\Delta\tilde{\mu}_\theta} \right) \right) + \mathrm{v}(\widehat{\mathrm{r}_1} - \widehat{\mathrm{r}_2} - \mathrm{j}\omega\Gamma \frac{\theta_0\,(1-\theta_0)}{\mathrm{RT}} \cdot \widehat{\Delta\tilde{\mu}_\theta}) \right] \mathrm{d}\overrightarrow{x} \\ \text{for all } \mathrm{v} \in \mathrm{H}^1(\Omega)\end{gathered} \tag{204}$$

The boundary flux term $\widehat{\overrightarrow{J}}_\theta \cdot \overrightarrow{n}$ may be both zero and nonzero. The flux is zero at boundaries (1D edges of the surface domain) where there is no TPB reaction. The flux is nonzero at edges where there is a TPB, in which case $\widehat{\overrightarrow{J}}_\theta \cdot \overrightarrow{n} = \widehat{\mathrm{r}_{\mathrm{tpb}}}$ where $\widehat{\mathrm{r}_{\mathrm{tpb}}}$ is the AC perturbed rate of reaction.

6.9.3.2 Expression for perturbed reaction rates

Let r be the rate of some reaction–e.g. adsorption, dissociation, incorporation–which is dependent upon some set of parameters $\{\mathrm{p_i}\}$

$$\mathrm{r} = \mathrm{r}(\mathrm{p}_1, \mathrm{p}_2, \ldots, \mathrm{p}_\mathrm{n}) \tag{205}$$

The set $\{\mathrm{p_i}\}$ contains chemical potentials, fractional concentration of the adsorbed species, concentration of other relevant adsorbed species, concentration of relevant point defects within the mixed conductor, and any other parameters relevant to a phenomenological model of the rate of the particular reaction. In general r is nonlinear. At steady state, the parameter set is denoted $\{\overline{\mathrm{p_i}}\}$ and the rate is

$$\overline{\mathrm{r}} = \mathrm{r}(\overline{\mathrm{p}_1}, \overline{\mathrm{p}_2}, \ldots, \overline{\mathrm{p}_\mathrm{n}}) \tag{206}$$

which requires simultaneous solution for all parameters.

In simulating the response to an AC perturbation, the deviation from steady state is of interest. Here, the standard linearized approximation for impedance spectroscopy [128] will be employed, where only the first-order perturbations are considered. The

first-order, multi-variable, complex Taylor series expansion is appropriate

$$\begin{aligned} \mathrm{r}(\mathrm{p}_1, \mathrm{p}_2, \ldots, \mathrm{p}_\mathrm{n}) \approx \mathrm{r}(\overline{\mathrm{p}_1}, \overline{\mathrm{p}_2}, \ldots, \overline{\mathrm{p}_\mathrm{n}}) &+ \frac{\partial \mathrm{r}}{\partial \mathrm{p}_1}(\overline{\mathrm{p}_1}, \overline{\mathrm{p}_2}, \ldots, \overline{\mathrm{p}_\mathrm{n}}) \cdot (\mathrm{p}_1 - \overline{\mathrm{p}_1}) \\ &+ \frac{\partial \mathrm{r}}{\partial \mathrm{p}_2}(\overline{\mathrm{p}_1}, \overline{\mathrm{p}_2}, \ldots, \overline{\mathrm{p}_\mathrm{n}}) \cdot (\mathrm{p}_2 - \overline{\mathrm{p}_2}) \\ &+ \ldots \\ &+ \frac{\partial \mathrm{r}}{\partial \mathrm{p}_\mathrm{n}}(\overline{\mathrm{p}_1}, \overline{\mathrm{p}_2}, \ldots, \overline{\mathrm{p}_\mathrm{n}}) \cdot (\mathrm{p}_\mathrm{n} - \overline{\mathrm{p}_\mathrm{n}}) \end{aligned} \tag{207}$$

In accordance with the previous definition of the complex quantities let all parameters be expressed

$$\mathrm{p}_\mathrm{i} = \overline{\mathrm{p}_\mathrm{i}} + \widehat{\mathrm{p}_\mathrm{i}} \mathrm{e}^{\mathrm{j}\omega \mathrm{t}} \tag{208}$$

Therefore, the rate is given as

$$\begin{aligned} \mathrm{r} \quad \approx \quad \overline{\mathrm{r}} \quad &+ \frac{\partial \mathrm{r}}{\partial \mathrm{p}_1}(\overline{\mathrm{p}_1}, \overline{\mathrm{p}_2}, \ldots, \overline{\mathrm{p}_\mathrm{n}}) \cdot \widehat{\mathrm{p}_1} \mathrm{e}^{\mathrm{j}\omega \mathrm{t}} \\ &+ \frac{\partial \mathrm{r}}{\partial \mathrm{p}_2}(\overline{\mathrm{p}_1}, \overline{\mathrm{p}_2}, \ldots, \overline{\mathrm{p}_\mathrm{n}}) \cdot \widehat{\mathrm{p}_2} \mathrm{e}^{\mathrm{j}\omega \mathrm{t}} \\ &+ \ldots \\ &+ \frac{\partial \mathrm{r}}{\partial \mathrm{p}_\mathrm{n}}(\overline{\mathrm{p}_1}, \overline{\mathrm{p}_2}, \ldots, \overline{\mathrm{p}_\mathrm{n}}) \cdot \widehat{\mathrm{p}_\mathrm{n}} \mathrm{e}^{\mathrm{j}\omega \mathrm{t}} \end{aligned} \tag{209}$$

Similarly partitioning the rate into steady state and perturbed terms

$$\mathrm{r} = \overline{\mathrm{r}} + \widehat{\mathrm{r}} \mathrm{e}^{\mathrm{j}\omega \mathrm{t}} \tag{210}$$

and rearranging Equation 209 leads to the final expression for the perturbed portion of the rate

$$\begin{aligned} \widehat{\mathrm{r}} \quad = \quad &\frac{\partial \mathrm{r}}{\partial \mathrm{p}_1}(\overline{\mathrm{p}_1}, \overline{\mathrm{p}_2}, \ldots, \overline{\mathrm{p}_\mathrm{n}}) \cdot \widehat{\mathrm{p}_1} \\ &+ \frac{\partial \mathrm{r}}{\partial \mathrm{p}_2}(\overline{\mathrm{p}_1}, \overline{\mathrm{p}_2}, \ldots, \overline{\mathrm{p}_\mathrm{n}}) \cdot \widehat{\mathrm{p}_2} \\ &+ \ldots \\ &+ \frac{\partial \mathrm{r}}{\partial \mathrm{p}_\mathrm{n}}(\overline{\mathrm{p}_1}, \overline{\mathrm{p}_2}, \ldots, \overline{\mathrm{p}_\mathrm{n}}) \cdot \widehat{\mathrm{p}_\mathrm{n}} \end{aligned} \tag{211}$$

The complex quantity $\widehat{\mathrm{r}}$ should be computed for every relevant reaction and, if applicable, every sub-step. The quantity $\widehat{\mathrm{r}_{\mathrm{tpb}}}$ should be computed at the 1D TPB

boundaries and used in Equation 204 as the quantity $\widehat{\vec{J}_\theta} \cdot \vec{n}$. Likewise, $\widehat{\mathrm{r_1}}$ corresponding to adsorption/dissociation, $\widehat{\mathrm{r_2}}$ corresponding to incorporation, etc., should be used as appropriate on the 2D particle surfaces. The perturbed parameter set $\{\widehat{\mathrm{p_i}}\}$ is subject to simultaneous FEM solution of the multiphysics problem coupling the mixed-conductor surface and bulk as well as possibly the electrolyte bulk. The expression for the reaction rate perturbation derived here is in agreement with analogous formulations appearing in the literature [161].

Specifically, the reaction rate $\mathrm{r_1}$ in Equation 178 is adapted as

$$\widehat{\mathrm{r_1}} = \frac{1}{2}\mathrm{k_1^0}\widehat{\Delta\mu_{\mathrm{O2}}(\mathrm{g})} - \mathrm{k_1^0}\widehat{\Delta\mu_\theta} \tag{212}$$

recalling that $\Delta\mu_\theta = \Delta\tilde{\mu}_\theta$ when the adsorbed, dissociated oxygen is uncharged as in this case. When gas diffusion is not considered, then $\widehat{\Delta\mu_{\mathrm{O2}}(\mathrm{g})} = 0$.

The reaction $\mathrm{r_{tpb}}$ (Equation 182) is perturbed and linearized as

$$\widehat{\mathrm{r_{tpb}}} = \mathrm{k_{tpb}^0}\widehat{\Delta\tilde{\mu}_\theta} + \mathrm{k_{tpb}^0}\widehat{\Delta\tilde{\mu}_{\mathrm{v,elyte}}} + 2\mathrm{k_{tpb}^0}\widehat{\Delta\tilde{\mu}_{\mathrm{e}}} \tag{213}$$

When the voltage is applied relative to a reference electrode on the electrolyte close to the working electrode, then $\widehat{\Delta\tilde{\mu}_{\mathrm{v,elyte}}} = 0$. A uniform Fermi level gives a constant electron electrochemical potential: $\widehat{\Delta\tilde{\mu}_{\mathrm{e}}} = -\mathrm{F}\widehat{\Delta\mathrm{E}}$, where $\widehat{\Delta\mathrm{E}}$ is the AC potential perturbation applied to the working electrode.

6.9.4 Parameters

The important parameters in the surface simulation are the equilibrium fractional surface coverage, θ_0, the surface transport coefficient, s_θ, the two reaction rate parameters adsorption, $\mathrm{k_1^0}$ and TPB, $\mathrm{k_{tpb}^0}$, and the double layer capacitance, $\mathrm{C_{dl}}$.

In investigating the kinetics of porous platinum on YSZ, Mitterdorfer proposed an isotherm for surface coverage [111]. The fractional surface coverage ranged from 0.65 at $\mathrm{pO_2} = 1\,\mathrm{atm}$ and $T = 550°C$ to 0.05 at $\mathrm{pO_2} = 10^{-5}\,\mathrm{atm}$ and $T = 950°C$. $\theta_0 = 0.25$ was chosen as an initial value here for $\mathrm{pO_2} = 0.21\,\mathrm{atm}$ and $T = 700°C$.

The surface transport parameter bundles surface concentration and mobility

$$s_\theta = b_\theta c_\theta^0 = b_\theta \Gamma \theta_0 \tag{214}$$

where b_θ is the mobility and Γ is the concentration of surface sites: $1\text{x}10^{-5}$ mol m^{-2}. The mobility is related to the diffusion coefficient by the Einstein equation

$$b_\theta = \frac{D_\theta}{RT} \tag{215}$$

Mitterdorfer also provided an estimate for surface species diffusivity in the platinum/YSZ system [111] which can serve as a reasonable starting point for exploration of the LSM/YSZ system [108]. The diffusivity is

$$D_\theta = D_\theta^0 \exp(-E_\theta^a/(RT)) \tag{216}$$

with values given in Table 6.

Table 6: Surface diffusion coefficients derived from reference [111].

Parameter	Value	Units
D_θ^0	$4.65\text{x}10^{-4}$	$m^2\,s^{-1}$
E_θ^a	$1.41\text{x}10^5$	$J\,mol^{-1}$

There is very little in the literature on suitable quantification of the reaction rate parameter k_1^0 corresponding to adsorption and dissociation. For the purpose of simulating LSM, it will be assumed that k_1^0 is many times greater than the tracer-derived exchange rate constant k_{rdn}^0 (Equation 141) used in the bulk-only simulations. The initial value was set to $k_1^0 = 1000\,k_{rdn}^0$.

The reaction rate parameter of the TPB can be roughly estimated from existing porous electrode data for the LSM-YSZ system. Mitterdorfer measured the overall impedance and extracted a charge-transfer resistance associated with the TPB reaction for a sintered porous LSM electrode on YSZ [108]. The reported values were normalized to area, but can be approximately normalized to TPB length using the quantification of those values reported in the same paper. The resulting TPB-specific

resistivity associated with only the charge-transfer TPB reaction (having already removed the surface-transport contribution) may be expressed as ρ_{ct} in units of $\Omega\,m$. The conversion is given in Equation 217.

$$\rho_{ct} = ASR_{ct} \cdot L_{tpb} \tag{217}$$

where ASR_{ct} is the area-normalized charge-transfer resistance ($\Omega\,m^2$) and L_{tpb} is the TPB length density (m^{-1}). Best-available approximate values are given in Table 7.

Table 7: Charge-transfer resistance parameters derived from reference [108].

Parameter	Value	Units	Note
ASR_{ct}	$4.5x10^{-4}$	$\Omega\,m^2$	Testing temperature: 620°C
L_{tpb}	$2.50x10^{6}$	m^{-1}	Sample sintered at 1100°C, 2 h.

Assuming that $\Delta\tilde{\mu}_{tpb} = 2\Delta\tilde{\mu}_{e}$ when surface and gas transport contributions are removed, then $\Delta\tilde{\mu}_{tpb} \approx 2z_eF\Delta E$, where ΔE is the change of electrode potential. Now recognizing that $i_{tpb} = -2Fr_{tpb}$, then

$$i_{tpb} \approx -2F\left(k^0_{tpb}[2z_eF\Delta E]\right) \tag{218}$$

The resistivity, ρ_{ct} is the ratio of ΔE to i_{tpb}. Thus,

$$\rho^{-1}_{ct} \approx 4F^2k^0_{tpb} \tag{219}$$

and the estimate of k^0_{tpb} is obtained

$$k^0_{tpb} \approx \left(4F^2\rho_{ct}\right)^{-1} \tag{220}$$

Finally, the double layer capacitance was taken as $5.5x10^{-2}\,F\,m^{-2}$ as per the value fit to sintered porous LSM on YSZ [108].

6.9.5 Results and Discussion

The AC impedance for the surface model was simulated using a 140 x 134 x 140 voxel segment of the reconstructed porous LSM electrode on polycrystalline YSZ

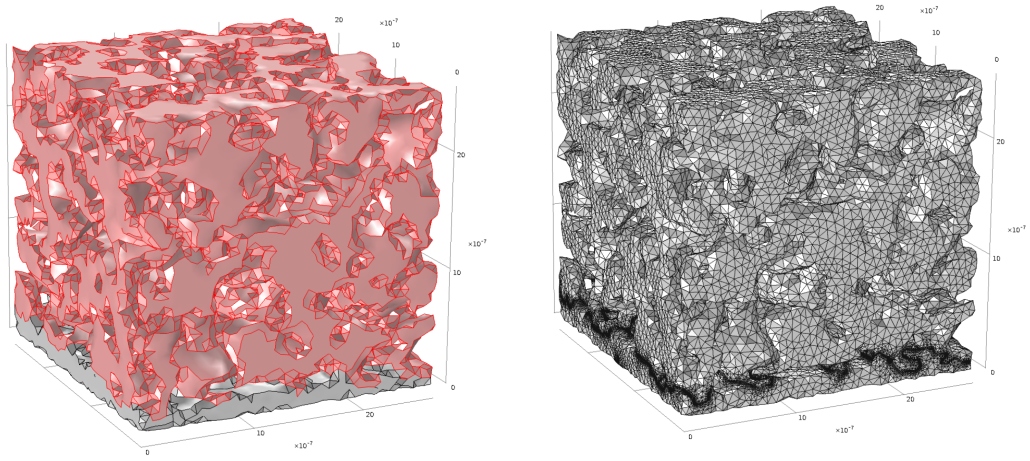

(a) (b)

Figure 66: Portion of reconstructed microstructure used for surface/TPB pathway simulation: a) Microstructure segment rendered by COMSOL, b) Meshed microstructure with 8x TPB mesh refinement. Side length is approximately 2.7 μm.

(approximate dimensions are 2.7 μm x 2.5 μm x 2.7 μm. The mesh along the TPB lines was refined eight times. The structure is shown in Figure 66.

The area-normalized impedance arising from the microstructure using the initial parameter set (previous section: 6.9.4) is shown in Figure 67. Since the impedance is with respect to a reference electrode placed on the solid electrolyte very close to the cathode, there is no Ohmic resistance associated with the simulated impedance. There are two impedance loops shown. The first, "Ads/diss/trans", indicated by square markers corresponds to the impedance associated with adsorption, dissociation, and surface transport process. The high-frequency real impedance intercept of approximately 2 $\Omega\,\mathrm{cm}^2$ is the charge-transfer resistance associated with the TPB. The second loop, "All processes", is the total impedance arising from the cathode including the adsorption, dissociation, and transport processes with TPB reaction impedance all in parallel with interfacial LSM-YSZ capacitive double-layer charging. The low-frequency loop corresponds to the adsorption, dissociation, and transport processes while the high-frequency loop corresponds to the relaxation associated with the interfacial capacitance and TPB reaction impedance. The characteristic angular

frequencies associated with the two relaxation processes are indicated.

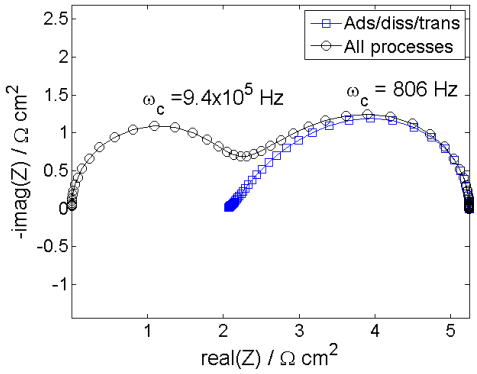

Figure 67: AC impedance from surface/TPB pathway of reconstructed microstructure using initial parameter set.

6.9.5.1 Parameter investigation

To better understand the effect of the individual parameters on the impedance, they were systematically varied and compared to the impedance arising from the original parameter set. The effect of increasing the double-layer capacitance is shown in Figure 68. The adsorption and transport-related impedance is unchanged but the shape of the overall impedance is significantly modified. The alteration is the result of the characteristic frequency of the charging-TPB relaxation process decreasing with larger interfacial capacitance. The loops from each relaxation process are more thoroughly merged with a 10x change (a) and are completely merged with a 100x increase (b). The Nyquist plot appears to have only one important process when such a complete merger occurs.

The effect of changing the TPB rate parameter k^0_{tpb} is shown in Figure 69. The rate parameter has a marked impact upon the high-frequency loop diameter and a significant impact upon which process dominates. Reducing k^0_{tpb} (a and b) makes the TPB reaction more sluggish and therefore increases the resistance associated with it, making the high-frequency loop diameter larger. A 100x decrease in the rate parameter makes the entire impedance spectrum almost completely dominated by

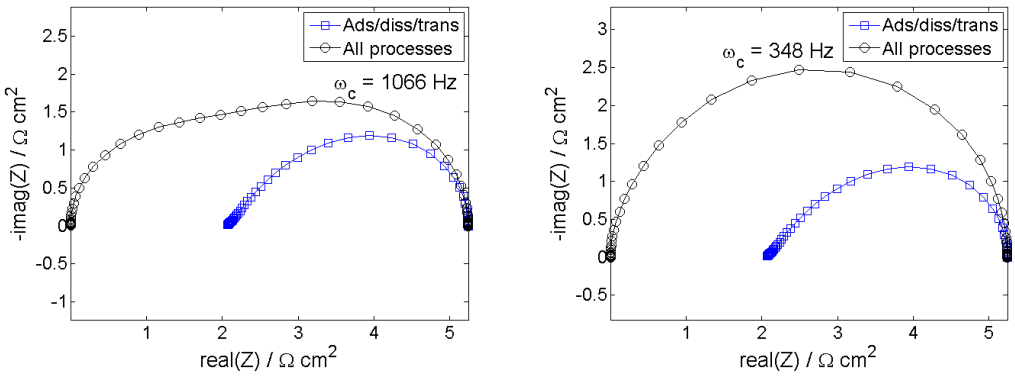

Figure 68: Impedance arising from a) 10x and b) 100x increase in C_{dl}, based on the original parameter set.

charge transfer. An increase to the rate parameter, on the other hand, makes the TPB reaction more facile and decreases the high-frequency loop diameter. A 100x increase in k^0_{tpb} (d) causes the impedance to be dominated solely by the process of adsorption, dissociation, and surface transport. The impedance associated with adsorption, dissociation, and transport is unaffected by the TPB rate parameter.

Impedance changes associated with varying the surface diffusion coefficient D_θ are shown in Figure 70. The low-frequency loop diameter associated with surface transport becomes larger as D_θ is decreased and shrinks as it is increase, reflecting a decrease or increase if the facility of surface transport, respectively. The characteristic frequency associated with the processes are not substantially affected by the diffusion coefficient, so even though the impedance increases or decreases in magnitude, the frequencies over which the processes occur are relatively unaffected.

The effect of varying the adsorption/dissociation parameter k^0_1 is shown in Figure 71. Decreasing the parameter increases the size of the low-frequency loop because it reduces the rate of resupply of adsorbed oxygen and therefore creates a bottleneck. Conversely, increasing k^0_1 provides easier resupply of adsorbed oxygen and a more facile reaction/diffusion pathway and smaller low-frequency loop diameter.

An important phenomenon that accompanies changing k^0_1 is the effect upon the

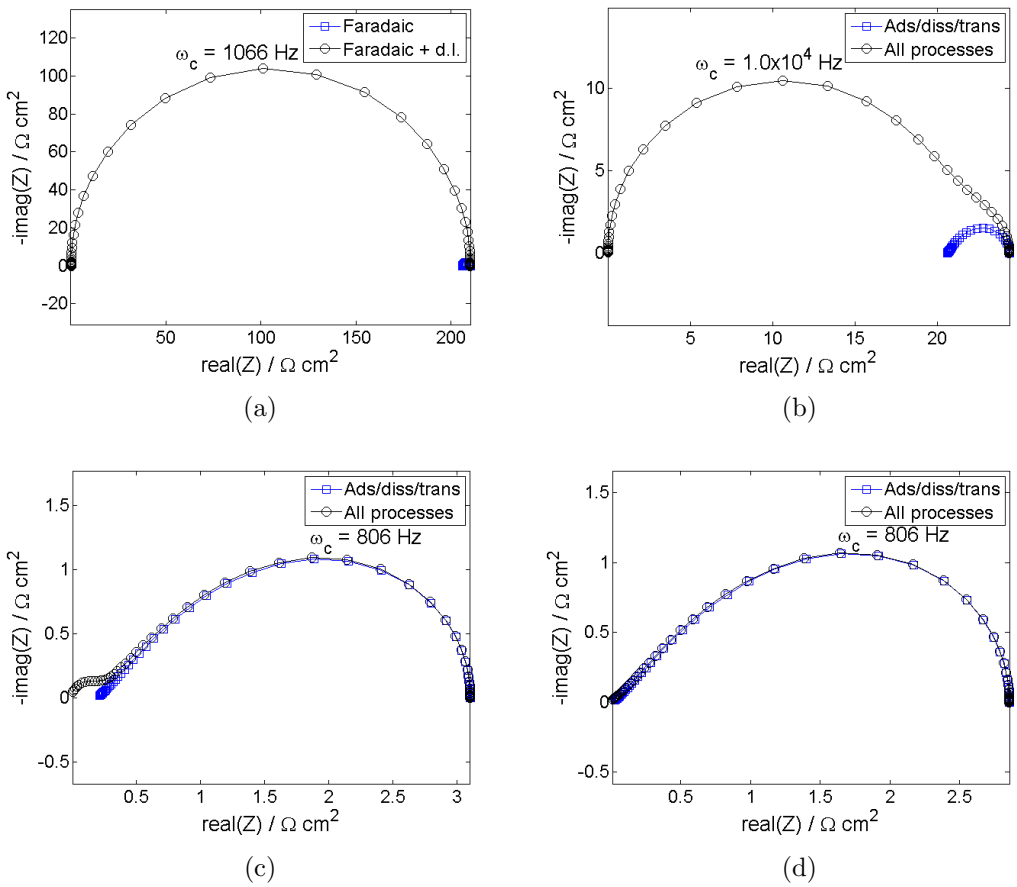

Figure 69: Impedance arising from a) 10^{-2}, b) 10^{-1}, c) 10^{1}, and d) 10^{2} change in k^0_{tpb}, based on the original parameter set.

characteristic frequency of the adsorption/dissociation/transport relaxation process. The characteristic frequency of the process as a function of k^0_1 multiplier is shown in Figure 72. As the rate parameter increases, the characteristic frequency increases as well.

6.9.5.2 Comparison with experimental values

The experimental results for the cathode fabricated by spray coating commercial LSM powder and sintering at 1150°C are shown in Figure 36 and tabulated in Table 8. At the median temperature of 700°C, the R_p was 179 $\Omega\,cm^2$ and ω_c was 50 Hz. Therefore, the model's polarization resistance with the default parameter set (Figure 67) was

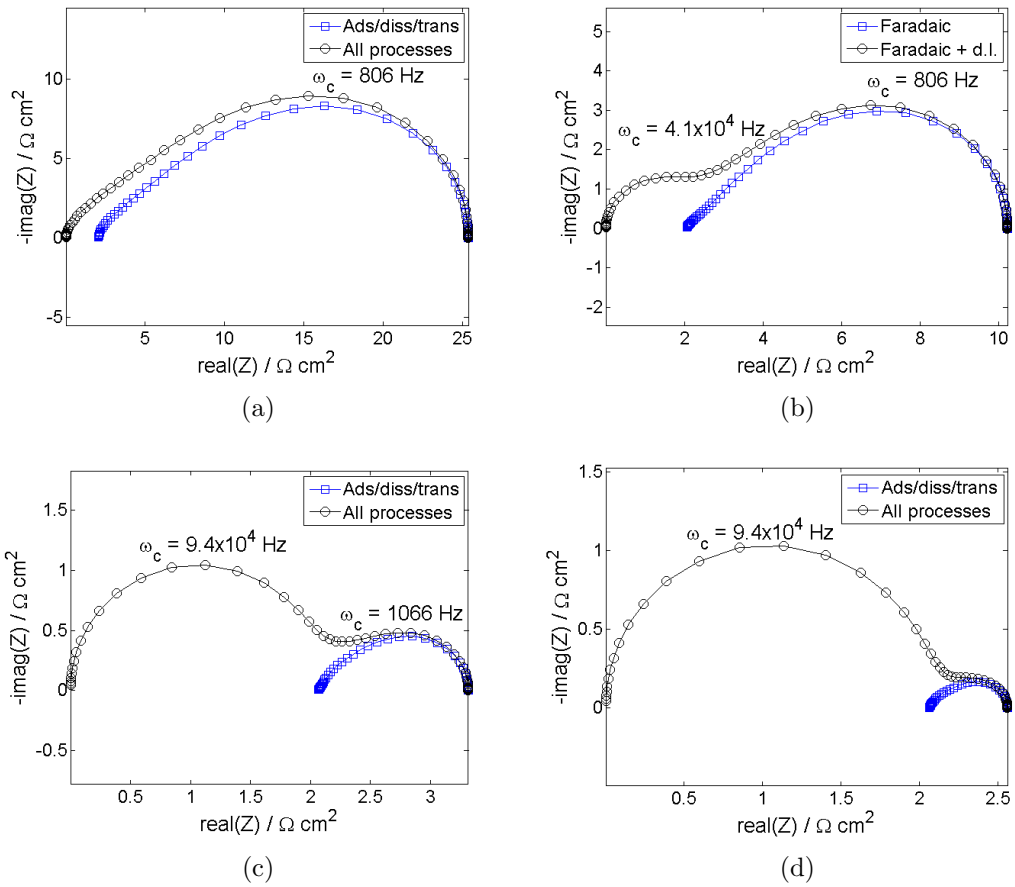

Figure 70: Impedance arising from a) 10^{-2}, b) 10^{-1}, c) 10^{1}, and d) 10^{2} change in D_θ, based on the original parameter set.

approximately 36 times smaller than than the experimental measurement. Furthermore, the default model parameterization gave a characteristic frequency that was approximately 16 times larger than the experimental value.

The Nyquist plot of the the impedance from this study at 700°C is replotted in Figure 73a with Ohmic resistance removed. The impedance spectrum is one arc, but there is a slight asymmetry: the left-hand side (high-frequency) shoulder appears to have a small bulge at real(Z) $\approx 25\,\Omega\,\mathrm{cm}^2$, indicating that there could be at least two relaxation processes. At higher frequencies than that, the slope of the line is diagonal rather than vertical. The asymmetry is more apparent at higher temperatures

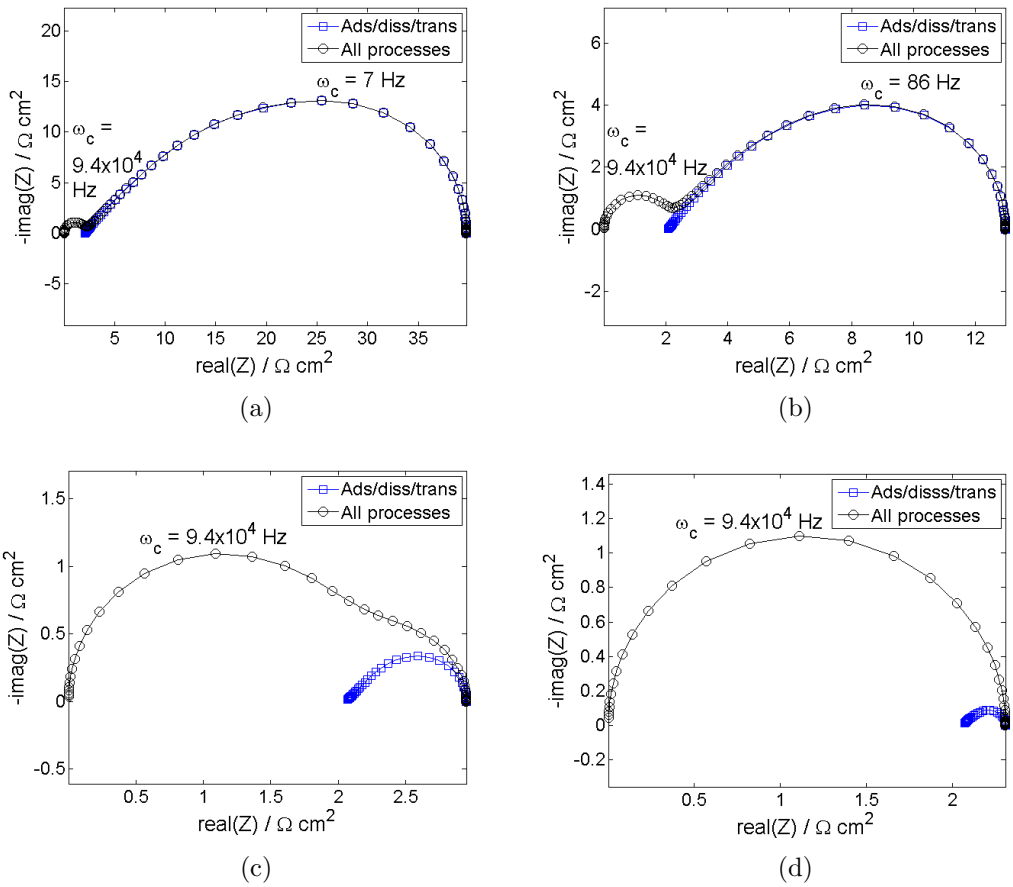

Figure 71: Impedance arising from a) 10^{-2}, b) 10^{-1}, c) 10^{1}, and d) 10^{2} change in k_1^0, based on the original parameter set.

Table 8: Polarization resistance and characteristic angular frequency of porous LSM electrode on dense YSZ derived from spray-coated commercial powder from this study. All cathode processes included. Electrode was sintered at 1150°C.

Testing temp. (°C)	Parameter	Value	Units	Note
600	R_p	1615	$\Omega\,cm^2$	
	ω_c	5	Hz	
650	R_p	546	$\Omega\,cm^2$	
	ω_c	16	Hz	
700	R_p	179	$\Omega\,cm^2$	
	ω_c	50	Hz	
750	R_p	64	$\Omega\,cm^2$	
	ω_c	125	Hz	
800	R_p	27	$\Omega\,cm^2$	
	ω_c	396	Hz	

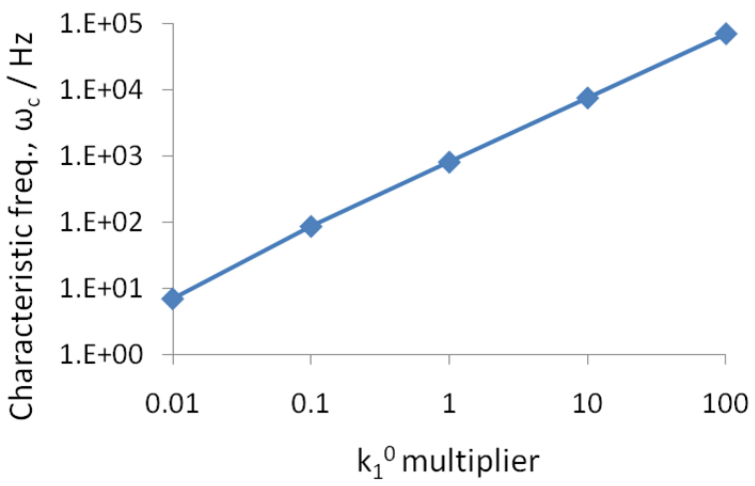

Figure 72: The effect of k_1^0 upon the characteristic frequency of the relaxation process associated with adsorption, dissociation, and transport.

(Figure 36) and its shape is reminiscent of that arising from an equivalent circuit containing a Gerischer element in series with a resistor, both in parallel to a capacitor. The physical meaning of the Gerischer element is reaction-diffusion, which could correspond to the process of adsorption, dissociation, and surface transport. The resistor could correspond to a charge-transfer, while the capacitor in parallel corresponds to interfacial capacitance. A similar equivalent circuit was suspected by Mitterdorfer to describe LSM on YSZ [108].

With an equivalent circuit corroborating the very same physical processes represented in this chapter by the microstructure-specific surface model, the model parameters were tailored by changing them from their default values. The resulting simulated impedance is shown in Figure 73b. The impedance loop representing all cathode processes is very similar in size (R_p), shape, and frequency distribution - in both the low- and high-frequency relaxation processes - to the experimental impedance. The curve associated with adsorption, dissociation, and transport shows that these processes are responsible for the low-frequency feature. The high-frequency bulge is a relaxation between the TPB charge-transfer resistance and interfacial charging which overlaps

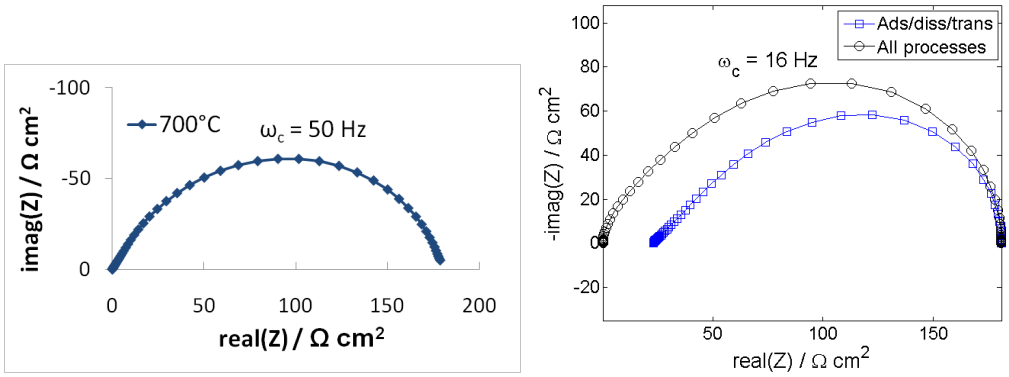

Figure 73: a) Experimental complex impedance plot without Ohmic resistance, testing temp of 700°C. LSM powder was commercial, spray coated onto dense YSZ, and sintered at 1150°C. b) Simulated impedance with tailored model parameters, T=700°C.

with the adsorption, dissociation, and transport process.

The tailored parameters required to generate the simulation in Figure 73b are given in Table 9. The diffusion coefficient was reduced substantially from the value on platinum at 700°C; however, considering the large differences between the surfaces of platinum and LSM, the difference is not unreasonable. The surface adsorption/dissociation coefficient was made to be 30 times larger than the tracer-derived isotope exchange coefficient, k^0_{rdn}, rather than 1000 time larger as initially assumed. The TPB rate constant k^0_{tpb} was set to be about 10% of the value of the rate constant derived from sintered LSM, which is reasonable considering the uncertainties associated with estimating TPB length [108] and with differences in sintering profiles. The interfacial capacitance C_{dl} was made to be 20 times the value derived from porous, sintered LSM. However, the interfacial capacitance on sintered LSM was taken as the average over an entire area including contacted and non-contacted area. The uncertainties with contact area can explain some of the difference, along with the lack of *quantitative* fitting. The new C_{dl} value is closer the interfacial capacitance derived from porous platinum on YSZ [111]. All of these parameters could be substantially

affected by the differences between this study and the literature in the exact chemical composition of the LSM powder as well as in the sintering step. The conformal FEM tool developed here is a powerful tool for probing the kinetics of a porous LSM cell in a quantitative manner while taking into account all of these material and process-dependent specifics - a tool that has never been available before.

Table 9: Tailored surface model parameters.

Parameter	Value
D_θ	$0.01 \cdot D_\theta^{(Pt)}$
k_1^0	$30 \cdot k_{rdn}^{0,(LSM)}$
k_{tpb}^0	$0.09 \cdot k_{tpb}^{0,(sint.LSM)}$
C_{dl}	$20 \cdot C_{dl}^{(sint.LSM)}$

The distribution of adsorbed oxygen electrochemical potential is shown in Figure 74. The depletion length is approximately 0.5-1 μm. Close views (b and c) show that there appears to be variation in the electrochemical potential parallel to the electrode, caused by the microstructure.

An important observation is that the surface model may be used to accommodate low-frequency relaxation processes. Other authors [83] have concluded that a bulk process explains the electrochemical behavior of an LSM cathode, in particular the low characteristic frequencies. However, it is seen here that the adsorption/dissociation rate coefficient has a large effect upon characteristic frequency (Figure 72). Moreover, bulk explanations require the equilibrium vacancy concentration of LSM to be far too high compared to all LSM bulk defect chemistry models. It therefore appears that the surface/TPB pathway is a more realistic explanation for the electrochemical behavior than the bulk pathway.

To further increase the agreement between model and experiment, the pure interfacial double-layer capacitance, C_{dl}, was substituted for a constant phase element (CPE). The important parameters of the CPE are Q and α, whose roles are shown in Equation 221. The parameter α varies between 0 and 1. The closer to 1, the

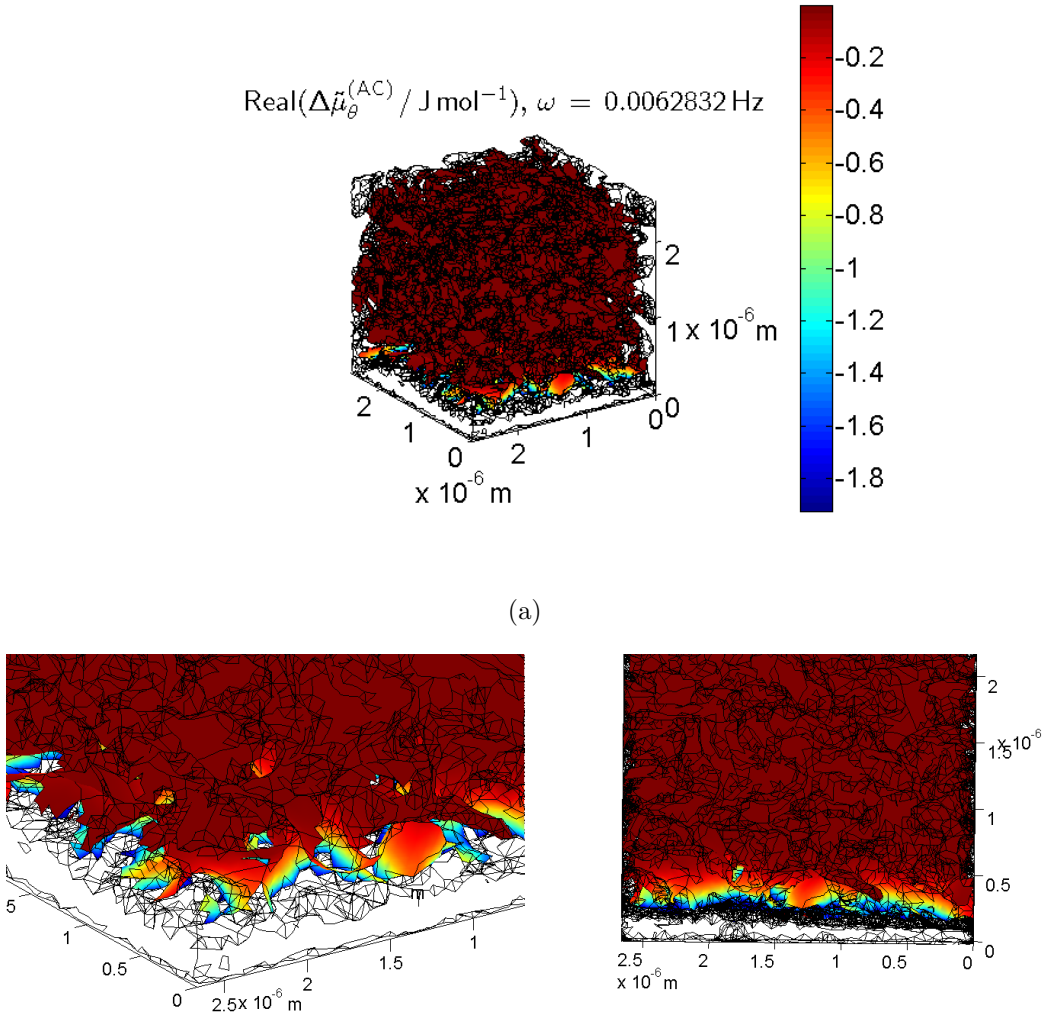

(a)

(b)

(c)

Figure 74: Distribution of adsorbed oxygen electrochemical potential in the reconstructed microstructure. a) Wide view, b) and c) two close views. T=700°C, $\widehat{\Delta \mathrm{E}} = -1\mathrm{x}10^{-5}\,\mathrm{V}$.

closer the CPE impedance is to that of an ideal resistor. Q corresponds with the capacitance, though has different units and can vary substantially from the actual value of capacitance [128]. In general, CPEs are used to fit experimental data whose interfacial capacitance is distributed over range of values due to a combination of microstructural and chemical composition inhomogeneities.

The simulated impedance spectrum with CPEs did appear closer in shape to the

experimental impedance: the slope of the curve at high- and low-frequency became diagonal to the real impedance axis as opposed to vertical. Two simulated impedance spectra with different values of CPE parameter Q are shown in Figure 75. The CPE exponent α in both cases was 0.7.

$$Z_{CPE} = \frac{1}{Q\,(j\omega)^{\alpha}} \tag{221}$$

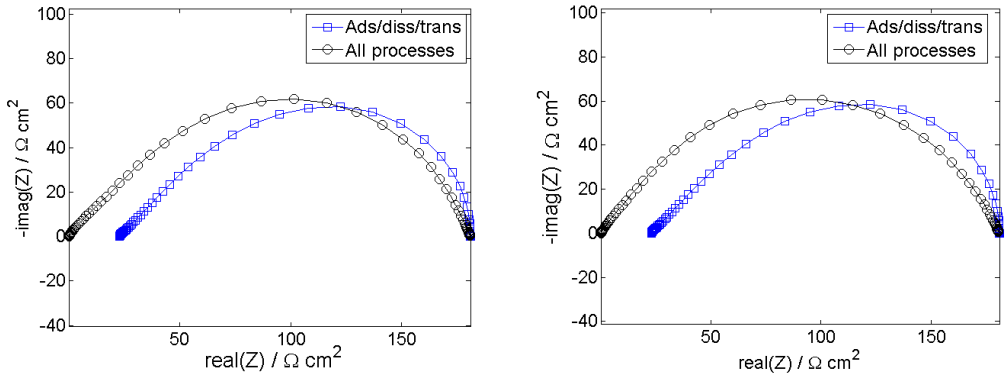

Figure 75: Simulated impedance spectra using tailored parameter set and CPE instead of pure interfacial capacitor: a) $Q = 5 \cdot C_{dl}$, b) $Q = 10 \cdot C_{dl}$. T=700°C, $\alpha = 0.7$.

6.9.5.3 Role of near-TPB micro/nano-structure: theoretical study

To investigate the role of near-TPB micro/nano-structure in overall response, a simple geometric model was assembled consisting of a flat, dense electrolyte and simple LSM solids making a circular contact with diameter 200 nm. The exact shape of the LSM was varied and the effect on the impedance was examined. Each shape had a 200-nm circular contact with the electrolyte and all impedance was normalized to TPB length.

Volumetric data - voxels belonging to the LSM and electrolyte - was generated by custom MATLAB script according to the desired morphology, always carefully preserving the constant TPB structure. The mesh near the TPB line was refined eight

times. The tailored parameter set corresponding to the commercial LSM powder-derived electrodes was used for surface electrochemical simulation at 700°C.

As a baseline, a cylindrical morphology was used for the LSM, yielding an impedance and an adsorbed oxygen low-frequency electrochemical potential distribution in Figure 76. The impedance spectrum had a similar general shape as that of the porous electrode (Figure 73b), though with distinct differences at high frequencies (left-hand side of the spectrum). The depletion distance of the adsorbed oxygen was between 0.5 and 1 μm, similar to the observation from the previous porous electrode simulation (Figure 74). The cylindrical shape made it the 3D analogue of the standard 1D model typically used to interpret data from porous LSM electrodes.

An expanding cylinder was then generated and simulated (Figure 77). The steady state R_p of this structure was notably lower than the pure cylinder. The decrease in polarization resistance could be attributed to more surface available for resupply of the TPB reaction, making the adsorption, dissociation, transport process more facile. The increase in surface area occurs because the radius of the solid increases with distance from the TPB. This result demonstrates that the micro/nano-structure in the near-TPB region *does* have the ability to appreciably impact the electrochemical response when surface reaction and surface transport is an important component of the impedance.

A second variation of the cylindrical structure is to consider the effect of possible connections with other particles in the near-TPB region. A cylindrical cross-beam was added to the structure at several different points, two of which are shown in Figure 78. When the cross-beam was placed at the edge of the adsorbed oxygen depletion region, it had little effect upon the impedance (Figure 78a and b). However, when the cross-beam was placed well within the depletion region, the impedance was decreased (Figure 78c and d). The effect was suspected to be caused by the addition of surface area in the near-TPB region which was close enough to participate in transport to the

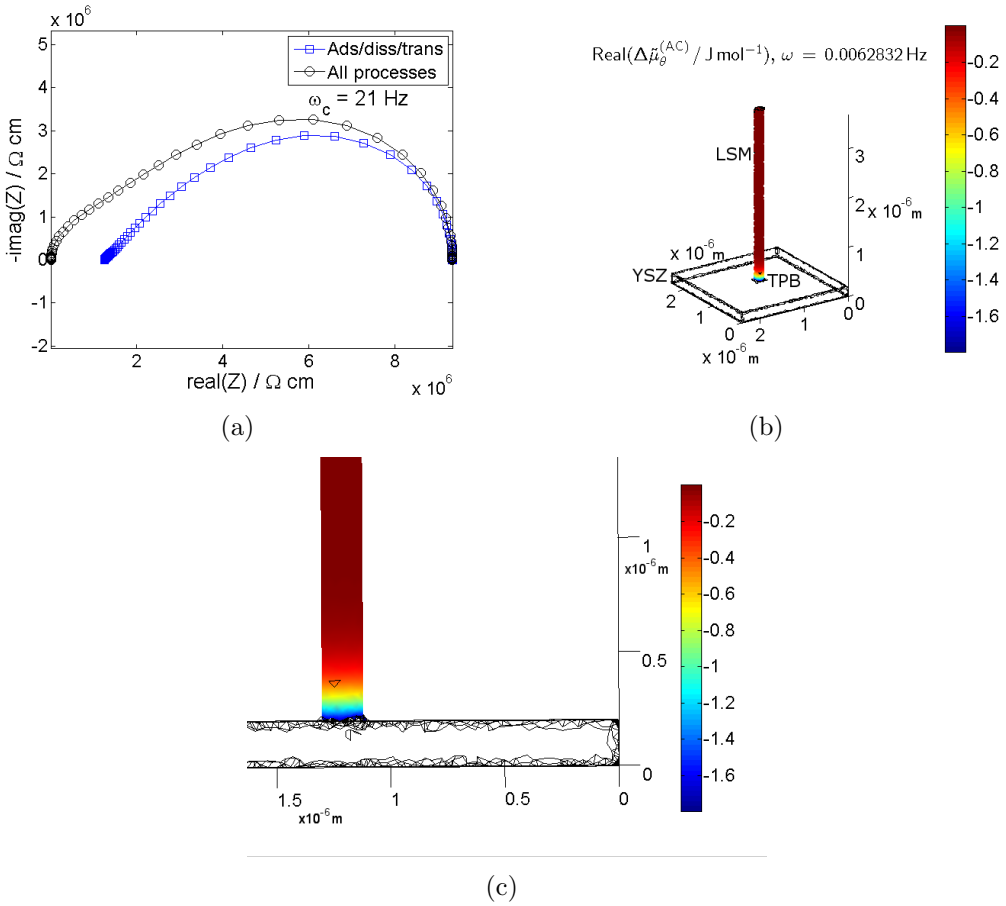

Figure 76: Results using the baseline cylindrical LSM structure: a) Simulated electrochemical impedance spectrum, normalized to TPB length. b) Real change of adsorbed oxygen electrochemical potential at low frequency (axis units are length, in m). c) Close side view of b). T=700°C, $\widehat{\Delta E} = -1\text{x}10^{-5}$ V.

TPB. Figure 78e shows a close view of the effect of the cross-beam on the adsorbed oxygen electrochemical potential field, in particular how it is distributed over a larger region than on a plain cylinder. These results indicate that a nanostructured network of particles in the near-TPB region could be beneficial for the activity if it provides increased surface area to aid transport to the reaction sites.

A third variation was to simulate the effect of particle necks. The cylinder surface was replaced by one where the radius was computed by a sine function, while maintaining the 200-nm diameter contact with the electrolyte. An example is shown in Figure 79. For a very small neck size and short distance to the neck from the TPB, the

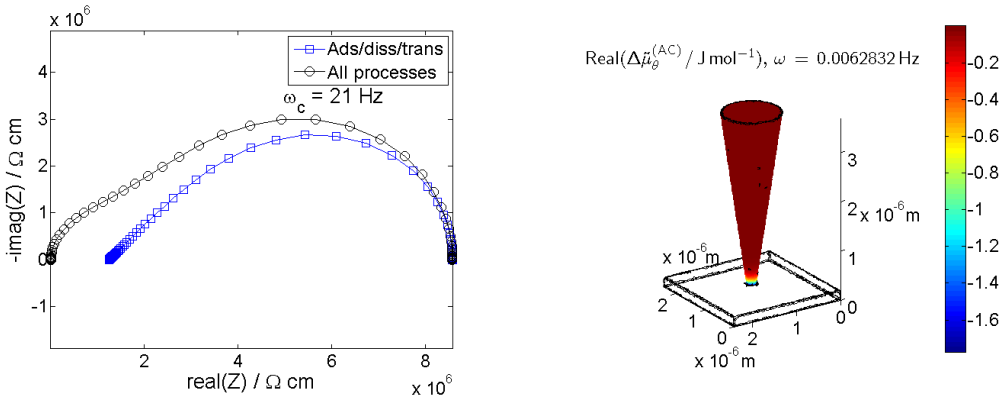

Figure 77: Expanding LSM cylinder structure: a) Simulated electrochemical impedance spectrum, normalized to TPB length. b) Real change of adsorbed oxygen electrochemical potential at low frequency (axis units are length, in m). T=700°C, $\widehat{\Delta E} = -1x10^{-5}$ V.

surface adsorption, dissociation, and transport is impeded and R_p increases. A direct comparison of Figure 79d to Figure 76c shows that the depletion length is forced to be shorter than the case of a pure cylinder when a neck inhibits surface transport.

This investigation into the effect of near-TPB micro/nano-structure indicates that morphology in this region is important to the overall electrochemical response of the TPB when adsorption, dissociation, and surface transport limit or co-limit the response. Given several different configurations, the TPB-normalized impedance changed significantly. It is not enough to consider only the TPB length of a given microstructure, nor is it enough to interpret the results of a porous LSM electrode experiment with a 1D model. It is also not enough to consider the total surface area: the cross-beam simulation demonstrated that added surface area even 1-1.5 μm from the TPB may not impact the response. Clearly, the nanostructure *near* the TPB is critical to the response. Conformal finite element modeling of the electrochemistry occurring on the surfaces and TPBs provides the necessary tools for rational design at this level. It allows the effect of nanostructure to be simulated, visualized, and can be of use in providing target nanostructures for novel cathodes fabricated based

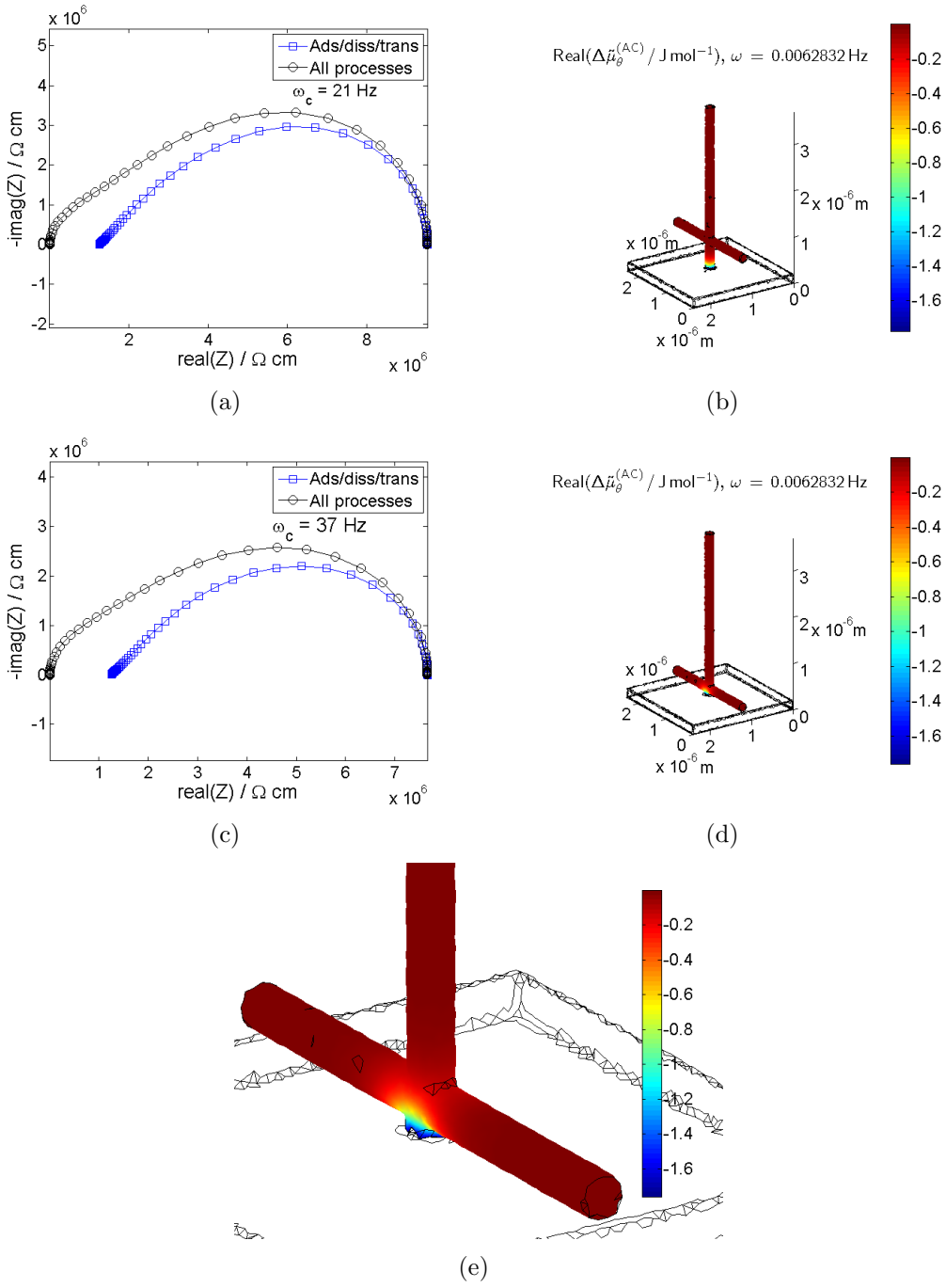

Figure 78: LSM cylinder with cross-beam. Cross-beam on edge of depletion zone: a) Simulated TPB-normalized impedance, b) real change of adsorbed oxygen electrochemical potential at low frequency. Cross-beam within depletion zone: c) Simulated TPB-normalized impedance, d) real change of adsorbed oxygen electrochemical potential at low frequency, e) close view of d). T=700°C, $\widehat{\Delta E} = -1\text{x}10^{-5}$ V.

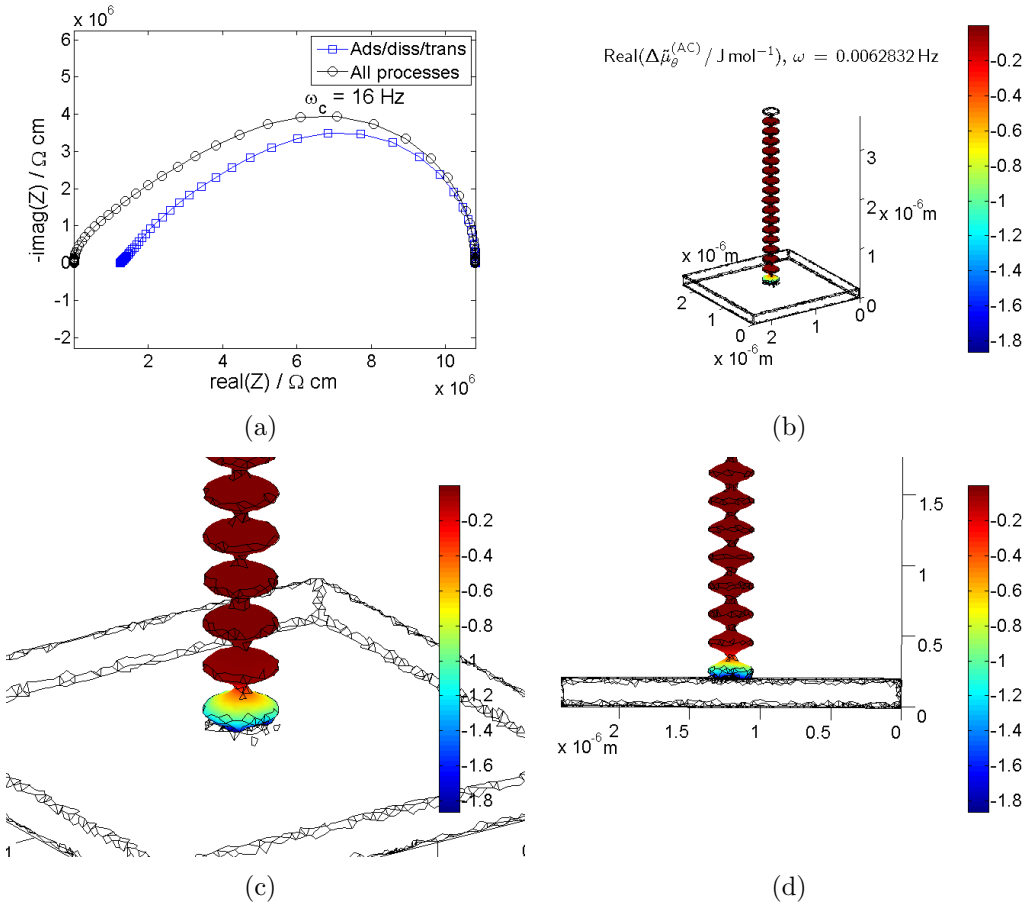

Figure 79: LSM particles described by sine function: a) Simulated TPB-normalized impedance, b) real change of adsorbed oxygen electrochemical potential at low frequency, c) and d) close views of b). T=700°C, $\widehat{\Delta E} = -1\text{x}10^{-5}$ V.

upon these design principles.

6.10 Conclusion

In this chapter, several means of multiphysics simulations on a 3D digital electrode representation were assessed. The voxel-by-voxel method and slice extrusion methods were found to be unwieldy and impractical. The direct meshing method proved to be very practical. The open-source package iso2mesh was combined with the commercial packages COMSOL Multiphysics and MATLAB to mesh volumetric data representing the porous structure, apply relevant transport and electrochemical equations, and solve the finite element problem. The use of commonly available packages with

minimal custom coding makes the technique within the reach of the general audience interested in the role of microstructure. This technique allows both the surface pathway and the bulk pathway to be simulated, which is important in making the modeling technique applicable to a wide variety of candidate cathode materials such as LSM, whose surface pathway is dominant, and LSCF which is a very good mixed conductor and therefore has a dominant bulk pathway.

In particular, the bulk pathway of LSM was examined using a refined mesh and found to be very small under cathodic bias, in agreement with the general understanding of LSM. The role of the bulk pathway was visualized under successively larger cathodic bias and found to increase in both utilization length and oxygen vacancy concentration, resulting in Tafel-like polarization behavior. The bulk pathway was also examined for various mixed conductors described by the empirical relationship between the surface exchange coefficient and the oxygen tracer diffusivity.

The surface pathway was also examined for LSM. Electrochemical impedance spectra were simulated for a wide selection of parameter values and agreement with experiments was found. The electrochemical impedance of porous LSM on a dense YSZ electrolyte is likely dominated by this surface pathway, as opposed to the bulk pathway which contributes very little current at OCV. The surface model can be extended to porous composite cathodes.

The effect of near-TPB particle micro/nano-structure was evaluated using the surface model. When oxygen adsorption, dissociation, and surface transport limit or co-limit the electrochemical response, the near-TPB region was found to be critical to the impedance. Generally more surface area available for oxygen adsorption within the depletion zone was found to increase performance, but severe particle necks were found to hinder surface transport and decrease performance. The finite element modeling tool developed in this chapter provides a means of further investigation of this effect and provides a quantitative tool for rational design of nanostructures

complying with these design principles in novel cathodes.

Developing a tool that can apply the finite element method to transport constitutive equations on the surface and in the bulk of a mixed conductor is a critical component in the rational design of SOFC cathode materials. This technique allows the fine details of microstructure to be fully taken into consideration in a DC or AC condition. It also allows simple or very complex reaction rate expressions to be used, and therefore links together several modeling scales. Quantum chemical models can provide insight into reaction mechanisms, which can inform phenomenological models and can predict local reaction rates based upon the potential/concentration fields described by the finite element solution of transport on the detailed microstructure. If desired, the FEM solution could inform higher levels of modeling. FEM modeling that can capture such detail is an important step in moving toward implementing the rational design philosophy in SOFC cathodes.

CHAPTER VII

CONCLUSION

The SOFC cathode is a critical component and in need of further development to aid widespread SOFC commercialization. This need for improvement is especially true at intermediate temperatures where cheaper components in other parts of the fuel cell may be used. Among the main challenges facing SOFC cathodes are the activity toward the oxygen reduction reaction and the competition between active surfaces and transport pathways. Heretofore, design of SOFC cathodes has tended to be empirical owing to the lack of mechanistic understanding and multi-scale modeling tools. In order to achieve rational design, better fundamental understanding and quantitative engineering tools are required. The objective of this work was to develop and use tools for the modeling, simulation, and rational design of SOFC cathodes.

Some of the contributions of this thesis are targeted to thin-film test cells with well-controlled geometries. A focus at this level is important to modeling and simulation of porous SOFCs because it provides fundamental understanding of mechanisms and constitutive equations for important processes by removing complications associated with geometry. Models conformal to the porous structure, a second major emphasis of this thesis, are informed by that level of focus and as a consequence are made more accurate, relevant, and significant.

The specific contributions to the development of modeling tools include:

1. Extension of phenomenological reaction rate modeling technique to include the triple phase boundaries between a mixed conductor and electrolyte, taking into account transport limitations on local electrical state, concentration fields of point defect and adsorbed oxygen atoms, and material geometry

2. Development of a numerical finite volume method for application to a patterned mixed conducting electrode

3. Establishment of a tool to aid the design of thin-film mixed-conducting test cells with respect to sheet resistance, and presentation of design charts

4. Application of phenomenological reaction rate expressions to thin-film mixed-conducting test cell experiments

5. Development of a novel use of conservative point defect ensembles and a method of unpacking the ensembles at interfaces to enable efficient finite element simulations using few variables under large nonlinear cathodic driving forces

6. Development of a 3D finite element method modeling approach using commercial/open source packages and custom coding that is conformal to the particles comprising a porous SOFC cathode providing maximum accessibility to a wide audience

7. Treatment of bulk and surface pathways in the conformal modeling approach

8. Implementation of an algorithm to refine the finite element mesh in the vicinity of triple phase boundaries in conformal, porous mesh

Specific contributions to the fundamental understanding of SOFC cathode materials include:

1. Study of the role of TPB versus bulk contributions in LSM patterned electrodes

   (a) A potential for bulk-pathway dominance over the TPB/surface pathway at moderate bias was demonstrated.

   (b) The effect of sheet resistance on electrical potential and kinetics was illustrated.

(c) Physical parameter values were investigated.

2. The effect of sheet resistance upon electrochemical impedance measurements

   (a) A high-frequency feature was discovered as the result of severe sheet resistance limitation in thin-film test cells.

   (b) The implications of sheet resistance upon global test cell measurements was examined and found to be substantial in some cases.

   (c) It appears to be possible in general to design a test cell that may reduce or eliminate the practical effects of sheet resistance upon thin-film test cell experiments if the proper precautions are observed with respect to current collector spacing and film thickness. This is not always true for very active materials or large cathodic bias, however.

3. Explanation of the experimentally observed increase in electrocatalytic activity and long-term stability of LSM-coated LSCF thin-film test cell and porous electrodes under a cathodic bias

   (a) LSM surface modification of LSCF which leads to enhanced performance and increased stability is suspected to be caused by better cathodic activation, better adsorption properties, and interdiffusion to form a hybrid LSM(C) layer.

   (b) The insight into the role of the Mn ion, cathodic activation, and stability of LSM(C) provides new directions in novel SOFC cathode development.

4. Examination and imaging of the relative role of the bulk and surface pathways in LSM in a porous electrode

   (a) The role of key parameters in the bulk and surface pathway were examined, with the effects of parameters visualized in terms of utilization/depletion length and impedance spectra.

(b) The surface pathway of LSM appears to dominate at OCV, but the bulk pathway is strongly activated under cathodic bias leading to increased utilization length and much larger relative contribution to electrochemical reduction of oxygen.

(c) The study of the bulk activation of LSM is believed to be the first-ever confirmation and visualization of this effect in porous LSM.

5. Investigation of the near-TPB nanostructure in LSM/YSZ

(a) The near-TPB nanostructure appears to be critical to determining the electrochemical response of the TPB when oxygen adsorption, dissociation, and surface transport limit or co-limit the behavior.

(b) TPB length alone is not an adequate descriptor of the activity of the TPB to oxygen reduction; surface area within a small region near the TPB critically affects the response by providing more facile supply of adsorbed oxygen to the TPB

(c) Particle necks can hinder additional benefit of added surface area.

The work detailed in this thesis will aid future fundamental investigations of cathode MIEC properties, including thin-film and patterned electrode investigations through the TPB phenomenological model and the sheet resistance-mitigation modeling. It will also be of use to the engineering design of porous cathodes through the use of conformal finite element modeling with or without conservative defect ensembles. The 3D FEM technique accounts for the local fine details of microstructure and can use sophisticated, phenomenological reaction rate kinetics that consider the complexities of point defect chemistry, local electrical state, and adsorbed oxygen concentration. Rational design approaches to SOFC cathode development can use these tools and apply these gains in fundamental knowledge for a more effective and scientific means of improving the prospects of commercial SOFC viability.

CHAPTER VIII

RECOMMENDATIONS

The work described in this thesis has provided both fundamental knowledge and useful tools for the modeling, simulation, and rational design of porous SOFC cathodes. There are a number of exciting new directions and possibilities for future research.

The coupling of sophisticated reaction rate and transport modeling with real microstructure is of particular interest. The approach developed for meshing and applying FEM models has opened the door to a wide range of microstructure-specific work. First, by using the conservative defect ensemble approach, the behavior of the SOFC cathode under large bias can be examined. With the proper knowledge of defect chemistry and other fundamental properties, a wide variety of mixed conductors can be simulated under various conditions of bias. Composite electrodes of LSM/YSZ, other electronic/ionic conductor combinations, or even composites of several mixed conductors can also be handled on a microstructure-specific level. Using the targeted mesh refinement, TPBs or interfaces can be selectively refined anywhere in the electrode where necessary. In addition to simulations performed here involving a uniform Fermi level, the contribution of electronic defects should also be considered for more accuracy, in particular near the TPBs where current constriction is likely to play a role [48]. Finally, the inclusion of gas diffusion would be helpful for large segments of microstructure or situations where concentration polarization could be significant.

The microstructure-specific modeling technique has also opened up important avenues for novel microstructural optimization having several advantages over more traditional electrode modeling. PET-type models require an input of porosity, tortuosity, surface area, and other homogenized microstructure descriptors for simulation

of performance. The models, of course, will provide some result no matter what combination of parameters is given to them, whether realistic or not. It is difficult to know whether combinations that optimize performance are achievable or realistic. Other models on the electrode-level assume spherical particles, simple kinetics, or make other compromises that degrade accuracy or usefulness in design.

Given the results of this thesis, it is now possible to use a *realistic* microstructure with sophisticated kinetics for electrode optimization. The starting point could be volumetric data, such as the data set from x-ray microtomography. In fact, one could start with a real microstructure as a baseline, perform a simulated annealing algorithm or other type of microstructural reconstruction, and then examine the performance of the modified structure by FEM. The use of a simulated annealing algorithm would help to determine optimal heat treatments or starting particle sizes. Such methods would implicitly apply rules to keep the microstructure realistic. Alternatively, one could begin with a hypothetical microstructure generated by some algorithm that enforces reasonableness: a code that generates a microstructure that could result from, for example, combustion chemical vapor deposition or the glycine nitrate process with certain basic rules enforced (porosity, minimum solid grouping size, connectivity) could be the starting point for volumetric data. Simulation results could be used to "suggest" morphologies or arrangements of particles that could lead to novel structures. Experimentalists could look for ways to fabricate the recommended structures if performance gains promise to be significant. Since the algorithms developed here are relatively cheap to run on a computer, performing such numerical experiments could be an excellent alternative to slow and costly heuristic laboratory experimentation with microstructure.

The size of computations is also an exciting area for future efforts. The work reported in this thesis was performed on a desktop computer and, therefore, limited in system resources and in the microstructure included in the simulations. The logical

next step is to begin using cluster computing to leverage memory and parallelization. Both COMSOL and MATLAB are capable of running efficiently on cluster. In particular, COMSOL's solvers can run in parallel in a shared memory configuration on a single node. Parametric studies (useful for impedance) or other suitable tasks can be run on many nodes in a distributed memory configuration. At the time of writing of this thesis, the microstructure simulations had been run successfully on the FoRCE cluster through the Partnership for an Advanced Computing Environment (PACE), Office of Information Technology (OIT) on the Georgia Tech campus and scale-up was underway.

The fundamental study of the mechanisms of oxygen reduction on MIECs remains an important focus area. Further use of patterned and thin-film electrodes of LSM, LSCF, and other mixed conductors studied under cathodic bias and a variety of gaseous atmosphere is recommended in conjunction with bulk-pathway and TPB-pathway phenomenological modeling. The guidelines on design for sheet resistance should be followed or extended to ensure that sheet resistance will not interfere with the measurements.

Multi-scale model coupling with DFT or other quantum chemical calculations is also a very useful way to discover likely reaction pathways, mechanisms, energetics, rate constants, and mobilities. Since so much of the study of MIECs relies on indirect observation, DFT provides perhaps the most direct access to such phenomena. In particular, the use of more standard LSM stoichiometries than those used in the past ($LaMnO_3$ and LSM 55 have been studied in detail but not LSM 82), evaluation of the adsorption and dissociation process onto LSM without the presence of an oxygen vacancy (due to their relative scarcity), the effect of A- and B-site vacancies on adsorption (due to their relative abundance), establishment of adsorption isotherms and fractional surface coverage, and computation of surface mobility would be particularly helpful.

One interesting modification of the phenomenological modeling approach is to allow for the possibility of metallic or semi-metallic MIEC band structure. Currently, the phenomenological models assume a small polaron structure because it is a good descriptor of LSM 82 and LSCF 6428. Therefore, the concentration of electron holes and/or electrons appears explicitly in the rate expressions. A mixed conductor with semi-metallic band structure, such as LSC, would need a term in the rate expression corresponding to electron *enthalpy* rather than concentration [4]. Making such modification is not incompatible with transition state theory, but would require a knowledge of the local density of states [87] at the surface. Quantum chemical modeling could provide this information.

The modeling investigation into LSM modification of LSCF has provided fundamental insight into the reason for stability and performance enhancement. It has also informed ongoing experiments on further modification of LSCF that could result in even better enhancements. Continued theoretical evaluation of candidate surface modifiers will be beneficial to guiding this research effort.

Finally, the techniques developed here were targeted specifically to the modeling, simulation, and rational design of SOFC cathode materials. Nevertheless, they provide a useful framework for design of other electrochemical devices, namely SOFC anodes, batteries, and supercapacitors. Applicability is especially true for the 3D FEM modeling, which can be directly used with digital reconstructions of many types of porous electrochemical devices.

APPENDIX A

LSM-MODIFIED LSCF: MODELING INVESTIGATION

A.1 Surface layer stability analysis

TEM micrographs of the as-deposited sol-gel coated flat, polished LSCF surface are given in Figure A-1. They indicate that the LSM layer was crystalline and epitaxial with the underlying LSCF prior to long-term annealing.

TEM micrographs of the sol-gel coated flat, polished LSCF surface after long-term annealing are given in Figure A-2. They indicate a loss of crystallinity in the top 40 nm of the coated film, but preservation of crystallinity and epitaxy in the bottom 10 nm portion that is on the interface with the underlying LSCF.

A.2 Bulk cathodic activation model

The model of section 4.3.2 links current simply to oxygen vacancy concentration. This simplistic kinetic treatment is justified because the oxygen reduction process via the bulk pathway of the MIEC is generally regarded as requiring oxygen vacancies for incorporation into the bulk as well as, in some cases, for promoting oxygen adsorption/dissociation onto the surface [22, 124, 158]. Focusing only on the surface and neglecting all other sources of impedance such as mass transport, electronic resistance, and loss over the electrolyte-MIEC phase boundary, then the cathodic overpotential, η, can be linked to the change in the effective internal oxygen partial pressure, $pO_2^{internal}$, of the MIEC

$$\eta = \frac{RT}{nF} \ln\left(\frac{pO_2^{internal}}{pO_2^0}\right) \tag{A-1}$$

where pO_2^0 is the gas-phase equilibrium oxygen partial pressure and n = 4 is the number of electrons associated with oxygen reduction. Equation A-1 can be rearranged

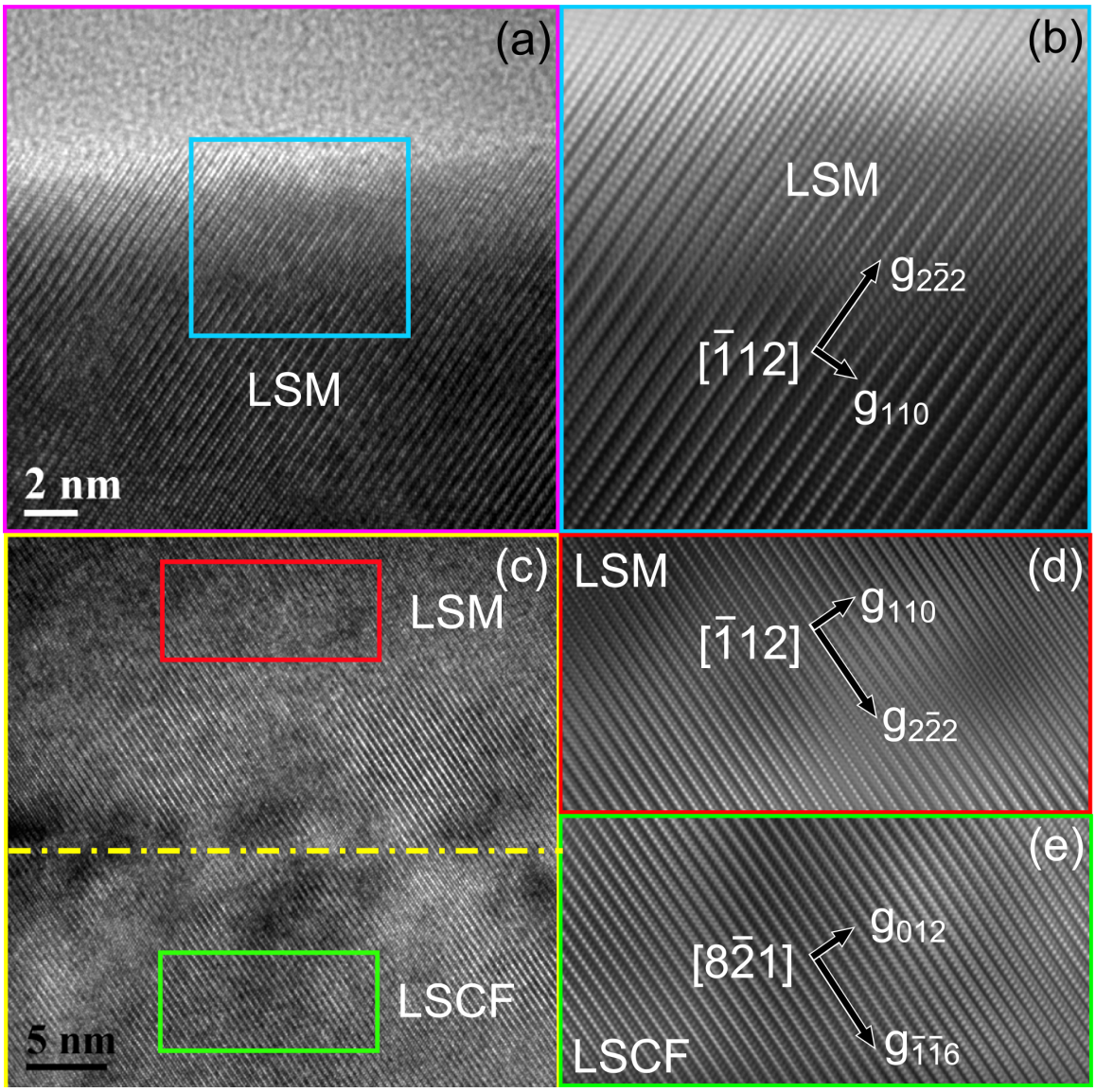

Figure A-1: TEM micrographs of the as-prepared LSM-coated LSCF pellet by the sol-gel method with one hour anneal at 900°C. The zone-axis lattice fringes in the a) surface and b) Fourier-filtered image of the light-blue rectangle in (a) show that the LSM film is crystalline, with perovskite structure. c) HRTEM image at the interface between the two phases, showing epitaxy between the underlying LSCF and deposited LSM. (d) and (e) are Fourier-filtered images of the red and green rectangles in (c) in the two phases near their interface. The lattice fringes of LSM extend from the bottom to the top of the film indicates that the film is single-crystalline throughout the entire thickness. Figure was created by Wentao Qin, who performed the microscopy.

to give $pO_2^{internal}$ as a function of η. This is a well-known approximation in solid state ionics.

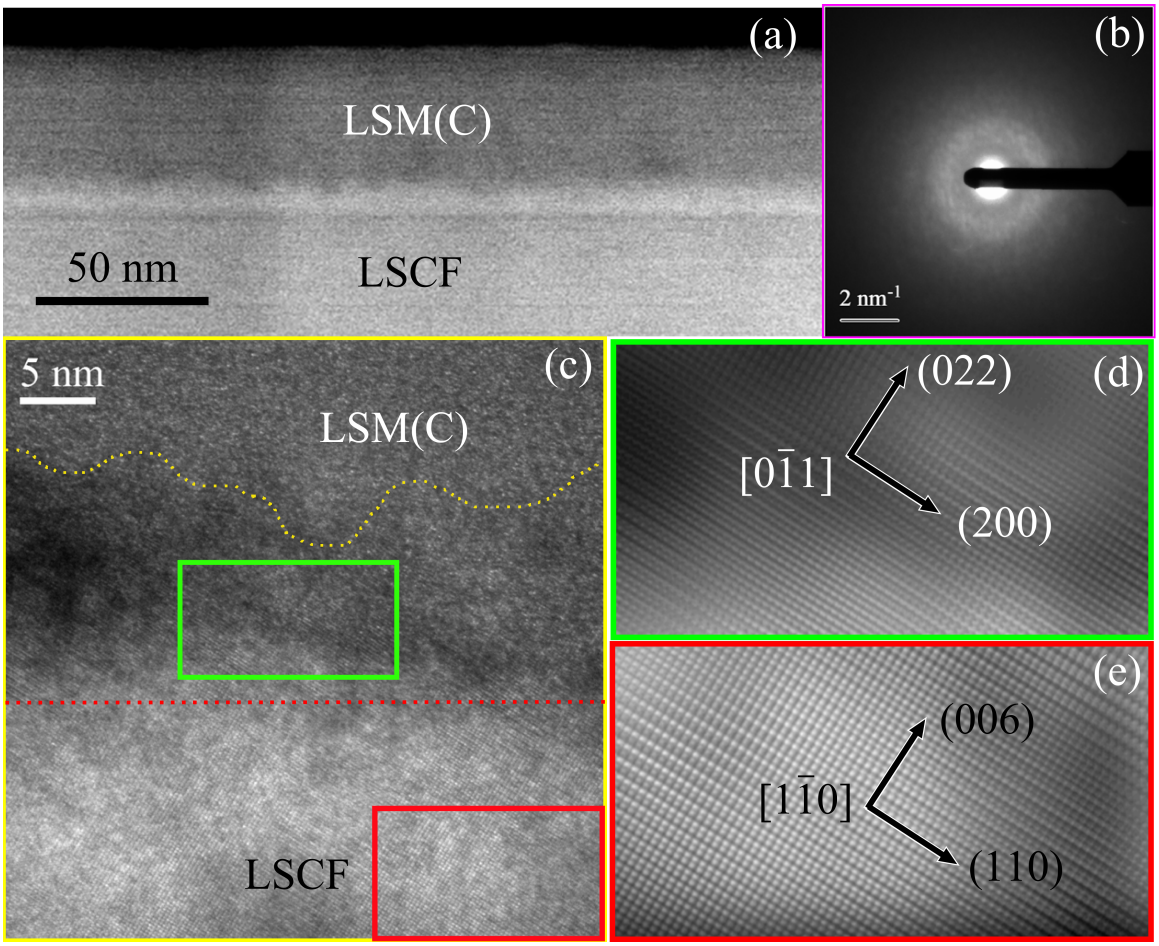

Figure A-2: TEM micrograph of the pellet surface after long-term annealing (850°C, 900 h). a) Z-contrast image of the interface. b) CBED indicating amorphous structure in the top 40 nm of the surface layer. Crystallinity is retained in bottom 10 nm near the LSCF interface. c) HRTEM image of the interface region. The yellow dashed curve marks the termination of lattice fringes on the LSM(C) side. The red dashed line corresponds to the interface seen in Figure 3(b) and the Z-contrast image in (a). d) and e) are Fourier-filtered images of the green and red rectangles in (c). The zone-axis lattice fringes in (d) indicate that epitaxial, perovskite crystal structure is retained in the bottom (crystalline) portion of the LSM(C) on the interface. e) The zone-axis lattice fringes in the bulk LSCF indicate that the perovskite structure is preserved. Figure was created by Wentao Qin, who performed the microscopy.

Point defect concentrations of $La_{0.6}Sr_{0.4}Co_{0.2}Fe_{0.8}O_{3-\delta}$ and $La_{0.8}Sr_{0.2}MnO_{3\pm\delta}$ used for this analysis are represented in the Brouwer diagram in Figure A-3 and computed using published models [13, 104]. Note that both models describe LSCF and LSM as hopping-type semiconductors.

In order to determine the point defect concentration at some η, the value of $pO_2^{internal}$ associated with η (Equation A-1) was used as the x-axis variable of the Brouwer diagram to determine the steady state defect point defect concentrations under the bias. The equilibrium point defect concentration were those dictated by the temperature and pO_2^0. The concentrations under η were those dictated by temperature and $pO_2^{internal}$.

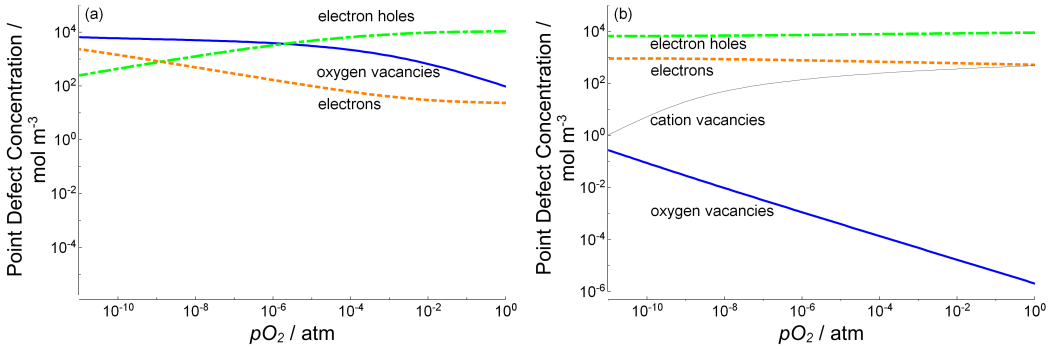

(a) (b)

Figure A-3: Brouwer diagrams showing computed bulk point defect equilibrium at 700°C of a) LSCF 6428 (according to its published defect model [13]) and b) LSM 82 (according to its published defect model [104]). Both models assume semiconducting small polaron electronic states.

The bulk point defect chemistries of LSM versus LSCF are markedly different from one another. Though both materials have been described by a small polaron model for their electronic defects [13, 104, 131], the magnitude of the oxygen vacancy concentrations and their behavior under sub-atmospheric pO_2's are quite different. Namely, the oxygen vacancy concentration of LSCF is quite high, leading to high tracer diffusivity and oxygen surface exchange, and may be directly measured by techniques such as TGA or coulometric titration. LSM, in contrast, has very low oxygen vacancy concentration and is generally regarded as superstoichiometric with respect to oxygen at equilibrium partial pressures because the A- and B-site vacancy concentrations are large. The exact equilibrium oxygen vacancy concentration is experimentally inaccessible in LSM precisely because of the large cation vacancy

concentration and so only estimates of it are available from models [104,113,131,163].

Despite the small oxygen vacancy concentration, there is evidence of an appreciable bulk pathway contribution from LSM in the literature [16, 82, 84, 144]. The bulk pathway is especially activated under a large cathodic bias [16, 144], an effect attributed to a large addition of oxygen vacancies to the LSM under polarization. Koep demonstrated that the contribution of the bulk increased with decreasing film thickness [82], showing that the bulk pathway of LSM depends in part on diffusion limitation. Thus, it seems possible for the LSM coating to be strongly activated under cathodic polarization due to large relative oxygen vacancy concentration increase with the requirement that it be very thin in order to mitigate oxygen vacancy transport losses.

The Brouwer diagram offers a guide to the strong activation of LSM. Oxygen vacancy concentration increases steadily with decreasing pO_2. LSCF in contrast has a much larger oxygen vacancy concentration at near-atmospheric pO_2, but the concentration does not increase as much relative to its initial value as pO_2 decreases. The change in oxygen vacancy concentration with pO_2 is directly proportional to the quantity commonly referred to as the thermodynamic factor of vacancies.

Figure A-4 is a plot of the oxygen vacancy concentration versus pO_2 without log-scale y-axis. Note that the LSM curve is concave up over the entire region. The LSCF curve has an inflection point at approximately 10^{-3} atm, where the sign of the second derivative of c_v changes.

Putting together the proportionalities for overpotential (Equation A-1) and current (Equation 70) shows that R_i is proportional to the inverse of the slope of the curves in Figure A-4.

$$R_i \propto -\frac{\partial \ln\left(pO_2^{int}\right)}{\partial c_v} = -\left(\frac{\partial c_v}{\partial \ln\left(pO_2^{int}\right)}\right)^{-1} \tag{A-2}$$

Since LSM has a positive second derivative over all relevant pO_2 values, R_i continuously decreases with decreasing $\log(pO_2^{internal})$). Since the c_v curve of LSCF initially

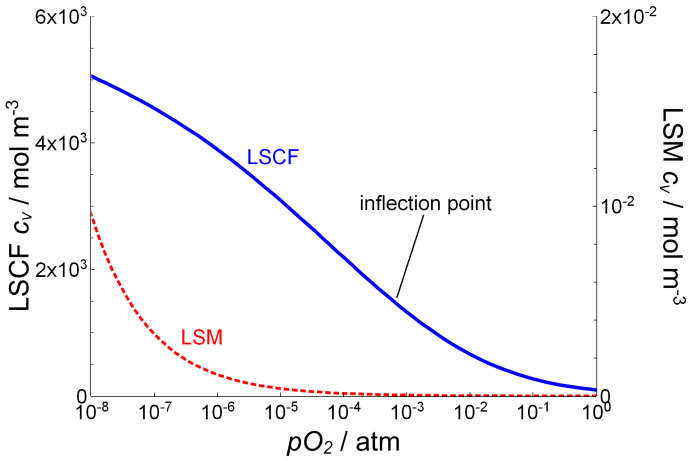

Figure A-4: Equilibrium oxygen vacancy concentration for LSCF 6428 and LSM 8020 predicted from the bulk models as a function of oxygen partial pressure.

has a positive second derivative near OCV, R_i initially decreases with decreasing $\log(pO_2^{internal})$. R_i increases again at the inflection point of the c_v curve.

Figure 24a shows these R_i values calculated by finite differences for both LSM and LSCF as a function of effective cathodic overpotential, normalized to their respective values at OCV. LSM resistance decreases monotonically as the overpotential becomes more negative strong activation caused by cathodic polarization. The resistance of LSCF does not decrease very much before it starts to increase again.

Now, examine the following thought experiment. Suppose that the bulk defect chemistry of LSCF is computed according to reference [13]. With this defect chemistry is associated some standard free energy of oxygen reduction, ΔG^0_{red}s, which corresponds to the following standard bulk point defect equilibrium written in Kröger-Vink notation

$$\frac{1}{2}O_2 + V_O^{\cdot\cdot} + 2B_B^x \rightleftharpoons O_O^x + 2B_B^{\cdot} \tag{A-3}$$

where $B_B^{\cdot}$ is an electron hole and B_B^x is a neutral B-site (B refers to the ABO_3 perovskite structure). A very negative ΔG^0_{red} shifts the reaction in favor of oxygen reduction and a lower equilibrium concentration of oxygen vacancies. A less negative ΔG^0_{red} shifts it in favor of oxygen production and in favor of high oxygen vacancy

concentration. The former case is similar to LSM.

If the value of ΔG^0_{red} is made more negative systematically and the defect equilibrium equations are solved for each value, the resulting trend of oxygen vacancies as a function of effective cathodic overpotential is shown in Figure A-5. As ΔG^0_{red} becomes more negative the equilibrium oxygen vacancy concentration not only decreases, but the overpotential at which the inflection point occurs is shifted to more negative cathodic overpotentials. From the prior analysis, it was shown that the inflection point leads to an increase in the resistance with further decrease of the cathodic overpotential. Therefore, the tighter oxygen binding associated with decreased ΔG^0_{red} forces the increase in resistance to more extreme cathodic overpotentials and thus causes better cathodic activation. The normalized resistances associated with these values of ΔG^0_{red} are shown in Figure 24b.

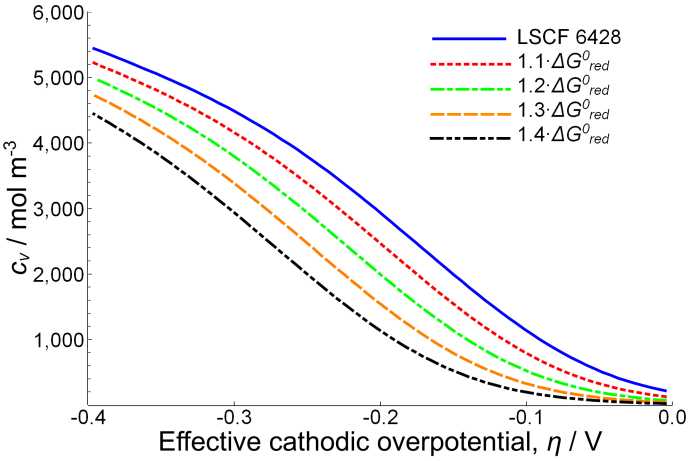

Figure A-5: Oxygen vacancy concentration versus effective cathodic overpotential for LSCF 6428 and LSCF with modified ΔG^0_{red}.

Of course, the exact trend of R_i is very dependent upon the precise kinetics used in the current expression. In fact, changing the expression does change the slope of the LSCF R_i curve as well as the location of its minimum. The preceding argument is intended to illustrate the strikingly different behavior of oxygen vacancies with cathodic polarization in LSM and LSCF and how it dramatically impacts the bulk

pathway. A surface layer that is strongly activated under cathodic polarization has the potential to be somewhat blocking at OCV but much more active toward oxygen reduction under cathodic polarization.

A.3 Promoted adsorption/dissociation model

The model presented in section 4.3.3 links solid-phase point defect and adsorbed oxygen concentrations expected under a steady state cathodic polarization to the rate of oxygen reduction via Equations 75- 77. The model is surface-specific in that it neglects sources of losses not associated with the air-MIEC surface. The intention of this section is to provide supporting details for that model.

In the rate equations, the surface potential difference across the surface, χ_{ms}, was approximated using a parallel plate capacitor model

$$\chi_{\mathrm{ms}} = \frac{\mathrm{dQ}}{\epsilon_0} = \frac{\mathrm{dF}\Gamma(2\gamma + \theta)}{\epsilon_0} \tag{A-4}$$

where Q is the surface charge per unit area, Γ is the density of surface adsorption sites, d is the distance of separation between the adsorbates and surface, and ϵ_0 is the permittivity of free space. The values of these quantities are listed in Table A-1.

Table A-1: Blank LSCF parameters specified for the simulation.

Parameter	Value	Units
$\mathrm{k_{ads,f}}$	$4.5\mathrm{x}10^{0}$	$\mathrm{mol\,m^{-2}\,s^{-1}\,atm^{-1}}$
$\mathrm{k_{ads,b}}$	$1.7\mathrm{x}10^{-10}$	$\mathrm{m^{4}\,mol^{-1}\,s^{-1}}$
$\mathrm{k_{diss,f}}$	$5.0\mathrm{x}10^{-5}$	$\mathrm{m\,s^{-1}}$
$\mathrm{k_{diss,b}}$	$3.4\mathrm{x}10^{-10}$	$\mathrm{m^{4}\,mol^{-1}\,s^{-1}}$
$\mathrm{k_{inc,f}}$	$2.8\mathrm{x}10^{-3}$	$\mathrm{m\,s^{-1}}$
$\mathrm{k_{inc,b}}$	$1.1\mathrm{x}10^{-9}$	$\mathrm{m^{4}\,mol^{-1}\,s^{-1}}$
$\mathrm{c_{Ositem}}$	$7.9\mathrm{x}10^{4}$	$\mathrm{mol\,m^{-3}}$
$\Delta \mathrm{G}_{\mathrm{red}}^{0(\mathrm{LSCF})}$	$-1.0\mathrm{x}10^{0}$	eV
$\Delta \mathrm{G}_{\mathrm{ads}}^{0(\mathrm{LSCF})}$	$-3.0\mathrm{x}10^{-1}$	eV
$\Delta \mathrm{G}_{\mathrm{diss}}^{0(\mathrm{LSCF})}$	$-1.4\mathrm{x}10^{-1}$	eV
T	$9.73\mathrm{x}10^{2}$	K
Γ	$1.0\mathrm{x}10^{-5}$	$\mathrm{mol\,m^{-2}}$
d	$1.0\mathrm{x}10^{-10}$	m

The rate equations were developed with the implicit assumption that elementary steps preceding and following the rate limiting step were at equilibrium. The adsorption reaction was assumed to proceed as follows:

$$\begin{aligned} O_2(g) + * &\rightleftharpoons O_2(s) \\ O_2(s) &\rightarrow O_2^-(s) + h^{\cdot} \\ O_2^-(s) &\rightleftharpoons O_2^{2-}(s) + h^{\cdot} \end{aligned} \tag{A-5}$$

where the second step is rate-limiting. Equilibrium of the reactant and product in the second step with preceding and subsequent steps leads to the rate expression of Equation 72. A further assumption was that the surface site fractions $[O_2(s)]$ and $[O_2^-(s)]$ are minimal and may be neglected when expressing the concentration of free surface sites as $(1 - \gamma - \theta)$. Finally, the role of neutral B-sites was neglected in Equation 75-77, including only the mass-action effect of electrons holes associated with B-sites. Mass action of neutral B-sites may be important in the rate of reaction of hopping-type, small-polaron conductors but there is very little literature discussing it and is still a matter under theoretical investigation.

Likewise, the dissociation reaction was divided into elementary steps as

$$\begin{aligned} O_2^{2-}(s) + V_O^{\cdot\cdot} &\rightarrow O_O^{\cdot} + O^-(s) \\ O_O^{\cdot} &\rightleftharpoons O_O^x + h^{\cdot} \end{aligned} \tag{A-6}$$

and the incorporation reaction divided as

$$\begin{aligned} O^-(s) + V_O^{\cdot\cdot} &\rightarrow O_O^{\cdot} + * \\ O_O^{\cdot} &\rightleftharpoons O_O^x + h^{\cdot} \end{aligned} \tag{A-7}$$

in order to generate the reaction rates in Equations 76-77.

Of course, assuming different elementary steps or a different set of overall adsorption, dissociation, or incorporation reactions would result in different kinetics. The

assumptions used here are justified because the authors is aware of no conclusive identification of LSCF surface reaction mechanisms but does note that vacancy mediated adsorption/dissociation has been suggested for LSF [124, 158] and LSM [23].

The rate expressions for adsorption associated with a total current, i, of oxygen reduction on the surface was

$$\mathrm{i} = -4\mathrm{F}\mathrm{r}_{\mathrm{ads}} \tag{A-8}$$

In order to use the rate expressions for $\mathrm{r}_{\mathrm{ads}}$ and $\mathrm{r}_{\mathrm{inc}}$ corresponding to a given η, the concentration of solid-state point defects (oxygen vacancies, electron holes) at the surface as well as the surface oxygen coverage (γ, θ) should be known. Values of c_{v} and c_{h} were determined from the Brouwer diagram, as described in appendix A.2.

Having established the point defect concentrations inside the MIEC surface at equilibrium and under a bias, γ and θ should then be determined. If the rate constants are specified (equivalent to specifying $\Delta\mathrm{G}^{0}_{\mathrm{ads}}$), then the equilibrium value, γ_0 and θ_0, can be computed simply by setting the equilibrium rate of adsorption and incorporation to zero and solving the set of nonlinear equations.

Under bias, the reaction rates are not zero and so the surface species cannot be determined from a single set of forward and backward rates. Instead, steady state requires that the rate of these reactions be the same, e.g. $\mathrm{r} = \mathrm{r}_{\mathrm{ads}} = \mathrm{r}_{\mathrm{diss}} = \mathrm{r}_{\mathrm{inc}}$ where r is the overall oxygen reduction rate. Imposing that condition allows the solution of

$$0 = \mathrm{r}_{\mathrm{ads}} - \mathrm{r}_{\mathrm{diss}} \tag{A-9}$$

$$0 = \mathrm{r}_{\mathrm{diss}} - \mathrm{r}_{\mathrm{inc}} \tag{A-10}$$

for γ_0 and θ_0 under bias.

With the concentrations at equilibrium and under a bias known, i can be computed from Equation A-8. The overall interfacial resistance, R_{i}, is computed from the change of current and overpotential at steady state by Equation 71. This derivative was

applied by calculating i at discrete values of η using the link to defect chemistry and surface coverage already examined and then using finite differences.

The parameters used in the simulation of the blank LSCF appearing in Figure 24c and d are listed in Table A-1. The values of the quantities derived from them are listed in Table A-2.

Table A-2: Blank LSCF derived quantities, solved for based upon specified parameters at $pO_2 = 0.21$ atm.

Parameter	Value	Units
c_v^0	2.0x10^2	mol m^{-3}
c_h^0	1.1x10^4	mol m^{-3}
γ_0	7.0x10^{-3}	unitless
θ_0	2.0x10^{-2}	unitless
k_{ads}^0	1.0x10^{-1}	mol m^{-2} s^{-1}
$k_{diss}^{0\,¶}$	6.3x10^{-4}	mol m^{-2} s^{-1}
k_{inc}^0	1.0x10^{-1}	mol m^{-2} s^{-1}

¶ Based upon the surface exchange coefficient [12] and assuming that oxygen dissociation is the rate limiting step at equilibrium.

The equilibrium surface coverage, γ_0 and θ_0, relate to the free energies of reaction of the adsorption and dissociation steps as follows:

$$K_{ads} = \exp\left(-\frac{\Delta G_{ads}^{0(LSCF)}}{RT}\right) = \frac{\gamma_0}{(1-\gamma_0-\theta_0)} x_h^2 pO_2^{-1} \exp\left(\frac{2F}{RT}\chi_{ms}\right) \tag{A-11}$$

$$K_{diss} = \exp\left(-\frac{\Delta G_{diss}^{0(LSCF)}}{RT}\right) = \frac{\theta_0}{\gamma_0}\frac{x_O^0}{x_v^0} x_h \exp\left(-\frac{F}{RT}\chi_{ms}\right) \tag{A-12}$$

where x_h is the site fraction of electron holes associated with B-sites, x_v and x_O are site fraction of oxygen vacancies and filled oxygen sites, respectively, and the 0 superscript or subscript indicates the equilibrium value.

Likewise, the overall oxygen reduction equilibrium was written (see Equation A-3) [13]

$$K_{red} = \exp\left(-\frac{\Delta G_{red}^{0(LSCF)}}{RT}\right) = \frac{x_O^0}{x_v^0}\left(\frac{x_{B\cdot}^0}{x_{Bx}^0}\right)^2 pO_2^{-1/2} \tag{A-13}$$

The quantities k^0_{ads} and k^0_{inc} in Table A-2 indicate the forward/backward rate of oxygen adsorption and incorporation, respectively, at equilibrium (OCV). They were computed according to the following equations (c.f. Equations 75-77):

$$k^0_{ads} = k_{ads,f} pO_2 (1 - \gamma_0 - \theta_0) \exp\left(-\frac{\alpha_a F}{RT}\chi^0_{ms}\right) = k_{ads,b}\gamma_0 (c^0_h)^2 \exp\left(\frac{(2-\alpha_a)F}{RT}\chi^0_{ms}\right) \tag{A-14}$$

$$k^0_{diss} = k_{diss,f}\gamma_0 c^0_v \exp\left(\frac{\alpha_d F}{RT}\chi^0_{ms}\right) = k_{diss,b}\theta_0 c^0_O c^0_h \exp\left(-\frac{(1-\alpha_d)F}{RT}\chi^0_{ms}\right) \tag{A-15}$$

$$k^0_{inc} = k_{inc,f}\theta_0 c^0_v \exp\left(\frac{\alpha_i F}{RT}\chi^0_{ms}\right) = k_{inc,b}(1 - \gamma_0 - \theta_0) c^0_O c^0_h \exp\left(-\frac{(1-\alpha_i)F}{RT}\chi^0_{ms}\right) \tag{A-16}$$

In order to mimic LSM modification of the surface in Figure 24c and d, the parameters were adjusted as a function of changes to bulk point defect concentrations, θ and γ, in that order, shifting them from their values associated with blank LSCF toward what was suspected for LSM. It was assumed that if the concentration of an oxygen vacancy or either surface adsorbed species changed, the equilibrium exchange rate changed in direct proportion to it.

The use and modification of LSCF bulk defect chemistry and surface properties serves only as an instructive guide to the possible trends arising from an LSM coating. Over the long-term as the LSM(C) hybrid coating forms, the properties may be expected to be between these two extremes. The adjusted ΔG^0_{red} mimicked the behavior of LSM in that the concentration of oxygen vacancies at OCV was much less than LSCF 6428 and the surface was more activated under bias. The standard free energy of adsorption, ΔG^0_{ads}, and dissociation, ΔG^0_{diss}, were also made more negative, simulating the suspected more energetically favorable adsorption/dissociation [24] and consequently providing the surface with a larger adsorbed oxygen concentration.

Care must be taken in order to assure thermodynamic consistency with this approach. A chief concern is properly preserving the relationship between the forward and backward rate constants:

$$K = \frac{k_f}{k_b} \tag{A-17}$$

A representative example of the surface parameter modification is given here for the dissociation reaction:

$$k_{diss}^{0(1)} = k_{diss}^{0(0)} \frac{c_v^{0(1)}}{c_v^{0(0)}} \qquad k_{diss,f}^{(1)} = k_{diss,f}^{(0)} \tag{A-18}$$

$$k_{diss,b}^{(1)} = \frac{k_{diss}^{0(1)}}{\theta_0^{(1)} c_O^{0(1)} c_h^{0(1)} \exp\left(-\frac{(1-\alpha_d)F}{RT}\chi_{ms}^{0(1)}\right)}$$

$$k_{diss}^{0(2)} = k_{diss}^{0(1)} \frac{\theta_0^{(2)} \exp\left(-\frac{(1-\alpha_d)F}{RT}\chi_{ms}^{0(2)}\right)}{\theta_0^{(1)} \exp\left(-\frac{(1-\alpha_d)F}{RT}\chi_{ms}^{0(1)}\right)} \tag{A-19}$$

$$k_{diss,f}^{(2)} = \frac{k_{diss}^{0(2)}}{\gamma_0^{(2)} c_v^{0(2)} \exp\left(\frac{\alpha_d F}{RT}\chi_{ms}^{0(2)}\right)} \qquad k_{diss,b}^{(2)} = k_{diss,b}^{(1)}$$

$$k_{diss}^{0(3)} = k_{diss}^{0(2)} \frac{\gamma_0^{(3)} \exp\left(\frac{\alpha_d F}{RT}\chi_{ms}^{0(3)}\right)}{\gamma_0^{(2)} \exp\left(\frac{\alpha_d F}{RT}\chi_{ms}^{0(2)}\right)} \qquad k_{diss,f}^{(3)} = k_{diss,f}^{(2)} \tag{A-20}$$

$$k_{diss,b}^{(3)} = \frac{k_{diss}^{0(3)}}{\theta_0^{(3)} c_O^{0(3)} c_h^{0(3)} \exp\left(-\frac{(1-\alpha_d)F}{RT}\chi_{ms}^{0(3)}\right)}$$

The (0) superscript indicates the blank LSCF quantity and the (3) superscript indicates the final quantity used in Figure 24c and d. The (1) superscript indicates changing the bulk defect concentration by manipulating ΔG_{red}^0, the (2) superscript indicates changing θ_0 by manipulating ΔG_{diss}^0, and the (3) superscript indicates changing γ_0 by manipulating ΔG_{ads}^0. Note that $c_v^{0(3)} = c_v^{0(2)} = c_v^{0(1)}$ because c_v, as a bulk quantity, is only changed from (0) to (1). The same logic applies to θ_0 (changed in

Table A-3: Modified LSCF derived quantities corresponding to Figure 24c, solved for based upon specified parameters at $pO_2 = 0.21\,atm$.

Parameter	Value	Units
c_v^0	$3.6x10^{1}$	$mol\,m^{-3}$
c_h^0	$1.1x10^{4}$	$mol\,m^{-3}$
γ_0	$9.8x10^{-3}$	unitless
θ_0	$2.5x10^{-2}$	unitless
k_{ads}^0	$3.2x10^{-1}$	$mol\,m^{-2}\,s^{-1}$
k_{diss}^0	$2.1x10^{-4}$	$mol\,m^{-2}\,s^{-1}$
k_{inc}^0	$2.2x10^{-2}$	$mol\,m^{-2}\,s^{-1}$

Table A-4: Modified LSCF derived quantities corresponding to Figure 24d, solved for based upon specified parameters at $pO_2 = 0.21\,atm$.

Parameter	Value	Units
c_v^0	$1.1x10^{1}$	$mol\,m^{-3}$
c_h^0	$1.1x10^{4}$	$mol\,m^{-3}$
γ_0	$9.8x10^{-3}$	unitless
θ_0	$2.5x10^{-2}$	unitless
k_{ads}^0	$3.2x10^{-1}$	$mol\,m^{-2}\,s^{-1}$
k_{diss}^0	$2.6x10^{-4}$	$mol\,m^{-2}\,s^{-1}$
k_{inc}^0	$6.8x10^{-3}$	$mol\,m^{-2}\,s^{-1}$

step 2) and γ_0 (changed in step 3) as well. The final quantities (3) are shown in Tables A-3 and A-4.

The assumption that underlies this scheme is that when the reactant appears as a first order term, e.g. c_v^0 in one direction, it modifies the equilibrium exchange rate in direct proportion to its change and also that the associated rate constant is not changed. If the species is on the surface, then the surface potential term is included as well. Since the associated rate constant is not changed, the activation energy barrier in that direction is unchanged and therefore all changes to the rate of reaction in that direction are configurational, not energetic.

As previously mentioned, the rate constant in the opposing direction is related via the equilibrium constant for the step. Since the equilibrium constant changes due to a change in the step free energy of reaction but the forward rate constant does not, then the backward rate constant must change as shown. This modification means

that the opposing direction activation energy is modified.

Constant activation energy in one direction while requiring the activation energy in the other direction to change is somewhat arbitrary. Unfortunately, no information is available about the comparative nature of the transition states. Therefore, the most straightforward approach is to ignore any change to the activation energy in the direction that directly involves the modified quantity while allowing thermodynamics to dictate the reverse quantity.

The effect of varying the different parameters is shown in Figure A-6, assuming that the dissociation reaction is rate-limiting in the case of blank LSCF. The equilibrium concentration of O^{-}(s), θ_0, has little effect upon the interfacial resistance except at large polarization (part a). However, increasing the equilibrium concentration of O^{2-}(s), γ_0, has a significant effect in lowering the interfacial resistance at all bias (part b). A more negative ΔG^0_{red} and hence fewer oxygen vacancies (part c) causes R_i to increase near OCV, but its superior activation causes R_i to be decrease to less than the blank value at large overpotential.

The effect of lowering the activation energy barrier in both directions by modifying the equilibrium exchange rates k^0_{ads} and k^0_{diss} was also examined. This change in reaction barrier would be expected to increase the equilibrium rate of exchange by increasing the forward and backward rate constants in proportion to one another but leaving the overall reaction free energy the same. This corresponds to a true catalytic enhancement on the surface due to LSM coating. Increasing the adsorption exchange rate (part d) has little effect except at large overpotential because adsorption is not rate limiting near OCV. Increasing the dissociation rate constant (part e), in contrast, suppresses R_i significantly near OCV.

Figure 24c and d show the results of putting these different LSCF surface modifications together. Figure 24c shows how an adjustment to the concentrations of oxygen vacancies and adsorbed surface species affects the performance. The trend is

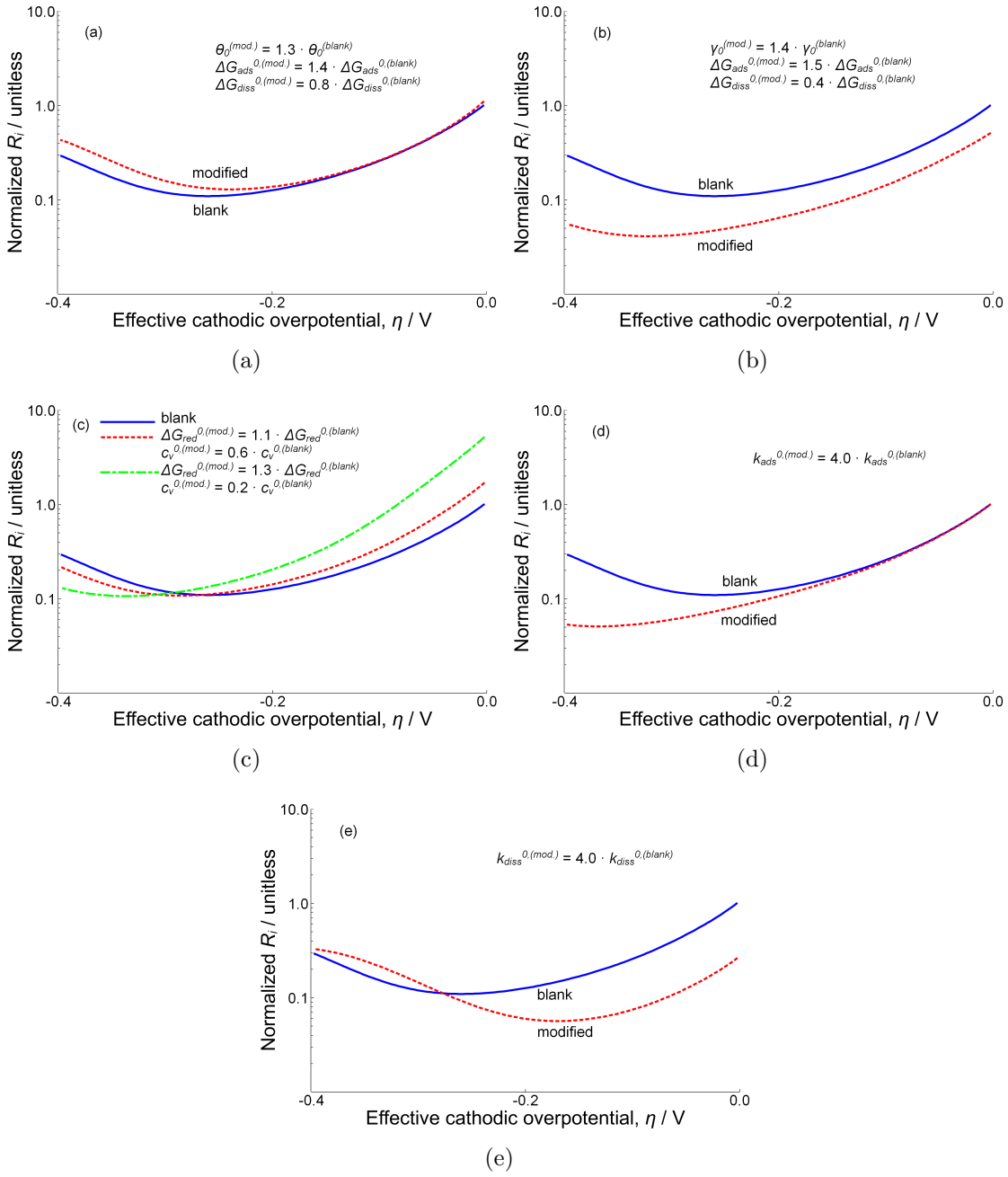

Figure A-6: Normalized resistance plots for the case of increased a) θ_0, b) γ_0, c) more negative ΔG^0_{red}, d) increased equilibrium exchange rate for adsorption, k^0_{ads}, and e) increased equilibrium exchange rate for dissociation, k^0_{diss}.

very similar to that observed experimentally, with R_i of the modified surface greater near OCV but less at large overpotential. Figure 24d incorporates a modification of k^0_{diss} and a further modification of ΔG^0_{red}. A surface simulation with all of the chemical

equilibria shifted toward those suspected for LSM from those associated with blank LSCF demonstrates electrochemical response similar to that observed experimentally, namely inferior performance near OCV but superior performance at moderate to large cathodic overpotentials.

When these reactions were shifted from their starting points associated with LSCF in the direction suspected for LSM, the resulting simulations showed behavior that was qualitatively similar to the experimental results. Interfacial resistance for the modified surface was larger than the blank LSCF at OCV but decreased more rapidly as cathodic overpotential increased, resulting in superior performance at larger cathodic overpotential. This behavior resulted from more favorable and faster oxygen adsorption/dissociation kinetics despite more sluggish oxygen incorporation kinetics. Similar behavior might be expected for an LSM(C) hybrid layer, though it may lie between the two extremes.

APPENDIX B

MODELING USING CONSERVATIVE POINT DEFECT ENSEMBLES

B.1 Formulation of the defect ensembles and transport equations

In this section, the defect ensemble for an MIEC featuring oxygen vacancies and localized electrons and holes is formulated, for application to the case of LSF/LSCF 6428. Other ensemble formulations could be derived following analogous logic if different point defects are present in the material system.

The oxygen reduction reaction is

$$\frac{1}{2}\mathrm{O_2} + \mathrm{V_O^{\cdot\cdot}} + 2\mathrm{B_B'} \rightleftharpoons \mathrm{O_O^x} + 2\mathrm{B_B^x} \tag{B-1}$$

where $\mathrm{V_O^{\cdot\cdot}}$ denotes an oxygen vacancy in Kröger-Vink notation, $\mathrm{O_O^x}$ denotes an occupied oxygen lattice site, $\mathrm{B_B'}$ denotes a localized electron, and $\mathrm{B_B^x}$ denotes an effectively neutral B-site. Writing in terms of building units [88]

$$\frac{1}{2}\mathrm{O_2} + \{\mathrm{V_O^{\cdot\cdot}}\} + 2\{\mathrm{B_B'}\} \rightleftharpoons \mathrm{nil} \tag{B-2}$$

where the building unit $\{\mathrm{V_O^{\cdot\cdot}}\}$ represents $\mathrm{V_O^{\cdot\cdot}} - \mathrm{O_O^x}$ and $\{\mathrm{B_B'}\} = \mathrm{B_B'} - \mathrm{B_B^x}$. The thermodynamic equilibrium expression is

$$\frac{1}{2}\mu_{\mathrm{O_2}} + \mu_{\mathrm{v}} + 2\mu_{\mathrm{e}} = 0 \tag{B-3}$$

where μ_{v} is the chemical potential of $\{\mathrm{V_O^{\cdot\cdot}}\}$ and μ_{e} is the chemical potential of $\{\mathrm{B_B'}\}$.

The disproportionation reaction in terms of building units is

$$\mathrm{nil} \rightleftharpoons \{\mathrm{B_B'}\} + \{\mathrm{B_B^{\cdot}}\} \tag{B-4}$$

and the equilibrium is written

$$\tilde{\mu}_{\mathrm{e}} + \tilde{\mu}_{\mathrm{h}} = 0 \tag{B-5}$$

where $\{\mathrm{B}_{\mathrm{B}}^{\cdot}\} = \mathrm{B}_{\mathrm{B}}^{\cdot} - \mathrm{B}_{\mathrm{B}}^{\mathrm{x}}$ and $\tilde{\mu}_{\mathrm{h}}$ is the electrochemical potential of $\{\mathrm{B}_{\mathrm{B}}^{\cdot}\}$.

Following the original ensemble concept proposed by Maier [98] and the excellent review by Lankhorst [88], several quantities are first defined. The formal charges of the ensembles are:

$$\mathrm{z}_{\mathrm{O}^*} = -2 \tag{B-6}$$

and

$$\mathrm{z}_{\mathrm{e}^*} = -1 \tag{B-7}$$

Oxygen vacancies belong in the O^* ensemble. The electrochemical potential of the O^* is related to oxygen vacancies by definition

$$\tilde{\mu}_{\mathrm{O}^*} = -\tilde{\mu}_{\mathrm{v}} \tag{B-8}$$

The concentration of the O^* ensemble is defined to be

$$\mathrm{c}_{\mathrm{O}^*} = \mathrm{c}_{\mathrm{Ositem}} - \mathrm{c}_{\mathrm{v}} \tag{B-9}$$

where $\mathrm{c}_{\mathrm{Ositem}}$ is the concentration of oxygen lattice sites. Both electrons and electron holes belong to the e^* ensemble. The electrochemical potential of the e^* ensemble is defined to be

$$\tilde{\mu}_{\mathrm{e}^*} = \tilde{\mu}_{\mathrm{e}} = -\tilde{\mu}_{\mathrm{h}} \tag{B-10}$$

The concentration of the e^* ensemble is defined[1]to be

$$\mathrm{c}_{\mathrm{e}^*} = \mathrm{c}_{\mathrm{e}} - \mathrm{c}_{\mathrm{h}} \tag{B-11}$$

To develop transport equations, start with the well-known vacancy conservation equation

$$\frac{\partial \mathrm{c}_{\mathrm{v}}}{\partial \mathrm{t}} = -\nabla \cdot \mathrm{J}_{\mathrm{v}} \tag{B-12}$$

[1]If electron holes outnumber electrons, then $\mathrm{c}_{\mathrm{O}^*}$ will be negative. While a physical concentration cannot be negative, the ensemble concentration is a mathematically useful construct and therefore may take on a negative concentration.

From irreversible thermodynamics, the flux of a species k can be modeled [99,135]

$$J_k = -s_k \nabla \tilde{\mu}_k \tag{B-13}$$

where the cross-coefficients are neglected and s_k is a transport coefficient

$$s_k = b_k c_k = \frac{\sigma_k}{z_k^2 F^2} \tag{B-14}$$

b_k is the mobility of species k and σ_k is the conductivity of species k.

Expressed as such, the flux of vacancies is

$$J_v = -s_v \nabla \tilde{\mu}_v \tag{B-15}$$

Then,

$$\frac{\partial c_v}{\partial t} = -\nabla \cdot (-s_v \nabla \tilde{\mu}_v) \tag{B-16}$$

Since $\tilde{\mu}_{O^*} = -\tilde{\mu}_v$ and $\delta c_{O^*} = -\delta c_v$ by definition,

$$\frac{\partial c_v}{\partial t} = -\nabla \cdot (-s_v \nabla \tilde{\mu}_v) \Rightarrow \frac{\partial c_{O^*}}{\partial t} = -\nabla \cdot (-s_v \nabla \tilde{\mu}_{O^*}) \tag{B-17}$$

Writing the conservation in terms of an ensemble transport coefficient,

$$\frac{\partial c_{O^*}}{\partial t} = -\nabla \cdot (-s_{OO^*} \nabla \tilde{\mu}_{O^*}) \tag{B-18}$$

where

$$s^*_{OO} = s_v \tag{B-19}$$

For the electronic ensemble, the bulk conservation equations are

$$\frac{\partial c_e}{\partial t} = -\nabla \cdot J_e + G \tag{B-20}$$

$$\frac{\partial c_h}{\partial t} = -\nabla \cdot J_h + G \tag{B-21}$$

where G is the rate of generation/recombination. By the definition of c_{e^*}, $\delta c_{e^*} = \delta c_e$ and $\delta c_{e^*} = -\delta c_h$. Therefore,

$$\frac{\partial c_{e^*}}{\partial t} = \frac{\partial c_e}{\partial t} - \frac{\partial c_h}{\partial t} \tag{B-22}$$

which leads to a cancellation of the homogeneous generation/recombination term.

$$\frac{\partial c_{e^*}}{\partial t} = -\nabla \cdot (J_e - J_h) = -\nabla \cdot J_{e^*} \tag{B-23}$$

where

$$J_{e^*} \equiv J_e - J_h \tag{B-24}$$

The individual fluxes are:

$$J_h = -s_h \nabla \tilde{\mu}_h = -(-s_h \nabla \tilde{\mu}_{e^*}) \tag{B-25}$$

$$J_e = -s_e \nabla \tilde{\mu}_e = -s_e \nabla \tilde{\mu}_{e^*} \tag{B-26}$$

and

$$J_{e^*} = -s_{ee^*} \nabla \tilde{\mu}_{e^*} \tag{B-27}$$

Now, substituting into the fluxes,

$$J_e - J_h = -s_e \nabla \tilde{\mu}_e + s_h \nabla \tilde{\mu}_h = -(s_e + s_h) \nabla \tilde{\mu}_{e^*} \tag{B-28}$$

and therefore

$$s_{ee^*} = s_e + s_h \tag{B-29}$$

The transport coefficients in all cases were calculated assuming constant mobility. For the O^* ensemble, drawing from Equation B-14

$$s_{OO^*} = s_v = b_v c_v \tag{B-30}$$

where b_v is the mobility derived from the oxygen vacancy diffusivity, D_v

$$b_v = D_v \left(1 + \frac{\partial \ln \gamma_v}{\partial \ln x_v}\right)^{-1} / (RT) \tag{B-31}$$

where $\partial \ln \gamma_v / \partial \ln x_v$ is the thermodynamic factor of vacancies. The value of b_v is reported in Table B-1. The value of D_v was taken from oxygen tracer measurements [12]. To calculate the local value of s_{OO^*} iteratively during solution, the constant factor b_v was multiplied by the local vacancy concentration.

Table B-1: Constant coefficients for determination of s_{OO^*} and s_{ee^*} at 700° C, in units of $\mathrm{mol\,m^2\,J^{-1}\,s^{-1}}$ (s_{OO^*} and s_{ee^*} have units of $\mathrm{mol^2\,J^{-1}\,s^{-1}\,m^{-1}}$).

Parameter	Value	Reference
b_v	$2.0\text{x}10^{-14}$	[12, 13]
$b_{electronic}$	$3.1\text{x}10^{-10}$	[13, 156]

For the e^*, the transport coefficient of electrons is

$$s_e = \frac{\sigma_e}{z_e^2 F^2} \tag{B-32}$$

and for holes

$$s_h = \frac{\sigma_h}{z_h^2 F^2} \tag{B-33}$$

Connecting the conductivity with mobility, b_k

$$\sigma_k = |z_k|^2 F^2 c_k b_k \tag{B-34}$$

A simple model with equal and constant mobility was used. Assuming $b_{electronic} = b_e = b_h$, then

$$s_{ee^*} = b_{electronic}\,(c_e + c_h) \tag{B-35}$$

The value of b was determined from

$$b_{electronic} = \frac{\sigma_0}{F^2(c_e^0 + c_h^0)} \tag{B-36}$$

where σ_0 is the total electrical conductivity at $pO_2 = 0.21\,\mathrm{atm}$, approximately all electronic because the ionic transference number for LSCF 6428 is very low. The value of σ_0 for LSCF 6428 was taken from [156]. The 0 superscript on the concentrations indicate the equilibrium value at $pO_2 = 0.21\,\mathrm{atm}$, from the prediction of the bulk defect model [13]. The value of $b_{electronic}$ is also reported in Table B-1.

To calculate the local value of s_{ee^*} during solution of the transport problem, the constant factor $b_{electronic}$ is multiplied by the sum of the local electron and electron hole calculations.

B.2 Point defect equilbrium

The point defect thermodynamics of the LSCF/LSF system [13, 119] are described using site limitation (Fermi-Dirac statistics) in the chemical potential terms to accommodate the large relative concentrations of the point defects. The chemical potential of $\{V_O^{\cdot\cdot}\}$ is [88]

$$\mu_v = \mu_v^0 + RTln\left(\frac{c_v}{c_{Osite} - c_v}\right) \tag{B-37}$$

Likewise for localized electrons, $\{B_B'\}$, and holes, $\{B_B^{\cdot}\}$

$$\mu_e = \mu_e^0 + RTln\left(\frac{c_e}{c_{Bsite} - c_h - c_e}\right) \tag{B-38}$$

$$\mu_h = \mu_h^0 + RTln\left(\frac{c_h}{c_{Bsite} - c_h - c_e}\right) \tag{B-39}$$

where c_{Osite} is the concentration of O-lattice sites in the crystal and c_{Bsite} is the concentration of B-lattice sites in the crystal.

The chemical portion of the change in electrochemical potential is

$$\Delta\mu_v = RTln\left(\frac{c_v}{c_{Osite} - c_v}\frac{c_{Osite} - c_v^0}{c_v^0}\right) \tag{B-40}$$

$$\Delta\mu_e = RTln\left(\frac{c_e}{c_{Bsite} - c_h - c_e}\frac{c_{Bsite} - c_h^0 - c_e^0}{c_e^0}\right) \tag{B-41}$$

$$\Delta\mu_h = RTln\left(\frac{c_h}{c_{Bsite} - c_h - c_e}\frac{c_{Bsite} - c_h^0 - c_e^0}{c_h^0}\right) \tag{B-42}$$

The relevant defect equilibrium expressions for LSF/LSCF [13, 119] are

$$K_{red} = \left(\frac{c_{Osite} - c_v}{c_v}\right)\left(\frac{c_h}{c_{Bsite} - c_h - c_e}\right)^2 pO_2^{-1/2} \tag{B-43}$$

$$K_{dis} = \left(\frac{c_e}{c_{Bsite} - c_h - c_e}\right)\left(\frac{c_h}{c_{Bsite} - c_h - c_e}\right) \tag{B-44}$$

$$0 = \rho_b + F\left(z_v c_v + z_e c_e + z_h c_h\right) \tag{B-45}$$

Table B-2: Bulk point defect equilibrium constants for $La_{0.6}Sr_{0.4}Co_{0.2}Fe_{0.8}O_{3-\delta}$ [13].

Parameter	Description	Value
K_{red}	Oxygen reduction	$8.2x10^{1}$
K_{dis}	B-site disproportionation	$1.4x10^{-3}$

Table B-3: Bulk point defect concentrations for $La_{0.6}Sr_{0.4}Co_{0.2}Fe_{0.8}O_{3-\delta}$ at 700° C and $pO_2 = 0.21$ atm.

Point Defect Concentration	Value	Units
c_v^0	$2.0x10^{2}$	$mol\,m^{-3}$
c_h^0	$1.1x10^{4}$	$mol\,m^{-3}$
c_e^0	$2.5x10^{1}$	$mol\,m^{-3}$
c_{Osite}	$7.9x10^{4}$	$mol\,m^{-3}$

where K_{red} and K_{dis} are equilibrium constants for oxygen reduction and disproportionation, respectively, and ρ_b is the background charge density, established by degree of strontium doping and A-site vacancy concentration (assumed fixed at 0.5%). The equilibrium constant values are listed in Table B-2. The values of equilibrium point defect concentrations at 700° C and $pO_2 = 0.21$ atm are given in Table B-3.

B.3 Unpacking of the ensembles

B.3.1 Fundamental concepts

If $\Delta\tilde{\mu}_{O^*}$ and $\Delta\tilde{\mu}_{e^*}$ are known, then a quantity C can be defined such that

$$C = 2\Delta\tilde{\mu}_{O^*} - 4\Delta\tilde{\mu}_{e^*} \tag{B-46}$$

Now, recognize that since $\tilde{\mu}_v = -\tilde{\mu}_{O^*}$ and $\tilde{\mu}_e = \tilde{\mu}_{e^*}$ and using the traditional method of splitting the electrochemical potentials:

$$\Delta\tilde{\mu}_{O^*} = -\Delta\tilde{\mu}_v = -\Delta\mu_v - z_v F\Delta\Phi \tag{B-47}$$

$$\Delta\tilde{\mu}_{e^*} = \Delta\tilde{\mu}_e = \Delta\mu_e + z_e F\Delta\Phi \tag{B-48}$$

Canceling out the electrostatic parts due to the choice of coefficients, results in

$$C = -2\Delta\mu_v - 4\Delta\mu_e \tag{B-49}$$

This equation uses the result of the bulk FEM simulation, $\Delta\tilde{\mu}_{O^*}$ and $\Delta\tilde{\mu}_{e^*}$ to compute C and to relate to the local defect chemical potentials.

Now, consider the electroneutrality equation, which must hold at any point in the bulk

$$0 = \rho_b + F(z_v c_v + z_h c_h + z_e c_e) \tag{B-50}$$

expressed as

$$0 = \mathcal{F}(\Delta\mu_v, \Delta\mu_e) \tag{B-51}$$

where c_v, c_h, and c_e are functions of $\Delta\mu_v$ and $\Delta\mu_e$. Combining Equation B-49 with Equation B-51, there is a nonlinear system of equations

$$\begin{aligned} C &= -2\Delta\mu_v - 4\Delta\mu_e \\ 0 &= \mathcal{F}(\Delta\mu_v, \Delta\mu_e) \end{aligned} \tag{B-52}$$

with two equations and two unknowns. This allows solution for $\Delta\mu_v$ and $\Delta\mu_e$ as long as the defect concentrations can be determined from $\Delta\mu_v$ and $\Delta\mu_e$ in order to inform $\mathcal{F}$.

The concentrations are determined through the solution of three equations that take advantage of the thermodynamic definitions and enforced thermodynamic point defect equilibrium.

First, the quantity c_v may be determined solely from $\Delta\mu_v$ by Equation B-40.

The disproportionation equilibrium, $\Delta\mu_e = -\Delta\mu_h$, is enforced and the two other equations, Equation B-41 and B-51 can be used to solve for c_e and c_h.

From a practical standpoint, solution of the problem can start with an initial guess for $\Delta\mu_v$ and $\Delta\mu_e$ that fulfills Equation B-49, which is used to determine c_v, c_h, and c_e by solving the set of three equations mentioned above (B-40, B-41, B-51) and then computing the residual of Equation Set B-52. Iterative methods deliver a solution for $\Delta\mu_v$ and $\Delta\mu_e$ that satisfies Equation Set B-52 and as a consequence the enforced link

ensures that local defect concentrations fulfill thermodynamics, electroneutrality, and are consistent with the transport occurring in the MIEC.

B.3.2 Effective, internal pO_2 as a proxy variable

This procedure for unpacking would be very computationally intensive because it requires the solution of a nonlinear set of equations at every point in order to determine the transfer coefficients in the bulk and the rates of reaction at the boundaries. However, there is a shortcut that makes repeatedly solving the system at every point unnecessary.

Consider the oxygen reduction thermodynamic equilibrium equation in B-3. According to it, $\mu_{O_2} = -2\mu_v - 4\mu_e$ and therefore $\Delta\mu_{O_2} = -2\Delta\mu_v - 4\Delta\mu_e$. The quantity $\Delta\mu_{O_2}$ is exactly C from Equation B-49, which was already defined to be a linear combination of the two independent variables in the FEM simulation. Because of the choice of coefficients, C can be linked to pO_2^{solid} via Equation 95. Here, pO_2^{solid} is not a requirement imposed upon the defects: there is no enforced equilibrium with any imaginary internal gas phase. Rather it is a convenient tool that falls out of the local equilibrium of the other point defects. It can be used as shorthand to make numerical computations easier.

Instead of solving Equation Set B-52 at every point in the bulk, $C = \Delta\mu_{O_2}^{solid}$ can be computed and used to interpolate the set of (c_v, c_e, c_h) based on bulk defect chemistry calculations at various values of pO_2 carried out *ahead of time*. The lookup functions described in the implementation section 5.2.3 do exactly that. One single global defect computation can be made and C can be used to simply interpolate (c_v, c_e, c_h) as a function of pO_2^{solid} at every node in the FEM simulation.

B.4 Derivation of MIEC-electrolyte vacancy transfer rate for large vacancy concentration

B.4.1 Nonideal transition state rate expression

The vacancy transfer reaction over the electrolyte-MIEC interface may be written in terms of structural units as

$$\mathrm{V}^{\cdot\cdot}_{\mathrm{O,e}} + \mathrm{O}^{\mathrm{x}}_{\mathrm{O,m}} \longleftrightarrow \mathrm{O}^{\mathrm{x}}_{\mathrm{O,e}} + \mathrm{V}^{\cdot\cdot}_{\mathrm{O,m}} \tag{B-53}$$

In the case of very low oxygen vacancy concentration in the MIEC, the following relationship has been derived [101]:

$$\mathrm{r_v} = \mathrm{k_v^0}\left[\exp\left(\frac{2\alpha_\mathrm{v}\mathrm{F}}{\mathrm{RT}}\Delta\chi_\mathrm{i}\right) - \frac{\mathrm{c_{v,m}}}{\mathrm{c^0_{v,m}}}\exp\left(\frac{-2\left(1-\alpha_\mathrm{v}\right)\mathrm{F}}{\mathrm{RT}}\Delta\chi_\mathrm{i}\right)\right] \tag{B-54}$$

This expression must be extended to accommodate large oxygen vacancy concentration in the MIEC. The reaction in terms of building units can be written

$$\{\mathrm{V}^{\cdot\cdot}_{\mathrm{O,e}}\} \longleftrightarrow \{\mathrm{V}^{\cdot\cdot}_{\mathrm{O,m}}\} \tag{B-55}$$

Let state I be the left hand side and state II be the right hand side. The difference in the electrical component of electrochemical potential between the transition state, ‡, and state I is [130]

$$\tilde{\mu}^0_{\ddagger,\mathrm{e}} - \tilde{\mu}^0_{\mathrm{I,e}} = \alpha\left(\tilde{\mu}^0_{\mathrm{II,e}} - \tilde{\mu}^0_{\mathrm{I,e}}\right) \tag{B-56}$$

$$= \alpha\left(\mathrm{z_v F}\Phi_\mathrm{m} - \mathrm{z_v F}\Phi_\mathrm{e}\right) \tag{B-57}$$

$$= -\alpha \mathrm{z_v F}\chi_\mathrm{i} \tag{B-58}$$

where $\chi_\mathrm{i} = \Phi_\mathrm{elyte} - \Phi_\mathrm{WE}$. The standard free energy of activation in the forward direction then becomes

$$\Delta\mathrm{G}^0_\ddagger = \tilde{\mu}^0_\ddagger - \tilde{\mu}^0_\mathrm{I} - \alpha \mathrm{z_v F}\chi_\mathrm{i} \tag{B-59}$$

The equilibrium assumed between the transition state and state I is

$$\mathrm{K_f} = \exp\left(\frac{-(\tilde{\mu}^0_\ddagger - \tilde{\mu}^0_\mathrm{I})}{\mathrm{RT}}\right)\exp\left(\frac{\alpha \mathrm{z_v F}\chi_\mathrm{i}}{\mathrm{RT}}\right) = \frac{\mathrm{a}_\ddagger}{\mathrm{a_I}} \tag{B-60}$$

where a indicates activity.

The activity of state I is equivalent to the activity of the electrolyte-phase oxygen vacancy building unit. Since

$$\mu_{v,e} = \mu^0_{v,e} + \mathrm{RTln}\left(\frac{x_{v,e}}{1 - x_{v,e}}\right) \tag{B-61}$$

then $a_{v,e} = x_{v,e}/(1 - x_{v,e})$, where $x_{v,e}$ is the vacancy site fraction in the electrolyte.

The activity of the transition state is linked to the concentration by an as-yet-unidentified activity coefficient $\gamma_\ddagger$.

$$a_\ddagger = \gamma_\ddagger x_\ddagger \tag{B-62}$$

where $x_\ddagger$ is the fractional concentration of transition states.

The fractional concentration of transition states may be solved for:

$$x_\ddagger = \exp\left(\frac{-(\tilde{\mu}^0_\ddagger - \tilde{\mu}^0_I)}{RT}\right)\gamma_\ddagger^{-1}\frac{x_{v,e}}{1 - x_{v,e}}\exp\left(\frac{\alpha z_v F}{RT}\chi_i\right) \tag{B-63}$$

The rate of reaction is proportional to the concentration of transition states multiplied by the density of interfacial sites Γ_i (in units of $\mathrm{mol\,m^{-2}}$), and the frequency factor [15]

$$r_f = k_f\gamma_\ddagger^{-1}\frac{x_{v,e}}{1 - x_{v,e}}\exp\left(\frac{\alpha z_v F}{RT}\chi_i\right) \tag{B-64}$$

where the rate constant k_f absorbs the frequency factor, the chemical free energy of activation, and Γ_i.

Using an analogous derivation, the backward rate of reaction is

$$r_b = k_b\gamma_\ddagger^{-1}\frac{x_{v,m}}{1 - x_{v,m}}\exp\left(-\frac{(1-\alpha) z_v F}{RT}\chi_i\right) \tag{B-65}$$

where $x_{v,m}$ is the vacancy site fraction in the MIEC. The next step is to derive an appropriate term for the activity coefficient $\gamma_\ddagger$.

B.4.2 Transition state activity coefficients

To arrive at the activity coefficients, the statistical thermodynamics along the electrolyte-MIEC interface are considered. Let $N_{o,e}$ be the number of oxygen lattice sites in the

electrolyte phase along a two-dimensional electrolyte-MIEC boundary. Likewise, let $N_{o,m}$ be the number of oxygen lattice sites in the MIEC phase along the boundary. There are three oxygen-site defects to consider. The first two are oxygen vacancy building units which have already been mentioned, each residing in only one phase, either the electrolyte or the MIEC. Let $N_{v,e}$ and $N_{v,m}$ be the number of these defects, respectively. The third oxygen-site defect is the transition state, which for this purpose is treated as a distinct species with respect to a full oxygen sublattice. Let $N_{\ddagger}$ be the number of transition states.

Let Ω_i be the total number of ways of arranging defects along the two-dimensional interface. It is computed by the number of ways of arranging defects in the electrolyte multiplied by the number of ways of arranging defects in the MIEC:

$$\Omega_i = \left(\frac{N_{o,e}!}{(N_{o,e} - N_{v,e} - N_{\ddagger})!N_{v,e}!N_{\ddagger}!}\right)\left(\frac{(N_{o,m} - N_{\ddagger})!}{(N_{o,m} - N_{v,m} - N_{\ddagger})!N_{v,m}!}\right) \tag{B-66}$$

The left parenthesis represents the number of ways of arranging oxygen vacancies and transition states on the interface on the electrolyte side. The placement of vacancies does not affect the MIEC because they are not shared. However, the placement of transition states does affect the MIEC because they are shared.

The transition states represent a tie between an electrolyte oxygen vacancy and a filled oxygen lattice site in the MIEC or vice versa. Therefore a placement of the transition state in the electrolyte also specifies the placement of the transition state in the MIEC (perhaps every electrolyte oxygen site has one nearest neighbor site in the MIEC with which the exchange could occur - consideration of more than one possible MIEC site per electrolyte site would add complication to this derivation). The corresponding filled lattice site in the MIEC is now considered a point defect - it is no longer the same as any unaffected oxygen site. In short, there is one degree of freedom in the placement of the transition state. It may be included in either lattice's configuration, but not both.

The second parenthesis in the equation represents the number of ways to arrange

only the oxygen vacancies along the MIEC side of the interface. Only $N_{o,m} - N_{\ddagger}$ sites are available for placement instead of $N_{o,m}$ sites because the transition state has already been placed in the MIEC by choosing a placement in the electrolyte.

Recognizing that configurational entropy is equal to $S = kln\Omega$ and applying Stirling's approximation $ln(N!) \approx NlnN - N$,

$$\begin{aligned} S \approx\ k\Big[&+ (N_{o,e}lnN_{o,e} - N_{o,e}) \\ &- ((N_{o,e} - N_{v,e} - N_{\ddagger})ln(N_{o,e} - N_{v,e} - N_{\ddagger}) - (N_{o,e} - N_{v,e} - N_{\ddagger})) \\ &- (N_{v,e}lnN_{v,e} - N_{v,e}) \\ &- (N_{\ddagger}lnN_{\ddagger} - N_{\ddagger}) \\ &+ ((N_{o,m} - N_{\ddagger})ln(N_{o,m} - N_{\ddagger}) - (N_{o,m} - N_{\ddagger})) \\ &- ((N_{o,m} - N_{v,m} - N_{\ddagger})ln(N_{o,m} - N_{v,m} - N_{\ddagger}) - (N_{o,m} - N_{v,m} - N_{\ddagger})) \\ &- (N_{v,m}lnN_{v,m} - N_{v,m})\Big] \end{aligned} \tag{B-67}$$

differentiating with respect to $N_{\ddagger}$,

$$\frac{\partial S}{\partial N_{\ddagger}} = kln\left(\frac{(N_{o,e} - N_{v,e} - N_{\ddagger})(N_{o,m} - N_{v,m} - N_{\ddagger})}{(N_{o,m} - N_{\ddagger})N_{\ddagger}}\right) \tag{B-68}$$

If it is assumed that $N_{\ddagger} << N_{v,e}, N_{v,m}$, then

$$\frac{\partial S}{\partial N_{\ddagger}} = kln\left(\frac{N_{o,e} - N_{v,e}}{N_{\ddagger}}\frac{N_{o,m} - N_{v,m}}{N_{o,m}}\right) \tag{B-69}$$

Dividing the top and bottom of the left fraction by $N_{o,e}$ and dividing the top and bottom of the right fraction by $N_{o,m}$, then $\partial S/\partial N_{\ddagger}$ is expressed in terms of site fractions

$$\frac{\partial S}{\partial N_{\ddagger}} = kln\left(\frac{1 - x_{v,e}}{x_{\ddagger,e}}\frac{1 - x_{v,m}}{1}\right) \tag{B-70}$$

leading to an expression for the chemical potential of the transition state

$$\mu_{\ddagger} = \mu_{\ddagger}^{0} + RTln\left(\frac{x_{\ddagger,e}}{(1 - x_{v,e})(1 - x_{v,m})}\right) \tag{B-71}$$

This leads to an activity

$$a_{\ddagger} = \gamma_{\ddagger} x_{\ddagger} \tag{B-72}$$

where the activity coefficient is

$$\gamma_{\ddagger} = (1 - x_{v,e})^{-1}(1 - x_{v,m})^{-1} \tag{B-73}$$

B.4.3 Implementation and Implications

Inserting Equations B-73 into Equations B-64 and B-65, respectively, leads to cancellation of terms

$$r_f = k_f(1 - x_{v,m})x_{v,e}\exp\left(\frac{\alpha z_v F}{RT}\chi_i\right) \tag{B-74}$$

$$r_b = k_b(1 - x_{v,e})x_{v,m}\exp\left(-\frac{(1-\alpha) z_v F}{RT}\chi_i\right) \tag{B-75}$$

Combining into a net rate, replacing the site fractions with concentration ratios, inserting a reference to the equilibrium state, and simplifying

$$\begin{aligned} r = k_v^0 \Bigg[&\left(\frac{c_{Ositem} - c_{v,m}}{c_{Ositem} - c_{v,m}^0}\right)\frac{c_{v,e}}{c_{v,e}^0}\exp\left(\frac{\alpha z_v F}{RT}\Delta\chi_i\right) \\ &- \left(\frac{c_{Ositee} - c_{v,e}}{c_{Ositee} - c_{v,e}^0}\right)\frac{c_{v,m}}{c_{v,m}^0}\exp\left(-\frac{(1-\alpha) z_v F}{RT}\Delta\chi_i\right)\Bigg] \end{aligned} \tag{B-76}$$

Finally, if no change in electrolyte vacancy concentration is assumed (due to the requirements of electroneutrality with the charged, immobile Y'_{Zr}) and $c_{Ositem} - c_{v,m}$ is replaced with the notation $c_{O,m}$ denoting filled oxygen lattice sites in the MIEC, then Equation 99 is obtained.

REFERENCES

[1] Abbaspour, A., Nandakumar, K., Luo, J., and Chuang, K. T., "A novel approach to study the structure versus performance relationship of sofc electrodes," *Journal of Power Sources*, vol. 161, pp. 965–970, 2006.

[2] Adler, S. B., "Reference electrode placement in thin solid electrolytes," *Journal of The Electrochemical Society*, vol. 149, no. 5, pp. E166–E172, 2002.

[3] Adler, S. B., "Factors governing oxygen reduction in solid oxide fuel cell cathodes," *Chemical Reviews*, vol. 104, no. 10, pp. 4791–4843, 2004.

[4] Adler, S. B., Chen, X. Y., and Wilson, J. R., "Mechanisms and rate laws for oxygen exchange on mixed-conducting oxide surfaces," *Journal of Catalysis*, vol. 245, no. 1, pp. 91–109, 2007.

[5] Adler, S. B., Lane, J. A., and Steele, B. C. H., "Electrode kinetics of porous mixed-conducting oxygen electrodes," *Journal of The Electrochemical Society*, vol. 143, no. 11, pp. 3554–3564, 1996.

[6] Anderson, H. U., Chen, C.-C., Tai, L.-W., and Nasrallah, M. M., "Electrical conductivity and defect structure of (La, Sr)(Co, Fe)O3," *Proceedings - Electrochemical Society*, vol. 94-12, no. Ionic and Mixed Conducting Ceramics, pp. 376–387, 1994.

[7] Ashby, M. F., *Materials Selection in Mechanical Design*. Oxford, UK: Butterworth-Heinemann, second ed., 1999.

[8] Ashcroft, N. W. and Mermin, N. D., *Solid State Physics*. Singapore: Thomson Learning, 1976.

[9] Baumann, F. S., Fleig, J., Habermeier, H.-U., and Maier, J., "Impedance spectroscopic study on well-defined (La,Sr)(Co,Fe)O3-δ model electrodes," *Solid State Ionics*, vol. 177, pp. 1071–1081, 2006.

[10] Baumann, F. S., Fleig, J., Konuma, M., Starke, U., Habermeier, H.-U., and Maier, J., "Strong performance improvement of La0.6Sr0.4Co0.8Fe0.2O3-δ SOFC cathodes by electrochemical activation," *Journal of The Electrochemical Society*, vol. 152, no. 10, p. A2074, 2005.

[11] Benson, S. J., Chater, R. J., and Kilner, J. A., "Oxygen diffusion and surface exchange in the mixed conducting perovskite La0.6Sr0.4Fe0.8Co0.2O3-δ," *Proceedings - Electrochemical Society*, vol. 97-24, no. Ionic and Mixed Conducting Ceramics, pp. 596–609, 1998.

[12] Benson, S. J., *Oxygen Transport and Degradation Processes in Mixed Conducting Perovskites*. PhD thesis, Imperial College, 1999.

[13] Bishop, S. R., Duncan, K. L., and Wachsman, E. D., "Surface and bulk defect equilibria in strontium-doped lanthanum cobalt iron oxide," *Journal of The Electrochemical Society*, vol. 156, no. 10, pp. B1242–B1248, 2009.

[14] Bockris, J. O., Reddy, A., and Gamboa-Aldeco, M., *Modern Electrochemistry 2A: Fundamentals of Electrodics*, vol. 2A of *Modern Electrochemistry*. New York: KluwerAcademic / Plenum Publishers, second ed., 2000.

[15] Boudart, M., *Kinetics of Chemical Processes*. Englewood Cliffs, NJ, USA: Prentice-Hall, 1968.

[16] Brichzin, V., Fleig, J., Habermeier, H.-U., Cristiani, G., and Maier, J., "The geometry dependence of the polarization resistance of Sr-doped LaMnO3 microelectrodes on yttria-stabilized zirconia," *Solid State Ionics*, vol. 152-153, pp. 499–507, 2002.

[17] Brichzin, V., Fleig, J., Habermeier, H. U., and Maier, J., "Geometry dependence of cathode polarization in solid oxide fuel cells investigated by defined Sr-doped LaMnO3 microelectrodes," *Electrochemical And Solid State Letters*, vol. 3, no. 9, pp. 403–406, 2000.

[18] Britz, D., *Digital Simulation in Electrochemistry*. New York: Springer, 3rd ed., 2005.

[19] Chen, X. J., Chan, S. H., and Khor, K. A., "Simulation of a composite cathode in solid oxide fuel cells," *Electrochimica Acta*, vol. 49, no. 11, pp. 1851–1861, 2004.

[20] Chiang, Y.-M., Birnie, D. P. I., and Kingery, W. D., *Physical Ceramics: Principles for Ceramic Science and Engineering*. New York: Wiley, 1997.

[21] Choi, J., Qin, W., Liu, M., and Liu, M., "Preparation and characterization of (La0.8Sr0.2)0.95MnO3-theta (LSM) thin films and LSM/LSCF interface for solid oxide fuel cells," *Journal of the American Ceramic Society*, 2011, accepted.

[22] Choi, Y. M., Lynch, M. E., Lin, M. C., and Liu, M. L., "Prediction of O-2 dissociation kinetics on lamno3-based cathode materials for solid oxide fuel cells," *Journal of Physical Chemistry C*, vol. 113, no. 17, pp. 7290–7297, 2009.

[23] Choi, Y. M., Mebane, D. S., Lin, M. C., and Liu, M., "Oxygen reduction on LaMnO3-based cathode materials in solid oxide fuel cells," *Chemistry of Materials*, vol. 19, no. 7, pp. 1690–1699, 2007.

[24] Choi, Y., Lin, M. C., and Liu, M., "Rational design of novel cathode materials in solid oxide fuel cells using first-principles simulations," *Journal of Power Sources*, vol. 195, no. 5, pp. 1441–1445, 2010.

[25] Christie, G. and Huijsmans, J., "State of art SOFC component development at ECN," in *Proceedings of the Fifth International Symposium on Solid Oxide Fuel Cells (SOFC-V)* (Stimming, U., Singhal, S., Tagawa, H., and Lehnert, W., eds.), pp. 718–726, Pennington, N.J.: The Electrochemical Society, 1997.

[26] Chueh, W. C., Lai, W., and Haile, S. M., "Electrochemical behavior of ceria with selected metal electrodes," *Solid State Ionics*, vol. 179, no. 21-26, pp. 1036–1041, 2008.

[27] Ciucci, F., Chueh, W. C., Goodwin, D. G., and Haile, S. M., "Surface reaction and transport in mixed conductors with electrochemically-active surfaces: a 2-D numerical study of ceria," *Physical Chemistry Chemical Physics*, vol. 13, pp. 2121–2135, 2011.

[28] Coffey, G. W., Pederson, L. R., and Rieke, P. C., "Competition between bulk and surface pathways in mixed ionic electronic conducting oxygen electrodes," *Journal of The Electrochemical Society*, vol. 150, no. 8, pp. A1139–A1151, 2003.

[29] Costamagna, P., Costa, P., and Antonucci, V., "Micro-modelling of solid oxide fuel cell electrodes," *Electrochimica Acta*, vol. 43, no. 3-4, pp. 375–394, 1998.

[30] Costamagna, P., Costa, P., and Arato, E., "Some more considerations on the optimization of cermet solid oxide fuel cell electrodes," *Electrochimica Acta.*, vol. 43, no. 8, pp. 967–972, 1998.

[31] Crandall, R. S. and Faughnan, B. W., "Dynamics of coloration of amorphous electrochromic films of wo3 at low voltages," *Applied Physics Letters*, vol. 28, no. 2, pp. 95–97, 1976.

[32] Crawford, R. P., Rosenberg, W. S., and Keaveny, T. M., "Quantitative computed tomography-based finite element models of the human lumbar vertebral body: Effect of element size on stiffness, damage, and fracture strength predictions," *Journal of Biomechanical Engineering-Transactions of the Asme*, vol. 125, no. 4, pp. 434–438, 2003.

[33] De Souza, R. A., "A universal empirical expression for the isotope surface exchange coefficients (k*) of acceptor-doped perovskite and fluorite oxides," *Physical Chemistry Chemical Physics*, vol. 8, pp. 890–897, 2006.

[34] De Souza, R. A. and Kilner, J. A., "Oxygen transport in La1-xSrxMn1-yCoyO3±d perovskites - part I. oxygen tracer diffusion," *Solid State Ionics*, vol. 106, no. 3-4, pp. 175–187, 1998.

[35] De Souza, R. A. and Kilner, J. A., "Oxygen transport in La1-xSrxMn1-yCoyO3±d perovskites part II. oxygen surface exchange," *Solid State Ionics*, vol. 126, no. 1-2, pp. 153–161, 1999.

[36] De Souza, R. A., Kilner, J. A., and Walker, J. F., "A SIMS study of oxygen tracer diffusion and surface exchange in La0.8Sr0.2MnO3+delta," *Materials Letters*, vol. 43, no. 1-2, pp. 43–52, 2000.

[37] Deseure, J., Bultel, Y., Dessemond, L., and Siebert, E., "Theoretical optimisation of a SOFC composite cathode," *Electrochimica Acta*, vol. 50, no. 10, pp. 2037–2046, 2005.

[38] Deseure, J., Bultel, Y., Dessemond, L., Siebert, E., and Ozil, P., "Modelling the porous cathode of a SOFC: oxygen reduction mechanism effect," *Journal of Applied Electrochemistry*, vol. 37, no. 1, pp. 129–136, 2007.

[39] Doyle, M., Meyers, J. P., and Newman, J., "Computer simulations of the impedance response of lithium rechargeable batteries," *Journal of The Electrochemical Society*, vol. 147, no. 1, pp. 99–110, 2000.

[40] Drews, T. O., Krishnan, S., Alameda, J. C., Gannon, D., Braatz, R. D., and Alkire, R. C., "Multiscale simulations of copper electrodeposition onto a resistive substrate," *IBM J. Res. Dev.*, vol. 49, no. 1, pp. 49–63, 2005.

[41] Endo, A., Fukunaga, H., Wen, C., and Yamada, K., "Cathodic reaction mechanism of dense La0.6Sr0.4CoO3 and La0.81Sr0.09MnO3 electrodes for solid oxide fuel cells," *Solid State Ionics*, vol. 135, no. 1-4, pp. 353–358, 2000.

[42] Endo, A., Ihara, M., Komiyama, H., and Yamada, K., "Cathodic reaction mechanism for dense Sr-doped lanthanum manganite electrodes," *Solid State Ionics*, vol. 86-88, pp. 1191–1195, 1996.

[43] Endo, A., Wada, S., Wen, C. J., Komiyama, H., and Yamada, K., "Low overvoltage mechanism of high ionic conducting cathode for solid oxide fuel cell," *Journal of The Electrochemical Society*, vol. 145, no. 3, pp. L35–L37, 1998.

[44] Fang, Q., "iso2mesh, url: http://iso2mesh.sourceforge.net."

[45] Fang, Q. and Boas, D., "Tetrahedral mesh generation from volumetric binary and gray-scale images," in *Proceedings of IEEE International Symposium on Biomedical Imaging 2009*, pp. 1142–1145, 2009.

[46] Feldberg, S. W., "Optimization of explicit finite-difference simulation of electrochemical phenomena utilizing an exponentially expanded space grid," *Journal of Electroanalytical Chemistry*, vol. 127, pp. 1–10, 1981.

[47] Fister, T. T., Fong, D. D., Eastman, J. A., Baldo, P. M., Highland, M. J., Fuoss, P. H., Balasubramaniam, K. R., Meador, J. C., and Salvador, P. A., "In situ characterization of strontium surface segregation in epitaxial La0.7Sr0.3MnO3 thin films as a function of oxygen partial pressure," *Applied Physics Letters*, vol. 93, no. 15, p. 151904, 2008.

[48] Fleig, J., "Solid oxide fuel cell cathodes: Polarization mechanisms and modeling of the electrochemical performance," *Annual Review Of Materials Research*, vol. 33, pp. 361–382, 2003.

[49] Fleig, J., "On the current-voltage characteristics of charge transfer reactions at mixed conducting electrodes on solid electrolytes," *Physical Chemistry Chemical Physics*, vol. 7, no. 9, pp. 2027–2037, 2005.

[50] Fleig, J., Baumann, F. S., Brichzin, V., Kim, H. R., Jamnik, J., Cristiani, G., Habermeier, H. U., and Maier, J., "Thin film microelectrodes in sofc electrode research," *Fuel Cells*, vol. 6, no. 3-4, pp. 284–292, 2006.

[51] Fleig, J. and Maier, J., "Finite element calculations of impedance effects at point contacts," *Electrochimica Acta*, vol. 41, no. 7-8, pp. 1003–1009, 1996.

[52] Fleig, J. and Maier, J., "The influence of current constriction on the impedance of polarizable electrodes - application to fuel cell electrodes," *Journal of The Electrochemical Society*, vol. 144, no. 11, pp. L302–L305, 1997.

[53] Fleig, J., Merkle, R., and Maier, J., "The p(O-2) dependence of oxygen surface coverage and exchange current density of mixed conducting oxide electrodes: model considerations," *Physical Chemistry Chemical Physics*, vol. 9, no. 21, pp. 2713–2723, 2007.

[54] Fukunaga, H., Ihara, M., Sakaki, K., and Yamada, K., "The relationship between overpotential and the three phase boundary length," *Solid State Ionics*, vol. 86-88, pp. 1179–1185, 1996.

[55] Garboczi, E. J. and Day, A. R., "Algorithm for computing the effective linear elastic properties of heterogeneous materials - 3-dimensional results for composites with equal phase Poisson ratios," *Journal of the Mechanics and Physics of Solids*, vol. 43, no. 9, pp. 1349–1362, 1995.

[56] Gockenbach, M. S., *Understanding and Implementing the Finite Element Method*. Philadelphia: SIAM, 2006.

[57] Gostovic, D., Smith, J. R., Kundinger, D. P., Jones, K. S., and Wachsman, E. D., "Three-dimensional reconstruction of porous LSCF cathodes," *Electrochemical and Solid-State Letters*, vol. 10, no. 12, p. B214, 2007.

[58] Grew, K. N., Chu, Y. S., Yi, J., Peracchio, A. A., Izzo, J. R., Hwu, Y., De Carlo, F., and Chiu, W. K. S., "Nondestructive nanoscale 3D elemental mapping and analysis of a solid oxide fuel cell anode," *Journal of The Electrochemical Society*, vol. 157, no. 6, pp. B783–B792, 2010.

[59] Guldberg, R. E., Hollister, S. J., and Charras, G. T., "The accuracy of digital image-based finite element models," *Journal of Biomechanical Engineering-Transactions of the Asme*, vol. 120, no. 2, pp. 289–295, 1998.

[60] Harten, A., Engquist, B., Osher, S., and Chakravarthy, S. R., "Uniformly high-order accurate essentially nonoscillatory schemes .3.," *Journal of Computational Physics*, vol. 71, no. 2, pp. 231–303, 1987.

[61] Huang, V. M. W., Vivier, V., Orazem, M. E., Pebere, N., and Tribollet, B., "The apparent constant-phase-element behavior of a disk electrode with faradaic reactions. a global and local impedance analysis ," *Journal of The Electrochemical Society*, vol. 154, no. 4, pp. S8–S8, 2007.

[62] Huang, Y. Y., Vohs, J. M., and Gorte, R. J., "An examination of LSM-LSCO mixtures for use in SOFC cathodes," *Journal of The Electrochemical Society*, vol. 153, no. 6, pp. A951–A955, 2006.

[63] Imanishi, N., Matsumura, T., Sumiya, Y., Yoshimura, K., Hirano, A., Takeda, Y., Mori, D., and Kanno, R., "Impedance spectroscopy of perovskite air electrodes for SOFC prepared by laser ablation method," *Solid State Ionics*, vol. 174, p. 245, 2004.

[64] Ioroi, T., Hara, T., Uchimoto, Y., Ogumi, Z., and Takehara, Z., "Preparation of perovskite-type La1-xSrxMnO3 films by vapor-phase processes and their electrochemical properties," *Journal of The Electrochemical Society*, vol. 144, no. 4, pp. 1362–1370, 1997.

[65] Ioroi, T., Hara, T., Uchimoto, Y., Ogumi, Z., and Takehara, Z.-i., "Preparation of perovskite-type La1-xSrxMnO3 films by vapor-phase processes and their electrochemical properties II. effects of doping strontium to LaMnO3 on the electrode properties," *Journal of The Electrochemical Society*, vol. 145, no. 6, pp. 1999–2004, 1998.

[66] Jamnik, J. and Maier, J., "Generalized equivalent circuits for mass and charge transport: chemical capacitance and its implications," *Physical Chemistry Chemical Physics*, vol. 3, no. 9, pp. 1668–1678, 2001.

[67] Ji, Y., Yuan, K., and Chung, J., "Monte-Carlo simulation and performance optimization for the cathode microstructure in a solid oxide fuel cell," *Journal of Power Sources*, vol. 165, pp. 774–785, 2007.

[68] Jiang, S. P. and Wang, W., "Fabrication and performance of GDC-impregnated (La,Sr)MnO3 cathodes for intermediate temperature solid oxide fuel cells," *Journal of The Electrochemical Society*, vol. 152, no. 7, pp. A1398–A1408, 2005.

[69] Joos, J., Carraro, T., Ender, M., Ruger, B., Weber, A., and Ivers-Tiffee, E., "Detailed microstructure analysis and simulations of porous electrodes," *ECS Transactions*, vol. 35, pp. 2357–2368, 2011.

[70] Joshi, A. S., Grew, K. N., Peracchio, A. A., and Chiu, W. K. S., "Lattice Boltzmann modeling of 2D gas transport in a solid oxide fuel cell anode," *Journal of Power Sources*, vol. 164, no. 2, pp. 631–638, 2007.

[71] Joslin, T. and Pletcher, D., "Digital-simulation of electrode processes - procedures for conserving computer time," *Journal of Electroanalytical Chemistry*, vol. 49, no. 2, pp. 171–186, 1974.

[72] Kawada, T., Masuda, K., Suzuki, J., Kaimai, A., Kawamura, K., Nigara, Y., Mizusaki, J., Yugami, H., Arashi, H., Sakai, N., and Yokokawa, H., "Oxygen isotope exchange with a dense La0.6Sr0.4CoO3-δ electrode on a Ce0.9Ca0.1O1.9 electrolyte," *Solid State Ionics*, vol. 121, pp. 271–279, 1999.

[73] Kawada, T., Suzuki, J., Sase, M., Kaimai, A., Yashiro, K., Nigara, Y., Mizusaki, J., Kawamura, K., and Yugami, H., "Determination of oxygen vacancy concentration in a thin film of La0.6Sr0.4CoO3-δ by an electrochemical method," *Journal of The Electrochemical Society*, vol. 149, no. 7, pp. E252–E259, 2002.

[74] Keil, R. G., "Resistive electrode effects on cyclic voltammetry," *Journal of The Electrochemical Society*, vol. 133, no. 7, pp. 1375–1379, 1986.

[75] Kenjo, T. and Nishiya, M., "LaMnO3 air cathodes containing ZrO2 electrolyte for high-temperature solid oxide fuel-cells," *Solid State Ionics*, vol. 57, no. 3-4, pp. 295–302, 1992.

[76] Kenjo, T., Osawa, S., and Fujikawa, K., "High-temperature air cathodes containing ion conductive oxides," *Journal of The Electrochemical Society*, vol. 138, no. 2, pp. 349–355, 1991.

[77] Kenney, B. and Karan, K., "Engineering of microstructure and design of a planar porous composite sofc cathode: a numerical analysis," *Solid State Ionics*, vol. 178, pp. 297–306, 2007.

[78] Keyak, J. H., Meagher, J. M., Skinner, H. B., and Mote, C. D., "Automated 3-dimensional finite-element modeling of bone - a new method," *Journal of Biomedical Engineering*, vol. 12, no. 5, pp. 389–397, 1990.

[79] Kilner, J. A., DeSouza, R. A., and Fullarton, I. C., "Surface exchange of oxygen in mixed conducting perovskite oxides," *Solid State Ionics*, vol. 86-88, pp. 703–709, 1996.

[80] Kim, J. H., Song, R. H., Song, K. S., Hyun, S. H., Shin, D. R., and Yokokawa, H., "Fabrication and characteristics of anode-supported flat-tube solid oxide fuel cell," *Journal of Power Sources*, vol. 122, no. 2, pp. 138–143, 2003.

[81] Koep, E., Compson, C., Liu, M. L., and Zhou, Z. P., "A photolithographic process for investigation of electrode reaction sites in solid oxide fuel cells," *Solid State Ionics*, vol. 176, no. 1-2, pp. 1–8, 2005.

[82] Koep, E., Mebane, D. S., Das, R., Compson, C., and Liu, M., "Characteristic thickness for a dense La0.8Sr0.2MnO3 electrode," *Electrochemical and Solid State Letters*, vol. 8, no. 11, pp. A592–A595, 2005.

[83] Kuznecov, M., Otschik, P., Eichler, K., and Schaffrath, W., "Structure and electrochemical properties of the cathode/electrolyte interface in the planar SOFC," *Berichte Der Bunsen-Gesellschaft-Physical Chemistry Chemical Physics*, vol. 102, no. 10, pp. 1410–1417, 1998.

[84] la O', G. J., Yildiz, B., McEuen, S., and Shao-Horn, Y., "Probing oxygen reduction reaction kinetics of Sr-doped LaMnO3 supported on Y2O3-stabilized ZrO2: EIS of dense, thin-film microelectrodes," *Journal of The Electrochemical Society*, vol. 154, no. 4, pp. B427–B438, 2007.

[85] Lane, J. A., Benson, S. J., Waller, D., and Kilner, J. A., "Oxygen transport in La0.6Sr0.4Co0.2Fe0.8O3-delta," *Solid State Ionics*, vol. 121, no. 1-4, pp. 201–208, 1999.

[86] Lankhorst, M. H. R., Bouwmeester, H. J. M., and Verweij, H., "High-temperature coulometric titration of La1-xSrxCoO3-delta: Evidence for the effect of electronic band structure on nonstoichiometry behavior," *Journal of Solid State Chemistry*, vol. 133, no. 2, pp. 555–567, 1997.

[87] Lankhorst, M. H. R., Bouwmeester, H. J. M., and Verweij, H., "Importance of electronic band structure to nonstoichiometric behaviour of La0.8Sr0.2CoO3-delta," *Solid State Ionics*, vol. 96, no. 1-2, pp. 21–27, 1997.

[88] Lankhorst, M. H. R., Bouwmeester, H. J. M., and Verweij, H., "Thermodynamics and transport of ionic and electronic defects in crystalline oxides," *Journal of the American Ceramic Society*, vol. 80, no. 9, pp. 2175–2198, 1997.

[89] Lankhorst, M. H. R. and tenElshof, J. E., "Thermodynamic quantities and defect structure of La0.6Sr0.4Co1-yFeyO3-delta(y=0-0.6) from high-temperature coulometric titration experiments," *Journal of Solid State Chemistry*, vol. 130, no. 2, pp. 302–310, 1997.

[90] Lauret, H. and Hammou, A., "Localization of oxygen cathodic reduction zone at lanthanum manganite zirconia interface," *Journal Of The European Ceramic Society*, vol. 16, no. 4, pp. 447–451, 1996.

[91] Lee, J. W., Liu, Z., Yang, L., Abernathy, H., Choi, S. H., Kim, H. E., and Liu, M. L., "Preparation of dense and uniform La(0.6)Sr(0.4)Co(0.2)Fe(0.8)O(3-delta) (LSCF) films for fundamental studies of SOFC cathodes," *Journal of Power Sources*, vol. 190, no. 2, pp. 307–310, 2009.

[92] Liu, M. L., "Equivalent circuit approximation to porous mixed-conducting oxygen electrodes in solid-state cells," *Journal of The Electrochemical Society*, vol. 145, no. 1, pp. 142–154, 1998.

[93] Liu, M., Lynch, M. E., Blinn, K., Choi, Y., and Alamgir, F., "Toward rational design of SOFC materials: Challenges and opportunities," *Materials Today*, 2011, submitted.

[94] Lu, Y. X., Kreller, C., and Adler, S. B., "Measurement and modeling of the impedance characteristics of porous La1-xSrxCoO3-delta electrodes," *Journal of The Electrochemical Society*, vol. 156, no. 4, pp. B513–B525, 2009.

[95] Lynch, M., L., Y., Qin, W., Choi, J., M., L., Blinn, K., and M., L., "Enhancement of La0.6Sr0.4Co0.2Fe0.8O3-δ durability and surface electrocatalytic activity by La0.85Sr0.15MnO3$\pm\delta$ investigated using a new test electrode platform," *Energy & Environmental Science*, vol. 4, pp. 2249–2258, 2011.

[96] Lynch, M. E., Mebane, D. S., Liu, Y., and Liu, M., "Triple phase boundary and surface transport in mixed conducting patterned electrodes," *Journal of The Electrochemical Society*, vol. 155, no. 6, pp. B635–B643, 2008.

[97] Maier, J., "On the correlation of macroscopic and microscopic rate constants in solid state chemistry," *Solid State Ionics*, vol. 112, no. 3-4, pp. 197–228, 1998.

[98] Maier, J. and Schwitzgebel, G., "Theoretical treatment of the diffusion coupled with reaction, applied to the example of a binary solid compound-MX," *Physica Status Solidi B-Basic Research*, vol. 113, no. 2, pp. 535–547, 1982.

[99] Maier, J., *Physical Chemistry of Ionic Materials*. Chichester, England: Wiley, 2004.

[100] Masuda, K., Kaimai, A., Kawamura, K.-i., Nigara, Y., Kawada, T., Mizusaki, J., Yugamni, H., and Arashi, H., "Electrochemical reaction kinetics of mixed conducting electrodes on CeO2-based solid electrolytes," *ECS Proceedings*, PV 97-40, pp. 473–482, 1997.

[101] Mebane, D. S. and Liu, M., "Classical, phenomenological analysis of the kinetics of reactions at the gas-exposed surface of mixed ionic electronic conductors," *Journal of Solid State Electrochemistry*, vol. 10, pp. 575–580, 2006.

[102] Mebane, D. S. and Liu, M., "Classical, phenomenological analysis of the kinetics of reaction at the gas-exposed surface of mixed ionic electronic conductors: Erratum," *Journal of Solid State Electrochemistry*, vol. 11, p. 448, 2007.

[103] Mebane, D. S., Liu, Y., and Liu, M., "A two-dimensional model and numerical treatment for mixed conducting thin films: the effect of sheet resistance," *Journal of The Electrochemical Society*, vol. 154, no. 5, pp. A421–A426, 2007.

[104] Mebane, D. S., Liu, Y., and Liu, M., "Refinement of the bulk defect model for LaxSr1-xMnO3$\pm\delta$," *Solid State Ionics*, vol. 178, no. 39-40, pp. 1950–1957, 2008.

[105] Mims, C., Joos, N., Heide, P. v. d., Jacobson, A., Chen, C., Chu, C., Kim, B., and Perry, S., "Oxygen transport in oxide thin film structures: Oriented La0.5Sr0.5CoO3-x on single-crystal yttria-stabilized zirconia," *Electrochemical and Solid State Letters*, vol. 3, no. 1, pp. 59–61, 2000.

[106] Minh, N. Q. and Takahashi, T., *Science and Technology of Ceramic Fuel Cells*. Amsterdam: Elsevier, 1995.

[107] Mishnaevsky, L. L., "Automatic voxel-based generation of 3D microstructural FE models and its application to the damage analysis of composites," *Materials Science and Engineering A-Structural Materials Properties Microstructure and Processing*, vol. 407, no. 1-2, pp. 11–23, 2005.

[108] Mitterdorfer, A. and Gauckler, L. J., "La2Zr2O7 formation and oxygen reduction kinetics of the La0.85Sr0.15MnO3, O-2(g)|YSZ system," *Solid State Ionics*, vol. 111, no. 3-4, pp. 185–218, 1998.

[109] Mitterdorfer, A. and Gauckler, L. J., "Identification of the reaction mechanism of the Pt, O-2(g)|yttria-stabilized zirconia system - part I: General framework, modelling, and structural investigation," *Solid State Ionics*, vol. 117, no. 3-4, pp. 187–202, 1999.

[110] Mitterdorfer, A. and Gauckler, L. J., "Identification of the reaction mechanism of the Pt, O-2(g)|yttria-stabilized zirconia system - part II: Model implementation, parameter estimation, and validation," *Solid State Ionics*, vol. 117, no. 3-4, pp. 203–217, 1999.

[111] Mitterdorfer, A. and Gauckler, L. J., "Reaction kinetics of the Pt, O-2(g)|c-ZrO2 system: precursor-mediated adsorption," *Solid State Ionics*, vol. 120, no. 1-4, pp. 211–225, 1999.

[112] Mizusaki, J., "Nonstoichiometry, diffusion, and electrical-properties of perovskite-type oxide electrode materials," *Solid State Ionics*, vol. 52, no. 1-3, pp. 79–91, 1992.

[113] Mizusaki, J., Mori, N., Takai, H., Yonemura, Y., Minamiue, H., Tagawa, H., Dokiya, M., Inaba, H., Naraya, K., Sasamoto, T., and Hashimoto, T., "Oxygen nonstoichiometry and defect equilibrium in the perovskite-type oxides La1-xSrxMnO3+d," *Solid State Ionics*, vol. 129, no. 1-4, pp. 163–177, 2000.

[114] Mizusaki, J., Saito, T., and Tagawa, H., "A chemical diffusion-controlled electrode reaction at the compact La1-xSrxMnO3/stabilized zirconia interface in oxygen atmospheres," *Journal of The Electrochemical Society*, vol. 143, no. 10, pp. 3065–3073, 1996.

[115] Mizusaki, J., Sasamoto, T., Cannon, W. R., and Bowen, H. K., "Electronic conductivity, Seebeck coefficient, and defect structure of La1-xSrxFeO3(x=0.1,0.25)," *Journal of the American Ceramic Society*, vol. 66, no. 4, pp. 247–252, 1983.

[116] Mizusaki, J., Tabuchi, J., Matsuura, T., Yamauchi, S., and Fueki, K., "Electrical-conductivity and Seebeck coefficient of nonstoichiometric La1-xSrxCoO3-delta," *Journal of The Electrochemical Society*, vol. 136, no. 7, pp. 2082–2088, 1989.

[117] Mizusaki, J., Tagawa, H., Tsuneyoshi, K., and Sawata, A., "Reaction-kinetics and microstructure of the solid oxide fuel-cells air electrode La0.6Ca0.4MnO3/YSZ," *Journal of The Electrochemical Society*, vol. 138, no. 7, pp. 1867–1873, 1991.

[118] Mizusaki, J., Yonemura, Y., Kamata, H., Ohyama, K., Mori, N., Takai, H., Tagawa, H., Dokiya, M., Naraya, K., Sasamoto, T., Inaba, H., and Hashimoto, T., "Electronic conductivity, seebeck coefficient, defect and electronic structure of nonstoichiometric La1-xSrxMnO3," *Solid State Ionics*, vol. 132, no. 3-4, pp. 167–180, 2000.

[119] Mizusaki, J., Yoshihiro, M., Yamauchi, S., and Fueki, K., "Nonstoichiometry and defect structure of the perovskite-type oxides La1-xSrxFeO3-delta," *Journal of Solid State Chemistry*, vol. 58, no. 2, pp. 257–266, 1985.

[120] Mizusaki, J., Amano, K., Yamauchi, S., and Fueki, K., "Electrode reaction at Pt, O2(g)/stabilized zirconia interfaces, part II: electrochemical measurements and analysis," *Solid State Ionics*, vol. 22, pp. 323–330, 1987.

[121] Mizusaki, J., Amano, K., Yamauchi, S., and Fueki, K., "Electrode reaction at the Pt, O2(g)/stabilized zirconia interfaces, part I: theoretical consideration of reaction model," *Solid State Ionics*, vol. 22, pp. 313–322, 1987.

[122] Monk, P. M. S., *Electrochromism and electrochromic devices*. Cambridge: Cambridge University Press, 2007.

[123] Mori, D., Oka, H., Suzuki, Y., Sonoyama, N., Yamada, A., Kanno, R., Sumiya, Y., Imanishi, N., and Takeda, Y., "Synthesis, structure, and electrochemical properties of epitaxial perovskite La0.8Sr0.2CoO3 film on YSZ substrate," *Solid State Ionics*, vol. 177, pp. 535–540, 2006.

[124] Mosleh, M., Sogaard, M., and Hendriksen, P. V., "Kinetics and mechanisms of oxygen surface exchange on La0.6Sr0.4FeO3-delta thin films," *Journal of The Electrochemical Society*, vol. 156, no. 4, pp. B441–B457, 2009.

[125] Newman, J. and Thomas-Alyea, K., *Electrochemical Systems*. Hoboken, NJ: Wiley-Interscience, third ed., 2004.

[126] Nicholas, J. D. and Barnett, S. A., "Finite-element modeling of idealized infiltrated composite solid oxide fuel cell cathodes," *Journal of The Electrochemical Society*, vol. 156, no. 4, pp. B458–B464, 2009.

[127] Niebur, G. L., Yuen, J. C., Hsia, A. C., and Keaveny, T. M., "Convergence behavior of high-resolution finite element models of trabecular bone," *Journal of Biomechanical Engineering-Transactions of the Asme*, vol. 121, no. 6, pp. 629–635, 1999.

[128] Orazem, M. E. and Tribollet, B., *Electrochemical Impedance Spectroscopy*. Hoboken, N.J.: Wiley, 2008.

[129] Ostergard, M. J. L., Clausen, C., Bagger, C., and Mogensen, M., "Manganite-zirconia composite cathodes for SOFC - influence of structure and composition," *Electrochimica Acta*, vol. 40, no. 12, pp. 1971–1981, 1995.

[130] Parsons, R., "General equations for the kinetics of electrode processes," *Transactions of the Faraday Society*, vol. 47, pp. 1332–44, 1951.

[131] Poulsen, F. W., "Defect chemistry modelling of oxygen-stoichiometry, vacancy concentrations, and conductivity of (La1-xSrx)(y)MnO3 +/-delta," *Solid State Ionics*, vol. 129, no. 1-4, pp. 145–162, 2000.

[132] Prestat, M., Infortuna, A., Korrodi, S., Rey-Mermet, S., Muralt, P., and Gauckler, L. J., "Oxygen reduction at thin dense La0.52Sr0.48Co0.18Fe0.82O3-delta electrodes. part II: Experimental assessment of the reaction kinetics," *Journal of Electroceramics*, vol. 18, no. 1-2, pp. 111–120, 2007.

[133] Radhakrishnan, R., Virkar, A. V., and Singhal, S. C., "Estimation of charge-transfer resistivity of La0.8Sr0.2MnO3 cathode on Y0.16Zr0.84O2 electrolyte using patterned electrodes," *Journal of The Electrochemical Society*, vol. 152, no. 1, pp. A210–A218, 2005.

[134] Reinhardt, G. and Gopel, W., "Electrode reactions at solid electrolytes: finite difference calculations to describe geometric and electrical properties of planar devices," *ECS Proceedings*, PV 97-24, pp. 610–630, 1998.

[135] Rickert, H., *Electrochemistry of Solids: An Introduction*, vol. 7. Berlin: Springer, 1982.

[136] Ringuedé, A. and Fouletier, J., "Oxygen reaction on strontium-doped lanthanum cobaltite dense electrodes at intermediate temperatures," *Solid State Ionics*, vol. 139, no. 3-4, pp. 167–177, 2001.

[137] Rivara, M. C., "Algorithms for refining triangular grids suitable for adaptive and multigrid techniques," *International Journal for Numerical Methods in Engineering*, vol. 20, no. 4, pp. 745–756, 1984.

[138] Rivara, M. C. and Levin, C., "A 3-D refinement algorithm suitable for adaptive and multigrid techniques," *Communications in Applied Numerical Methods*, vol. 8, no. 5, pp. 281–290, 1992.

[139] Rüger, B., Weber, A., and Ivers-Tiffée, E., "3D-modelling and performance evaluation of mixed conducting (MIEC) cathodes," *ECS Transactions*, vol. 7, no. 1, pp. 2065–2074, 2007.

[140] Sasaki, K., Wurth, J. P., Gschwend, R., Godickemeier, M., and Gauckler, L. J., "Microstructure-property relations of solid oxide fuel cell cathodes and current collectors - cathodic polarization and ohmic resistance," *Journal of The Electrochemical Society*, vol. 143, no. 2, pp. 530–543, 1996.

[141] Schmalzried, H., *Solid State Reactions*. New York: Academic Press, 1974.

[142] Schneider, L., Martin, C., Bultel, Y., Bouvard, D., and Siebert, E., "Discrete modeling of the electrochemical performance of sofc electrodes," *Electrochimica Acta*, vol. 52, pp. 314–324, 2006.

[143] Shikazono, N., Kanno, D., Matsuzaki, K., Teshima, H., Sumino, S., and Kasagi, N., "Numerical assessment of SOFC anode polarization based on three-dimensional model microstructure reconstructed from FIB-SEM images," *Journal of The Electrochemical Society*, vol. 157, no. 5, pp. B665–B672, 2010.

[144] Siebert, E., Hammouche, A., and Kleitz, M., "Impedance spectroscopy analysis of La1-xSrxMnO3-yttria-stabilized zirconia electrode-kinetics," *Electrochimica Acta*, vol. 40, no. 11, pp. 1741–1753, 1995.

[145] Singhal, S. C. and Kendall, K., *High Temperature Solid Oxide Fuel Cells: Fundamentals, Design and Applications*. Amsterdam: Elsevier, 2003.

[146] Sitte, W., Bucher, E., Benisek, A., and Preis, W., "Oxygen nonstoichiometry and ionic transport properties of La0.4Sr0.6CoO3-delta," *Spectrochimica Acta Part A-Molecular and Biomolecular Spectroscopy*, vol. 57, no. 10, pp. 2071–2076, 2001.

[147] Smith, J. R., Chen, A., Gostovic, D., Hickey, D., Kundinger, D., Duncan, K. L., DeHoff, R. T., Jones, K. S., and Wachsman, E. D., "Evaluation of the relationship between cathode microstructure and electrochemical behavior for SOFCs," *Solid State Ionics*, vol. 180, no. 1, pp. 90–98, 2009.

[148] Steele, B. C. H., "Survey of materials selection for ceramic fuel cells .2. cathodes and anodes," *Solid State Ionics*, vol. 86-88, pp. 1223–1234, 1996.

[149] Sunde, S., "Monte Carlo simulations of conductivity of composite electrodes for solid oxide fuel cells," *Journal of The Electrochemical Society*, vol. 143, no. 3, pp. 1123–1132, 1996.

[150] Sunde, S., "Monte Carlo simulations of polarization resistance of composite electrodes for solid oxide fuel cells," *Journal of The Electrochemical Society*, vol. 143, no. 6, pp. 1930–1939, 1996.

[151] Sunde, S., "Calculation of conductivity and polarization resistance of composite SOFC electrodes from random resistor networks," *Journal of The Electrochemical Society*, vol. 142, no. 4, pp. L50–L52, 1995.

[152] Svensson, A. M., Sunde, S., and Nisancioglu, K., "Mathematical modeling of oxygen exchange and transport in air-perovskite-YSZ interface regions .1. reduction of intermediately adsorbed oxygen," *Journal of The Electrochemical Society*, vol. 144, no. 8, pp. 2719–2732, 1997.

[153] Svensson, A. M., Sunde, S., and Nisancioglu, K., "Mathematical modeling of oxygen exchange and transport in air-perovskite-yttria-stabilized zirconia interface regions - II. direct exchange of oxygen vacancies," *Journal of The Electrochemical Society*, vol. 145, no. 4, pp. 1390–1400, 1998.

[154] Svensson, A. M., Sunde, S., and Nisancioglu, K., "A mathematical model of the porous SOFC cathode," *Solid State Ionics*, vol. 86, pp. 1211–1216, 1996.

[155] Tai, L. W., Nasrallah, M. M., and Anderson, H. U., "Thermochemical stability, electrical-conductivity, and Seebeck coefficient of Sr-doped LaCo0.2Fe0.8O3-delta," *Journal of Solid State Chemistry*, vol. 118, no. 1, pp. 117–124, 1995.

[156] Tai, L. W., Nasrallah, M. M., Anderson, H. U., Sparlin, D. M., and Sehlin, S. R., "Structure and electrical properties of La1-xSrxCo1-yFeyO3. part 2. the system La1-xSrxCo0.2Fe0.8O3," *Solid State Ionics*, vol. 76, no. 3,4, pp. 273–283, 1995.

[157] Takeda, Y., Kanno, R., Noda, M., Tomida, Y., and Yamamoto, O., "Cathodic polarization phenomena of perovskite oxide electrodes with stabilized zirconia," *Journal of The Electrochemical Society*, vol. 134, no. 11, pp. 2656–2661, 1987.

[158] ten Elshof, J. E., Lankhorst, M. H. R., and Bouwmeester, H. J. M., "Oxygen exchange and diffusion coefficients of strontium-doped lanthanum ferrites by electrical conductivity relaxation," *Journal of The Electrochemical Society*, vol. 144, no. 3, pp. 1060–1067, 1997.

[159] Thursfield, A. and Metcalfe, I. S., "Air separation using a catalytically modified mixed conducting ceramic hollow fibre membrane module," *Journal of Membrane Science*, vol. 288, no. 1-2, pp. 175–187, 2007.

[160] Tietz, F., Buchkremer, H.-P., and Stover, D., "Components manufacturing for solid oxide fuel cells," *Solid State Ionics*, vol. 152-153, pp. 373–381, 2002.

[161] Tribollet, B. and Newman, J., "Impedance model for a concentrated solution. application to the electrodissolution of copper in chloride solutions," *Journal of The Electrochemical Society*, vol. 131, no. 12, pp. 2780–5, 1984.

[162] Tucceri, R. I. and Posadas, D., "Theoretical approach to the resistive behavior of thin solid film electrodes under direct-current polarization," *Journal of The Electrochemical Society*, vol. 128, no. 7, pp. 1478–1483, 1981.

[163] van Hassel, B. A., Kawada, T., Sakai, N., Yokokawa, H., Dokiya, M., and Bouwmeester, H. J. M., "Oxygen permeation modeling of perovskites," *Solid State Ionics*, vol. 66, no. 3-4, pp. 295–305, 1993.

[164] van Leer, B., Lo, M., and Van Raalte, M., "A discontinuous Galerkin method for diffusion based on recovery," in *18th AIAA Computational Fluid Dynamics Conference*, vol. 1 of *Collection of Technical Papers - 18th AIAA Computational Fluid Dynamics Conference*, (Miami, FL, United States), pp. 763–774, American Institute of Aeronautics and Astronautics Inc., Reston, VA 20191-4344, United States, 2007.

[165] van Leer, B. and Nomura, S., "Discontinuous Galerkin for diffusion," in *17th AIAA Computational Fluid Dynamics Conference*, Collection of Technical Papers - 17th AIAA Computational Fluid Dynamics Conference, (Toronto, Ontario Canada), pp. 1–30, American Institute of Aeronautics and Astronautics Inc., Reston, VA 20191-4344, United States, 2005.

[166] Vohs, J. M. and Gorte, R. J., "High-performance SOFC cathodes prepared by infiltration," *Advanced Materials*, vol. 21, no. 9, pp. 943–956, 2009.

[167] Wang, S. R., Katsuki, M., Dokiya, M., and Hashimoto, T., "High temperature properties of La0.6Sr0.4Co0.8Fe0.2O3-delta phase structure and electrical conductivity," *Solid State Ionics*, vol. 159, no. 1-2, pp. 71–78, 2003.

[168] Watanabe, M., Uchida, H., Shibata, M., Mochizuki, N., and Amikura, K., "High-performance catalyzed-reaction layer for medium-temperature operating solid oxide fuel-cells," *Journal of The Electrochemical Society*, vol. 141, no. 2, pp. 342–346, 1994.

[169] Wilson, J. R., Kobsiriphat, W., Mendoza, R., Chen, H.-Y., Hiller, J. M., Miller, D. J., Thornton, K., Voorhees, P. W., Adler, S. B., and Barnett, S. A., "Three-dimensional reconstruction of a solid-oxide fuel-cell anode," *Nature Materials*, vol. 5, no. 7, pp. 541–544, 2006.

[170] Winkler, J., Hendriksen, P. V., Bonanos, N., and Mogensen, M., "Geometric requirements of solid electrolyte cells with a reference electrode," *Journal of The Electrochemical Society*, vol. 145, no. 4, pp. 1184–1192, 1998.

[171] Wu, Z. and Liu, M., "Modelling of ambipolar transport properties of composite mixed ionic-electronic conductors," *Solid State Ionics*, vol. 93, pp. 65–84, 1997.

[172] Yamamoto, O., Takeda, Y., Kanno, R., and Noda, M., "Perovskite-type oxides as oxygen electrodes for high-temperature oxide fuel-cells," *Solid State Ionics*, vol. 22, no. 2-3, pp. 241–246, 1987.

[173] Yang, Y., Chen, C., Chen, S., Chu, C., and Jacobson, A., "Impedance studies of oxygen exchange on dense thin film electrodes of La0.5Sr0.5CoO3-δ," *Journal of The Electrochemical Society*, vol. 147, no. 11, pp. 4001–4007, 2000.

[174] Yang, Y. L., Jacobson, A., Chen, C., Luo, G., Ross, K., and Chu, C., "Oxygen exchange kinetics on a highly oriented La0.5Sr0.5CoO3-δ thin film prepared by pulsed-laser deposition," *Applied Physics Letters*, vol. 79, no. 6, pp. 776–778, 2001.

[175] Yoo, S., Shin, J. Y., and Kim, G., "Thermodynamic and electrical characteristics of NdBaCo2O5+delta at various oxidation and reduction states," *Journal of Materials Chemistry*, vol. 21, no. 2, pp. 439–443, 2011.

[176] Zhao, F. and Virkar, A. V., "Effect of morphology and space charge on conduction through porous doped ceria," *Journal of Power Sources*, vol. 195, no. 19, pp. 6268–6279, 2010.

[177] Zhou, W., Ran, R., and Shao, Z. P., "Progress in understanding and development of Ba0.5Sr0.5Co0.8Fe0.2O3-delta-based cathodes for intermediate-temperature solid-oxide fuel cells: A review," *Journal of Power Sources*, vol. 192, no. 2, pp. 231–246, 2009.

[178] Zhou, W., Sunarso, J., Chen, Z.-G., Ge, L., Motuzas, J., Zou, J., Wang, G., Julbe, A., and Zhu, Z., "Novel B-site ordered double perovskite Ba2Bi0.1Sc0.2Co1.7O6-x for highly efficient oxygen reduction reaction," *Energy & Environmental Science*, vol. 4, no. 3, pp. 872–875, 2011.

VITA

Education

- Ph.D., Materials Science and Engineering, Georgia Institute of Technology, expected Dec. 2011
- M.S., Materials Science and Engineering, Virginia Tech, Aug. 2006
- B.S., Materials Science and Engineering, Virginia Tech, May 2005
- B.S., Mathematics, Virginia Tech, May 2005

Publications

First Author

1. M.E. Lynch, S. Feng, and M. Liu, "A Method for Electrochemical Simulation on Porous Composite SOFC Cathodes using Conservative Point Defect Ensembles," in preparation.
2. M.E. Lynch and M. Liu, "Finite Element Electrochemistry Models Conformal to Porous Microstructure Applied Using Commonly Available Packages," in preparation.
3. M. E. Lynch, L. Yang, W. Qin, J.-J. Choi, Mingfei Liu, K. Blinn, and Meilin Liu, "Enhancement of $La_{0.6}Sr_{0.4}Co_{0.2}Fe_{0.8}O_{3-\delta}$ Durability and Surface Electrocatalytic Activity by $La_{0.85}Sr_{0.15}MnO_{3\pm\delta}$ Investigated using a New Test Electrode Platform," Energy & Environmental Science, 4, 2249-2258 (2011).
4. M.E. Lynch and M. Liu, "Investigation of Sheet Resistance in Thin-Film Mixed-Conducting SOFC Cathodes," Journal of Power Sources, 195, 5155-5166 (2010).

5. M.E. Lynch, D.S. Mebane, and M. Liu, "Numerical Continuum Modeling and Simulation of Mixed-Conducting Thin Film and Patterned Electrodes," in Proceedings of the 33rd International Conference on Advanced Ceramics and Composites (2009).

6. M.E. Lynch, D. S. Mebane, Y. Liu and M. Liu, "Triple Phase Boundary and Surface Transport in Mixed Conducting Patterned Electrodes," Journal of The Electrochemical Society, 155 (6), B635-B643 (2008).

7. M.E. Lynch, D.C. Folz, and D.E. Clark, "The Effect of Microwaves on Migration of Lithium and Silicon from Lithium Disilicate (Li2O-2SiO2) Glass," Food Additives and Contaminants, 25(4), 519-526 (2008).

8. M.E. Lynch, D.C. Folz, and D.E. Clark, "Use of FTIR Reflectance Spectroscopy to Monitor Corrosion Mechanisms on Glass Surfaces," Journal of Non-Crystalline Solids, 353, 2667 (2007).

9. M. Lynch, J. Langman, D. Clark, and D. Folz, "Deposition and Single-Step Processing of YBCO Thick Films for Multilayered Electronics," in Proceedings of the 107th Annual Meeting & Exposition of the American Ceramic Society (2005).

Co-Author

1. M. Liu, M.E. Lynch, K. Blinn, Y. Choi, F. Alamgir, "Rational SOFC Material Design: New Advances and Tools," Materials Today, invited review, accepted.

2. S. Zhang, M. Lynch, A.M. Gokhale, and M. Liu, "Unbiased Characterization of Three-Phase Microstructure of Porous Lanthanum Doped Strontium Manganite/Yttria-Stabilized Zirconia Composite Cathodes for Solid Oxide Fuel Cells Using Atomic Force Microscopy and Stereology," Journal of Power Sources, 192, 367 (2009).

3. Y. Choi, M.E. Lynch, M.C. Lin, and M. Liu, "Prediction of O2 Dissociation Kinetics on LaMnO3-Based Cathode Materials for Solid Oxide Fuel Cells," Journal of Physical Chemistry C, 113(17), 7290 (2009).

Selected Presentations

1. M.E. Lynch, W. Qin, J. Choi, Mingfei Liu, Meilin Liu, "Theory, Investigation, and Stability of Cathode Electrocatalytic Activity," 11th Annual US DOE SECA Workshop, Pittsburgh, Pennsylvania, USA, July 2010.

2. M.E. Lynch, X. Li, L. Yang, D. Mebane, M. Liu, "Investigation of SOFC Cathode Kinetics by Means of Continuum Modeling and Well-Defined Electrodes," 217th Meeting of The Electrochemical Society, Vancouver, BC, Canada, April 2010.

3. M.E. Lynch, D.S. Mebane, Y.M. Choi, and M. Liu, "Numerical Continuum Modeling of Thin Film Solid Oxide Fuel Cell Cathode Materials," International Center for Materials Research Workshop on Modeling of Fuel Cell Electrocatalysts, Santa Barbara, California, USA, July 2009.

4. M.E. Lynch, "An Overview of Continuum-Level Modeling of SOFC Electrode Processes," (invited student tutorial) International Center for Materials Research Workshop on Modeling of Fuel Cell Electrocatalysts, Santa Barbara, California, USA, July 2009.

5. M.E. Lynch, D.S. Mebane, and M. Liu, "Numerical Continuum Modeling and Simulation of Mixed-Conducting Thin Film and Patterned Electrodes," American Ceramic Society, 33rd International Conference on Advanced Ceramics and Composites, Daytona Beach, Florida, USA, January 2009.

Honors and Awards

· National Science Foundation Graduate Research Fellowship, Aug. 2005-Aug. 2008

· Research Initiation Award, School of Materials Science and Engineering, Georgia Tech, 2008

· Tau Beta Pi (engineering honor society), 2003

Professional Affiliations

· The Electrochemical Society, student member

· Material Advantage

· Society for Industrial and Applied Mathematics (SIAM), student member

Skills

· Computer: MATLAB, COMSOL Multiphysics, C++, LabView, ImageJ, LaTeX, Inkscape, SciDaVis, Microsoft Office

· Numerical simulation: Multiphysics modeling, finite element, finite volume, finite difference methods

· Materials processing and characterization: Electrochemical impedance spectroscopy, high-temperature electrochemical testing, scanning electron microscopy, x-ray diffraction, quantitative microscopy, metallography, ceramic powder processing, spray coating, microwave and conventional thermal processing of materials